

# Shape and size control of colloidal CdSe nanocrystals in the presence of carboxylate and alkylamine ligands

Thèse N° 7298

Présentée le 26 septembre 2019

à la Faculté des sciences et techniques de l'ingénieur  
Laboratoire de microsystemes 2  
Programme doctoral en microsystemes et microélectronique

pour l'obtention du grade de Docteur ès Sciences

par

**Xiaopeng HUANG**

Acceptée sur proposition du jury

Prof. L. G. Villanueva Torrijo, président du jury  
Prof. M. Gijs, V. K. Parashar, directeurs de thèse  
Prof. T. Bürgi, rapporteur  
Dr D. Dirin, rapporteur  
Prof. J. Brugger, rapporteur

2019



# Acknowledgements

Time flies! How can I believe that I have spent four years for the PhD study in Lausanne! This experience, in a word, is really wonderful, meaningful and unforgettable! During this period of time, I get the chance to study and work in a highly internationalized and multicultural environment with people from distinct cultural backgrounds. Many people and organizations have given me valuable help and suggestions towards the successful preparation of this thesis. Upon the completion of this study, I would like to take this opportunity to express my sincere gratitude to all of them.

Foremost, I would like to express my deepest gratitude to Prof. Martin Gijs, my supervisor, for accepting me as his PhD student to do the search in his prestigious group. His constant encouragement and full support are of particular importance for me to obtain the achievement in this thesis. Under his supervision, I obtained very high freedom in doing scientific research, from searching the topics of interest, investigating the possible approaches to solve the problem, trying out more new ideas to finally collecting and summarizing the data to publish. I learned to think of issues independently, critically and insightfully. His healthy, relaxing and easy lifestyle also triggers me to think of the importance of balancing work and life. I highly appreciate his great effort to check each chapter of this thesis as well as each research article, which is crucial for the completion of this thesis. I would also like to express my heartfelt gratitude for Dr. Parashar Virendra for guiding me into the field of colloidal semiconductor nanocrystals. He is smart and easygoing, already with a smile on his face. I particularly thank him for the tough questions he raised during the subgroup meeting. In many cases, knowing a question is more much important than finding the solution to resolve it. I also appreciate his bridging role in correctly conveying some of my viewpoints to Prof. Gijs.

Secondly, I would like to express my great thanks to Prof. Brugger, Prof. Bürgi, Dr. Dmitry and Prof. Villanueva, for their efforts as the jury members of the oral exam, reading and evaluating my thesis. I owe a special debt of gratitude to the collaborators. Dr. Thomas LaGrange and Dr. Marco Cantoni from CIME have given me very useful assistance and instruction in performing the electron microscopy characterization. Jacques Morisod and Pierre Mettraux from MHMC helped me a lot in using the instruments for material characterization, including UV-vis, Fluorescence, FTIR, TGA, DSC and XPS. Dr. Wenhua Bi from the physics department is thanked for helping me with the XRD characterization. Prof. Zhimin Ao from GDUT China is acknowledged for the instructive discussion on the DFT simulation. Their efforts greatly contribute to the

successful acquisition of the data in this thesis. I also want to thank the CMI staff for their instruction on the machines in the cleanroom and discussion on the process flow of my chip. Although the related projects finally turn out to be not as feasible as expected, I indeed reap a lot of experience and skills in various microfabrication techniques. Additionally, special thanks should also be given to Swiss National Science Foundation (Grant 200021-146237) and China Scholarship Council (201406360047) for providing the financial support.

Thirdly, I would like to give my special thanks to the colleagues in LMIS2. A harmonious and cozy lab atmosphere is indispensable for doing excellent research. Dr. Dong Li is greatly appreciated for providing me with critical help and suggestions whenever I had difficulty in the lab. It was really a great time to enjoy the research in the lab and the life outside the lab with him. Baris Atakan, being my officemate for four years, is thanked for sharing the joy and sadness in daily life and providing every immediate assistance once needed. Martin Melis, the secretary of the lab, is thanked for her unlimited support in administrative matters and giving me every kind reminder. Abdeljalil Sayah, knowing almost everything hidden in the lab, is thanked for helping me find the necessary stuff for the experimental setup. Prof. Hui Yang is thanked for providing me with some earnest advices before I joined the group. Roger Krenger, Vittorio Viri, Muaz Draz, Daniel Migliozi, Farzad Rezaeianaran, Dr. Raphaël Trouillon, Dr. Cristina Letizia, Dr. Matteo Cornaglia and Dr. Gergely Huszka are thanked for every quick help in the daily life. It is really of great honor for me to have you as my colleagues.

Fourthly, I would like to give my sincere thanks to my roommates in Lausanne, including Jian Wang, Rensheng Pan, Lingfeng Zhang, Zujie Zhong, Yuya Wakabayashi, Ivo Aguiar Maceira and Haitham Kandil. I thank them for sharing the apartment with me, giving me so much fun and knowledge during the afterwork life. Special thanks should be given to Jian Wang, being like my brother, for his sincere help in every aspect of study and life. I also want to express my thanks to all my Chinese friends in Switzerland, especially including Junrui Zhang, Xiao Di, Zhenzhu Meng, Hao Xue, Minghua Zhu, Zaiwei Wang, Prof. Jingshan Luo, Jingwei Zhang, Rongrong Xiang, Zhiwei Yang, Ya Wang, Dr. Shoufan Cao, He Gao, Dr. Yunpeng Qu, Huachuan Du, Prof. Jingshan Luo, Dr. Chao Liu, Jiangtao Zhou, Prof. Hua Wu, Prof. Delong Xie, Prof. Xin Sheng, Dr. Lu Jin, Dr. Xia Meng, Dr. Xiaobao Cao, Dr. Feng Shao, Tong Liang, Prof. Weixin Huang, Yanrui Ju and Dr. Huan Ma. Thanks for enjoying each ping-pong match, hot-pot dinner, dumpling dinner, barbecue, card game, skiing and hiking with me. Your presence in my life really makes my PhD study in Lausanne colorful and wonderful. Particularly, I should



give special thanks to Zhenzhu Meng for helping me translating the abstract into a French version.

Last but not least, my thanks would go to my beloved parents, Jianwen Huang and Biyue Huang, for their unconditional love, support and encouragement during my pursuit for the academic career. This thesis is dedicated to them for their 30 years of hard-working endeavors, with all my love.

Xiaopeng Huang

18 September, 2019 in Lausanne



# Abstract

In the past decades, colloidal cadmium selenide nanocrystals (CdSe NCs) have intrigued extensive academic interests due to their unique and easily-adjustable electronic and optical properties, leading to a wide range of applications in biological imaging, displays, lasers, and solar energy conversion. Control over the shape and size of these nanoscale materials is of great importance for a fundamental understanding of crystal growth and of high practical significance for obtaining NCs with on-demand properties. Due to the large specific area of the nanostructures, organic surface ligands play a critical role in the controlled synthesis of NCs in solution. In this thesis, we focus on investigating the shape and size evolution of colloidal CdSe nanomaterials in the presence of carboxylate and alkylamine surface ligands. By elaborating the combination of carboxylates and alkylamines with different hydrocarbon chains, zero-dimensional (0D) quantum dots (QDs), one-dimensional (1D) nanorods, two-dimensional (2D) nanotubes, nanosheets and nanoplatelets were successfully obtained in a controllable way and their growth kinetics and formation mechanism were further explored.

First, we study the evolution of shape, size and optical quality of colloidal CdSe NCs upon adding both a carboxylic acid and an amine ligand to the cadmium acetate green chemistry source. Four reaction routes are designed to distinguish the role of the carboxylic acid and the primary amine. The effect of ligand length is further investigated by using carboxylate complexes of lauric acid (LAc), myristic acid (MAc), stearic acid (SAc) and oleic acid (OAc), along with the Lewis bases octyl amine (OAm), dodecyl amine (DDAm), hexadecyl amine (HDAm) and octadecyl amine (ODAm). While single use of either acid or amine ligands does not lead to an advantageous change in producing high-quality CdSe QDs, an evident synergistic effect is observed by forming QDs with smaller size, more isotropic morphology, less agglomerated behavior and higher PLQY upon concurrent use of a long-chain carboxylic acid and a long-chain amine ligand.

Second, we establish the dual role played by oleylamine (OLAm) during the synthesis of CdSe QDs using cadmium oleate as the Cd source. Earlier reports suggested the role of alkylamine either as nucleating or as passivating agent in controlling the growth of CdSe QDs. Remarkably, by exploring four different synthesis routes, in which the reactant addition, timing and concentration are varied, we find that both these two phenomena coexist and control the synthesis. While examining if there is any effect of concentration of OLAm on this synthesis, we find that, at lower contents of OLAm (< 0.5 mmol), the latter prominently acts as an agent acting on nucleation, increasing the number of nuclei, reducing the nuclei (initial monomer units) size and thereby increasing the NCs concentration resulting in a small NCs size, down to 2.7 nm. Whereas at higher contents (> 1.0 mmol), it serves more as a passivating agent by deterring both nucleation and growth processes, so generating fewer NCs with larger size up to 3.6 nm. Thus, by adjusting the influence between nucleation and passivation, we can better control the final NCs size and so tune their size-dependent optical properties.

Third, we demonstrate the synthesis of 2D CdSe NCs and nanotubes when short-chain acetate and alkylamines are used as the ligands. Most interestingly, with a combination of acetate and dioctylamine (DOAm), CdSe nanotubes with atomically-flat walls are formed via a template-free

protocol. They feature a multi-walled structure, sharp absorption and emission at around 460 nm, and Cd-terminated {100} planes as top and bottom surface in the wall thickness direction. Anisotropic growth is found to result from the utilization of acetate ligand; meanwhile, the addition of DOAm assists in formation of more regular tubular structures. We further elucidate the growth mechanism as consisting of a non-planar 2D oriented attachment approach; that is, simultaneous lateral and angular attachment of early-stage nanoplatelets into curved nanosheets and finally a tubular architecture.

Finally, we further elucidate the formation mechanism of anisotropic CdSe NCs in the presence of dioctylamine ligand and carboxylate ligands having different chain length. Both short- and long-chain carboxylate ligands are found to induce the anisotropic growth of CdSe NCs by the attachment of early-formed NC building blocks. A morphological transition from nanotubes and nanosheets to irregular nanorods and finally to QDs is observed when the carbon number of carboxylate ligands increases from 2 to 18. The main reason is that two different NC building blocks, namely kinetically stable primary NCs exposing by {110} and {100} facets and thermodynamically stable primary NCs exposing by {100} and {111} facets, are formed in the presence of short- and long-chain carboxylates, respectively. A conversion between these two building blocks can be triggered by using a medium-chain carboxylate ligand at different concentration and temperature. Density functional theory (DFT) simulation is performed to reveal the surface structure of zincblende CdSe NCs in the absence and presence of carboxylate ligands. We propose that the different local monomer supersaturations caused by different chain-length carboxylates are responsible for the production of intrinsically different building blocks.

## Keywords

colloidal nanocrystals, cadmium selenide, carboxylate, alkylamine, quantum dots, nanorods, nanotubes, nanosheets, nanoplatelets, 2D materials, growth kinetics, particle assembly, oriented attachment

# Résumé

Au cours des dernières décennies, les nanocristaux de séléniure de cadmium colloïdal (CdSe NC) ont suscité de nombreux intérêts universitaires car leurs propriétés électroniques, leur optiques uniques et leur réglaciation facile, attribuant à un large éventail d'applications en imageries biologiques, affichages, lasers et conversions de l'énergie solaire. Le contrôle de la forme et de la taille de ces matériaux à l'échelle nanométrique est très important pour la compréhension fondamentale de la croissance des cristaux, et pour obtenir des CN avec des propriétés à la demande. En raison de la grande surface spécifique des nanostructures, les ligands organiques de surface jouent un rôle essentiel dans la synthèse contrôlée des NC pour les résoudre. Dans cette thèse, nous nous concentrons sur l'étude de l'évolution de la forme et de la taille de nanomatériaux colloïdaux de CdSe en présence de ligands de surface de carboxylate et d'alkylamine. En élaborant la combinaison de carboxylates et d'alkylamines avec des différentes chaînes d'hydrocarbures, des points quantiques (QD), des nanorodes unidimensionnels (1D), des nanotubes, des nanosheets et des nanoplatelets à une dimension (1D) ont été obtenus avec succès, leur cinétique de croissance et leur mécanisme de formation ont aussi été approfondis.

Tout d'abord, au moyen de l'ajout d'un acide carboxylique et d'un ligand d'amine à la source de chimie verte de l'acétate de cadmium, nous étudions l'évolution de la forme, de la taille et de la qualité optique des nanoparticules de CdSe colloïdales. Les rôles de l'acide carboxylique et de l'aminé primaire sont distingués par quatre voies de réaction. Ensuite, l'effet de la longueur du ligand est étudié par la façon d'utiliser des complexes carboxylates d'acide laurique (LAc), d'acide myristique (MAc), d'acide stéarique (SAC) et d'acide oléique (OAc), ainsi que des bases de Lewis octyl amine (OAm), dodécyl amine (DDAm), l'hexadécylamine (HDAm) et l'octadécylamine (ODAm). Malgré l'utilisation unique de ligands acides ou d'aminés ne conduit pas à un changement avantageux dans la production de QD CdSe de haute qualité, on observe un effet synergique évident en formant des QD avec une taille plus petite, une morphologie plus isotrope, un comportement moins aggloméré et une efficacité de photoluminescence qui sont plus élevées utilisation d'un acide carboxylique à longue chaîne et d'un ligand d'amine à longue chaîne.

Deuxièmement, nous établissons le double rôle joué par l'oléylamine (OLAm) pendant la synthèse de QD CdSe en utilisant l'oléate de cadmium comme source de Cd. Des rapports antérieurs suggéraient le rôle de l'alkylamine soit comme agent nucléant, soit comme agent passivant dans le contrôle de la croissance des QD CdSe. En explorant quatre voies de synthèse différentes, dans lesquelles l'addition, la synchronisation et la concentration des réactifs sont variées de manière remarquable. Nous constatons que ces deux phénomènes coexistent et contrôlent la synthèse. En examinant s'il existe un quelconque effet de concentration en OLAm sur cette synthèse, nous trouvons que, aux teneurs plus faibles en OLAm (<0,5 mmol), ce dernier joue un rôle important en tant qu'agent agissant sur la nucléation, augmentant le nombre de noyaux, réduisant le nombre de noyaux (unités monomères initiales), ce qui augmente la concentration en NC, et se traduit par une petite taille, jusqu'à 2,7 nm. Tandis qu'à des teneurs plus élevées (> 1,0 mmol), il sert davantage d'agent de passivation en

dissuadant les processus de nucléation et de croissance, générant ainsi moins de NC de plus grande taille jusqu'à 3,6 nm. Donc, nous pouvons mieux contrôler la taille finale des CN et ajuster leurs propriétés optiques dépendantes de la taille en ajustant l'influence entre la nucléation et la passivation.

Troisièmement, nous démontrons la synthèse de NCs et de nanotubes 2D CdSe lorsque l'acétate et les al-kyamines à chaîne courte qui sont utilisés comme ligands. Ce qui plus intéressant, c'est des nanotubes de CdSe à parois atomiques sont formés via un protocole sans matrice avec une combinaison d'acétate et de dioctylamine (DOAm). Ils se caractérisent par une structure à plusieurs parois, une absorption et une émission pointues aux environs de 460 nm et des plans {100} à extrémité Cd comme surfaces supérieure et inférieure dans le sens de l'épaisseur de la paroi. La croissance anisotrope résulte de l'utilisation d'un ligand acétate. L'ajout de DOAm rend la formation de structures tubulaires plus régulières pendant ce processus. En outre, nous éluciderons le mécanisme de croissance comme une approche de fixation orientée 2D n'est pas planaire; c'est-à-dire la fixation simultanée latérale et angulaire de nanoplaquettes au stade précoce dans des feuilles nanométriques incurvées et finalement une architecture tubulaire.

Enfin, nous éluciderons davantage le mécanisme de formation des NCs CdSe anisotropes en présence de ligand de di-octylamine et de ligands carboxylates ayant une longueur de chaîne différente. Il a été constaté que les ligands carboxylate à chaîne courte et à chaîne longue induisent la croissance anisotrope des NC de CdSe par la fixation de blocs de construction de NC précocement formés. Une transition morphologique des nanotubes et des nanosheets en nanorods irréguliers et finalement en QD est observée lorsque le nombre de carbones des ligands carboxylates augmente de 2 à 18. La principale raison est que deux blocs de construction de CN différents, y compris des CN primaires cinétiquement stables, exposant par {110} et {100} facettes et les CN primaires thermodynamiquement stables, exposant par les facettes {100} et {111}, sont formés en présence de carboxylates à chaîne courte et longue, respectivement. Une conversion entre ces deux blocs de construction peut être déclenchée en utilisant un ligand carboxylate à chaîne moyenne par différentes concentrations et températures. Une simulation de la théorie de la fonction de densité (DFT) est réalisée pour révéler la structure de surface des CN de CdSe à zinceblende en l'absence et la présence de ligands carboxylates. Nous proposons que les différentes sursaturations de monomères locales causées par des carboxylates et de différentes longueurs de chaîne soient responsables de la production de blocs de construction intrinsèquement différents.

## Mots-clés

nanocristaux colloïdaux, séléniure de cadmium, carboxylate, alkylamine, points quantiques, nanorods, nanotubes, nanofeuilles, nanoplaquettes, matériaux 2D, croissance cinétique, assemblage de particules, fixation orientée

# Contents

Acknowledgements.....	i
Abstract.....	v
Keywords.....	vi
Résumé.....	vii
Mots-clés.....	viii
Contents.....	ix
List of Abbreviations.....	xiii
List of Figures.....	xv
List of Tables.....	xxi
List of Equations.....	xxiii
<b>Chapter 1</b> <b>Introduction.....</b>	<b>1</b>
1.1 Colloidal Semiconductor NCs.....	1
1.1.1 Size- and shape- dependent properties.....	1
1.1.2 Brief history on the synthesis of colloidal semiconductor NCs.....	2
1.2 Size control in QDs.....	4
1.2.1 The La Mer Model.....	4
1.2.2 Monomer Accumulation.....	5
1.2.3 Nucleation.....	6
1.2.4 Crystal Growth.....	8
1.2.5 Size and size uniformity control strategies.....	12
1.3 Shape control in anisotropic CdSe NCs.....	13
1.3.1 Equilibrium shape: Gibbs-Curie-Wulff construction rule.....	14
1.3.2 Steady shape.....	15
1.3.3 Shape control towards anisotropic 1D and 2D morphology.....	17
1.3.4 Non-classical growth: Oriented Attachment.....	21

---

1.3.5	Shape control strategies.....	23
1.4	Surface ligands in colloidal CdSe NCs synthesis.....	24
1.5	Thesis objective and outline .....	27
<b>Chapter 2</b>	<b>Synergistic effect of carboxylic and amine ligands on the synthesis of CdSe NCs</b>	<b>29</b>
2.1	Introduction.....	30
2.2	Results and Discussion.....	31
2.2.1	Synergistic effect of carboxylic and amine ligands.....	31
2.2.2	Influence of the ligands with different chain length .....	35
2.3	Experimental section .....	38
2.3.1	Synthetic Methods .....	38
2.3.2	Characterization.....	39
2.4	Conclusion .....	39
<b>Chapter 3</b>	<b>Nucleation and growth behavior of CdSe NCs synthesized in presence of oleylamine coordinating ligand .....</b>	<b>41</b>
3.1	Introduction.....	42
3.2	Results and Discussion.....	43
3.2.1	Influence of OLAm on size and concentration of CdSe NCs .....	43
3.2.2	Influence of OLAm on size distribution of CdSe NCs.....	49
3.2.3	Two competitive roles of the primary amine .....	51
3.3	Experimental Section.....	53
3.3.1	Synthetic Methods .....	53
3.3.2	Characterization.....	53
3.4	Conclusion .....	55
<b>Chapter 4</b>	<b>Spontaneous formation of CdSe photoluminescent nanotubes .....</b>	<b>57</b>
4.1	Introduction.....	58
4.2	Results and Discussion.....	59
4.2.1	Morphology and Crystal Structure of CdSe Nanotubes.....	59
4.2.2	Multiwalled character of the CdSe nanotubes.....	63
4.2.3	Role of the amine and acetate ligands in CdSe nanotube synthesis.....	67



4.2.4 CdSe nanotubes growth mechanism .....	73
4.3 Experimental Section.....	81
4.3.1 Synthetic Methods.....	81
4.3.2 Characterization .....	83
4.4 Conclusions .....	83
<b>Chapter 5</b> <b>Anisotropic Growth of CdSe Nanocrystals via Particle Attachment of Intrinsically Different Building Blocks.....</b>	<b>85</b>
5.1 Introduction.....	86
5.2 Results and Discussion.....	87
5.2.1 Particle-mediated Anisotropic growth of CdSe NCs in the Presence of Different Carboxylate Ligands .....	87
5.2.2 Factors Triggering the Shape Conversion between 2D and 1D CdSe NCs.....	92
5.2.3 DFT simulation of CdSe surface structure with and without carboxylate passivation .....	95
5.2.4 Formation Mechanism of Intrinsically Different Building Blocks.....	98
5.3 Experimental Section.....	101
5.3.1 Synthetic Methods .....	101
5.3.2 Characterization.....	101
5.3.3 DFT simulation.....	102
5.4 Conclusions .....	103
<b>Chapter 6</b> <b>Conclusion .....</b>	<b>105</b>
6.1 Main results achieved in this thesis .....	105
6.2 Future development.....	106
References .....	109
Curriculum Vitae .....	115



## List of Abbreviations

NC: nanocrystal	TOAm: trioctylamine
QD: quantum dot	TOP-Se: tri-n-octylphosphine selenide
0D: zero-dimensional	ODE: 1-octadecene
1D: one-dimensional	TOPO: tri-n-octylphosphine oxide
2D: two-dimensional	CVD: chemical vapor deposition
CdSe: cadmium selenide	MBE: molecular beam epitaxy
CdS: cadmium sulfide	DFT: density functional theory
CdTe: cadmium telluride	SEM: scanning electron microscopy
PbS: lead sulfide	TEM: transmission electron microscopy
PbSe: lead selenide	HRTEM: high-resolution TEM
CdMe <sub>2</sub> : dimethyl cadmium	HAADF-STEM: high-angle annular dark-field scanning transmission electron microscopy
Cd(Ac) <sub>2</sub> : cadmium acetate	SAED: selected-area electron diffraction
Cd(OAc) <sub>2</sub> : cadmium oleate	XRD: X-ray diffraction
Ac: acetic acid	UV-vis: ultraviolet-visible
LAc: lauric acid	PL: photoluminescence
MAc: myristic acid	PLOQY: photoluminescence quantum yield
SAc: stearic acid	PLE: photoluminescence excitation
OAm: octadecylamine	FWHM: full width at half maximum
DDAm: dodecylamine	ML: molecular monolayers
HDAm: hexadecylamine	FTIR: Fourier-transform infrared spectroscopy
ODAm: octadecylamine	fcc: face-centered cubic
OLAm: oleylamine	
DOAm: dioctylamine	



## List of Figures

Figure 1.1 Schematic of quantum confinement effect as the size of the semiconductor is reduced.....	1
Figure 1.2 Schematic of the electronic density of states for a bulk semiconductor (yellow dashed line), 0D (left), 1D (middle) and 2D (right) semiconductor NCs. ....	2
Figure 1.3 Schematic of the La Mer model which describes different stages for the formation of colloidal NCs from precursor solution. ....	5
Figure 1.4 The change of Gibbs free energy as a function of NC size during the crystallization process. ....	7
Figure 1.5 Schematic of diffusion-reaction model to describe the growth of colloidal NCs .....	8
Figure 1.6 Plot of the linear growth rate of the NCs as a function of radius in a diffusion-controlled growth model.....	11
Figure 1.7 Different Wulff-Gibbs equilibrium shapes according to the different surface energies of {100} and {111} facets in a fcc crystal structure .....	15
Figure 1.8 Schematic of a cuboid crystal growing in a diffusion sphere... ..	15
Figure 1.9 Proposed mechanism for the 1D anisotropic growth of cadmium chalcogenide NCs .....	18
Figure 1.10 Several proposed mechanisms for the 2D anisotropic growth of colloidal NCs by monomer addition approach.....	20
Figure 1.11 Several examples of anisotropic NCs formed by oriented attachment mechanism .....	22
Figure 1.12 Classification of surface ligands according to the type of covalent bonds.....	25
Figure 2.1 Possible coordination complex formation of carboxylic acids and primary amines with cadmium(II) and their reaction towards the selenium precursor TOP-Se at 200 °C .....	32
Figure 2.2 Synergistic effect of carboxylic acid and amine ligands on the optical properties and morphologies of synthesized CdSe NCs.....	33
Figure 2.3 Absorption, PL spectra of the CdSe NCs synthesized from route 1, route 2, route 3 and route 4 during 30 s to 10 min.....	34

Figure 2.4 High-resolution TEM (HRTEM) images of a tetrapod-like and tripod-like CdSe NCs synthesized from route 3.....	34
Figure 2.5 TEM images of CdSe NCs synthesized in the presence of stearic acid (SAC) and primary amines having different chain length.....	36
Figure 2.6 Temporal evolution of size, PLQY and PL FWHM of CdSe NCs synthesized in the presence of SAC and primary amines having different chain length .....	36
Figure 2.7 TEM images of CdSe NCs synthesized in the presence of octadecylamine (ODAm) and carboxylic acids having different chain length. ....	37
Figure 2.8 Temporal evolution of size, PLQY and PL FWHM of CdSe NCs synthesized in the presence of octadecylamine (ODAm) and carboxylic acids having different chain length .....	37
Figure 3.1 The reported studies on the role of the alkylamine on the nucleation and growth of CdSe NCs. ....	42
Figure 3.2 Schematic of designed four reaction routes to investigate the influence of oleylamine (OLAm) on the synthesis of CdSe NCs .....	43
Figure 3.3 UV-vis absorbance spectra of CdSe NCs prepared using different routes .....	44
Figure 3.4 The intensity and the FWHM of the first excitonic peak of the CdSe NCs .....	45
Figure 3.5 Temporal evolution of the size, volumetric growth rate and NC concentration of CdSe NCs.....	46
Figure 3.6 Temporal evolution of the size, volumetric growth rate and concentration of the CdSe NCs synthesized by route 1.....	46
Figure 3.7 Temporal evolution of the CdSe concentration in the form of NC .....	47
Figure 3.8 Temporal evolution of rate of the total concentration of CdSe units in the form of NCs .....	48
Figure 3.9 Temporal evolution of rate of the NC concentration.....	48
Figure 3.10 PL spectra of CdSe NCs extracted after a reaction time of 15 min .....	49
Figure 3.11 TEM graphs and size distribution profiles of the CdSe NCs ...	50
Figure 3.12 TEM graphs and size distribution profiles of the CdSe NCs. ...	51

Figure 4.1 An overview of reported 2D colloidal CdSe NCs with atomically scale thickness. ....	58
Figure 4.2 Synthesis and morphological characterization of the tubular CdSe structures.....	60
Figure 4.3 Structural and elemental characterization of CdSe nanotubes by SEM, EDX and HRTEM .....	61
Figure 4.4 EDX spectra and semi-quantitative analysis of the elements in the CdSe nanotubes.....	61
Figure 4.5 Crystallographic structure characterization of the 2D CdSe NCs .	62
Figure 4.6 HRTEM characterization of the growth orientations in CdSe nanotubes .....	62
Figure 4.7 Multi-walled character of the CdSe nanotubes, as observed by TEM, STEM, PL, and UV-vis absorption spectroscopy.....	64
Figure 4.8 PLE and PL spectra of a CdSe nanotubes in hexane solution. ...	65
Figure 4.9 High-magnification STEM and TEM images of CdSe nanotubes observed along the tube-opening direction .....	65
Figure 4.10 FTIR spectra of CdSe NCs synthesized at different conditions.	66
Figure 4.11 TEM and STEM graphs of the CdSe nanotubes after ligand exchange with oleic acid.....	67
Figure 4.12 Control experiments to study the role of acetate and amine ligand in the synthesis of 2D CdSe NCs.....	68
Figure 4.13 FTIR spectra of DOAm, Cd(Ac) <sub>2</sub> ·2H <sub>2</sub> O, Cd(Ac) <sub>2</sub> -DOAm solution and Cd(Ac) <sub>2</sub> -DOAm precipitates.....	69
Figure 4.14 Morphological and structural characterization of Cd(Ac) <sub>2</sub> ·2H <sub>2</sub> O powders and Cd(Ac) <sub>2</sub> -DOAm by TEM. ....	70
Figure 4.15 Structural characterization of Cd(Ac) <sub>2</sub> ·2H <sub>2</sub> O powders treated at different temperatures .....	71
Figure 4.16 Influence of primary and tertiary alkylamines on the morphology of the CdSe NCs .....	73
Figure 4.17 Characterization of 2D CdSe NCs synthesized at 80 °C for 17 hours .....	74
Figure 4.18 Characterization of 2D CdSe NCs synthesized at 140 °C for 8, 32 and 256 minutes .....	74
Figure 4.19 Characterization of 2D CdSe NCs synthesized at 200 °C for 1, 8 and 128 minutes .....	75

Figure 4.20 Characterization of 2D CdSe NCs synthesized at 260 °C for 0.5, 1, 8, 32 and 256 minutes.....	76
Figure 4.21 TEM and HRTEM study of early formation stages of CdSe nanotubes .....	77
Figure 4.22 TEM characterization of early stage formation of the 2D CdSe NCs from Cd precursor matrix.....	78
Figure 4.23 HRTEM study of the angular building block assembly mechanism .....	79
Figure 4.24 Final and incomplete formation of CdSe nanotubes observed along the tube opening direction.....	80
Figure 4.25 Characterization of nanostructures after growing a CdS shell on the CdSe nanotubes.....	80
Figure 4.26 Characterization of nanostructures after reacting CdSe nanotubes with thioacetamide.....	81
Figure 5.1 Optical, structural and morphological characterization of CdSe NCs synthesized in the presence of carboxylate ligands having different chain length. ....	89
Figure 5.2 Temporal evolution of the absorption spectra of CdSe NCs synthesized in the presence of carboxylate ligands having different chain length, including acetate, butyrate, hexanoate, octanoate, laurate and oleate.....	90
Figure 5.3 HRTEM characterization of crystallographic orientation in the as-synthesized CdSe nanotubes, nanosheets, nanorods and nanodots .....	92
Figure 5.4 Morphological and spectroscopic characterization of CdSe NCs synthesized in the presence of hexanoate ligand at different precursor concentration.....	93
Figure 5.5 Morphological and spectroscopic characterization of CdSe NCs synthesized in the presence of hexanoate ligand at different reaction temperature.....	94
Figure 5.6 DFT simulation of surface structure of the zincblende CdSe slabs before and after passivated with different chain-length carboxylate ligands . ....	95
Figure 5.7 Side view of the relaxed surface structure of {100}, {111} and {110} slabs after passivated with butyrate, hexanoate and octanoate, obtained by DFT simulation.....	97
Figure 5.8 The calculated binding energy and inter-ligand interaction of {100} (triangle), {111} (circle), {110} (square) slabs surface after passivated with	



carboxylate ligands having a carbon number of 2 (acetate), 4 (butyrate), 6 (hexanoate) and 8 (octanoate)..... 98

Figure 5.9 Schematic illustration showing the formation mechanism of the anisotropic CdSe NCs ..... 98



## List of Tables

Table 5.1 The surface area per CdSe unit, dangling bond density, surface energy of unpassivated and acetate-passivated surface of {100}, {111} and {110} slabs. ....	96
Table 5.2 Partition coefficient ( $\log P_{oct/wat}$ ) of carboxylic acids with different chain length and the solvent, ODE. ....	100



## List of Equations

Equation 1.1 Gibbs–Thomson relationship describing the equilibrium concentration of NCs as a function of size and surface energy. ....	6
Equation 1.2 The change of the volume Gibbs free energy due to the supersaturation.....	6
Equation 1.3 The total change of the Gibbs free energy as a function of the particle radius.....	6
Equation 1.4 The definition formula of critical nucleation radius. ....	7
Equation 1.5 The equilibrium concentration of a nucleus. ....	7
Equation 1.6 The nucleation energy barrier formula. ....	7
Equation 1.7 The nucleation rate formula.....	8
Equation 1.8 Fick's first diffusion law describing the monomer addition through diffusion.....	9
Equation 1.9 The total diffusion flux of monomers on a spherical particle.	9
Equation 1.10 The total diffusion flux of monomers used for surface chemical reaction.....	9
Equation 1.11 The monomer concentration at the interface of reaction zone and diffusion zone.....	9
Equation 1.12 The total diffusion flux as a function of linear growth rate..	9
Equation 1.13 The linear growth rate considering the diffusion and reaction stages. ....	10
Equation 1.14 Equation 1.14 The linear growth rate in reaction-controlled mode. ....	10
Equation 1.15 The monomer concentration in bulk solution.....	10
Equation 1.16 The monomer concentration on the surface of a crystallite.	10
Equation 1.17 The linear growth rate in reaction-controlled mode after considering Gibbs-Thompson equation.....	10
Equation 1.18 The linear growth rate in diffusion-controlled mode.....	10
Equation 1.19 The linear growth rate in diffusion-controlled mode after considering Gibbs-Thompson equation.....	11

Equation 1.20 Relationship among the precursor rate and subsequent nucleation rate and growth rate during the colloidal synthesis of NCs. ....	13
Equation 1.21 Relationship among the final growth rate, the precursor rate and the final number density of NCs. ....	13
Equation 1.22 Wulff construction rule.....	14
Equation 1.23 The total surface energy of a cuboid geometry. ....	16
Equation 1.24 The volume of a cuboid geometry. ....	16
Equation 1.25 The surface chemical potential of facet 1.....	16
Equation 1.26 The surface chemical potential of facet 2 and 3.....	16
Equation 1.27 The equilibrium monomer concentration of a given facet as a function of its chemical potential.....	16
Equation 1.28 The growth distance relationship of a steady shape in a diffusion-controlled mode.....	16
Equation 1.29 The growth distance relationship of a steady shape in a reaction-controlled mode.....	17
Equation 1.30 The equilibrium concentration of a concave surface. ....	19
Equation 1.31 The collision frequency of colloidal particles in solution. ..	24
Equation 2.1 Equation used to calculate the PLQY of the CdSe NCs based on relative method.....	39
Equation 3.1 Empirical formula of the average sizes of CdSe NCs as a function of the first excitonic peak. ....	54
Equation 3.2 The volumetric growth rate calculated based on change of the NC volume. ....	54
Equation 3.3 Empirical equation to calculate the NC concentration based on the average size and absorption intensity at 350 nm of the sample. ....	54
Equation 3.4 Relationship between the total CdSe concentration in the form of NC, the number of the CdSe unit in each NC and the number of CdSe NCs. ....	54
Equation 3.5 The number of the CdSe unit in each NC as a function of the NC size.....	54
Equation 5.1 Formula used for the surface energy calculation of bare surface. ....	102
Equation 5.2 Formula used for the surface energy calculation of carboxylate-passivated surface. ....	102
Equation 5.3 Formula used for adsorption energy calculation.....	103

Equation 5.4 Formula used for binding energy calculation. ....	103
Equation 5.5 Formula used for inter-ligand interaction calculation. ....	103





# Chapter 1 Introduction

## 1.1 Colloidal Semiconductor NCs

### 1.1.1 Size- and shape- dependent properties

Semiconductor materials are the cornerstones of the information era. They typically possess a bandgap of 0.1~3 eV between the conduction band and valence band. When the size of crystalline semiconductor materials is extremely tiny, smaller than their exciton Bohr radius (around several nanometers), we call them semiconductor NCs. Particularly, when all the three dimensions of the NCs are confined, they are known as QDs. In this dimension range, quantum confinement effects occur: their continuous energy bands become discrete levels, and the energy bandgap expands with the decrease of the size, as shown in Figure 1. Because many physical and chemical properties of the semiconductor are closely related to bandgap structure, we can easily and effectively adjust these properties by varying the size of NCs. Taking CdSe QDs as an example, Figure 1.1 displays the blue shift of the PL of their size decreases from 4 nm to 2 nm. This feature allows us to obtain multiple emission colors under a single excitation wavelength, which is highly desirable in the applications of bioimaging and optoelectronic display. Moreover, the size-dependent absorption of CdSe QDs also provides a simple and reliable route to fundamentally investigate the nucleation and growth of colloidal NCs [1-3].

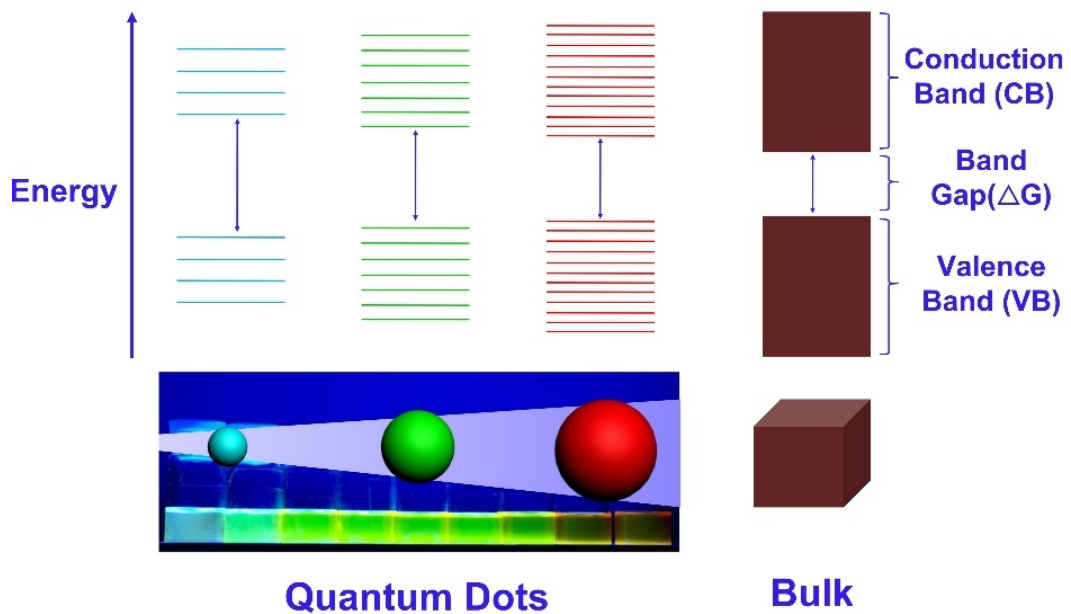


Figure 1.1 Schematic of quantum confinement effect as the size of the semiconductor is reduced. When the semiconductor becomes smaller, a wider energy band gap and more blue-shift PL of the material appear.

Apart from the isotropic dot-like morphology, semiconductor NCs may also grow into non-spherical anisotropic shapes, including 1D nanowires and 2D nanoplatelets. In these two cases, the quantum confinement effect is exerted in two dimensions and one dimension, respectively. Consequently, the discrete electronic density of states (DOS) in QDs evolve into a saw-like and step-like relationship for 1D and 2D NCs, respectively (Figure 1.2) [4]. This leads to very interesting shape-related properties. For example, ultrathin 2D CdSe nanoplatelets exhibit discrete band-edge absorption spectra and very sharp emission peaks [5–8]; elongated 1D CdSe nanorods were demonstrated to have purely linearly polarized emission and larger Stokes shift than QDs [9]. Obviously, by tuning the shape into complex non-spherical shapes, semiconductor NCs could be endowed with very unique and anisotropic properties. These size- and shape- dependent properties make semiconductor NCs promising candidates for a wide range of applications including bioimaging, electronic display, solar cell, photocatalysis and laser. This, in turn, triggers more academic studies to well control the size and shape of the semiconductor NCs.

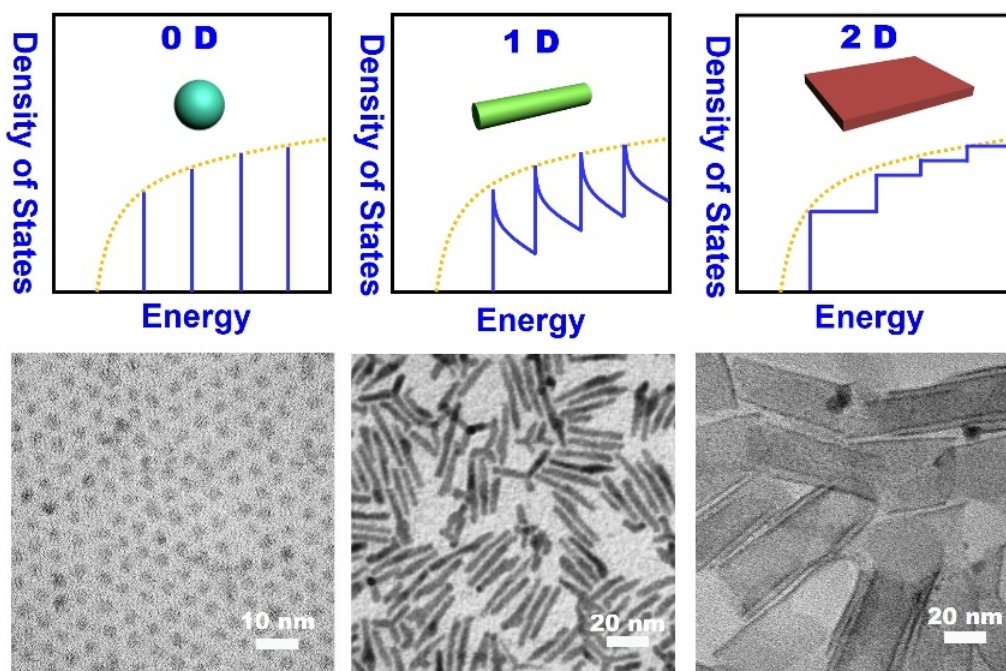


Figure 1.2 Schematic of the electronic density of states for a bulk semiconductor (yellow dashed line), 0D (left), 1D (middle) and 2D (right) semiconductor NCs. TEM graphs of typical 0D, 1D and 2D CdSe NCs are shown in the bottom panel.

Among a variety of semiconductor materials, group II-VI cadmium chalcogenide, including CdSe, CdS and CdTe, have attracted extensive investigations in the past 30 years because their size- and shape- tunable absorption and PL spectra are primarily located in the visible-light range. The following discussion in this thesis will mainly focus on this type of materials.

### 1.1.2 Brief history on the synthesis of colloidal semiconductor NCs

The preparation of semiconductor NCs has been well established by several techniques such as colloidal synthesis, CVD and MBE. NCs prepared by the colloidal chemistry approach are known as colloidal NCs. Compared with CVD and MBE methods, the colloidal approach is able to produce a large quantity of NCs at a low equipment and operational cost and in a less toxic condition. More importantly,

it offers great advantages in precise control over the shape, size and structure of the NCs, thus being the most promising method for commercial production of NCs.

Pioneering works on preparing the colloidal semiconductor NCs date back to the 1980s. In 1983, Brus et al first coined the concept of colloid QDs during their synthesis of CdS crystallites in an aqueous reaction [10]. In 1993, Bawendi et al proposed a hot-injection protocol to obtain high-quality monodisperse cadmium chalcogenide QDs in organic solvent [11]. In their procedure, organometallic precursors such as dimethyl cadmium ( $\text{CdMe}_2$ ) and TOPSe were quickly injected into a hot coordinating solvent (at 300 °C), TOPO, followed by the subsequent growth stage occurring at a slightly lower temperature (230~260 °C). Rapid injection at high temperature helps to induce a short nucleation period for the NCs. For an ensemble of NCs, this approach enables the size adjustment of the CdSe NCs from 1.2 to 11.5 nm, with deviation of the size distribution to be less than 5% after a size-selection process. This seminal work boomed the academic interests in in this field, which developed into several branches as shown below.

First of all, greener and less air-sensitive reagents were explored to reduce the toxicity in cadmium source and the solvent, making the synthesis of semiconductor NCs more accessible in a normal laboratory. Peng et al made an important contribution by introducing air-stable cadmium oxide ( $\text{CdO}$ ) [12] and cadmium acetate ( $\text{Cd}(\text{Ac})_2$ ) [13] as the cadmium source, enabling the large-scale synthesis of high-quality cadmium chalcogenide NCs without a glovebox. They also proposed the use of a noncoordinating solvent, 1-octadecene (ODE), for the high-temperature reaction, thus paving the way for studying the influence of a given surface ligand [14].

Secondly, various surface passivation approaches, including inorganic shells and organic ligands, were investigated to eliminate the surface defects and thus improve the luminescence quality of the NCs. Hines et al first demonstrated the increase of luminescence by growing the QDs with a shell of semiconductor with a wider bandgap. In their CdSe/ZnS core-shell nanostructures, a PLQY of 50 % was achieved at room temperature [15]. To enhance the controllability over the shell thickness, Peng et al provided a technique termed as “successive ion layer adsorption and reaction” (SILAR). In case of CdSe/CdS core-shell nanostructure, the preparation was performed by alternating injection of the cationic Cd and anionic S precursors into the solution of CdSe NCs [16]. Surface passivation by organic ligand was first demonstrated by Talapin and coworkers. They obtained CdSe QDs with a PLQY of 40-50% at room temperature by capping their surface of with a long-chain primary amine, HDAm, in a TOPO-TOP system [17] .

Thirdly, controlled synthesis of NCs with various non-spherical anisotropic morphologies, such as 1D and 2D CdSe NCs, became also one of the popular research directions. Peng et al. observed the 1D growth of wurtzite CdSe QDs into rod-like nanostructures in the presence of phosphonic acid [18]. Buhro et al. synthesized the CdSe nanowires with characteristic 2D confinement effect through a solution-liquid-solid (SLS) method using Bi nanoparticles as the catalysts [19]. Manna et al. reported the formation of tetrapod-like CdSe and CdTe NCs, the structure of which was proposed to be consist of a zincblende core and four wurtzite arms [20, 21]. For 2D CdSe NCs, Hyeon et al. provided a protocol to synthesize wurtzite CdSe nanoribbons with the help of amine ligand, which possessed a uniform

thickness of 1.4 nm and exhibited a sharp first excitonic peak at 449 nm [22]. Zincblende CdSe nanoplatelets were first published by Dubertret et al. in the presence of both short-chain and long-chain carboxylate ligand, and four discrete uniform thicknesses including 2, 3, 4 and 5 monolayers were further determined [23, 24].

In addition, other synthetic protocols suitable for practical production were explored. Hot-injection has shown advantages on synthesizing high-quality QDs in a batch, yet when the recipe is accommodated for scale-up production, it might cause bad reproducibility due to the uncontrolled mixing effect during injection. In comparison, a heat-up method is much more suitable for industrial-scaled synthesis. Cao et al. demonstrated the successful production of CdSe QDs with quality comparable to the best samples prepared by hot injection and argue the key point in this method is to use precursors with suitable reactivity [25]. Additionally, microreactors based on microfluidic technology also provide another possibility. Bawendi et al realized the synthesis of monodisperse CdSe QDs in a gas-liquid segmented flow embedded in a silicon-glass chip [26]. Kilogram-per-day production level was achieved in deMello group by employing multichannel droplet reactors embedded in a polytetrafluoroethylene (PTFE) capillary microfluidic system [27] (*J. Mater. Chem. A*, 2013, 1, 4067–4076).

Overall, great efforts have pushed the development of colloidal NCs into greener and cost-effective synthesis as well as broader and more practical applications. Unfortunately, although a great number of synthesis protocols have been proposed to acquire NCs with well controlled size, shape and structure, they are still “more empirical art rather than science” [28]. More in-depth research on the formation mechanism of NCs is therefore necessary to advance the art of colloidal synthesis.

## 1.2 Size control in QDs

Since the quantum confinement effect offers a great advantage to tune the properties of CdSe QDs by size, the central task in the synthesis of CdSe QDs is to control their size on demand and make their size uniformity as monodisperse as possible. The significance of the monodispersity is comparable to the purity of products in organic chemistry. The controlled synthesis is closely related with the fundamental knowledge on the crystallization of NCs in solution. Several classical models and theories are shown below.

### 1.2.1 The La Mer Model

Crystallization is a process of forming well-organized and long-term ordered crystals from gas, supercooled liquid or supersaturated solutions. Characteristic examples include the emergence of snowflakes in cool weather, the molding of steel from molten iron, the extraction of salt from sea water and the synthesis of NCs in materials research. To describe the formation of NCs in a colloidal condition, a classical model was proposed by La Mer et al during the preparation of sulfur hydrosol in 1950s [29]. In this model, a general scenario based on the concept of supersaturation of the monomer is provided by dividing the whole process into three critical stages: monomer accumulation, nucleation and growth (Figure 1.3). The first stage concerns the chemical reaction between the precursors, while the latter two stages as a whole are known as the crystallization process. They proposed there exist a short period of

nucleation stage, or burst nucleation, which is responsible for the formation of monodisperse hydrosols in an aqueous solution. Although the synthetic systems and conditions varied a lot the in the colloidal synthesis of semiconductor NCs, to some extent, this model is still reasonable and available to account for most of the observed behaviors during the formation of colloidal NCs.

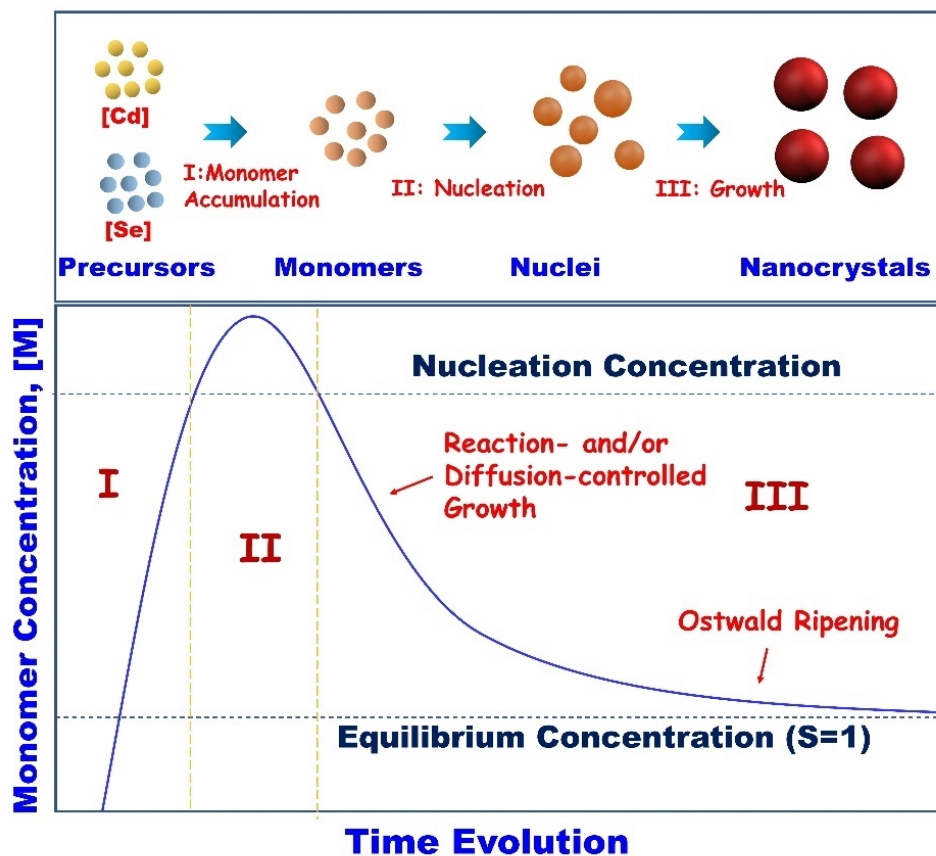


Figure 1.3 Schematic of the La Mer model which describes different stages for the formation of colloidal NCs from precursor solution.

### 1.2.2 Monomer Accumulation

Monomer accumulation is the first stage, in which precursors, such as the cadmium source and selenium source, undergo a chemical reaction and turn into a large quantity of basic molecular units, “monomers”. The monomer has a limited equilibrium concentration (or solubility) in the solution. Accordingly, the rapid increase of the monomer concentration can surpass the saturation limit, leading to a non-equilibrium supersaturation state. Excess monomers precipitate and aggregate into dimers, trimers and finally larger particles. However, these particles are still thermodynamically unstable and inclined to dissolving back into monomers rather than continuing to grow into crystallites. From the perspective of solubility, there already exists a dynamic equilibrium between the precipitation and dissolution for the particle, which is related to size of the particle. According to the Gibbs–Thomson equation, the equilibrium concentration of a spherical particle,  $[M]_r$ , can be expressed as function of its radius  $r$  as follows [30],

$$[M]_r = [M]_\infty \exp\left(\frac{2\gamma V_m}{rRT}\right)$$

Equation 1.1 Gibbs–Thomson relationship describing the equilibrium concentration of NCs as a function of size and surface energy.

where  $[M]_\infty$  is the equilibrium concentration of material with infinite dimension (or zero curvature),  $V_m$  is the molar volume of the bulk crystal,  $\gamma$  is surface energy of the particle per unit area,  $R$  is the gas constant and  $T$  is the temperature. This relationship manifests a larger solubility for smaller particles. The activity of the precursors and the participation of capping ligands play a critical role in this process, which will influence of the morphology and particle quality of the final products.

### 1.2.3 Nucleation

The second stage is the nucleation process, which happens when the degree of supersaturation is high enough to exceed a critical threshold for the generation of stable particles, or “nuclei”. Considering a homogenous nucleation condition where the nucleation is basically dependent on the energy fluctuation in the solution, we have the following expression for the change of the volume Gibbs free energy ( $\Delta G_v$ ) caused by the supersaturation [31],

$$\Delta G_v = -\frac{RT \ln S}{V_m}$$

Equation 1.2 The change of the volume Gibbs free energy due to the supersaturation.

Where  $S=[M]/[M]_\infty$  is the degree of supersaturation, and  $[M]$  is the practical monomer concentration provided by the monomer accumulation, respectively. It is clear that during the supersaturation condition ( $S > 1$ ),  $\Delta G_v$  is always negative and will make a positive contribution to the crystal formation. At the same time, a competing factor coming from the newly formed surface would impede the crystal growth. Accordingly, the total change of Gibbs energy for a particle with radius  $r$  is expressed as,

$$\Delta G = 4\pi r^2 \gamma + \frac{4}{3} \pi r^3 \Delta G_v$$

Equation 1.3 The total change of the Gibbs free energy as a function of the particle radius.

Where  $\gamma$  is surface energy of the particle per unit area. As the surface term scales with  $r^2$  while the volume term is proportional with  $r^3$ , there exists a minimum radius  $r^*$ , after which the particle can continue growing into larger crystals (Figure 1.4).

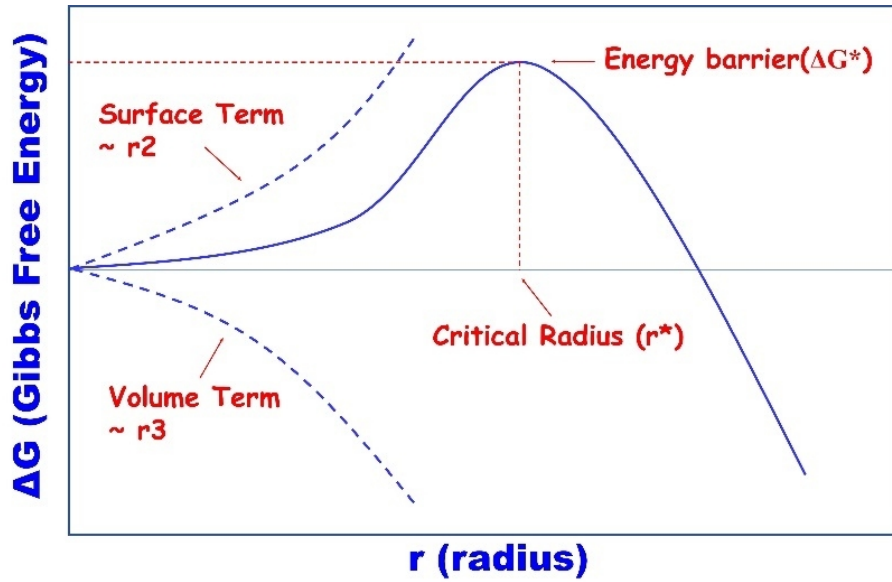


Figure 1.4 The change of Gibbs free energy as a function of NC size during the crystallization process.

This radius is called critical nucleation radius, which can be deduced from the condition when  $d\Delta G/dr = 0$ , thus we obtain

$$r^* = -\frac{2\gamma}{\Delta G_v} = \frac{2\gamma V_m}{RT \ln S}$$

Equation 1.4 The definition formula of critical nucleation radius.

A particle reaching such a size can be called as a nucleus, which is energetically stable for further growth. It is worth mentioning that this critical radius is not constant but tends to increase due to the decrease of supersaturation during the reaction process. By inserting equation 1.4 into the Gibbs-Thomson relationship, we can find that

$$[M]_{r^*} = [M]$$

Equation 1.5 The equilibrium concentration of a nucleus.

Where  $[M]_{r^*}$  is the equilibrium concentration of a nucleus. This indicates the equilibrium concentration of the nuclei is equal to the monomer concentration. A higher monomer concentration leads to smaller nuclei with small radius. We can also deduce the energy barrier ( $\Delta G^*$ ) required to surpass for the formation of stable nuclei,

$$\Delta G^* = 4\pi r^{*2} \gamma + \frac{4}{3} \pi r^{*3} \Delta G_v = \frac{16\pi \gamma^3}{3\Delta G_v^2} = \frac{16\pi \gamma^3 V_m^2}{3(RT \ln S)^2} = \frac{4}{3} \pi r^{*2} \gamma$$

Equation 1.6 The nucleation energy barrier formula.

This implies the volume free energy compensates two thirds of energy increase caused by the surface energy, and the rest one third, or energy barrier, needs to be provided by the external energy input. the energy fluctuation in the global solution will endow some sites to surmount this barrier, thus turning into nuclei. Since the critical radius is time-dependent, this energy barrier will also change when the monomers are consumed. The reaction rate for the formation of nuclei can be written



$$\frac{dN}{dt} = A \exp\left(-\frac{\Delta G^*}{k_B T}\right) = A \exp\left(-\frac{16\pi\gamma^3 V_m^2}{3N_A^2 k_B^3 T^3 (\ln S)^2}\right)$$

Equation 1.7 The nucleation rate formula.

in which  $A$ ,  $k_B$  and  $N_A$  are the pre-exponential factor, the Boltzmann constant and Avogadro's number respectively. We can see the nucleation rate is positively related with the temperature and supersaturation, while inversely related to the surface energy. The simulation work by Hyeon et al showed that, as the degree of supersaturation is increased from  $S = 2$  to 4, the nucleation rate will increase by 70 orders of magnitude [31].

It is worth mentioning the above equations are obtained by assuming that the surface energy ( $\gamma$ ) and volume free energy ( $\Delta G_v$ ) are independent from the dimension of the particles. In fact, the surface energy would be minimized with time evolution by reconstructing the surface structure or changing the crystal structure due to the increase of the total surface area. Besides, as most of colloidal NCs require the participation of surface ligands to be stabilized in the solvent, their surface energy and equilibrium concentration are also inevitably varied when bound to the organic ligands [3].

## 1.2.4 Crystal Growth

The growth of crystal follows after the nucleation. Due to the consumption in the nucleation stage, the monomer concentration in this stage is below the threshold for homogenous nucleation and thus mainly consumed to grow the nuclei into crystals. This process is thermodynamically favorable, signifying that the nuclei can grow into large single crystal in principle. However, due to the competition among the enormous early-formed nuclei, the limited monomer concentration is unable to provide the unlimited growth of the crystals, especially in the case of colloidal synthesis. Many models have been proposed to elucidate the evolution behavior of crystal in this stage. Here, we mainly introduce the classical diffusion-reaction model and Ostwald ripening model, and correlated their influence on the size and size uniformity of the crystals.

### 1.2.4.1 Diffusion-reaction Growth

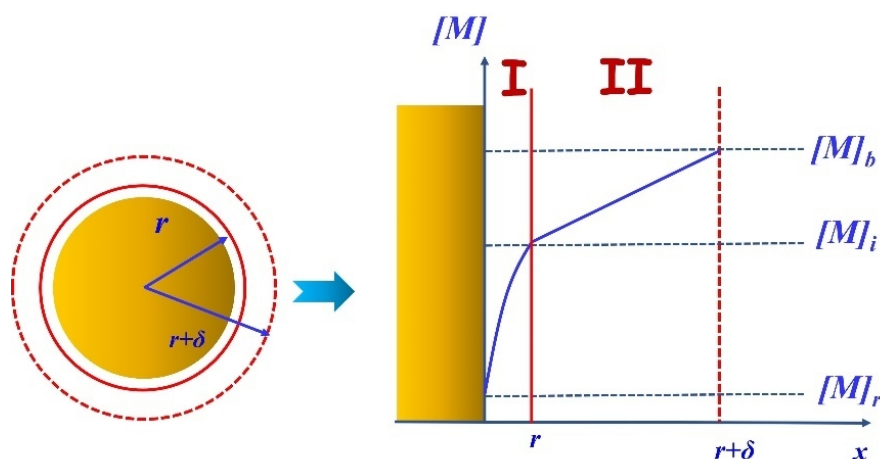


Figure 1.5 Schematic of diffusion-reaction model to describe the growth of colloidal NCs.



The diffusion-reaction growth theory was developed by H. Reiss, et al in 1951, and has been widely used in the crystal growth in colloidal condition [29, 32] This model was established based on the following two assumptions. First, the crystal growth proceeded by the monomer addition coming from the bulk solution. Second, the whole crystal growth event can be divided into two distinguishable two processes: a monomer diffusion process occurring inside a diffusion layer (zone II of Figure 1.5) and a surface reaction process taking place inside a stagnant layer (or reaction layer, zone I of Figure 1.5). In the first process, due to the influence of diffusion, the monomer concentration forms a gradient from the  $[M]$  in the bulk solution to  $[M]_i$  at the interface between diffusion layer and stagnant layer, which can be described by Fick's first diffusion law,

$$j = -D \frac{\partial [M]}{\partial x}$$

Equation 1.8 Fick's first diffusion law describing the monomer addition through diffusion.

Where  $j$  is the unit diffusion flux,  $D$  is the diffusion coefficient of the monomer. Then the total diffusion flux ( $J$ ) can be calculated by integrating the flux around the spherical particle (with a radius of  $r$  including the stagnant layer) from  $r$  to  $r+\delta$  (where  $\delta$  is the length of diffusion path), that is

$$J = 4\pi r D ([M] - [M]_i)$$

Equation 1.9 The total diffusion flux of monomers on a spherical particle.

In the second process, as a result of the surface chemical reaction, the interfacial monomer concentration  $[M]_i$  is consumed to reach an equilibrium concentration  $[M]_r$  at the particle surface, where  $[M]_r$  is a function of the particle size obeying the Gibbs-Thomson relationship. Due to the depletion of diffusion flux, we can have the following expression in the reaction zone

$$J = 4\pi r^2 k ([M]_i - [M]_r)$$

Equation 1.10 The total diffusion flux of monomers used for surface chemical reaction.

Where a simple first-order reaction is considered, and  $k$  is the reaction rate constant. We then can calculate the interfacial monomer concentration  $[M]_i$  by combining the above two equations,

$$[M]_i = \frac{D[M] + rk[M]_r}{D + kr}$$

Equation 1.11 The monomer concentration at the interface of reaction zone and diffusion zone.

On the other hand, according to definition, the total diffusion flux  $J$  can be expressed as a function of the linear growth rate of the crystallite ( $dr/dt$ ),

$$J = \frac{dm}{dt} = \frac{4\pi r^2 dr}{V_m dt}$$

Equation 1.12 The total diffusion flux as a function of linear growth rate.

Where  $m$  is the quantity of monomer used for growth,  $V_m$  is the molar volume of material. Combining the equation 1.9, 1.10 and 1.11, we can obtain the growth rate of a crystallite,

$$\frac{dr}{dt} = \frac{DkV_m([M] - [M]_r)}{D + kr}$$

Equation 1.13 The linear growth rate considering the diffusion and reaction stages.

The equation clearly describes the comprehensive influence of the diffusion coefficient and reaction rate constant on the growth rate. We can further simplify it by considering two cases: reaction-controlled and diffusion-controlled growth. When  $D \gg kr$ , which indicates that the surface reaction is the rate-limiting step, we can have

$$\frac{dr}{dt} = kV_m([M] - [M]_r)$$

Equation 1.14 Equation 1.14 The linear growth rate in reaction-controlled mode.

To correlate the growth rate with the size of the crystallite, we can convert the concentration in the bulk solution and on the surface of a crystallite according to the Gibbs-Thompson equation, that is,

$$[M] = [M]_\infty \exp\left(\frac{2\gamma V_m}{r^* RT}\right) \approx [M]_\infty \left(1 + \frac{2\gamma V_m}{r^* RT}\right)$$

Equation 1.15 The monomer concentration in bulk solution.

$$[M]_r = [M]_\infty \exp\left(\frac{2\gamma V_m}{r RT}\right) \approx [M]_\infty \left(1 + \frac{2\gamma V_m}{r RT}\right)$$

Equation 1.16 The monomer concentration on the surface of a crystallite.

Note that the bulk concentration is dependent on the critical radius ( $r^*$ ). By inserting equation 1.14 and 1.15 into equation 1.13, the equation of growth rate in a reaction-limiting regime is expressed as follows,

$$\frac{dr}{dt} = \frac{2k\gamma V_m^2 [M]_\infty}{RT} \left(\frac{1}{r^*} - \frac{1}{r}\right)$$

Equation 1.17 The linear growth rate in reaction-controlled mode after considering Gibbs-Thompson equation.

Apparently, when the size of the crystallite is smaller than the critical radius ( $r < r^*$ ), a negative growth rate is acquired. This is in accord with the definition of critical radius showing that the crystallite with such small size is inclined to dissolving rather than growing. Conversely, in the case of  $r > r^*$ , we have a positive growth rate, which is positively related to the increase of the crystallite size. In other words, a larger crystallite would grow faster than a smaller one. Accordingly, the size distribution of an ensemble of crystallites would become worse, that is, "size defocusing". On the other hand, when  $D \ll kr$ , we would go into the diffusion-limited zone, in which the following expression is obtained,

$$\frac{dr}{dt} = \frac{DV_m([M] - [M]_r)}{r}$$

Equation 1.18 The linear growth rate in diffusion-controlled mode.

Following a similar mathematic treatment by inserting equation 1.15 and 1.16 into equation 1.18, we can have

$$\frac{dr}{dt} = \frac{2D\gamma V_m^2 [M]_\infty}{RT r} \left( \frac{1}{r^*} - \frac{1}{r} \right)$$

Equation 1.19 The linear growth rate in diffusion-controlled mode after considering Gibbs-Thompson equation.

The plot of the growth rate according to the above equation is shown in Figure 1.6. Obviously, a positive growth rate can be only obtained when  $r > r^*$ . In case of  $r^* < r < 2r^*$ , the growth rate increases with the increase of the size of crystallite, which is an indication of size defocusing. This condition corresponds a relatively low supersaturation where the critical radius is relatively large. When  $r > 2r^*$ , we have a decreasing growth rate with the increase of the size of the crystallite, meaning that smaller crystallites grow faster than the larger ones. As a result, the size distribution of an ensemble of crystallite would become narrower, or known as “size focusing”. In terms of the monomer concentration, a relatively high supersaturation is needed to ensure  $r > 2r^*$  [33].

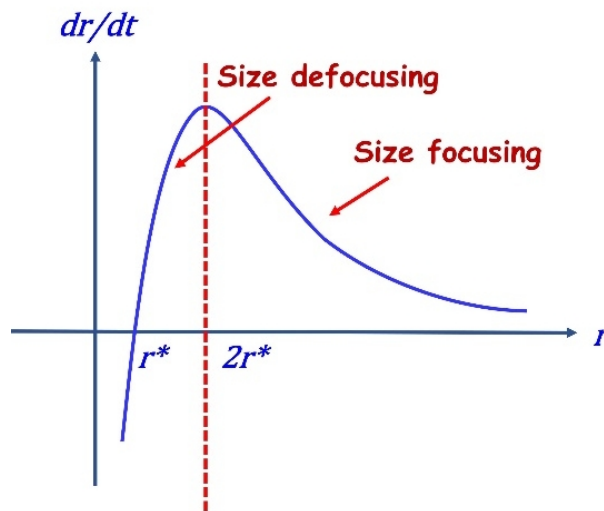


Figure 1.6 Plot of the linear growth rate of the NCs as a function of radius in a diffusion-controlled growth model.

#### 1.2.4.2 Ostwald Ripening

As the reaction proceeds, the monomer concentration will drop to a low level. In this condition, small crystallites would dissolve back to monomers in order to maintain the supersaturation; thus, larger crystallites can still grow by monomer feeding. In other word, large crystallites would become much larger while the small crystallites would gradually dissolve and eventually disappear. As a result, the average size of an ensemble of crystallites increases while their size uniformity becomes worse. This phenomenon is known as Ostwald ripening [34]. The emergence of Ostwald ripening can be explained by the aforementioned Gibbs-Thompson relationship (Equation 1.1), which reveals that the smaller NCs have a higher solubility. More specially, assuming the crystal growth is in the diffusion-controlled mode, as the supersaturation reduces, the critical radius becomes larger (Equation 1.4), therefore the more early-formed NCs would be exposed to the size-defocusing zone where  $r < 2r^*$  (Figure 1.6).

### 1.2.5 Size and size uniformity control strategies

As mentioned above, the formation of colloidal NCs involves a consecutive series of processes from precursor reaction to nucleation and growth of the NCs. In a practical reaction, these processes are normally overlapping with each other and it is impossible to have a clear dividing line in terms of time evolution. Some NCs may grow for a period of time while others just start to nucleate. Accordingly, without any size-controlled techniques, a batch of product typically contains NCs with a broad distribution in size. Their size-dependent physical and chemical properties thereby vary in a wide range, unable to meet the requirement of many applications. For example, in the field of bioimaging and optoelectronic display, QDs emitting light in a narrow range are usually demanded rather than the ones with broad luminescence spectra. Therefore, size control in QDs aims to obtain NCs with desired size and a monodisperse distribution. Based on the aforementioned fundamental understanding of the crystallization process, several size-controlled strategies to obtain uniform NCs can be summarized as follows.

First, separation between nucleation and growth. If the nucleation and growth stages are separated at utmost, a vast majority of NCs will nucleate and grow at the same time. Consequently, a collection of highly monodisperse NCs is expected. In view of the required higher supersaturation for the nucleation, this strategy can be carried out by so-called "supersaturation quench" techniques, such as a quick change of the reaction temperature, dilution with solvent and addition of chelating agent after a short period of nucleation. The hot injection technique used in the synthesis of QDs, as mentioned above, is a characteristic example taking advantage of the temperature factor to realize the supersaturation quench.

Second, careful choice of the growth model. As shown above, after the nucleation stage, NCs will successively undergo a reaction-controlled growth, a diffusion-controlled growth and finally an Ostwald ripening. Due to the Gibbs-Thomson effect, the reaction-controlled and Ostwald ripening are dominated by size-defocusing growth behavior. The size-focusing growth behavior will only take place in the diffusion-controlled mode at a moderate supersaturation. Therefore, careful control over the monomer concentration to maintain a moderate supersaturation is in favor of the formation of monodisperse NCs. Once the monomer is highly consumed to a low level controlled by Ostwald ripening, additional injection of precursors helps to turn the process into a diffusion-controlled regime for a size-focusing growth [2].

Third, creating a monomer reservoir. If the precursor reaction is too fast, the monomer concentration would immediately surge above the nucleation threshold, producing a large number of nuclei, followed by rapid plunge to a low level at which the NCs grow by Ostwald ripening [35]. The size-focusing stage, namely diffusion-controlled growth, is skipped because of the difficulty to maintain the monomer concentration at a moderate level. Complexing ligands are able to address this problem by coordinating to the cationic or anionic source and thus reducing the reaction rate of the precursor reaction. In other words, monomers in the presence of complexing agent seem to be confined in a reservoir that can continuously provide monomer for growth in the diffusion-controlled regime. Characteristic complexing agents used in aqueous reaction include citric acid, EDTA and triethanolamine.

In the non-aqueous synthesis of colloidal NCs, ligands like trialkyl phosphine oxide, trialkyl phosphoric acid, alkyl thiol, fatty acid and alkylamine are mainly used for cationic source while trialkyl phosphine is used for anionic source.

Last but not least, inhibition of aggregative growth. Due to the high specific surface area, NCs are also likely to grow by aggregation, coalescence and recrystallization. This kind of growth behavior should be avoided, as it is less controlled and typically results in a broad size distribution. To accomplish this aim, we can create a repulsive layer on the surface of NCs by using the complexing ligands as discussed in last strategy. Namely, the complexing ligands can also play a role of surface capping ligand by coordinating to the surface atoms on the NCs, creating a double electric layer for water-soluble NCs or bulky layer for NCs synthesized in organic solution. Accordingly, the contact and collision between NCs are reduced and aggregative growth is impeded.

On the other hand, to obtain NCs with a desired dimension, the precursor reaction rate and the number of the NCs should be considered as follows [36],

$$Q_0V_m = v_0\dot{N} + \dot{v}n$$

Equation 1.20 Relationship among the precursor rate and subsequent nucleation rate and growth rate during the colloidal synthesis of NCs.

where  $Q_0$  is the precursor reaction rate in molarity,  $V_m$  is molar volume of the material,  $v_0$  is the initial volume of the stable nuclei,  $\dot{N}$  is the nucleation rate,  $\dot{v}$  is the average volumetric growth rate of the NCs, and  $n$  is the number density of the formed NCs. In case of a classical La Mer mode, where the nucleation and growth mode are well separated, we can have  $\dot{N} \approx 0$  after the nucleation stage, which leads to

$$\dot{v}_f = Q_0V_m/n_f$$

Equation 1.21 Relationship among the final growth rate, the precursor rate and the final number density of NCs.

This equation means that under the same precursor reaction rate ( $Q_0$ ), the final volumetric growth rate of NCs is inversely related to the final number density of the NCs. In this regard, by carefully choosing precursor with a suitable reaction rate and good control over the nucleation process, we can acquire NCs with desired size.

### 1.3 Shape control in anisotropic CdSe NCs

Different from polymeric and amorphous nanoparticles, an inorganic NC consists of atoms or molecules periodically arranged in form of a lattice in 3D space. Especially, on different crystallographic facets, the atomic arrangement is intrinsically different. Hence, on the surface of a crystallite enclosed by different facets, the dangling bond density is different, leading to different surface energies on different facets. Once this point is considered, the morphology of a NC is normally polyhedral instead of spherical, as assumed above. Taking advantage of kinetic reaction conditions and surface capping ligands, they can grow into a diversity of anisotropic shapes, such as 1D nanorods, nanowires, 2D nanoplatelets, nanosheets and more other complex morphologies. In this part, we will begin with the

equilibrium shape of a NC, and then summarize different shape-control strategies to acquire NCs with various non-spherical morphologies.

### 1.3.1 Equilibrium shape: Gibbs-Curie-Wulff construction rule

The thermodynamically equilibrium principle governing the shape of a crystallite was first proposed by Gibbs in 1878, who suggested that a crystallite would like to adopt a polyhedral shape with a minimum total surface energy, namely,  $\sum A_j \gamma_j = \min$ , where  $A_j$  is the surface area of the  $j$ th facet having a surface energy of  $\gamma_j$ . In 1901, Wulff developed this principle into a more quantitative expression as follows [33, 37],

$$\frac{\gamma_1}{r_1} = \frac{\gamma_2}{r_2} = \dots = \frac{\gamma_i}{r_i} = \frac{k_B T \ln([M]_r/[M]_\infty)}{2V_m} = \text{const}$$

Equation 1.22 Wulff construction rule.

where  $r_j$  is the growth distance of the  $j$ th facet, which is defined by the distance from the surface to the center of the polyhedral. This equation is known as the Wulff construction rule, which can be used to predict the equilibrium morphology of a crystal. Based on these considerations, a facet with larger surface energy would grow faster and disappear earlier than the one with smaller surface energy, which evolves at a lower growth rate and tends to constitute the equilibrium surface. Figure 1.7 illustrates an example of applying the Wulff rule to a cubic crystal structure where only the surface energies of {111} and {100} facets are considered. When the difference between  $\gamma_{100}$  and  $\gamma_{111}$  is large, like  $\gamma_{111} < \frac{1}{\sqrt{3}}\gamma_{100}$  or  $\gamma_{111} > \sqrt{3}\gamma_{100}$ , a crystallite would prefer to adopt a shape of octahedron or cube, respectively. As a matter of fact, these two cases do not satisfy the Wulff rule due to geometric constraints, but they still well respect the Gibbs principle to keep a minimum surface energy. On the other hand, an intermediate tetradecahedron shape is formed in the case of  $\frac{1}{\sqrt{3}}\gamma_{100} \leq \gamma_{111} \leq \sqrt{3}\gamma_{100}$ , with a relationship of  $r_{111}/r_{100} = \gamma_{111}/\gamma_{100}$  as determined by the Wulff rule. In a face-centered cubic (fcc) structure with a bare surface, the surface energies can be roughly estimated according to their dangle bond density, as follows:  $\gamma_{100} = 4(\varepsilon/a^2)$ ,  $\gamma_{110} = 4.24(\varepsilon/a^2)$ , and  $\gamma_{111} = 3.36(\varepsilon/a^2)$ , where  $\varepsilon$  is the bond strength and  $a$  is the lattice constant [38]. Thus, we have  $\gamma_{111} < \gamma_{100} < \gamma_{110}$ , indicating that {111} and {110} facets would tend to expose on the equilibrium surface of a crystallite. Also, as  $\gamma_{100}/\gamma_{111}$  is equal to 1.19, an equilibrium shape of tetradecahedron is energetically favored for a crystallite with fcc structure. However, the surface of a NC would absorb the surface ligands in colloidal synthesis, through which the dangling bonds are compensated and surface energies on different facets are changed, so the equilibrium shape is much more complicated than what have discussed here. A recent study by density functional theory (DFT) simulation reveals that the equilibrium shape is a function of the ligand surface coverage, which can be controlled by changing the concentration of surface ligand during synthesis [39].

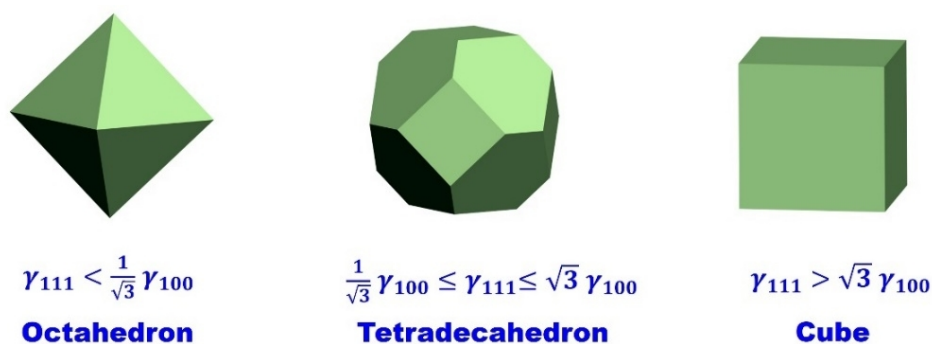


Figure 1.7 Different Wulff-Gibbs equilibrium shapes according to the different surface energies of {100} and {111} facets in a fcc crystal structure.

### 1.3.2 Steady shape

One might consider the growth of a crystal would proceed by maintaining this equilibrium shape. Curie was the first to propose this hypothesis, yet it is not well obeyed in many practical reactions. One reason is because Wulff-Gibbs rule is mainly valid in a crystal with tiny size, as  $[M]_r/[M]_\infty$  tends to be 1 with the increase of crystal size according to the Gibbs-Thompson equation. A more important reason is that an equilibrium shape is assumed to occur under thermodynamically stable condition where the driving force is approaching zero. However, in practical reaction condition for colloidal NCs, the driving force (supersaturation) is typically very high, far from the equilibrium conditions. Accordingly, the crystal might adopt a kinetically stable shape rather than an equilibrium shape.

To understand the stable growth shape under different supersaturation, Sugimoto defines a steady shape as a constant growth shape adopted by a crystal under a constant supersaturation [40, 41]. By correlating the surface chemical potential of a given facet with its surface energy and growth distance in a tetradecahedron geometry, the steady shape is found to be dependent on the growth regime. Here, a more general situation is considered, where a cuboid geometry grows in a diffusion sphere, as depicted in Figure 1.8.

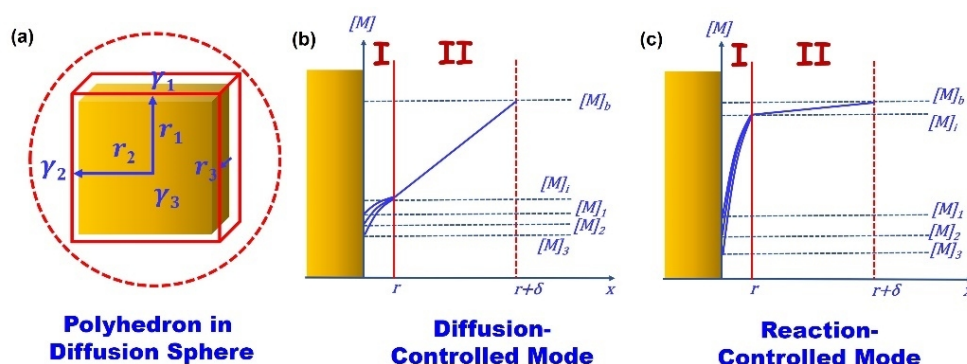


Figure 1.8 (a) Schematic of a cuboid crystal growing in a diffusion sphere. The variation of monomer concentration at the crystal interface under (b) diffusion-controlled mode and (c) reaction-controlled mode are shown.

The cuboid has three facets (marked as 1, 2 and 3) with respective surface energy ( $\gamma_1$ ,  $\gamma_2$  and  $\gamma_3$ ) and growth distance ( $r_1$ ,  $r_2$  and  $r_3$ ). The total surface energy of this configuration is

$$G = A_1\gamma_1 + A_2\gamma_2 + A_3\gamma_3 = 8(r_2r_3\gamma_1 + r_1r_3\gamma_2 + r_1r_2\gamma_3)$$

Equation 1.23 The total surface energy of a cuboid geometry.

where  $A_j$  is the surface area of the  $j$ th facet. Additionally, the volume of whole geometry ( $v$ ) is given as

$$v = 8r_1r_2r_3$$

Equation 1.24 The volume of a cuboid geometry.

The surface chemical potential of facet 1 ( $\mu_1$ ), defined as the change of the total surface energy by growing one mole of molecule on facet 1, can be given as,

$$\mu_1 = \left( \frac{\partial G}{\partial n} \right)_{r_2, r_3} = V_m \frac{\partial G / \partial r_1}{\partial v / \partial r_1} = \left( \frac{r_3\gamma_2 + r_2\gamma_3}{r_2r_3} \right) V_m$$

Equation 1.25 The surface chemical potential of facet 1.

where  $n = v/V_m$  is the mole number of the molecules (or atoms) comprising the whole geometry. Similarly, we can obtain the surface chemical potential of facet 2 ( $\mu_2$ ) and 3 ( $\mu_3$ ) as,

$$\mu_2 = \left( \frac{r_1\gamma_3 + r_3\gamma_1}{r_1r_3} \right) V_m; \mu_3 = \left( \frac{r_1\gamma_2 + r_2\gamma_1}{r_2r_3} \right) V_m$$

Equation 1.26 The surface chemical potential of facet 2 and 3.

These expressions suggest that the surface chemical potential of a specific facet in a polyhedron is dependent on the surface energy and growth distance of the other facets rather than its own. Moreover, we can build the relationship between the surface potential of the  $j$ th facet and its equilibrium monomer concentration  $[M]_j$  [33], such as

$$[M]_j = [M]_\infty \exp\left(\frac{\mu_j}{RT}\right)$$

Equation 1.27 The equilibrium monomer concentration of a given facet as a function of its chemical potential.

Apparently, the equilibrium concentration of a specific facet is positively related with its surface chemical potential. In a diffusion-controlled regime (Figure 1.8b), there exists a large difference between the bulk monomer concentration  $[M]$  and interfacial monomer concentration  $[M]_i$ . Hence, the equilibrium concentration of different facets can be treated as equal, approaching  $[M]_i$ , that is  $[M]_1 \approx [M]_2 \approx [M]_3 \approx [M]_i$ . In this case, we have  $\mu_1 = \mu_2 = \mu_3$ , leading to the steady state as follows,

$$r_1 : r_2 : r_3 = \gamma_1 : \gamma_2 : \gamma_3$$

Equation 1.28 The growth distance relationship of a steady shape in a diffusion-controlled mode.

We can find this relationship is the same to the equilibrium shape as governed by the Wulff rule, suggesting that the Curie rule is valid under an ideal diffusion-controlled growth model. In other words, the diffusion-controlled growth is predominated by the thermodynamic factor. On the other hand, in a reaction-controlled regime where the supersaturation is higher, the difference of surface chemical potentials on different facets is significant. According to equation 1.14, we can have the following expression,



$$r_1:r_2:r_3 = k_1([M] - [M]_1):k_2([M] - [M]_2):k_3([M] - [M]_3) = k_1:k_2:k_3$$

Equation 1.29 The growth distance relationship of a steady shape in a reaction-controlled mode.

Where  $k_j$  is the growth rate constant of the  $j$ th facet. The above relationship is obtained by assuming that the difference among  $[M]_j$  is much smaller than the difference between  $[M]$  and  $[M]_j$  [36]. In this case, the steady shape of a crystal is governed by the reaction rate of the monomers on a given facet rather than the minimum surface energy principle, which means it is more a kinetically stable form. Since the rate constant is highly dependent on the activation energy, different facets might have significantly different rate constants as a result of the different atomic arrangement and interaction with capping ligand. Therefore, anisotropic growth of the NCs is expected under this growth regime.

### 1.3.3 Shape control towards anisotropic 1D and 2D morphology

The fundamental knowledge of equilibrium shapes suggests that it is possible to thermodynamically control the shape of NCs with a range of non-spherical isotropic geometries, such as a cube, an octahedral and a tetradehedron. In the past 20 years, more efforts on the shape-controlled synthesis of NC have been focused on synthesizing NCs with much more complex kinetically controlled morphology, including 1D NCs (eg. nanorods, nanowires and nanotetrapods) and 2D NCs (e.g. nanoplate, nanosheets and nanobelts). These morphologies are not only non-spherical, but also anisotropic, and sometimes even break the restriction of crystallographic symmetry. Here, several models on the shape-controlled synthesis of 1D and 2D colloidal NCs are discussed, with particular focus on cadmium chalcogenide NCs.

Anisotropic 1D rod-like CdSe NCs were first discovered by Peng et al. during the hot-injection synthesis of QDs [18]. A CdSe nanorod has a wurtzite (hexagonal) structure with elongated growth along its  $c$ -axis, or  $\langle 0001 \rangle$  direction (Figure 1.9a,b). The anisotropic growth of nanorods is principally ascribed to two factors. The first factor is the ligand effect. Different from the traditional recipe using tri- $n$ -octylphosphine oxide (TOPO) as the only cationic capping ligand, alkylphosphonic acid with stronger binding affinity to cadmium is critically selected to induce the elongated growth. The length of hydrocarbon chain of the alkylphosphonic acid also significantly matters: a shorter ligand leads to more elongated morphologies [42]. A DFT simulation further reveals phosphonic acid has a selective binding interaction to the lateral facets of nanorods, thus supporting the preferential growth along the  $c$ -axis [43]. The other determinant factor is the monomer concentration. As monomer concentration is linked to the supersaturation driving force for crystallization in solution, its evolution governs the shape evolution of NCs in three regimes. At a high monomer concentration, 1D growth along the  $c$ -axis of the wurtzite structure is promoted, which is kinetically controlled. At an intermediate monomer concentration, both kinetic and thermodynamic factors play a role, leading to a 3D growth of NCs. At a low monomer concentration, a NC mainly grows by itself through intraparticle ripening, which is a thermodynamically controlled process [44] (Figure 1.9c). Obviously, the anisotropic 1D growth behavior of the nanorods at high monomer concentration can also be interpreted as a steady growth shape in a reaction-limited regime where the growth distance is dependent on the growth rate rather than surface energy.

The shape evolution of the CdSe NCs as a function of monomer concentration is shown in Figure 1.9d. The authors further pointed out that in case of extremely high monomer concentration, branched tetrapod-like CdSe NCs were found. Their structures were proposed to consist of a dot-like zincblende core terminated by four {111} facets and four rod-like wurtzite arms which grow along the  $\langle 001 \rangle$  direction. The coexistence of two crystal structures in different domains of the same nanostructure is attributed to a kinetically controlled nucleation and growth behavior. Extremely high monomer concentration results in the formation of zincblende magic-size nanoparticles as the cores, which have a tetrahedral closed-shell configuration and are thereby more stable than the normal nuclei. The subsequent 1D growth of the arms proceeds based on the four {111} facets in the core, turning them into {001} facets of wurtzite structure [45]. By comparison, nanoscale CdTe tetrapods can be obtained in a more well-defined manner with higher synthetic yield. The reason is that the energetic gap between wurtzite and zincblende structure is more favorable for a kinetically stable zincblende nuclei and thermodynamically stable wurtzite arms. In this regard, the nucleation of the zincblende core was generated due to the temperature drop after the injection of anionic precursor [21].

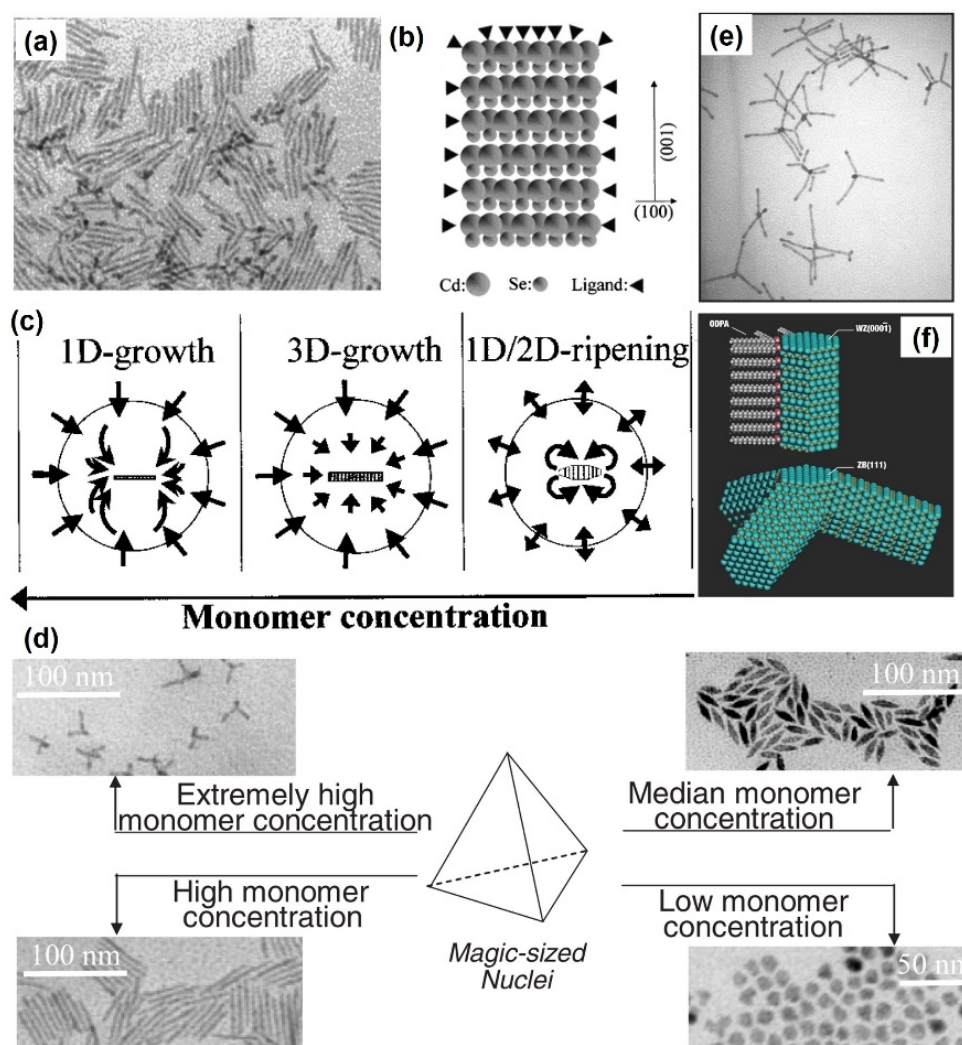


Figure 1.9 Proposed mechanism for the 1D anisotropic growth of cadmium chalcogenide NCs. (a,b) TEM graph and schematic of the wurtzite CdSe nanorods growing preferentially in  $\langle 001 \rangle$  direction (reproduced from [18] with permission). (c,d) Shape evolution of the wurtzite CdSe NCs as a function of monomer concentration (reproduced from [42] with permission). (e,f) TEM graphs of the tetrapod-like CdTe NCs as well as the proposed configuration (reproduced from [45] with permission).

Anisotropic 2D colloidal NCs with morphologies like plates and sheets are frequently observed in materials with a fcc lattice structure. Due to the high crystallographic symmetry of cubic structure, the anisotropic growth in two dimensions is involved with symmetry breaking, making the formation mechanism of 2D NCs more complicated than that of 1D NCs. Three characteristic formation mechanisms of 2D NCs, including twinning effect in metal NCs and kinetic instability in cadmium chalcogenide NCs are shown below.

Twinning effect first came up to explain the anisotropic growth of silver halide prism having morphologies of hexagonal and triangular plates (Figure 1.10a) [33], and then developed for the formation mechanism of silver and gold NCs with similar morphology [46]. All of these materials adopt a fcc lattice structure, the atomic planes of which are supposed to stack as “...abcabcabc...” sequence along the <111> direction [7]. However, owing to the low stacking fault energy in these materials, part of the atomic planes changed to a symmetrical arrangement, leading to twinning defect with a “...abcabacba...” sequence along the <111> direction, where the highlighted “b” is referred to as the twin plane. In this way, symmetry breaking is endangered by forming a platelet structure enclosed by {111} facets as bottom and top surfaces, and either a concave or convex plane as the side surface. Moreover, since the fcc structure owns 6-fold symmetry along <111> direction, the platelet would hold a hexagonal configuration, in which the concave and convex side surface were alternated every 60°, as schematically shown in Figure 1.10b. Due to the geometric feature, the concave side face turned out to be a preferential choice for the monomer addition and so the crystal growth compared to the convex face. This behavior can be understood from the perspective of the Gibbs-Thomson equation, where a negative curvature, or  $-1/r$ , is considered for a concave face, that is

$$[M]_{concave} = [M]_{\infty} \exp\left(-\frac{2\gamma V_m}{rRT}\right)$$

Equation 1.30 The equilibrium concentration of a concave surface.

Knowing that  $2\gamma V_m/rRT$  is larger than 0 according to the definition, we can get to that  $[M]_{concave} < [M]_{convex}$ . As the equilibrium concentration is positively related to the chemical potential, the smaller equilibrium concentration in concave surface corresponds to a smaller chemical potential, thus favorable for the crystal grow in a kinetically controlled condition. Normally, seeds containing singly twinned defect are inclined to form a triangular shape owing to the presence of a pair of concave and convex side surfaces at the same time. Besides, when there exists double or multiple parallel twinning defects in a crystallite, hexagonal plate is favored as each side surface could have a concave structure.

It is worth mentioning that the kinetic control to acquire these silver halides and metal plates are proposed to perform under slow precursor reaction rate, or low supersaturation driving force, different from the required high supersaturation for anisotropic growing 1D NCs as mentioned above [38]. This could be explained by the 2D nucleation and growth model. In this model, the crystal growth is considered to proceed on a smooth plane without any screw dislocation. When the driving force is too large, the monomer can continuously be fed on the thickness direction, resulting in a 3D isotropic growth (Figure 1.10c). Cahn et al calculate the critical free energy difference for this growth regime should be  $-\Delta G > \pi\gamma g/a$ , where  $g$  is the interface diffusion parameter,  $a$  is monatomic surface step height.

On the other hand, when the driving force is small, that is  $-\Delta G < \gamma g/a$ , the growth is dominated by a layer-by-layer way, where 2D island was first nucleated on a new layer to be the step for subsequent lateral growth. In this regime, formation of anisotropic plate-like structure is promoted (Figure 1.10d) [47].

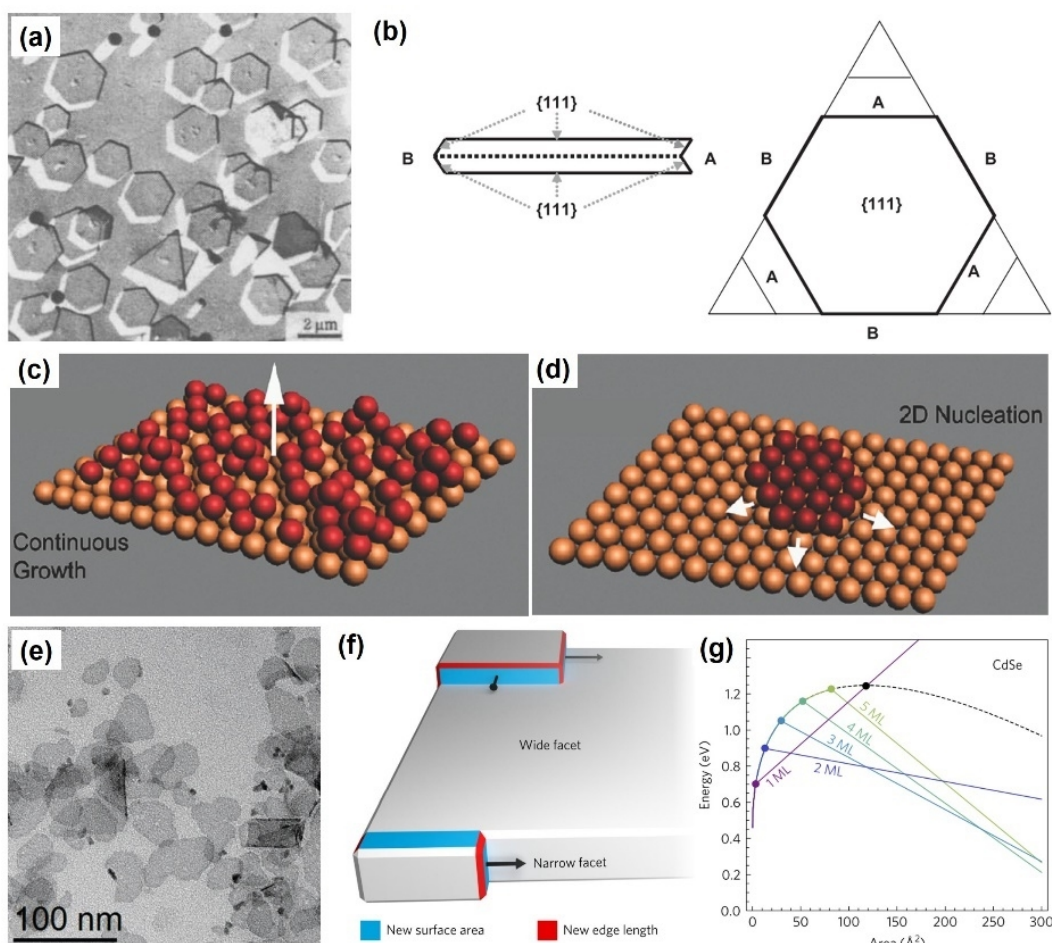


Figure 1.10 Several proposed mechanisms for the 2D anisotropic growth of colloidal NCs by monomer addition approach. (a,b) SEM image and schematic mechanism for the formation 2D AgCl nanoprisms (reproduced from [33] with permission). (c,d) Schematic of classical 2D nucleation and growth model showing the out-of-plane and in-plane crystal growth under high and low driving force, respectively (reproduced from [48] with permission). (e-g) TEM image and proposed kinetic instability mechanism for the formation 2D CdSe nanoplatelets (reproduced from [47] with permission).

2D colloidal semiconductor NCs have attracted tremendous academic interests in recent years. Similar to the metal NCs, they also present an isotropic fcc lattice structure. However, their thickness is just several molecular layers (MLs), while the thickness of metal plate-like NCs can reach 30-40 nm. For instance, 2D CdSe nanoplates are experimentally obtained with a thickness from 2 to 5 MLs, corresponding to the dimension range of 0.7~2 nm (Figure 1.10e). Moreover, their thickness plane is found to be {001} facets, rather than the {111} facets available for producing twinning defects. Therefore, 2D growth in these semiconductor NCs cannot be easily explained by the twinning defect model as mentioned above. A new mechanism based on 2D nucleation and growth model was recently provided by Norris and coworkers, who proposed that the anisotropic growth was caused by an intrinsically kinetic instability existed in isotropic materials during growth. (Figure 1.10f,g) [48] Given the reaction occurs in concentrated droplets or melts, this model assumes the growth of NCs is performed on specific flat facets, like the {100} facets of CdSe nanoplate, and governed by the 2D island nucleation. By

calculating the change of total free energy as a function of island areas, the nucleation barrier on the wide facets was found to be larger than that on the narrow facets with a thickness from 2 to 5 MLs. For example, the barrier on narrow facets with 2 ML thickness is 0.9 eV, compared to 1.25 eV on wide facets, leading to three orders of magnitude faster growth. Besides, the simulation demonstrates thinner CdSe nanoplates are more kinetically favorable, easy to acquire at early stage and low temperature, while thicker ones are more thermodynamically stable yet with higher nucleation barrier. When the thickness of the nanoplates reaches 6 MLs, the barrier on narrow facets approaches the wide-facet limit, thereby the anisotropic growth would be suppressed. In this way, appearance of discrete thickness from 2 to 5 MLs in CdSe nanoplates is expected.

#### 1.3.4 Non-classical growth: Oriented Attachment

In the past 20 years, a new crystal growth theory is rapidly developed to explain and direct the formation of NCs with various morphologies. Many technical terms are put forwards to define this theory, such as nanoparticle assembly [49], aggregative growth [28], particle attachment [50] and particle-mediated growth [51], yet the term “non-classical growth” seems more widely referred to in the literature. Different from classical growth theory, in which the crystal growth is proceeded by continuously feeding atomically or molecularly scale monomer, this theory elucidates crystal growth by aggregation, attachment and coalescence of nanoscale preformed particles. These particles, playing the role of building blocks, can be NCs, amorphous nanoparticles, droplets or complexes and so on. Especially, when the particles are inorganic NCs with polyhedral facets, they prefer to assemble and attach along specific facets to minimize the total surface energy and the strain energy, which is known as oriented attachment. This concept was first reported by Penn and Banfield in 1998 during their hydrothermal synthesis of anatase TiO<sub>2</sub> NCs [52] and has been clearly evidenced by advanced in-situ TEM microscopic technique in recent years. The process of oriented attachment can be carried out by rotation and alignment of the nanoseeds, followed by their attachment and coalescence into crystal with common crystallographic orientation, as in the case of Pt NCs [53]. Similar behavior was also found in iron oxyhydroxide nanoparticles, in which a sudden jump-to-contact of the building blocks occurred over a distance of less than one nanometer [54]. In contrast, in the growth of Pt<sub>3</sub>Fe nanorods, the building blocks were initially attached to each other, followed by the lattice rotation and mass redistribution to straighten the shape [55].

Due to the intrinsic direction-specific interaction, oriented attachment also allows the control over the shape of semiconductor NCs, leading to anisotropic 1D and 2D nanostructures. In 2002, CdTe nanowires with a length up to 1.5 micrometers were synthesized by assembling nanoparticles of 2-5 nm in size (Figure 1.11a) [56]. The key step was to remove the protective organic stabilizer on the nanoparticles surface, followed by aging over a period of 7 days. The intermediate of pearl-necklace aggregates strongly demonstrated the assembly of nanoparticles (Figure 1.11b). Although the nanoparticles had a zincblende structure, the obtained nanowires underwent a phase transition into more stable wurtzite structure, with the long axis of nanowire parallel to the <001> direction. In another example, PbSe nanowires with a diameter of 4~20 nm and a length of up to 30 μm were obtained via the oriented attachment approach (Figure 1.11c,d) [57]. By changing the surface ligand, the attached



facets were able to adjust among {100}, {110} and {110} facets. The crucial factor leading to the anisotropic 1D assemble was various oriented and magnitude of dipole moments in the early-formed building blocks. Consequently, besides the straight nanowires, zigzag, helical, branched, and tapered nanowires as well as single crystal nanorings were obtained by varying the reaction conditions.

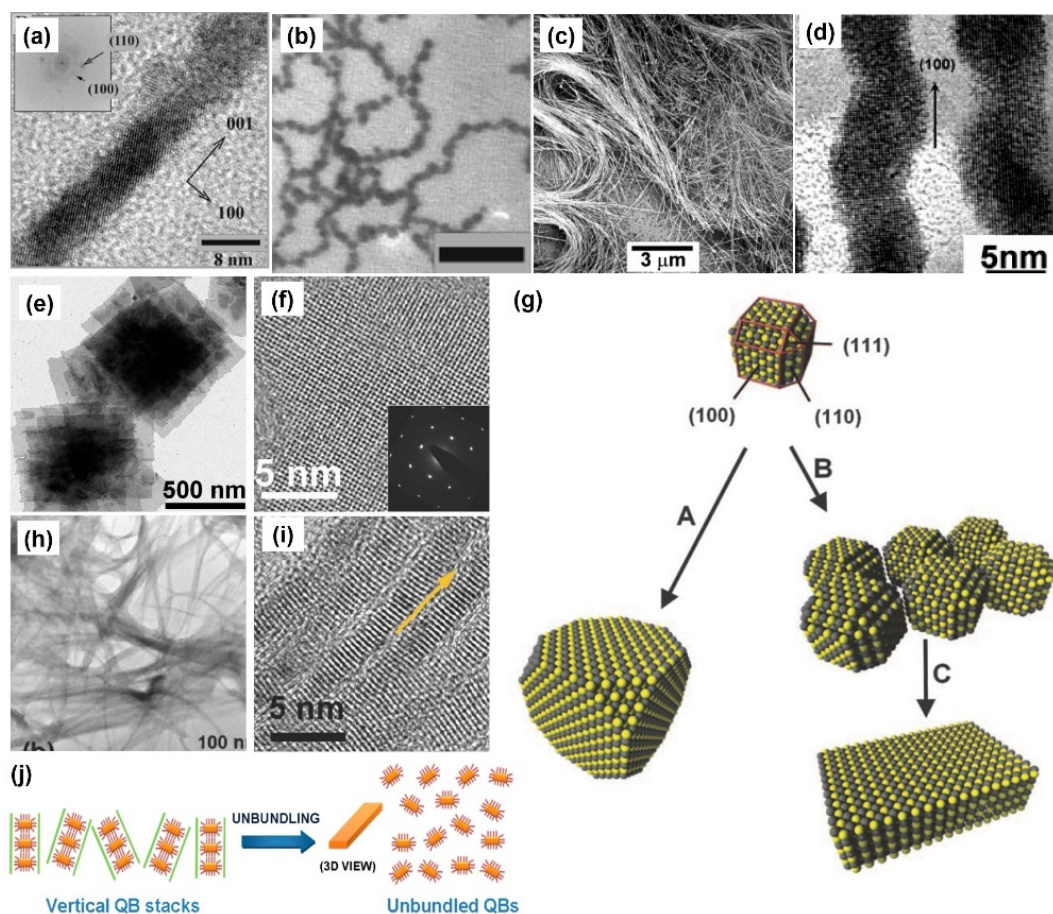


Figure 1.11 Several examples of anisotropic NCs formed by oriented attachment mechanism. (a,b) Wurtzite CdTe nanowires induced by assembling and fusing nanoparticles of 2-5 nm in size (reproduced from [56] with permission). (c, d) Rocksalt PbSe nanowires of several micrometers in length formed by the attachment of the nanoscale building blocks (reproduced from [57] with permission). (e-g) Rocksalt ultrathin PbS nanosheets grown by 2D oriented attachment of NCs along their {110} facets (reproduced from [58] with permission). (h-j) Wurtzite (hexagonal) CdSe nanobelts formed by directing the assembly of amorphous  $(\text{CdSe})_{13}$  nanoclusters in soft template (reproduced from [59] with permission).

In 2010, ultrathin PbS nanosheets induced by 2D oriented attachment was reported by Weller and coworkers [58]. The nanosheet, having rock-salt (cubic) structure and lateral dimension in micrometer scale and thickness of around 2 nm, was suggested to assemble from NCs of around 3 nm in dimension along their {110} facets (Figure 1.11e-g). The addition of chloride compounds plays a key role in the formation of NC building blocks by altering the nucleation and growth rate. The thickness plane of the nanosheet was formed of {100} facets, which were covered by dense packing of oleic acid ligands. In other words, the symmetry-breaking growth of NCs was attributed to a joint effect of oriented and templated assembly. A similar phenomenon was published by Buhro et al during their synthesis of 2D wurtzite (hexagonal) CdSe nanobelts [59]. Primary amine, n-octylamine, assembled into lamellar template in the  $\text{Cd}(\text{acetate})_2-(\text{n-octylamine})_x$  precursor, thereby confining the thickness of nanobelts in the subsequent growth stage. The building blocks were amorphous  $(\text{CdSe})_{13}$  nanoparticles, which were

produced at room temperature and could transform into crystalline after annealing. The long axis, width and thickness of the nanobelts were parallel to [0001], [1100] and [1120] direction, respectively. Using oleylamine (OLAm), the nanobelts were able to be unbundled to more separate ones (Figure 1.11h-i).

### 1.3.5 Shape control strategies

The above examples clearly show the possibility of synthesizing NCs with an enormous diversity of morphologies. Several important factors affecting the shape of NCs can be summarized as below.

First, monomer concentration. As the monomer concentration directly determines the driving force for crystallization, adjusting the monomer concentration turns out to be an important strategy to kinetically control the shape of the NCs. Generally speaking, a higher monomer concentration means a more deviation of the practical synthetic environmental from the thermodynamically stable condition. Hence, a variety of kinetically stable shapes can be obtained at an increased monomer concentration, depending on the crystal structure and surface energy on each facet. Parameters affecting the monomer concentration include precursor concentration, reaction temperature, feeding flowrate and additional chemical reagents such as pH adjuster or complexing ligands.

Second, surface ligands. Surface energy, as an opposing component for crystallization, is another important factor governing the crystal growth. The addition of surface ligands would reduce the total surface energy, and more importantly, rearrange the surface energy on each facet, thereby offering an important strategy for shape control. Parameters such as the nature of the functional group, the alkyl chain length as well as the concentration of the ligands can be modulated to produce NCs with different morphologies. Also, surface ligands can influence the monomer concentration by coordinating to cationic or anionic precursors. Besides, some long-chain organic ligands were found to play the role of soft template during the reaction and thus direct the anisotropic growth in a confined environment.

Third, crystal defects. Imperfections of crystals generated during the reaction offer a possibility to control the shape of NCs. The twinning defect model was reported as an important growth mechanism for the formation of 2D metal nanoprisms having a fcc lattice structure. The classical continuous growth model in metal solidification suggests screw dislocations act as the constant supply of kink sites for the out-of-plane growth. Recently, screw-dislocation mechanism driven growth was also regarded as an important model for the preparation of 1D nanowires [60] and 2D nanoplates [61].

Forth, oriented attachment. After investigation for twenty years, this model has been a widely recognized mechanism for anisotropic NCs with complex morphology. To control the NC morphology formed by this approach, the phase structure, dimension and concentration of the building blocks should be well considered. The phase structure of the building blocks, either amorphous or crystallized, is closely associated with the final assembled nanostructure. The strong Coulomb force on the reactive facets of the NC building blocks directly governs the attachment direction. The dipole-dipole interaction, as presented in some semiconductor NCs having cationic and anionic elements, is also reported as driving force for symmetry breaking in some anisotropic morphology. The oriented attachment can happen no matter if the building blocks are capped surface ligands or not. In the presence of surface

ligands, they can be elaborately selected to tailor the surface energy on different facets, eventually leading to NCs with fairly distinctive shapes. The influence of the size and concentration of the building blocks can be understood from the relationship of collision frequency ( $f$ ), that is [28],

$$f = \frac{k_B T \rho^2}{3\pi\eta r}$$

Equation 1.31 The collision frequency of colloidal particles in solution.

where  $\eta$  is the viscosity of the solution,  $\rho$  and  $r$  are the density and the radius of the nanoparticle building blocks, respectively. Since the possibility of aggregation-based growth is dependent on the collision frequency of building blocks, we could find this type of growth by increasing the concentration of building blocks or reducing their size; in this way, anisotropic growth of the NCs by oriented attachment is more kinetically favorable.

## 1.4 Surface ligands in colloidal CdSe NCs synthesis

Due to the high surface energy, surface ligands are indispensable to be used in the synthesis of colloidal NCs, which can passivate surface dangling bonds, decrease the total surface energy, thus stabilizing the NCs in colloidal solution. Besides, they also act as a reagent that affects the precursor reaction as well as the crystallization process, eventually leading to NCs with different morphology and quality [62].

For most metal chalcogenide NCs, their states in solution are widely accepted to be a stoichiometric core with a layer of metal–ligand complexes on the surfaces [63, 64]. A general classification of surface ligands based on the covalent bonds can be seen in Figure 1.12, in which three types of ligands are involved. L-type ligands, such as phosphine and alkylamine, refer to two-electron donors, neutral Lewis bases and normally bind to the metal center by coordination bonds. X-type ligands, such as carboxylate, phosphate, halide and thiols, are anionic one-electron donors, and bind to the metal center by normal covalent bonds. Z-type ligands, such as cadmium carboxylate and chloride, are two-electron acceptors that bind to the surface anions.



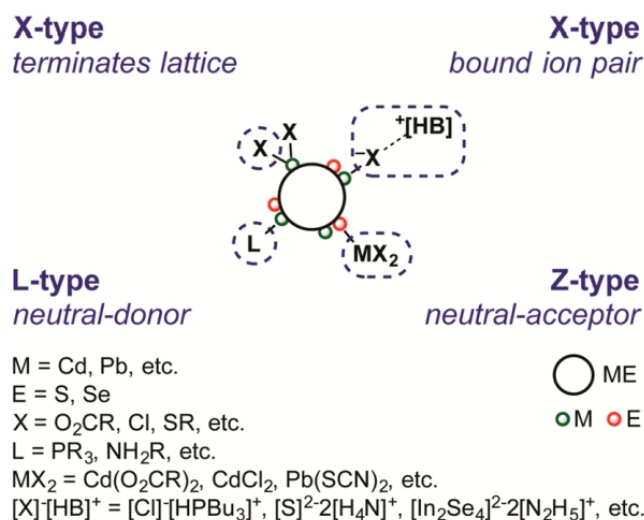
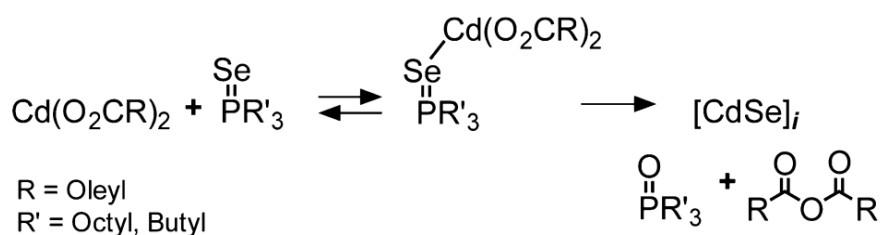


Figure 1.12 Classification of surface ligands according to the type of covalent bonds. Figure is reproduced from [63] with permission.

The successful preparation of CdSe NCs with quantum-confinement effect is highly dependent on the development of the coordination ligands, especially those bound to the Cd center. The earliest seminal discovery is TOPO, which acts as both ligand and solvent. Afterwards, X-type ligands, like phosphonate, were widely studied, which were able to induce the formation of high-quality 1D CdSe NCs besides the QDs. In recent ten years, carboxylate ligands brought broad interests due to its ability to produce 0D and 2D CdSe NCs with high quality and intriguing properties under reduced costs and more safe reaction conditions. It can coordinate to the Cd center, forming cadmium carboxylate (Cd(O<sub>2</sub>CR)<sub>2</sub>) by reacting cadmium oxide (CdO) with corresponding carboxylic acid. The binding state is in an asymmetric chelating bidentate structure, irrespective of aliphatic chain length. One oxygen atom in the carboxylate group could bind to two Cd<sup>2+</sup> cations, making the cadmium carboxylate present in the form of coordination polymer [65]. Alivisatos et al proposed a reaction mechanism between the cadmium carboxylate and a typical selenium source, alkylphosphine selenide (R'<sup>3</sup>PSe), as shown in Scheme 1.1.

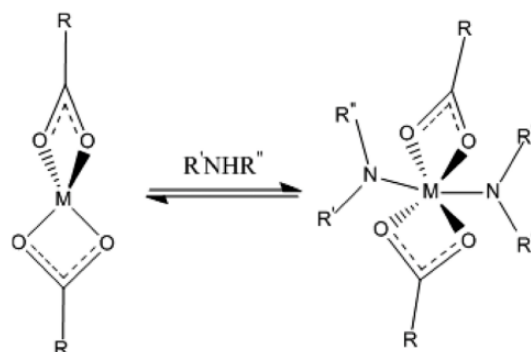


Scheme 1.1 A proposed reaction mechanism between cadmium carboxylate and alkylphosphine selenide to form CdSe NCs. Figure is reproduced from [66] with permission.

This mechanism is consistent with the experimental detection of tertiary phosphine oxide (e.g., TOPO) and the corresponding acid anhydride as the byproducts. The activated lewis acid-base transition state kinetically favors the cleavage of the phosphine-chalcogenide bond through the nucleophilic attack by a free carboxylate [66].

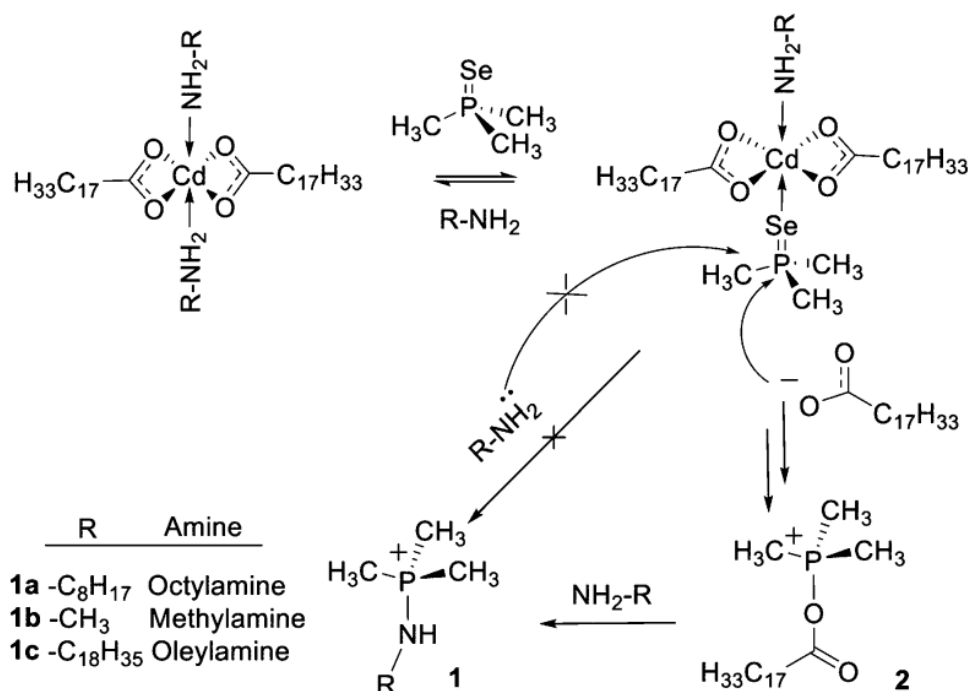
As a characteristic L-type ligand, alkylamines have been proved to be an excellent auxiliary additive during the synthesis of CdSe QDs. An early report showed primary long-chain amine like

hexadecyl amine (HDA) can well passivate the surface of the CdSe QDs, leading to a high PLOQ of 40–60%. When added in the cadmium carboxylate precursor, two amines would weakly coordinate to one metal center (Scheme 1.2), making the reaction mechanism and the subsequent nucleation and growth process are much more complicated [67].



Scheme 1.2 Coordination of alkylamine to the cadmium carboxylate. Figure is reproduced from [67] with permission.

A plausible mechanism proposed by Liu et al in the participation of amine ligands is shown in Scheme 3.



Scheme 1.3 A plausible reaction mechanism between cadmium carboxylate and alkylphosphine selenide to form CdSe NCs in the presence of alkylamine. Figure is reproduced from [68] with permission.

The presence of alkylamines would hinder the activation of the trialkyl phosphine oxide, inhibit the reactivity of the precursors and reduce the number of nuclei, which in turn leading to a higher growth rate for the NCs [68]. However, other reports draw inconsistent and even contradictory conclusions in the literature, suggesting the understanding of the role of alkylamines is still at its early stage and need more investigation [67].

## 1.5 Thesis objective and outline

Although huge developments have been achieved after investigation for almost 30 years, there remain plenty of mysteries to be explored in the controllable synthesis of colloidal CdSe NCs, especially when different types of ligands are used together. The objective of this thesis is to explore the role of the carboxylate and alkylamine ligands during the nucleation and growth of CdSe NCs, including isotropic CdSe QDs and anisotropic 1D and 2D CdSe NCs, thus leading to a control over their size, size distribution, shape and optical properties. In particular, this thesis is organized based an outline as shown below.

In chapter 2, we studied the effect of carboxylic acids and primary amines on the synthesis of CdSe NCs, when used separately or simultaneously. The evolution of shape, size and optical quality of colloidal CdSe NCs upon adding both a carboxylic acid and an amine ligand to the cadmium acetate precursor was investigated, followed by exploring the role of ligand length. In this part, the control over the shape, size and PL property are the main points of interest.

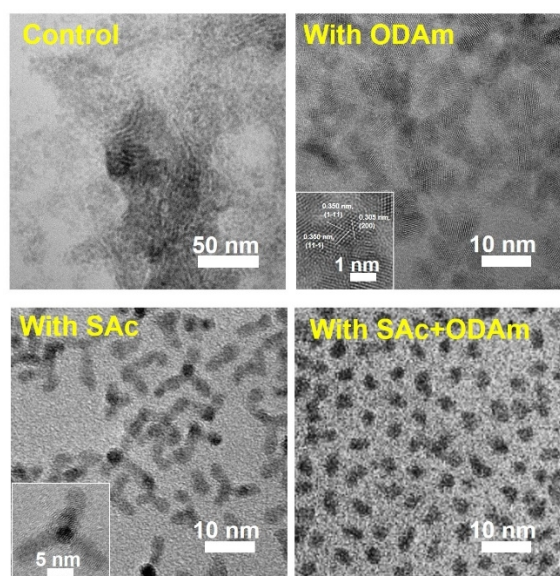
In chapter 3, we focused on the influence of a typical long-chain primary alkylamine, oleylamine, during the synthesis of CdSe QDs using cadmium oleate as the cadmium source. Special attention was paid on the concentration as well as the of the adding oleylamine. The temporal evolution of size, size uniformity, concentration, and optical property of the NCs as well as the precursor conversion was monitored and analyzed, which helps to build a clear view of the role of primary amine.

In chapter 4, we turned to the shape control of the CdSe NCs in the presence of short-chain acetate and different types of alkylamines. Earlier reports already showed the preparation of 2D CdSe NCs with atomically flat thickness in the presence of both long-chain and short-chain carboxylate ligands. Interestingly, we found the combined use of acetate and a secondary amine, dioctylamine, was able to produce CdSe nanotubes with well-defined multiple ultrathin walls, which were observed to be evolved from nanoplatelets and curved nanosheets. The structural and morphological characterization of the tube-like structure, their growth mechanism, and the role of acetate and amines ligands during the synthesis are the main aspects explored.

In chapter 5, we further elucidated the formation mechanism of anisotropic CdSe NCs by using dioctylamine and other carboxylate ligands with different chain length. A morphological transition from nanotubes and nanosheets to irregular nanorods and finally to QDs were observed when the carbon number of carboxylate ligands increased from 2 to 18. We proposed both short- and long-chain carboxylate ligands can lead to the growth of CdSe NCs by oriented attachment of early-formed NCs building blocks, a particle-assembly approach through the reactive facets. However, different carboxylate ligands would generate NC building blocks with different reactive facets as a result of different local supersaturation. We gave experimental observations and first-principle simulation to support the hypothesis.

In the last chapter, we concluded the main roles of carboxylate and alkylamine ligands during the size and shape control of synthesizing CdSe NCs from the results presented. An outlook on future opportunities in the field is discussed.

## Chapter 2 Synergistic effect of carboxylic and amine ligands on the synthesis of CdSe NCs



The evolution of shape, size and optical quality of colloidal CdSe NCs synthesized by using cadmium acetate as cadmium and precursor, a carboxylic acid and/or an amine ligand as surface ligands are investigated. An evident synergistic effect was observed by forming QDs with smaller size, more isotropic morphology, less agglomerated behavior and higher PLOQY upon concurrent use of a long-chain carboxylic acid and a long-chain amine ligand.

This chapter is adapted from following publication:

X. Huang, V. K. Parashar, M. A.M. Gijs, "Synergistic Effect of Carboxylic and Amine ligands on the Synthesis of CdSe Nanocrystals", RSC Adv. 2016, 6, 88911-88915.

## 2.1 Introduction

CdSe NCs are among the most important and, by far, most studied materials applicable in biological imaging, lasers, displays and solar energy conversion by virtue of their attractive electrical and optical properties, as enabled by the advantageous development of robust synthetic methods [69-73]. Several research papers have focused on understanding the reaction mechanism and developing simpler and greener alternatives to the Cd precursor by proposing the use of cadmium acetate ( $\text{Cd}(\text{Ac})_2$ ) and coordination complex ligands [13]. However, the optical properties of CdSe NCs prepared from  $\text{Cd}(\text{Ac})_2$  have not yet reached the same quality as when using CdO, and therefore these alternative methods still require more research. In particular, many reports have revealed the importance of  $\text{Cd}(\text{Ac})_2$  during the anisotropic growth of 2D zincblende CdSe NCs, making it a more mysterious precursor to be explored. This represents the primary motivation for investigating the effect of  $\text{Cd}(\text{Ac})_2$  precursor on the CdSe NCs synthesis.

Coordinated cadmium (II) carboxylate complexes are known to exist in a variety of forms, ranging from mono-, bi-, tri-, to tetra-dentate, and react with lewis bases (amines) to form mononuclear to multinuclear complexes, owed to the presence of a completely filled  $d^{10}$  electronic configuration of the cadmium ion and the flexible coordination modes exhibited by the carboxylate groups [74]. In the case of  $\text{Cd}(\text{Ac})_2$ , both acetate groups exist in bidentate chelating form with one of their oxygen atoms in a bridging position, thereby forming a continuous cadmium-oxygen spiral network [75]. Extensive hydrogen bonding reinforces this Cd-O spiral and further links to adjacent spirals. Amine addition coordinates to the apical position in bidentate  $\text{Cd}(\text{Ac})_2$ . This leads to a unique one-dimensional mesostructure formation in which amine bilayers separate  $\text{Cd}(\text{Ac})_2$  layers [76]. When the latter react with a long chain carboxylic acid, they break down into various fragments of bi-, tri-, tetra-dentate  $\text{Cd}^{2+}$  complexes in organic solvents [77]. The activity of the  $\text{Cd}^{2+}$  in these complexes varies and mostly relates to the steric effects of acids and their bonding strength. The reaction of the complex with the selenium precursor, in general trialkylphosphine-selenium, passes through the cleavage of the P=Se bond during the synthesis of the CdSe NCs. The cleavage of the P=Se bond is initiated by nucleophilic attack of carboxylate on  $\text{Cd}^{2+}$ -activated phosphine-selenide, followed by proton transfer from the carboxylic acid to the Se atom to break the P-Se linkage completely, forming the initial Cd-Se bond [78]. This implies the importance of carboxylic acid ligands to proceed the reaction. Similarly, reaction kinetics get altered on addition of amine ligands, which are known to deactivate the  $\text{Cd}^{2+}$  precursor by complexing the amine to cadmium carboxylate [68]. On the basis of these established mechanisms, we exploited the combined use of long chain carboxylate to open up the cadmium structure and of amine to fine-tune the reaction process.

In this part, we study the use of  $\text{Cd}(\text{Ac})_2$  precursor in combinations of carboxylate complexes including LAc, MAc, SAc and OAc, along with four different lewis bases OLAm, DDAm, HDAm and ODAm complexing ligands. We mainly investigate the influence of the ligands on the size, size

distribution, PLOQY as well as the morphology of the CdSe NCs. Characterization techniques including TEM, HRTEM, UV-vis absorption spectra and PL spectra were employed.

## 2.2 Results and Discussion

### 2.2.1 Synergistic effect of carboxylic and amine ligands

To distinguish the role of different ligands, four reaction routes were designed. Figure 2.1 describes the formation of possible cadmium coordination complexes along with their reaction to TOP-Se in four routes. In route 1, the short-chain acetate ligands of  $\text{Cd}(\text{Ac})_2$  that exist in bidentate chelating and bridging form allow very low solubility of the precursor in the nonpolar solvent, ODE. Therefore, reaction between  $\text{Cd}(\text{Ac})_2$  and TOP-Se is a solid-liquid phase reaction, primarily taking place on the surface  $\text{Cd}(\text{Ac})_2$ . The product is 2D CdSe NCs yet with ill-defined morphology due to the low stabilization of acetate ligands (Figure 2.1a). In route 2, the addition of primary amine, ODA, breaks up the polymeric structure into oligomeric species, enhance the solubility of the precursor by forming clear precursor solution, thus favorable for the nucleophilic attack on TOP-Se by acetate ligands and form 0D CdSe NCs (Figure 2.1b). Liu et al demonstrated it would probably form species less than a dimer [77]. However, without long-chain carboxylate ligands, the reaction is less controlled, making the crystallization process easy to go into the Ostwald ripening stage and finally obtain ill-defined morphology and bad optical properties. In route 3, however, long-chain carboxylic acids can replace the short-chain ligands in the reaction media, as supported by the obtained clear solution after adding the stearic acid (SAc) the  $\text{Cd}(\text{Ac})_2$  solution at 200 °C. The stearate ligands still coordinate to the Cd center by bidentate chelating and bridging, the good compatibility with TOP-Se facilitating the nucleophilic attack of carboxylate on  $\text{Cd}^{2+}$ -activated phosphine-selenide, thereby helping in release of selenium towards  $\text{Cd}^{2+}$  and resulting in CdSe NCs formation (Figure 2.1c). However, the short-chain acetate ligands may still bind to the surface of the NCs, thus being beneficial for the anisotropic growth of the NCs. Its joint effect with long-chain stearate ligands leads to elongated CdSe NCs with branched arms. To minimize the effect of acetate ligands, considering the amine effect in route 2, we speculated that the combined effect of carboxylic acid and amines on the lewis base-coordinated cadmium (II) carboxylate complexes would be a good idea to explore. As shown in route 4, additional carboxylic acids alter the coordinated cadmium carboxylate complex into various mixed bidentate chelates and bridges and facilitate the selenium attack to the electron-deficit cadmium site and simultaneously assist the ligand exchange with amines, which finally yields dot-like CdSe NCs with high controllability (Figure 2.1d).

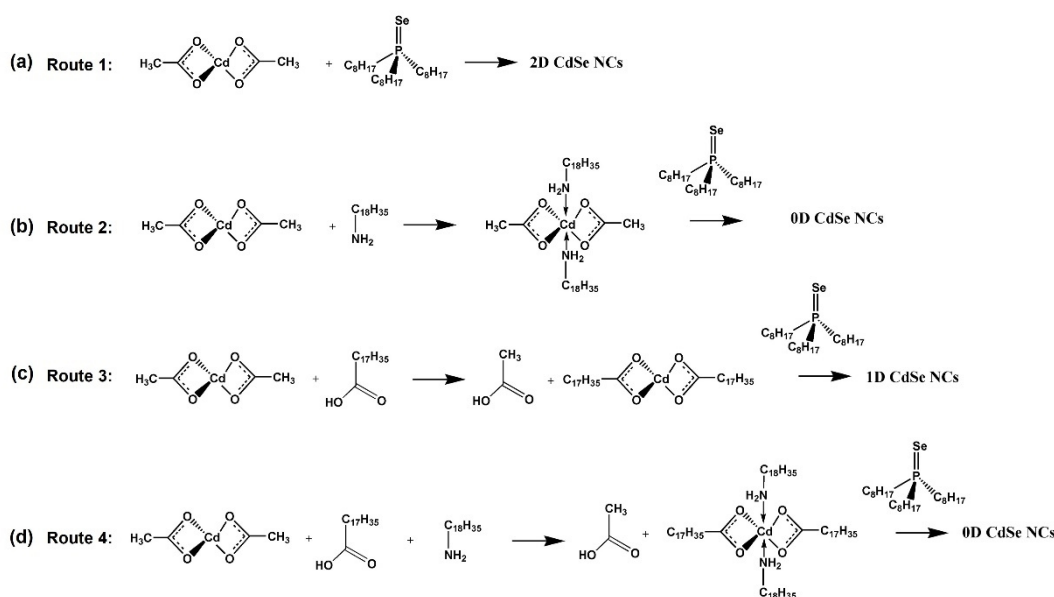


Figure 2.1 Possible coordination complex formation of carboxylic acids and primary amines with cadmium(II) and their reaction towards the selenium precursor TOP-Se at 200 °C. (a) In route 1, cadmium acetate (Cd(OAc)<sub>2</sub>) exists as a bidentate chelating and bridging coordination complex, showing very bad solubility in reactive media (TOP-Se in ODE). Its reaction with TOP-Se leads to ill-defined 2D CdSe NCs. (b) In route 2, adding ODAm to the Cd(OAc)<sub>2</sub> solution results in cadmium precursor with better solubility in solvent due to amine coordinating to the cadmium center. The product is ill-defined 0D CdSe NCs aggregates. (c) In route 3, adding a long-chain carboxylate acid (SAC) would replace the short-chain acetate ligands of the Cd(OAc)<sub>2</sub> solution, forming high soluble precursor solution in nonpolar solvent. The good compatibility with TOP-Se helps for the nucleophilic of carboxylate groups on TOP-Se bonds to release selenium towards cadmium (II), resulting in 1D branched CdSe NCs. (d) In route 4, a combination of primary amine (ODAm), and long-chain acid (SAC) with Cd(OAc)<sub>2</sub> leads to more stable bidentate chelating and bridging coordination complex formation. Competitive exchange amongst carboxylic and amine ligands at a temperature of 200 °C yields everywhere labile carboxylate groups that react with TOP-Se to release selenium towards cadmium (II) resulting in high-yield formation of CdSe NCs with strongly improved PL.

Figure 2.2 shows the experimental results, including UV-vis absorbance, PL spectra and TEM images of the CdSe NCs prepared on the basis of above stated reaction routes. In route 1, we observed some ill-defined sheet-like CdSe nanostructures with absorption peak at 472 nm (Figure 2.2c). This could be assigned to 2D CdSe NCs with a thickness of 3.5 MLs, which shows a characteristic peak position at around 462 nm [6, 7]. The redshift of around 10 nm might originate from the scattering due to the bad solubility of the reactant and product, as deduced from the large scattering shoulder after 472 nm in the absorption spectra. The temporal evolution of the absorption peaks starts from 463 nm at 30 s and shifts to 495 nm after 10 min (Figure 2.3a). We assume the bad solubility and quality of the products is responsible for such an evolution of the spectra. As expected, due to the bad quality, the PL peaks originating the 1D quantum confinement of 2D NCs is unseen. The peak at 514 nm in the PL spectra in Figure 2.3b is due to the scattering of large insoluble particles, which is a good indication of the bad solubility of the large-size CdSe and unreacted Cd(OAc)<sub>2</sub> particles. In route 2 where ODAm was added, the solubility was increased, making the mass transfer between Cd source and Se source more adequately. In this case, we obtained aggregates of 0D CdSe NCs more than 5 nm in size. They present an ill-defined first excitonic absorption peak, which is tunable during the reaction (Figure 2.3c). Obviously, a short-chain acetate ligand and a long-chain primary amine is not the optimal combination for CdSe NCs with high optical properties, which is further supported by the undetectable emission peaks (Figure



2.3d). By contrast, their crystallinity is relatively good, showing clear lattice fringe of zincblende CdSe NCs, as displayed in the inset of Figure 2.2d.

In route 3 where long-chain SAc was added (blue), 1D branched and elongated CdSe NCs were obtained. Apart from bipod and tripods, we found the formation of well-defined tetrapods nanostructures. Earlier reports have shown phosphoric acid [18], medium-chain carboxylate [79], and atomic X-type ligands such as  $\text{Cl}^-$  and  $\text{SO}_4^{2-}$  [80] are advantageous for the elongated and branched growth of the CdSe Ns. We here further found the combined effect of short-chain and long-chain carboxylate can lead to such nanostructures. High-resolution TEM (HRTEM) images in Figure 2.4 suggest the arm of a tetrapod is wurtzite structure growing along the  $\langle 0001 \rangle$  direction, and the core of a tripod is zincblende structure. Their absorption spectra show a sharp peak at 567 nm, suggesting a good quantum confinement effect. However, their emission peak is broad and weak, which might be attributed to the poor surface passivation. An improvement of the PL quality is observed in route 4 where both both ODA and SAc were added. Amines were loosely bound to  $\text{Cd}^{2+}$  in a rapid adsorption/desorption way [81], further improving the steric hindrance effect of the monomer as well as the subsequent NCs. This results in dot-like CdSe NCs with relatively small nuclei, as evidenced by the absorption peak at 524 nm in Figure 2.2a and TEM graphs in Figure 2.2f. Meanwhile, Figure 2.2b and 2.3h suggest their emission intensity is highly improved, which is ascribed to the auxiliary passivation effect by the primary amine [17]. Consequently, a noticeable synergistic effect on the optical properties of dot-like NCs is acquired by the combined use of long-chain carboxylic acids and primary amine ligands.

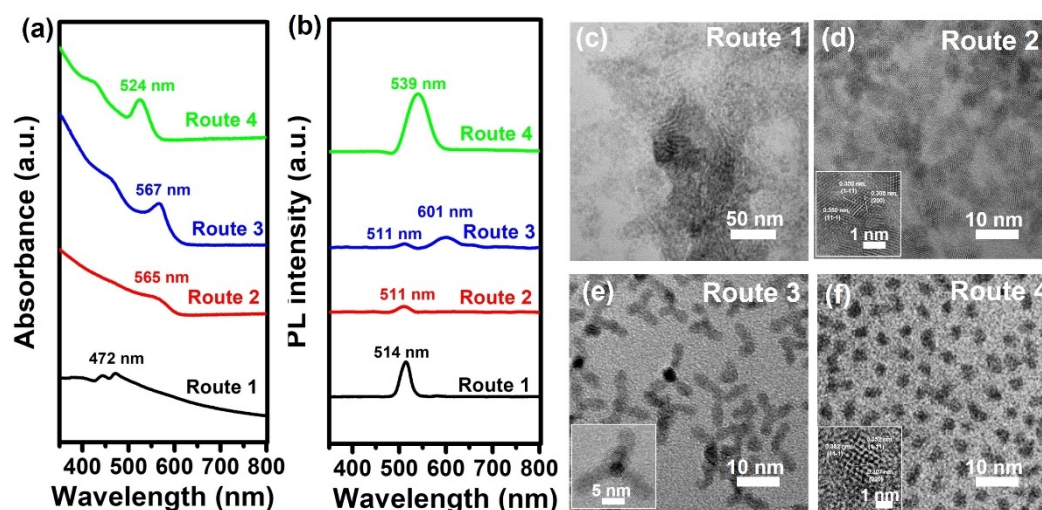


Figure 2.2 Synergistic effect of carboxylic acid and amine ligands on the optical properties and morphologies of synthesized CdSe NCs. (a) Absorption, (b) PL spectra of the CdSe NCs synthesized from route 1 to 4. Curves from the bottom to top correspond to route 1 where no additional ligands were used (black), route 2 where primary amine ODA was added (red), route 3 where long-chain acid SAc was added (blue) and route 4 where both both ODA and SAc were added (green). (c-f) The corresponding TEM graphs of CdSe NCs synthesized from route 1 to route 4. All the reactions were performed at 200 °C for 5 min.

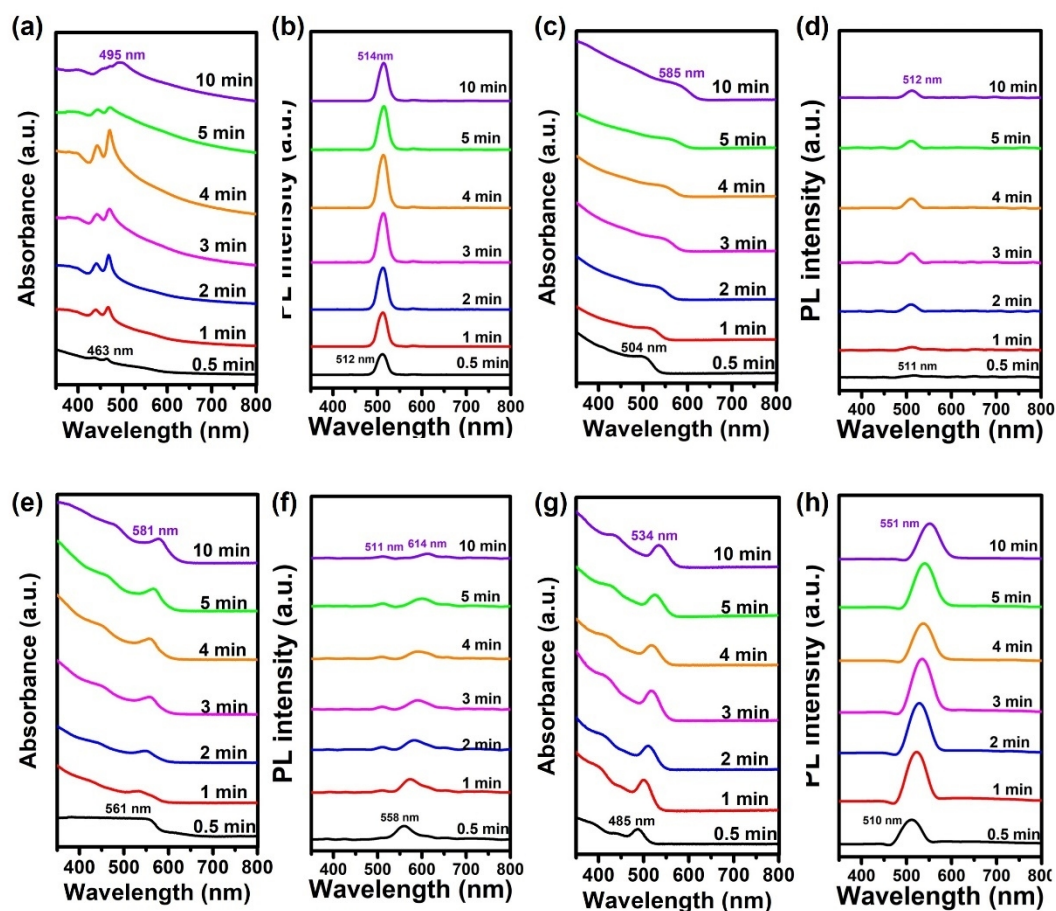


Figure 2.3 (a, c, e, g) Absorption, (b, d, f, h) PL spectra of the CdSe NCs synthesized from (a, b) route 1, (c, d) route 2, (e, f) route 3 and (g, h) route 4 during 30 s to 10 min. All the reactions were performed at 200 °C.

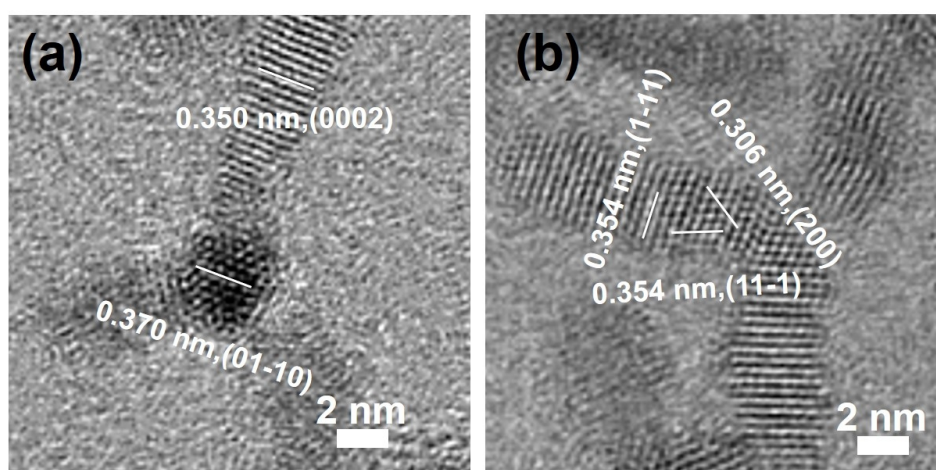


Figure 2.4 High-resolution TEM (HRTEM) images of a (a) tetrapod-like and (b) tripod-like CdSe NCs synthesized from route 3. (a) The lattice fringe of the core of the tetrapods is an overlap pattern of a cubic core along  $\langle 111 \rangle$  direction and a hexagonal arm along  $\langle 0001 \rangle$  direction, leading to the lattice spacing of 0.370 nm corresponding to (01-10) facets of the arm. (b) The lattice fringe of the core of the tripods can be clearly identified as zincblende pattern observed along the  $\langle 011 \rangle$  direction.

## 2.2.2 Influence of the ligands with different chain length

We further investigated the influence of ligands with different chain length. Figure 2.5 present the TEM graphs of CdSe NCs prepared with SAc alone and SAc combined with primary amines having different chain length, including octylamine (OAm), dodecylamine (DDAm), hexadecylamine (HDAm) and octadecylamine (ODAm). Obviously, with the increase of chain length of the primary amines, the obtained CdSe NCs become smaller, less anisotropic and agglomerated. Branched and elongated morphologies can still be clearly observed when OAm or DDAm was used. In other words, the use of primary amines would inhibit the anisotropic growth of CdSe NCs and benefited for the formation of isotropic dot-like CdSe NCs, or QDs, providing an interesting way to control the shape of the NCs. We guess the steric hindrance originating from the hydrocarbon chains of amines plays an important role during the precursor and crystallization process. The analysis of their size, PLQY and PL FWHM with the increase of reaction time is also shown in Figure 2.6. The size curve is evaluated according to the empirical equation provided by Peng and coworkers, which is based on the first excitonic peak of the UV-vis absorption spectra [82]. Although this indicator primarily applied to spherical CdSe QDs, it can also give a general information about average size of the non-spherical NCs after considering their anisotropic morphology. An early report suggests the absorption peak of branched NCs is mainly determined by the average size of the core, with a bit redshift caused by the arm structure [80]. Therefore, the size curves for the branched and elongated NCs in Figure 2.6 a might be a bit larger than they are observed under TEM. From Figure 2.6a, we can find the size of CdSe NCs evolved from 2.7 nm synthesized within 30 s to 3.7 nm synthesized within 10 min in the absence of amines, while in the case of ODAm, it evolved from 2.2 nm within 30 s to 2.7 nm within 10 min. This suggests a reduced growth rate if primary amines with longer carbon chain are used, which is consistent with the TEM images displayed in Figure 2.5d and e. Importantly, the PLQY of the NCs was found to be improved with the increase of chain length of the carboxylic acid, showing an enhancement from less than 1% for the NCs prepared without amine to around 15 % for the NCs prepared in the presence of ODAm. The size distribution, as denoted by the full width at half maximum (FWHM) of the PL spectra (Figure 2.6 c), seems no obvious trend after adding primary amines, varying in the range between 29 to 51 nm.



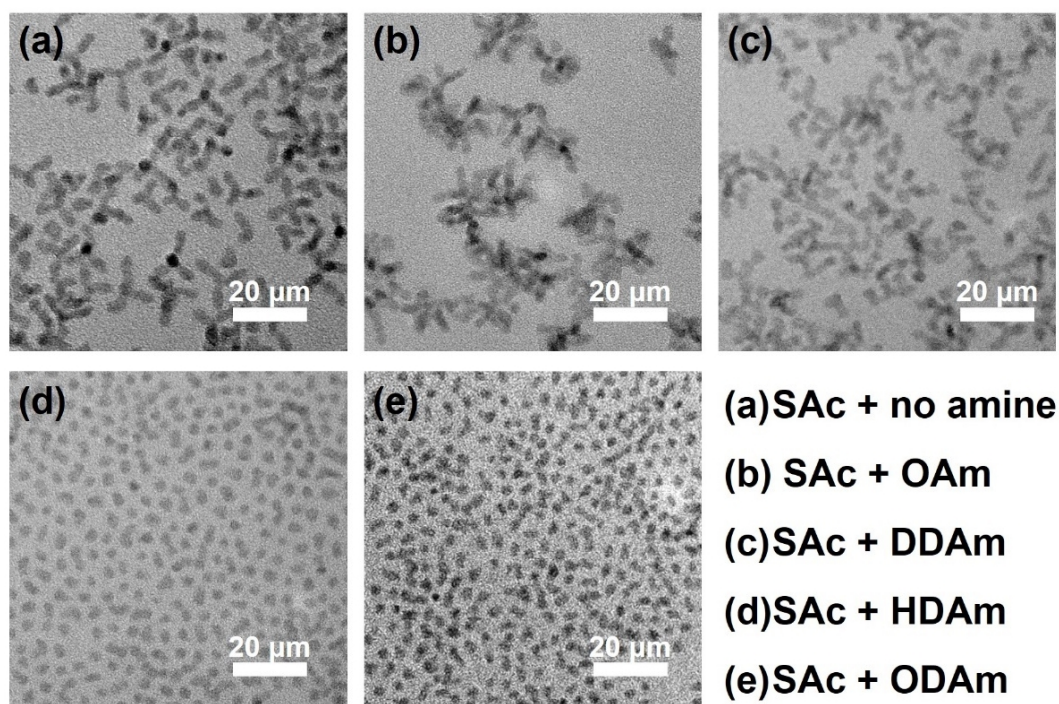


Figure 2.5 TEM images of CdSe NCs synthesized in the presence of stearic acid (SAC) and primary amines having different chain length. (a) Control experiment where only SAC was added to the Cd(Ac)<sub>2</sub> and TOP-Se precursor. (b) Both SAC and octylamine (OAm) were used. (c) Both ODAm and myristic acid (MAc) were used. (b) Both ODAm and stearic acid (SAC) were used. (e) Both ODAm and oleic acid (OAc) were used.

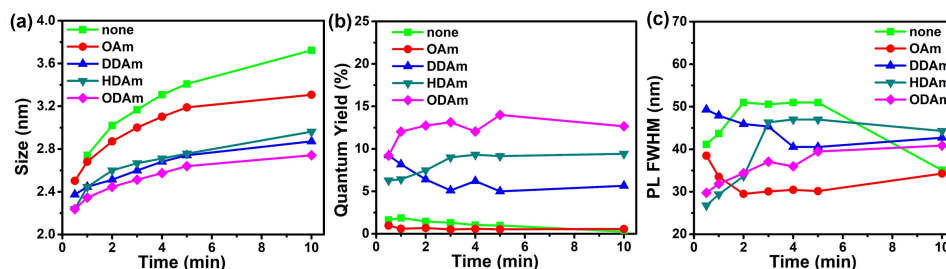


Figure 2.6 Temporal evolution of (a) size, (b) PLQY and (c) PL FWHM of CdSe NCs synthesized in the presence of SAC and primary amines having different chain length. Green curve corresponds to the sample synthesized with SAC and no amine. Red curve corresponds to the sample synthesized with SAC and OAm. Blue curve corresponds to the sample synthesized with SAC and DDAm. Cyan curve corresponds to the sample synthesized with SAC and HDAm. Pink curve corresponds to the sample synthesized with SAC and ODAm. Except the added different ligands, all the samples are synthesized at 200 °C by using Cd(Ac)<sub>2</sub> and TOP-Se as the precursors.

On the other hand, the situation where ODAm added alone and together with carboxylic acids having different chain length including LAc, MAc, SAC and OAc was also studied, as shown in Figure 2.7 and 2.8. Similarly, by using acids with longer chain, CdSe NCs showing less smaller size and less agglomeration were obtained, as seen by the TEM graphs in Figure 2.7. The temporal evolution of the size also demonstrates the NCs grow slower when the chain of the used acid is longer (Figure 2.8a). Enhanced PLQY can be benefited from acids having longer chain (Figure 2.8b). No clear trend of the FWHM of the PL peaks can be deduced (Figure 2.8c). These results are quite similar to those obtained in the presence of SAC with different amines as shown in Figure 2.5 and 2.6, both of which lead to the

observation that by using ligands with longer carbon chain, the NCs become smaller, more isotropic, less agglomerated and present higher PLQY.

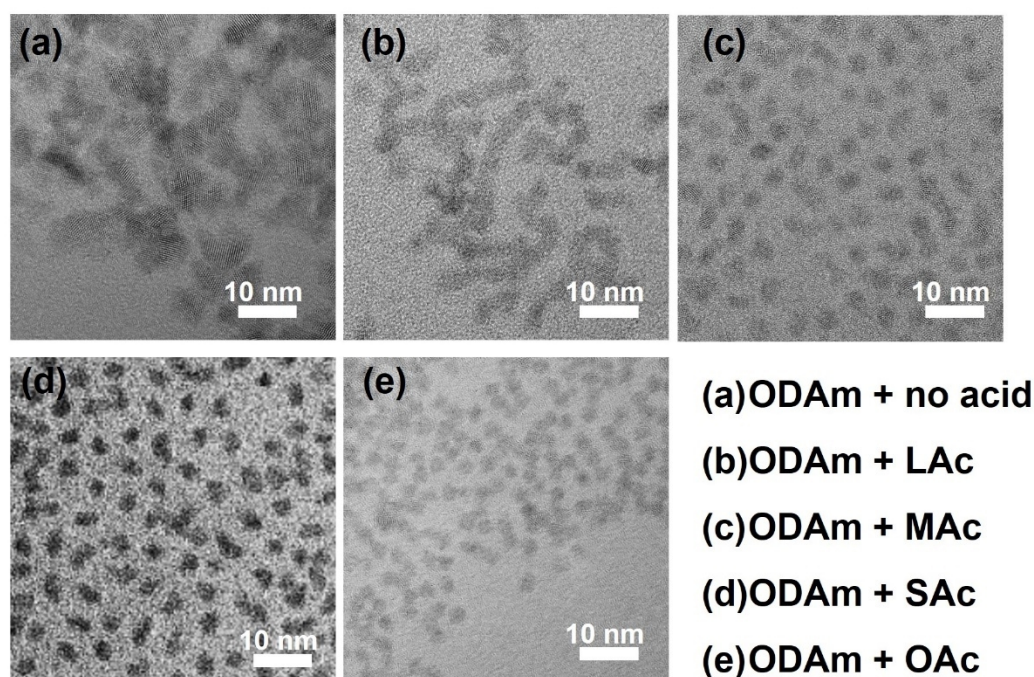


Figure 2.7 TEM images of CdSe NCs synthesized in the presence of octadecylamine (ODAm) and carboxylic acids having different chain length. (a) Control experiment where only ODAm was added to the Cd(Ac)<sub>2</sub> and TOP-Se precursor. (b) Both ODAm and lauric acid (LAc) were added. (c) Both ODAm and myristic acid (MAc) were added. (d) Both ODAm and stearic acid (SAc) were added. (e) Both ODAm and oleic acid (OAc) were added.

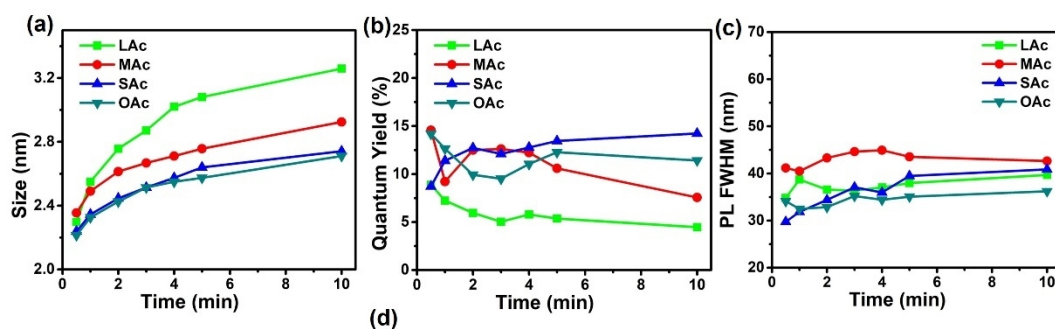


Figure 2.8 Temporal evolution of (a) size, (b) PLQY and (c) PL FWHM of CdSe NCs synthesized in the presence of octadecylamine (ODAm) and carboxylic acids having different chain length. Green curve corresponds to the sample synthesized with ODAm and lauric acid (LAc). Red curve corresponds to the sample synthesized with ODAm and myristic acid (MAc). Blue curve corresponds to the sample synthesized with ODAm and stearic acid (SAc). Cyan curve corresponds to the sample synthesized with ODAm and oleic acid (OAc). Except the added different ligands, all the samples are synthesized at 200 °C by using Cd(Ac)<sub>2</sub> and TOP-Se as the precursors.

We propose the following factors are responsible for the observed phenomena in the presence of long-chain carboxylate and primary amine ligands. The first factor is the synergistic coordination interaction in the coexistence of the carboxylate and amine. Carboxylate ligands bind to the Cd center in a bidentate chelating and bridging form. The addition of primary amine would 1) further coordinate to the complex to form more stable complex and 2) break up the originally polymeric structure of cadmium carboxylates into oligomeric pieces, thus increasing the solubility of the cadmium precursor

in the nonpolar solvent. As a result, the monomer diffusion would dominate the reaction, imposing the crystal growth under a diffusion-controlled regime, thus beneficial for the isotropic growth of NCs. The second factor is steric hindrance, which is much more pronounced when the chain length of ligands is increased. Long-chain ligands coordinating to the metal center would provide additional steric hindrance for the contact and collision between the cationic and anionic sources, inhibiting the precursor reaction, thus resulting with NCs with smaller size. Moreover, when the ligands cap the surface of the NCs, the long hydrocarbon chain would create a larger diffusion sphere that impedes the agglomeration between the NCs. In addition, the distribution coefficient effects might also play an important role in controlling the shape of the NCs. The distribution coefficient, denoted by  $K_{logP3}$  values, show a major increase with increasing amine carbon length, i.e. they range from 3.1 for OAm, 5.3 for DDAm, 7.4 for HDAm and 8.5 for ODAm. OAm with the lowest distribution coefficient does not diffuse well inside the reaction zone and thus creates hindrance to selenium entering towards  $Cd^{2+}$  [77, 78]. On the other hand, amine with a higher distribution coefficient like ODAm distributes/diffuses well in the reaction zone, providing easy access to the  $Cd^{2+}$  site for selenium approach. Consequently, a higher solubility can be obtained when shorter-chain amine is used, which can explain the appearance of branched NCs in the presence of SAc combined with OAm or DDAm. A higher distribution coefficient also helps in the passivation of the CdSe NCs, preventing agglomeration and resulting in a higher PLOY.

## 2.3 Experimental section

### 2.3.1 Synthetic Methods

**Materials.** Commercially available chemicals, including cadmium acetate hydrate ( $Cd(Ac)_2 \cdot 2H_2O$ , 99.9% purity), 1-octadecene (ODE), lauric acid (LAc), myristic acid (MAc), oleic acid (OAc), stearic acid (SAc), octylamine (97% purity, OAm), octylamine (99% purity, OAm), dodecylamine (DDAm), hexadecylamine (HDAm) and octadecylamine (ODAm), trioctyl phosphine (TOP, 97% purity), selenium powder (Se), hexane, methanol and chloromethane were purchased from Sigma-Aldrich.

**Synthesis of CdSe NCs.** The synthesis of the CdSe NCs mainly refer to the classic hot-injection procedures by Peng and Talapin with some modifications. Typically, a stock TOP-Se solution (1 M) was prepared by injecting the trioctylphosphine (TOP) into the selenium powder under the protection of argon atmosphere. It was kept stirring for more than 12 hours to ensure complete dissolution and finally stored in refrigerator. The Cd precursor solution was prepared by adding 0.2 mmol of cadmium and 1 mmol of fatty acid into 5 mL of octadecene (ODE), followed by stirring at 200 °C under the Ar atmosphere. Afterwards, it was cooled down and 1 mol of fatty amine was added. Finally, the solution was heated up and maintained at 200 °C. 1 mL of stock TOP-Se solution was rapidly injected into the Cd precursor solution and the reaction started immediately. After 0.5, 1, 2, 3, 4, 5 and 10 minutes, around 0.7 mL of the solution was withdrawn and quenched with 0.5 mL of chloroform. The purification was performed by repeated centrifugation and redispersion of the sample in a mixture of chloroform and ethanol (1:2) for 4 times and finally dissolved in hexane.

### 2.3.2 Characterization.

The UV-visible absorbance spectroscopy of the solution was performed on Varian Cary 100 Scan, before that 0.2 mL of the resulting solution was further diluted into 1 mL chloroform. The PL spectra were measured by a two-fiber system attached with a USB2000 spectrometer (Ocean Optics). The size of CdSe QDs was obtained through their absorbance peak based on the empirical formula proposed by Peng and coworkers [82]. PLQY was calculated through comparing the PL integral area and absorbance intensity of the QDs with that of the standard dyes, Rhodamine 6G, which presents a PLQY of 95% in ethanol ( $\phi_{st}$ ). The calculation is shown below,

$$\text{PLQY} = \phi_{st} \times \frac{F_x \times f_{st}}{F_{st} \times f_x} \times \frac{\eta_x^2}{\eta_{st}^2}$$

Equation 2.1 Equation used to calculate the PLQY of the CdSe NCs based on relative method.

where  $F$ ,  $f$  and  $\eta$  refer to the fluorescence area, absorption factor ( $f=1-10^{-A}$ , where  $A$  is the absorbance of the sample) and refractive index of the used solvent, respectively. The subscript "st" and "x" refer to the standard dye Rhodamine 6G and the CdSe NCs to be measured. TEM graphs and HRTEM graphs were captured by a Talos transmission electron microscope (FEI company), before which the CdSe NCs in hexane were dropped and dried in ultrathin carbon-supported copper grids.

## 2.4 Conclusion

In summary, we studied the effect of carboxylate and primary amine on the hot-injection synthesis of CdSe NCs by using  $\text{Cd}(\text{Ac})_2$  and TOP-Se as the precursors at 200 °C. The evolution of size, shape and optical quality of CdSe NCs in the presence of carboxylic acid and/or primary with different hydrocarbon chains were compared, by which we mainly obtained the following conclusions.

First of all, without additional ligands, the reaction between  $\text{Cd}(\text{Ac})_2$  and TOP-Se leads to 2D CdSe NCs with characteristic optical spectra yet ill-defined sheet-like morphology.

Second, single use of long-chain carboxylic acid generates branched 1D CdSe NCs with clear quantum confinement absorption, while single use of long-chain primary amine result in large 0D CdSe NCs aggregate with poor optical feature.

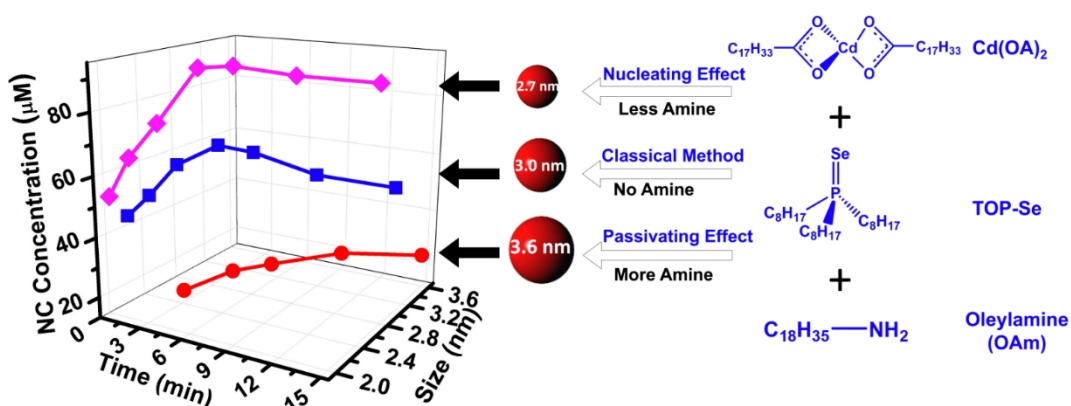
Third, the combined use of long-chain carboxylic acid and primary amine is favorable for the formation of NCs with high optical quality. Particularly, QDs with smaller size, more isotropic morphology, less agglomerated behavior and higher PLQY were obtained by increasing the length of hydrocarbon chain of the ligands.

In addition, some questions still remain, such as the effect of amine on the control of size and size distribution of CdSe QDS, as well as the origin of anisotropic growth in 2D and 1D CdSe NCs. These issues will be discussed in more details in the following chapter.





# Chapter 3 Nucleation and growth behavior of CdSe NCs synthesized in presence of oleylamine coordinating ligand



In this chapter, we studied the nucleation and growth behavior of the CdSe QDs using cadmium oleate, trioctylphosphine selenide and oleylamine as the precursors. We particularly focused on the influence of the concentration of oleylamine as well as its addition way, and found: 1) the oleylamine mainly played the role of nucleation promotor at low concentration and the role of passivating agent at high concentration; and 2) injecting the oleylamine after the precursor reaction is beneficial for producing QDs with better quality.

This chapter is adapted from following publication:

X. Huang, V. K. Parashar, M. A.M. Gijs, "Nucleation and Growth Behavior of CdSe NCs Synthesized in Presence of Oleylamine Coordinating Ligand", *Langmuir* 2018, 34, 6070-6076.

### 3.1 Introduction

In the last chapter, we have demonstrated the advantages by using primary alkylamines during the synthesis of CdSe NCs: they would weakly bond to the surface of NCs, forming a high packing density, effectively eliminating the unsatisfied dangling bonds, tuning the NCs size and size distribution and therefore resulting in an adjustment of the UV-vis and PL spectra and an enhancement of the PLQY [17, 83-85]. However, the role of the amine is still not understood to the extent that contradictory explanations for both NCs nucleation and passivation stages were reported. Few authors have reported that its addition would activate the cadmium precursor and thus promote the nucleation of NCs (Figure 3.1a,b) [86, 87]. These results were based upon the evidence that a smaller nuclei size can be observed at an earlier time and higher NC concentration as well as growth rate were found when primary amines were used. Whereas, others have reasoned a delayed nucleation in the amine-containing reaction, which was proposed to result from formation of low-activity Cd-amine complexes by the coordination strength or steric hindrance effect [88, 89]. Recently, it was demonstrated that alkyl amines restrained monomer activity by inhibiting the cleavage of the P=Se bond in the Se precursor while increasing the growth rate of CdSe NCs and reducing the NCs concentration (Figure 3.1c,d) [68]. These contradictory research results make it obvious that more in-depth studies are necessary to establish the role of amine in NCs synthesis.

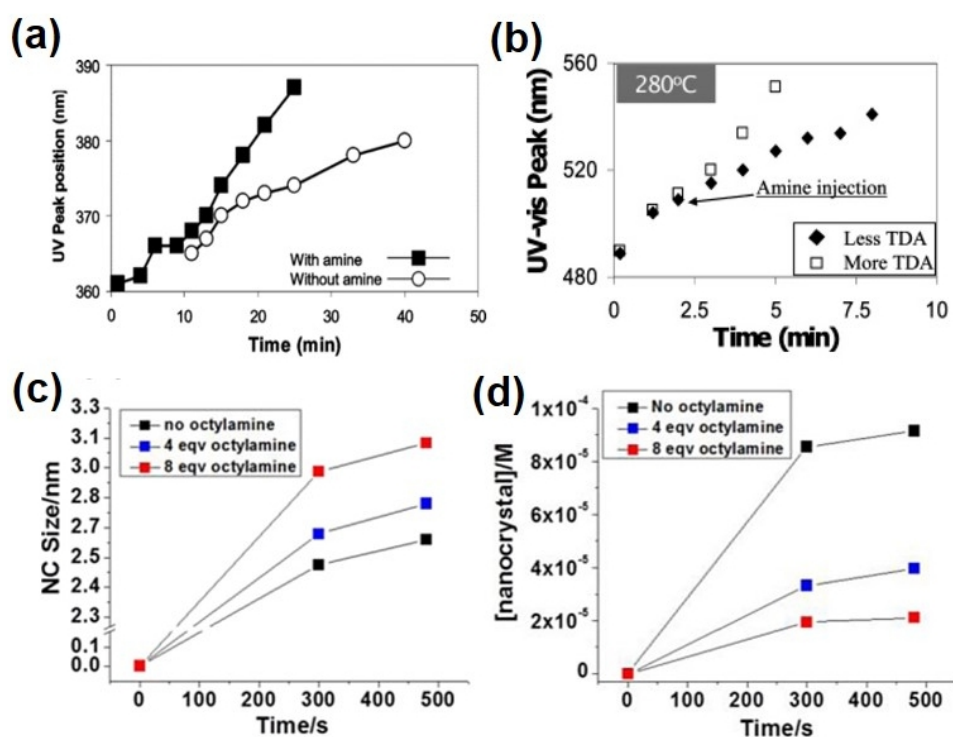


Figure 3.1 The reported studies on the role of the alkylamine on the nucleation and growth of CdSe NCs. (a,b) Temporal evolution of the first exciton absorption peak in the absence and presence of primary amine during the colloidal synthesis of (a) ZnSe NCs and (b) CdSe NCs reported by Peng et al (reproduced from [86, 87] with permission). (c,d) Temporal evolution of the NC (c) size and (d) concentration when different amount of octylamine was added, published by Liu et al (reproduced from [68] with permission).

In this chapter, we use oleylamine (OLAm) as a model to further study their influence on the nucleation and growth of CdSe NCs. We found both effect including activating the nucleation and passivating the precursor reaction could exist, depending on the amount of the added amine. We further demonstrated the addition way of amine also played an important role in size uniformity of NC, which could be effectively focused if the amine was injected after the precursor reaction.

## 3.2 Results and Discussion

### 3.2.1 Influence of OLAm on size and concentration of CdSe NCs

To interpret the influence of OLAm on the nucleation and growth behavior of NCs, different synthetic NCs routes were studied, by altering the time and sequence of addition of various reactants. Four reaction routes were designed, as schematically presented in Figure 1. Route 1 (classical amine-free route): Cd oleate precursor ( $\text{Cd}(\text{OAc})_2$ ) in ODE solution is prepared and thereafter the Se precursor, TOP-Se, is injected. Route 2: various concentrations of OLAm are added to the  $\text{Cd}(\text{OAc})_2$  in ODE solution, after which Se precursor is injected. Route 3: various concentrations of OLAm and Se precursor are mixed together in ODE, after which  $\text{Cd}(\text{OAc})_2$  is injected to induce the reaction. Route 4:  $\text{Cd}(\text{OAc})_2$  in ODE solution is prepared and then the Se precursor (TOP-Se) is injected. After 32 seconds, OLAm is injected into this reaction mixture.

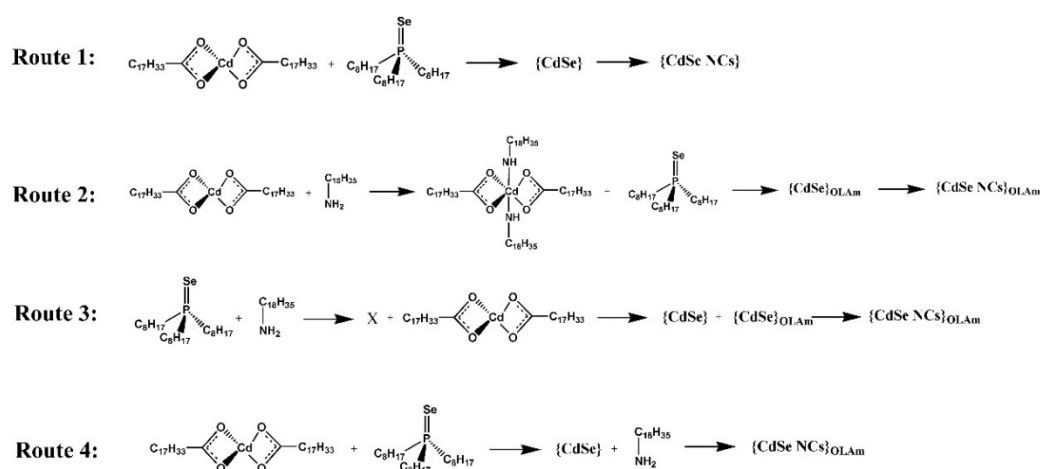


Figure 3.2 Schematic of designed four reaction routes to investigate the influence of oleylamine (OLAm) on the synthesis of CdSe NCs. Route 1: Cd oleate precursor ( $\text{Cd}(\text{OAc})_2$ ) in ODE solution is prepared and then the TOP-Se is injected. Route 2: various concentrations of OLAm are added to the  $\text{Cd}(\text{OAc})_2$  in ODE solution, after which Se precursor is injected. Route 3: various concentrations of OLAm and Se precursor are mixed together in ODE, after which  $\text{Cd}(\text{OAc})_2$  is injected to induce the reaction. Route 4:  $\text{Cd}(\text{OAc})_2$  in ODE solution is prepared and then the Se precursor (TOP-Se) is injected. After 32 seconds, OLAm is injected into this reaction mixture. X represents no reaction;  $\{\text{CdSe}\}$  represents the CdSe molecular building blocks ("monomers"), prepared without amine;  $\{\text{CdSe}\}_{\text{OLAm}}$  represents the CdSe monomers surrounded by OLAm molecules;  $\{\text{CdSe NCs}\}$  represents finally formed CdSe NCs without use of OLAm and  $\{\text{CdSe NCs}\}_{\text{OLAm}}$  represents finally formed CdSe NCs surrounded by OLAm molecules.

In route 2, synthesis starts by reacting OLAm with the cadmium precursor, followed by the addition of the selenium precursor. Accordingly, the influence of OLAm starts already prior to the nucleation process, resulting in the difficulty of distinguishing the respective influence on nucleation

and NC growth stage. Both routes 2 and 3 divulge the amine adduct formation with the cadmium precursor prior to the nucleation stage, whereas route 4 concentrates on the OLAM influence on the NC growth stage, avoiding its influence in both initial precursor and nucleation stages. We benchmarked all results with respect to route 1, which is the standard synthesis process. The reaction products from all the four routes were extracted at different times during the reaction to perform UV-vis absorbance and PL measurements. Figure 3.3 shows UV-vis absorbance spectra obtained for the four different routes (route 1 to 4). Reactions of routes 2 to 4 were done in presence of 2.5 mmol OLAM. The curves i, ii, iii, iv, v, vi and vii in each graph correspond to CdSe NCs extracted after a reaction time of 0.5, 1, 2, 4, 6, 10 and 15 min, respectively. It is evident that all the first excitonic peaks in the four reaction routes present red shifts with time evolution, signifying a time-dependent growth behavior of the NCs. Absorbance spectra of route 1 (Figure 3.3a) and route 4 (Figure 3.3d) look similar, having higher intensity (Figure 3.4a) and sharper peaks (Figure 3.4b) of the first excitonic peaks than those in route 2 (Figure 3.3b) and route 3 (Figure 3.3c). This implies a difference in growth behavior due to the presence of OLAM at the beginning of the reaction. In order to obtain comprehensive knowledge of the OLAM influence, the reaction was carried out under various concentrations of OLAM, namely 0.1 mmol (i.e. a molar ratio of 1:2 between Cd precursor and OLAM), 0.5 mmol (1:10), 1 mmol (1:20) and 2.5 mmol (1:50).

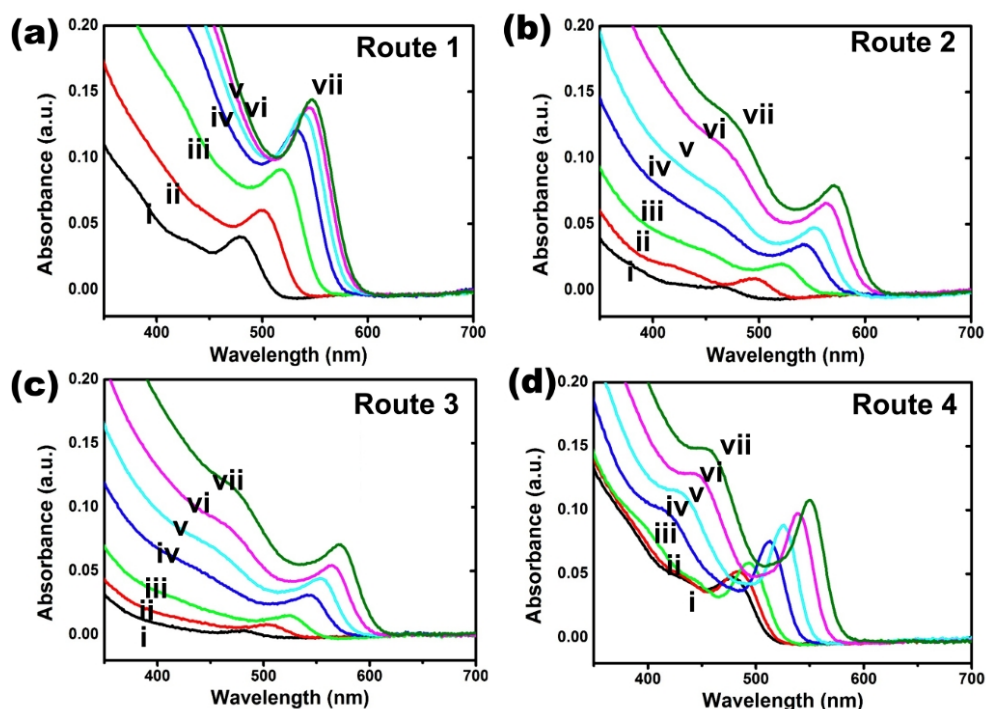


Figure 3.3 UV-vis absorbance spectra of CdSe NCs prepared using different routes. (a) route 1 in which no OLAM was added; (b) route 2 in which TOP-Se was injected into a mixture of Cd(OAc)<sub>2</sub> and OLAM; (c) route 3 in which Cd(OAc)<sub>2</sub> was injected into a mixture of TOP-Se and OLAM; (d) route 4 in which TOP-Se was injected into Cd(OAc)<sub>2</sub>, followed by the injection of OLAM. The curves i, ii, iii, iv, v, vi and vii in each graph are of the reaction product extracted at a reaction time of 0.5, 1, 2, 4, 6, 10 and 15 min, respectively. OLAM amounts used in reaction routes 2 to 4 is 2.5 mmol.

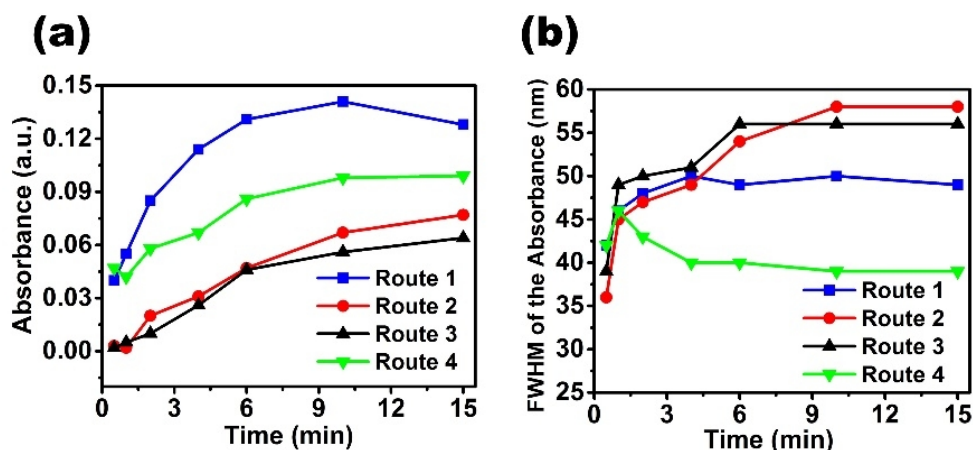


Figure 3.4 The intensity (a) and the FWHM (b) of the first excitonic peak of the CdSe NCs. Samples were prepared from route 1, 2, 3 and 4 during a reaction time of 15 min. 50  $\mu\text{L}$  of as-synthesis CdSe NCs in ODE were diluted in 1450  $\mu\text{L}$  of hexane for the measurement. For route 2, 3 and 4, the OAm amount used was kept at 2.5 mmol. These data are analyzed based on the absorbance spectra as shown in Figure 1 in the manuscript.

Figure 3.5 shows the temporal evolution of the NCs size (a,d,g), the volumetric growth rate (b, e, h), and concentration (c, f, i) of CdSe NCs, prepared by route 2 (a,b,c), route 3 (d,e,f) and route 4 (g,h,i), respectively. In general, the CdSe NCs size increases with time and a higher OAm concentration results in a larger size. Also, a higher growth rate is obtained for higher OAm concentrations. Moreover, the time-dependence of the NC concentration shows saturation for the longer reaction times with higher OAm concentrations resulting in lower concentrations. First of all, results obtained using route 2 and 3 are comparable. Both routes show a smaller NC size, lower growth rate and higher NC concentration compared to the standard route 1 (Figure 3.6) at low OAm concentration. When amine content was above 1 mmol, however, an opposite result was obtained, namely a larger NC size, higher growth rate and lower NC concentration than obtained using route 1. Most distinct information is the smaller initial size in route 2 with respect to route 3. The OAm influence at the growth stage was examined using route 4, in which OAm was injected 32s after the reaction of Cd and Se precursors. At the time of injecting OAm, nucleation has already started (around 20 out of 30  $\mu\text{M}$  CdSe nuclei were already formed at 32 s), and NCs of about 2.2 nm were formed and continued to grow (Figure 3.5g). It was seen that the NC final concentration was almost the same as with route 1, i.e. it was around 30  $\mu\text{M}$  (Figure 3.6c and 3.5i), while in the case that OAm was fully mixed with Cd(OAc)<sub>2</sub> before the reaction (route 2), the NC concentration increased from 30  $\mu\text{M}$  to 42  $\mu\text{M}$  (Figure 3.5c). This means the promotion of the NC nucleation at lower amine concentration (like 0.5 mmol) is closely related to the injection of OAm. We also observed a sharp decline of the growth rate in the first minutes after injection of OAm. At lower OAm concentration, the growth rate is smaller but, for longer reaction times, similar to the other routes (Figure 3.5h). Therefore, NCs size in the final stage is smallest for route 4. Growth rate evolution curves transform from an exponential-like decrease to a linear-like increase as a function of OAm concentration, which is clearly distinct from route 2 and 3.

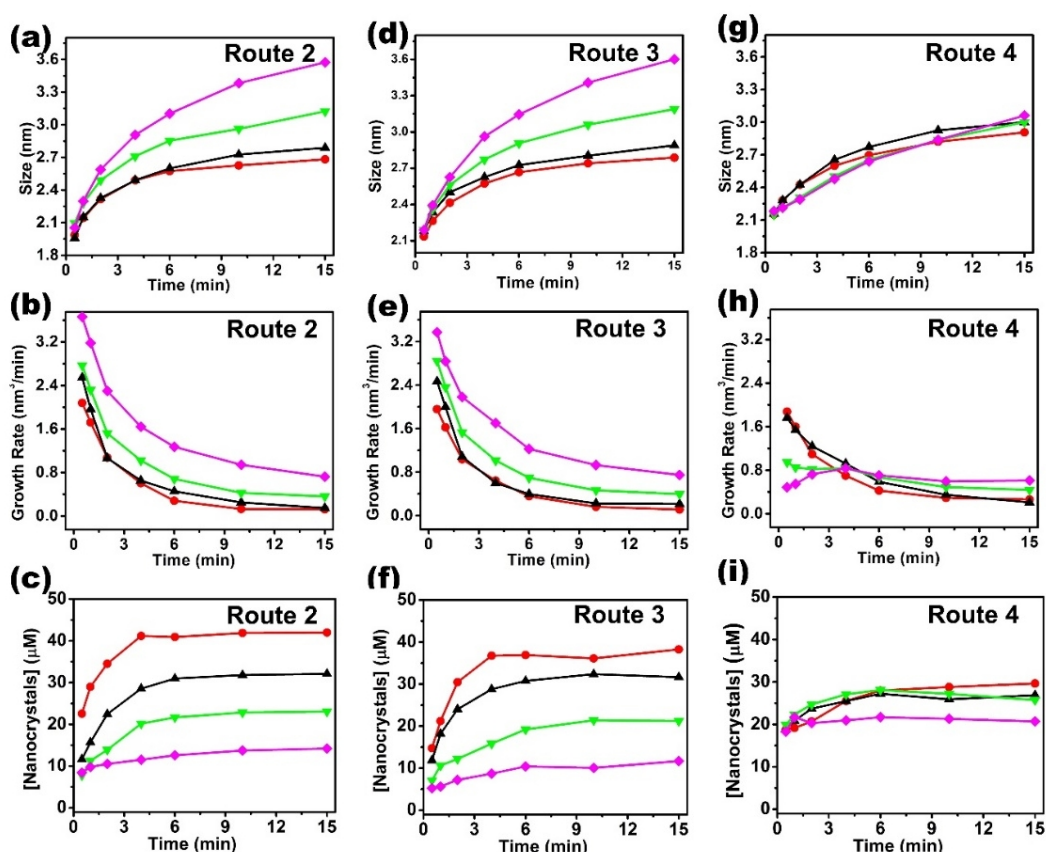


Figure 3.5 Temporal evolution of the size (a,d,g), volumetric growth rate (b,e,h) and NC concentration (c,f,i) of CdSe NCs. In route 2 (a,b,c), TOP-Se was injected into a mixture of Cd(OAc)<sub>2</sub> and OLA<sub>m</sub>; in route 3 (d,e,f), Cd(OAc)<sub>2</sub> was injected into a mixture of TOP-Se and OLA<sub>m</sub>; in route 4 (g,h,i), TOP-Se is injected into Cd(OAc)<sub>2</sub>, followed by the injection of OLA<sub>m</sub> after 32 sec of reaction. All these reaction routes employed various amounts of OLA<sub>m</sub>, namely, 0.1 mmol (●), 0.5 mmol (▲), 1.0 mmol (▼), and 2.5 mmol (◆).

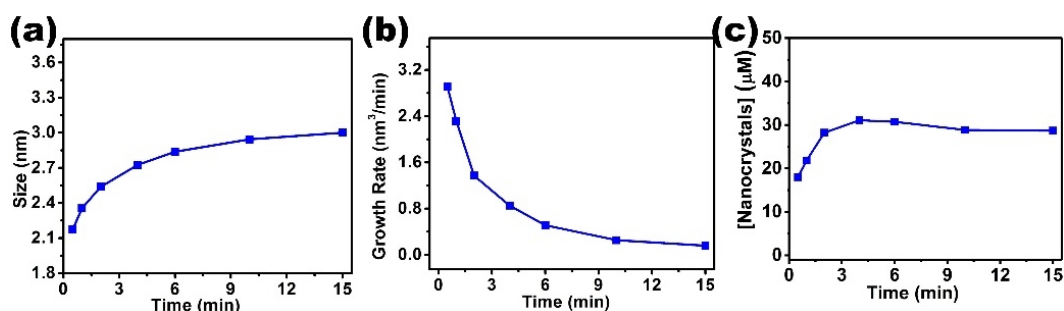


Figure 3.6 Temporal evolution of the size (a), volumetric growth rate (b) and concentration (c) of the CdSe NCs synthesized by route 1.

Furthermore, we calculate the temporal evolution of the CdSe concentration in the form of NC, as shown in Figure 3.7. In generally, the conversion of the precursor to CdSe NCs, no matter in which injection route, displays a decline with the increase of OLA<sub>m</sub> amount. From route 2 and 3, we can see that the addition of a little amount of OLA<sub>m</sub> (like 0.5 mmol, or a molar ratio of 1:2 between Cd and OLA<sub>m</sub>) has little effect on the CdSe formation. This is because the nucleation-promoting effect compensates the reduction on the growth of the NCs. The nucleation-enhanced effect is weak in route 4, therefore resulting in an obvious reduced number of CdSe units even, when only 0.5 mmol OLA<sub>m</sub>



was injected (Figure 3.7d). At higher OLAm concentration (above 1.0 mmol), although an enhancement on the NC growth rate is observed, the decreased production of new nuclei leads to a substantial reduction of the conversion to CdSe NCs. We also find the rate of CdSe formation (Figure 3.8) and the rate of NC number (Figure 3.9) have very similar trend with the increase of OLAm concentration. These observations imply that for the conversion of precursors to CdSe units, the concentration of NC plays the dominant role rather than the size of the NC. At lower concentration, amine is mainly used to coordinate to the Cd center to form Cd-amine complex precursor, thereby leading to the formation of high amounts of nuclei and CdSe units. At higher concentration, excess amine acts as the passivating agent, slowing down the nucleation process and thus resulting in reduced conversion of the precursors into CdSe products.

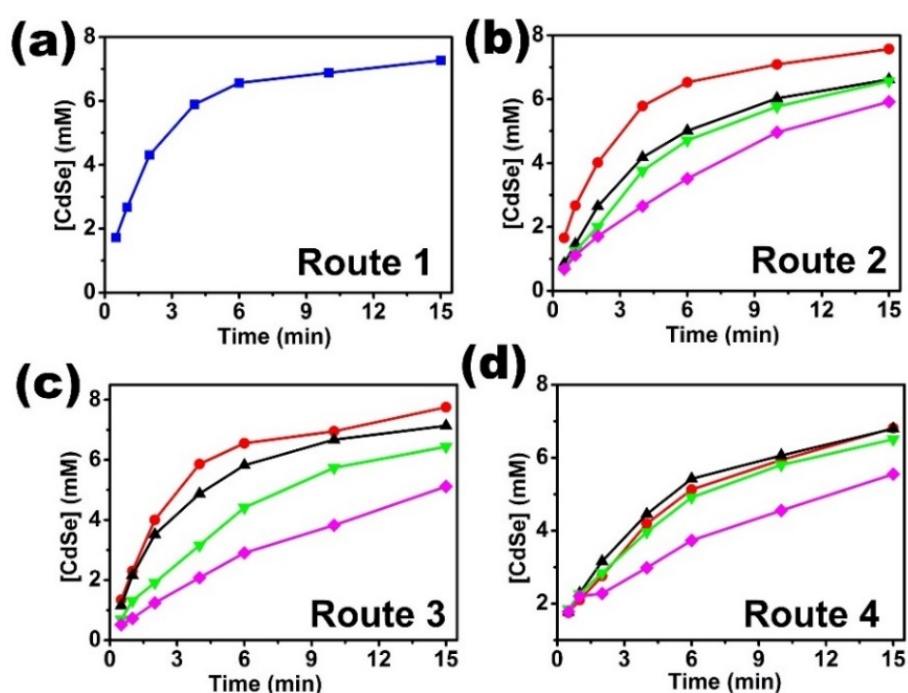


Figure 3.7 Temporal evolution of the CdSe concentration in the form of NC. NCs were synthesized from route 1 (a) without amine addition, route 2 (b) in which TOP-Se was injected into a mixture of Cd(OAc)<sub>2</sub> and OLAm, route 3 (c) in which Cd(OA)<sub>2</sub> was injected into a mixture of TOP-Se and OLAm, and route 4 (d) in which TOP-Se is injected into Cd(OAc)<sub>2</sub>, followed by the injection of OLAm after 32 sec of reaction. All these reaction routes employed various amounts of OLAm, namely, 0.1 mmol (●), 0.5 mmol (▲), 1.0 mmol (▼), and 2.5 mmol (◆).

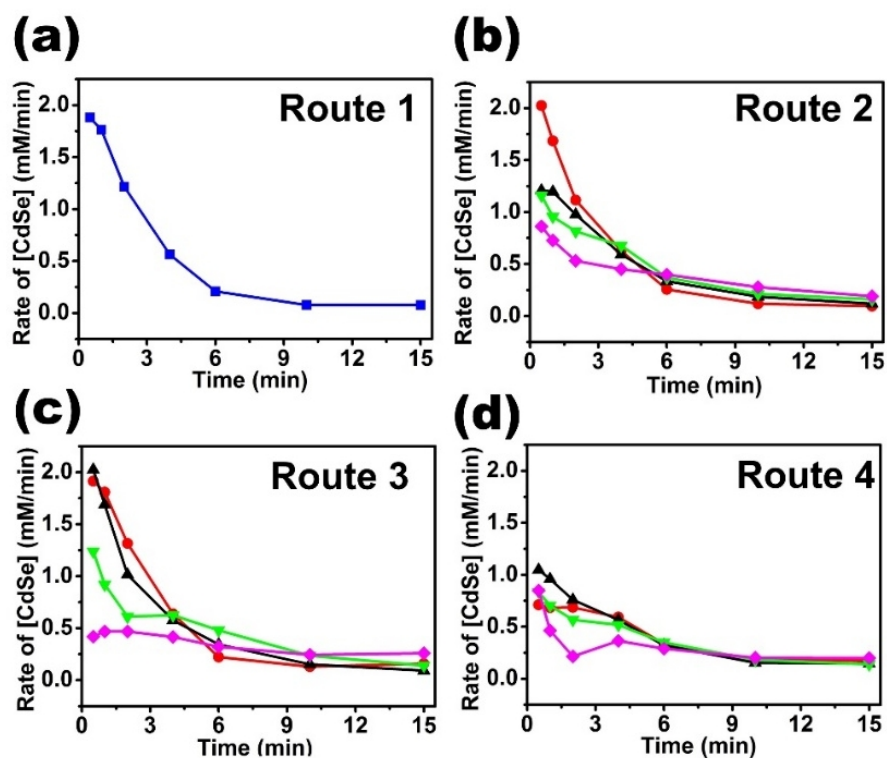


Figure 3.8 Temporal evolution of rate of the total concentration of CdSe units in the form of NCs. All these reaction routes employed various amounts of OAm, namely, no amine ( $\blacksquare$ ), 0.1 mmol ( $\bullet$ ), 0.5 mmol ( $\blacktriangle$ ), 1.0 mmol ( $\blacktriangledown$ ), and 2.5 mmol ( $\blacklozenge$ ).

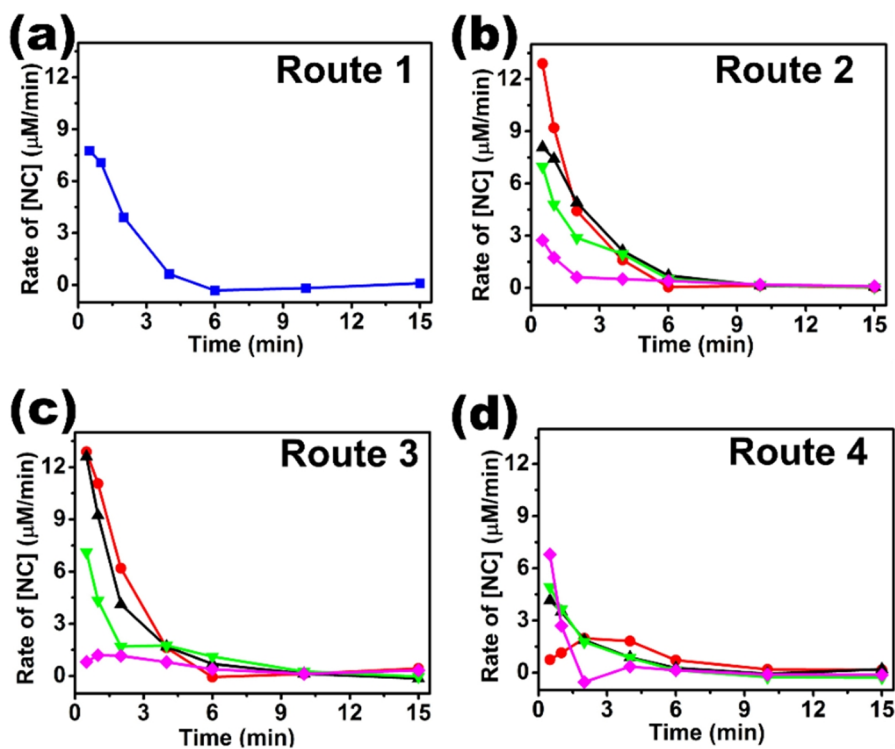


Figure 3.9 Temporal evolution of rate of the NC concentration. Samples were synthesized from route 1 (a), 2 (b), 3 (c) and 4 (d). All these reaction routes employed various amounts of OAm, namely, no amine ( $\blacksquare$ ), 0.1 mmol ( $\bullet$ ), 0.5 mmol ( $\blacktriangle$ ), 1.0 mmol ( $\blacktriangledown$ ), and 2.5 mmol ( $\blacklozenge$ ).



### 3.2.2 Influence of OLAm on size distribution of CdSe NCs

The Full Width at Half Maximum (FWHM) of the PL is an indicator of size distribution of CdSe NCs. Figure 3.10a-d demonstrates PL of CdSe NCs obtained by (a) route 2, (b) route 3 and (c) route 4, respectively, at a reaction time of 15 min with a OLAm content of 2.5 mmol. Figure 3.10e-h shows FWHM as a function of reaction times for route 2, route 3, route 4, respectively. During onset of NC growth, a rapid decline in FWHM during the first 2 min of the reaction happens, while, for route 2 and route 3, a slow rise takes place at the later growth stage. Contrarily, route 4 shows a continuously fall of FWHM with time, suggesting the size focusing. Our results here demonstrate the impact of amine on the size distribution depends not only on the ligand amount, but also on the way it is added. The increase of the amine amount is related with enhancement of the passivating effect, leading to the decrease of the NCs numbers and increase of the monomer supply for each NC during the growth stage. According to the size-focusing theory, when there are enough monomers in the solution, smaller particles can grow faster than the larger ones, eventually resulting in the size focusing. This is why we can see the FWHM decline with amine concentration in route 2, 3, and 4. Otherwise, in route 2 and 3, the emergence of a gradual nucleation stage of around 4 min leads to an increase of the PL width of the NCs with time, while that has been minimized in route 4, resulting in a continuous decrease of the FWHM and better focusing of the NC size. We proposed the addition of OLAm after the precursor can effectively “quench” the supersaturation, thus the nucleation event is inhibited and more monomers were provided for the NC growth.

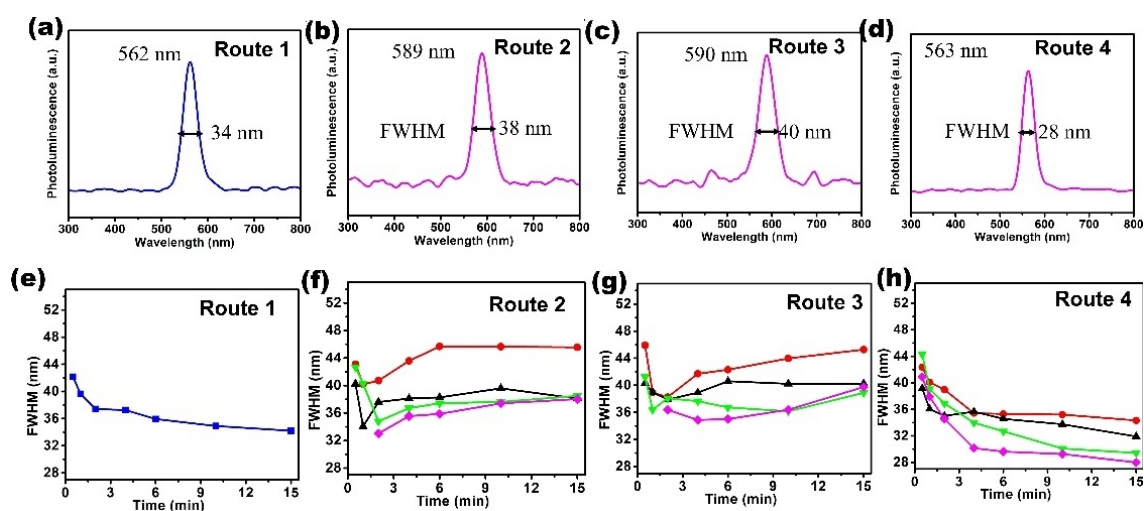


Figure 3.10 PL spectra of CdSe NCs extracted after a reaction time of 15 min. (a) NCs synthesized using route 1 in the absence of amine, (b) using route 2, in which TOP-Se was injected into a mixture of  $\text{Cd}(\text{OAc})_2$  and OLAm, (c) using route 3, in which  $\text{Cd}(\text{OAc})_2$  was injected into a mixture of TOP-Se and OLAm, and (d) using route 4, in which TOP-Se was injected into  $\text{Cd}(\text{OAc})_2$ , followed by the injection of OLAm. The OLAm concentration in routes 2 to 4 is 2.5 mmol. Temporal evolution of FWHM of the PL peaks of CdSe NCs obtained using (e) route 1, (f) route 2, (g) route 3, and (h) route 4. All these reaction routes employed various amounts of OLAm, namely, 0.1 mmol ( $\bullet$ ), 0.5 mmol ( $\blacktriangle$ ), 1.0 mmol ( $\blacktriangledown$ ), and 2.5 mmol ( $\blacklozenge$ ).

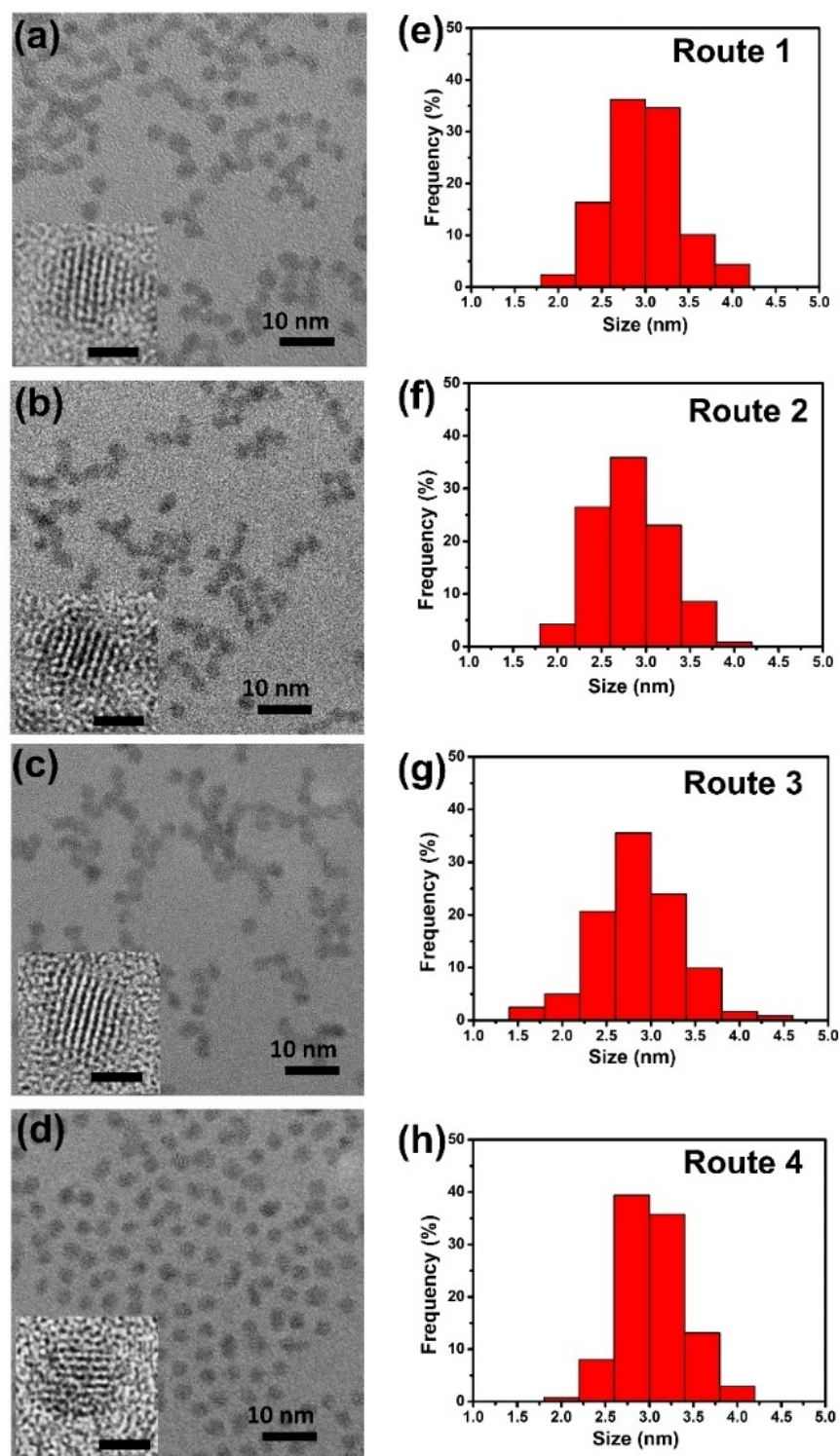


Figure 3.11 TEM graphs (a-d) and size distribution profiles (e-h) of the CdSe NCs. (a, e) CdSe NCs synthesized using route 1, (b, f) CdSe NCs synthesized using route 2, (c, g) CdSe NCs synthesized using route 3, (d, h) CdSe NCs synthesized using route 4. The OLAm concentration in routes 2 to 4 is 0.5 mmol. The insets in (a-d) are the corresponding HRTEM graphs with lattice fringes. Scale bars correspond to 2 nm for the insets.

HRTEM graphs apprise the size, shape, size distribution and crystal structure of CdSe NCs. Figure 3.11 shows TEM graphs (a-d) and size distribution profiles (e-h) of the CdSe NCs obtained from route 1 (a, e), route 2 (b, f), route 3 (c, g), and route 4(d, h). The OLAm amount used in routes 2 to 4 is 0.5

mmol. The insets in (a-d) are the corresponding HRTEM graphs with lattice fringes. CdSe NCs obtained from all the routes possess a well-defined spherical shape. The average size of NCs based on the TEM graphs are 2.98, 2.83, 2.85 and 3.04 nm for route 1-4, respectively, well corresponding to the 3.00, 2.79, 2.89 and 3.00 nm as calculated from the UV-vis absorbance data (Figure 3.5 a,d,g, Figure 3.6a). At higher OLAm concentration like 2.5 mmol, the average NC sizes calculated from TEM are 3.59 nm, 3.62 nm and 3.12 nm for route 2, 3 and 4 respectively (Figure 3.12), which is also in good agreement with those obtained from the absorbance spectra (3.60 nm, 3.57 nm and 3.06 nm respectively, Figure 3.5a,d,g). Very good crystallinity of these NCs is seen from the lattice fringe in HRTEM graphs.

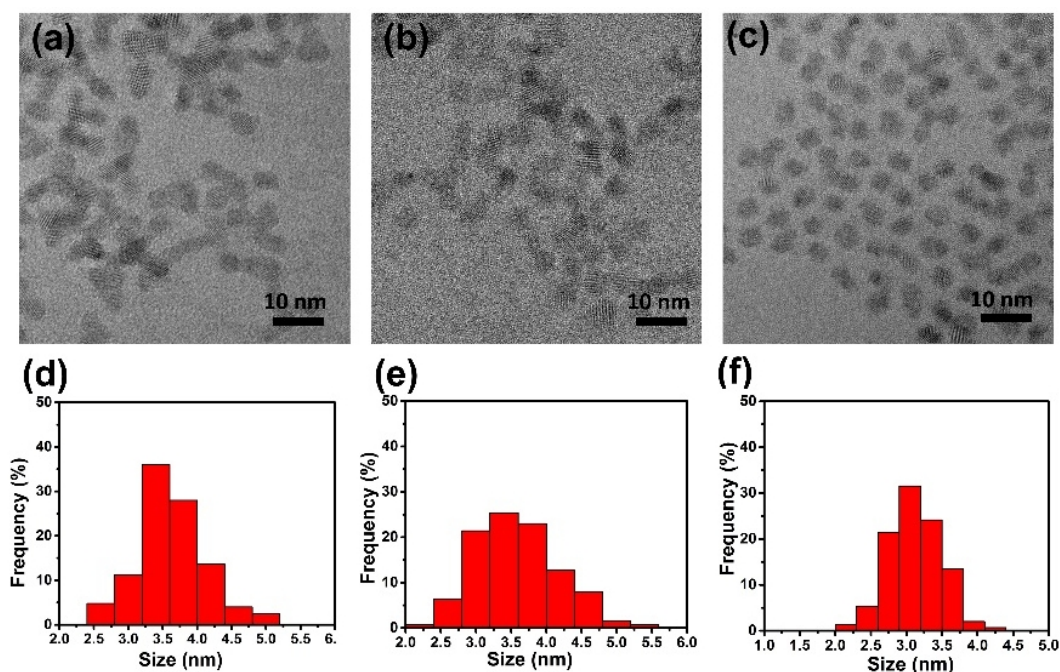


Figure 3.12 TEM graphs (a-c) and size distribution profiles (d-f) of the CdSe NCs. Samples were synthesized using route 2 (a, d), 3 (b, e) and 4 (c, f) in the presence of 2.5 mmol of OLAm after a reaction time of 15 min.

### 3.2.3 Two competitive roles of the primary amine

All of these results suggest following mechanism of OLAm on the nucleation and growth processes of the NCs. In terms of precursor conversion, the addition of OLAm would gradually decrease the formation of CdSe NCs, leading to about 30 % loss of CdSe units the in the presence of 2.5 mmol OLAm (Figure 3.7). However, with respect to the NC concentration and size, the tendency varies oppositely depending on the amount of OLAm. At lower OLAm concentration (below 0.5 mmol), the NC number is increased while the corresponding NC size reduce. It is worth mentioning this phenomenon is different from the surface activation effect of alkylamine as reported by Peng et al [86, 87, 90]. They claimed alkylamine would produce ZnSe NCs with smaller starting size, higher NC concentration and higher growth rate, therefore contrary to the results we obtained here. They further proposed amine was responsible for accelerating the CdSe NCs growth when the amine was used above its boiling temperature (quasi-gas window), while in our case the reaction was performed at 210 °C, far below the boiling temperature of OLAm (364 °C). We believe OLAm here acts as a “nucleating agent”,

which was considered to strongly bind to the NC surface, forming insoluble surface precipitates and kinetically delaying both dissolution and growth of nuclei [91]. Two observations are found to demonstrate the role of amine as nucleating agent. Firstly, enhanced NC concentrations are found when the amine content is relatively low (below 0.5 mmol). Secondly, the dissolution of unstable nuclei, which happens in route 1 (Figure 3.5c,f,i, 3.6c), disappears after the addition of alkylamine, indicating the unstable NC becomes more stable under the protection of amine.

The interaction of amine with precursors reduces the solubility of the monomer in the solution, forming a less stable monomer that is easier to precipitate and nucleate. We focus now on the temporal evolution of NC concentration for route 1, as shown in Fig 3.6c, and route 2 and route 3, as shown in Figure 3.5c,f. Standard route 1, where amine is absent, shows a prolonged nucleation period of 4 min, followed by partly dissolution of NCs. Critical NC radius dynamically grows larger at the cost of redissolution of unstable smaller NCs. In the presence of amine, the rapid increase of NC concentration is directly followed by a saturated plateau and the final NC concentrations are increased (route 2 and 3). Therefore, OLAm addition is proved to be beneficial to the nucleation process by effectively protecting the formed NCs and greatly extending the nucleation period. As a consequence, the final NC size becomes smaller (Figure 3.5a,d), but the size uniformity becomes inferior (Figure 3.10f,g).

We found that application of a higher OLAm concentration in route 2 and route 3 slowed down nucleation, as shown in Figure 3.5c,f. The increase of OLAm content results in a decrease of the collision frequency amongst nuclei, thereby, suggesting OLAm as a passivating agent. We know that the formation of nuclei comprised the binding of TOP-Se to the Cd center and cleavage of the P=Se bond. In the absence of amine, cadmium oleate exists as a tetradentate complex. During the reaction, TOP-Se coordinates to the Cd center and forms an activated metal-phosphine complex at the expense of removing a carboxylate ion. Afterwards, nucleophilic attack by the free carboxylate ion breaks the P=Se bond and forms a CdSe bond (route 1 in Figure 3.2) [78, 92]

When OLAm is used prior to the nucleation, it would coordinate to the Cd center and form a hexadentate complex. Thereafter, this complex is bound to TOP-Se by substituting the amine ligand to form an alkylaminophosphonium intermediate, which is subsequently attacked by the carboxylate and finally reacts to CdSe monomer (route 2 in Figure 3.2) [68]. Compared to the tetradentate precursor, the hexadentate metal-amine complex would create stronger resistance for the binding of the Cd center with TOP-Se and thus deactivate the precursor reaction. Furthermore, excess amines are inclined to dynamically cover the nuclei, producing a steric hindrance, deterring the contact, collision and agglomeration of the free monomers. This looks like an "isolation sphere" with nucleus as the core and OLAm at the surface. Due to the excess of OLAm, nucleation is impeded, subsequently resulting in higher NC growth rate. In route 4, OLAm was injected 32 s after the reaction of Cd and Se precursors, thus ensuring enough time for first nucleation to happen. However, subsequent nucleation slows down due to the addition of OLAm and this effect is more pronounced for the higher OLAm concentrations. Further on in the process, growth rate and NC concentration have less dependence on OLAm concentration, but the growth is slowed down with respect to the classical route 1. This points to the

main role of OLAm as a passivating agent at the nucleation/growth stage. In this way, an increase of the amine concentration would facilitate both the nucleation and growth, therefore contrary to the results we obtained here.

### 3.3 Experimental Section

#### 3.3.1 Synthetic Methods

**Materials.** Commercially available chemicals, cadmium oxide (CdO, 99.5% purity), 1-octadecene (ODE), oleic acid (OA), oleylamine (>98% purity, OLAm), trioctyl phosphine (TOP, 97% purity), selenium powder (Se), hexane, chloroform and ethanol were purchased from Sigma-Aldrich.

**Precursor preparation.** To minimize the influence of air and water, we used the Schlenk line to create an inert environment for the reaction. Before the synthesis of the CdSe NCs, the precursors were prepared in advance. A clear cadmium oleate ( $\text{Cd}(\text{OAc})_2$ ) precursor solution (0.1 M) was obtained by dissolving 3 mmol of CdO in 12 mmol of OA at 200 °C for more than 6 h under the protection of argon atmosphere, followed by diluted in 25.8 mL degassed ODE. For TOP-Se precursor, TOP solution and Se powder in a molar ratio of 1:1 were mixed and stirred at room temperature overnight in a glovebox, and then diluted in ODE to acquire a concentration of 0.5 M. The OLAm should also be degassed and heated to 50 °C to get fully clear solution just before addition.

**CdSe NCs synthesis.** The synthesis of CdSe NCs was performed based on classical hot injection methods with a modification. As discussed in Figure 1 (see article), four routes were designed to study the influence of amine on CdSe NCs. In route 1, 0.5 mL Cd precursor was mixed with 4 mL ODE, degassed for more than 20 min and stirred under 210 °C for more than 10 min. 0.5 mL of Se precursor was then quickly injected and timing started right at the moment. Aliquot volumes of the solution were fetched at different time interval for further analysis. In route 2, a certain amount of OLAm was added with Cd precursor and kept stirring for 10 min at 210 °C before the Se precursor injection. In contrast, in route 3, OLAm was first mixed with Se precursor before the Cd precursor injection. In route 4, cold Se precursor was first injected into hot Cd precursor and 32 s later, OLAm was injected. The first aliquot sample was extracted before the amine injection. In all the amine-containing reaction, the amine contents include 0.1 mmol, 0.5 mmol, 1.0 mmol and 2.5 mmol. Specially, for the amine injection solutions of 0.1 mmol, 0.5 mmol and 1.0 mmol in route 4, a certain amount of ODE was added to keep them same volume as that of 2.5 mmol in case of the influence of different volumes.

#### 3.3.2 Characterization

Typically, 50  $\mu\text{L}$  as-synthesis CdSe NCs in ODE were diluted in 1450  $\mu\text{L}$  hexane for the UV and fluorescence measurement without any purification. UV-visible absorbance spectroscopy was performed on a Varian Cary 100 Scan UV-vis spectrophotometer. Fluorescence spectra were measured by a two-fiber system attached with a USB2000 spectrometer (Ocean Optics). The CdSe NCs were

purified by repeated centrifugation and redispersion in a mixture of chloroform and ethanol (1:2) for 4 times and finally dissolved in hexane. TEM graphs and HRTEM graphs were captured by a Talos transmission electron microscope (FEI company), before which the CdSe NCs in hexane were dropped and dried in ultrathin carbon-supported copper grids.

NC size, growth rate and concentration calculation. The average sizes (D) of the CdSe NCs were calculated based on the absorbance peak ( $\lambda$ ) of the as-prepared products and the empirical fitting function reported by Peng et al [82], given as

$$D = (1.6122 \times 10^{-9}) \times \lambda^4 - (2.6575 \times 10^{-6}) \times \lambda^3 + (1.6242 \times 10^{-3}) \times \lambda^2 - (0.4277) \times \lambda + (41.57)$$

Equation 3.1 Empirical formula of the average sizes of CdSe NCs as a function of the first excitonic peak.

The corresponding growth rates were obtained by the derivative of NC volumes with respect to time, that is

$$R_{Growth} = \frac{dV}{dt} = \frac{\pi}{6} \times \frac{dD^3}{dt}$$

Equation 3.2 The volumetric growth rate calculated based on change of the NC volume.

The concentrations of the resulting CdSe NCs were estimated according to the method proposed by M. G. Bawendi et al [93] through counting the extinction coefficient at the wavelength of 350 nm,

$$[NCs] = \frac{A_{350}}{\epsilon L} = \frac{8 \times A_{350}}{1.438 \times 10^{26} \times D^3}$$

Equation 3.3 Empirical equation to calculate the NC concentration based on the average size and absorption intensity at 350 nm of the sample.

Where  $A_{350}$ ,  $\epsilon$ ,  $L$ ,  $D$  are the absorbance intensity at the wavelength of 350 nm, extinction coefficient per mole of NCs ( $M^{-1}cm^{-1}$ ), path length of the radiation beam (cm) and the corresponding average size of the CdSe NCs (cm), respectively.

To calculate the total CdSe concentration in the form of NC, we can combine the known NC number and size by the following equation,

$$[CdSe] = N \times [NCs]$$

Equation 3.4 Relationship between the total CdSe concentration in the form of NC, the number of the CdSe unit in each NC and the number of CdSe NCs.

in which  $N$  is the number of the CdSe unit in each particle. If we assume all the CdSe NC have a spherical shape and the solution has an extremely monodisperse population, then we can calculate  $N$  as,

$$N = \frac{\pi}{6} D^3 \times \frac{2}{V_{unit}}$$

Equation 3.5 The number of the CdSe unit in each NC as a function of the NC size.

Where  $V_{\text{unit}}$  is the volume of the unit cell containing two CdSe units, which equals to  $0.112 \text{ nm}^3$  in the case of the bulk wurtzite CdSe materials 22. The corresponding rate of CdSe formation (Figure 3.8) and the rate of NC number (Figure 3.9) were obtained by the derivative of the CdSe concentration and NCs concentration respectively.

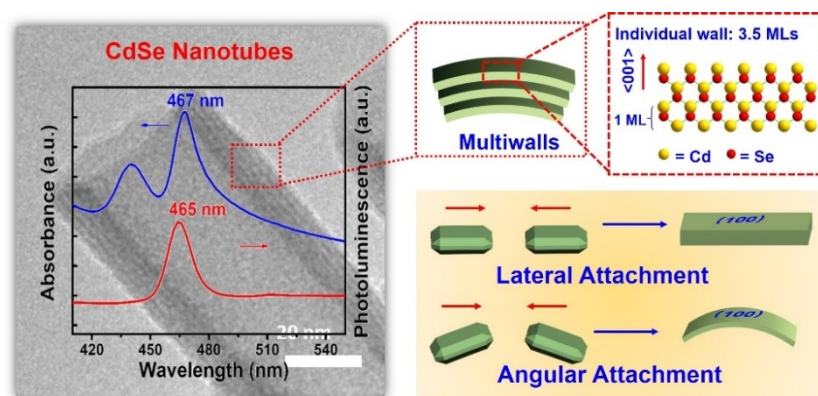
### 3.4 Conclusion

In summary, we have established that OLAm plays a dual role, acting both on nucleation and growth during synthesis of CdSe NCs by the hot injection method. The OLAm concentration in the reaction mixture plays a key role. We found that, at lower contents of OLAm ( $< 0.5 \text{ mmol}$ ), it prominently acts as an agent affecting nucleation, thereby increasing the number of nuclei, increasing the NCs concentration and, thus, decreasing the NCs size to  $2.6 \text{ nm}$ . Whereas at higher concentrations ( $> 1.0 \text{ mmol}$ ), it leads to passivation of nucleation as well as growth processes, so generating fewer NCs with larger size up to  $3.7 \text{ nm}$ . Accordingly, adjusting degree of nucleation and passivation by OLAm concentration, we can better control the final NCs size and so tune their size-dependent optical properties.





# Chapter 4 Spontaneous formation of CdSe photoluminescent nanotubes



In this chapter, we explored the synthesis of CdSe nanotubes with atomically flat walls. Their formation mechanism was elucidated to be lateral and angular attachment of nanoplatelet building blocks, in which both acetate and secondary amine ligand play important roles.

This chapter is adapted from following publication:

X. Huang, V. K. Parashar, M. A.M. Gijs, "Spontaneous Formation of CdSe Photoluminescent Nanotubes with Visible-light Photocatalytic Performance", *ACS Cent. Sci.* 2019, DOI: 10.1021/acscentsci.9b00184

## 4.1 Introduction

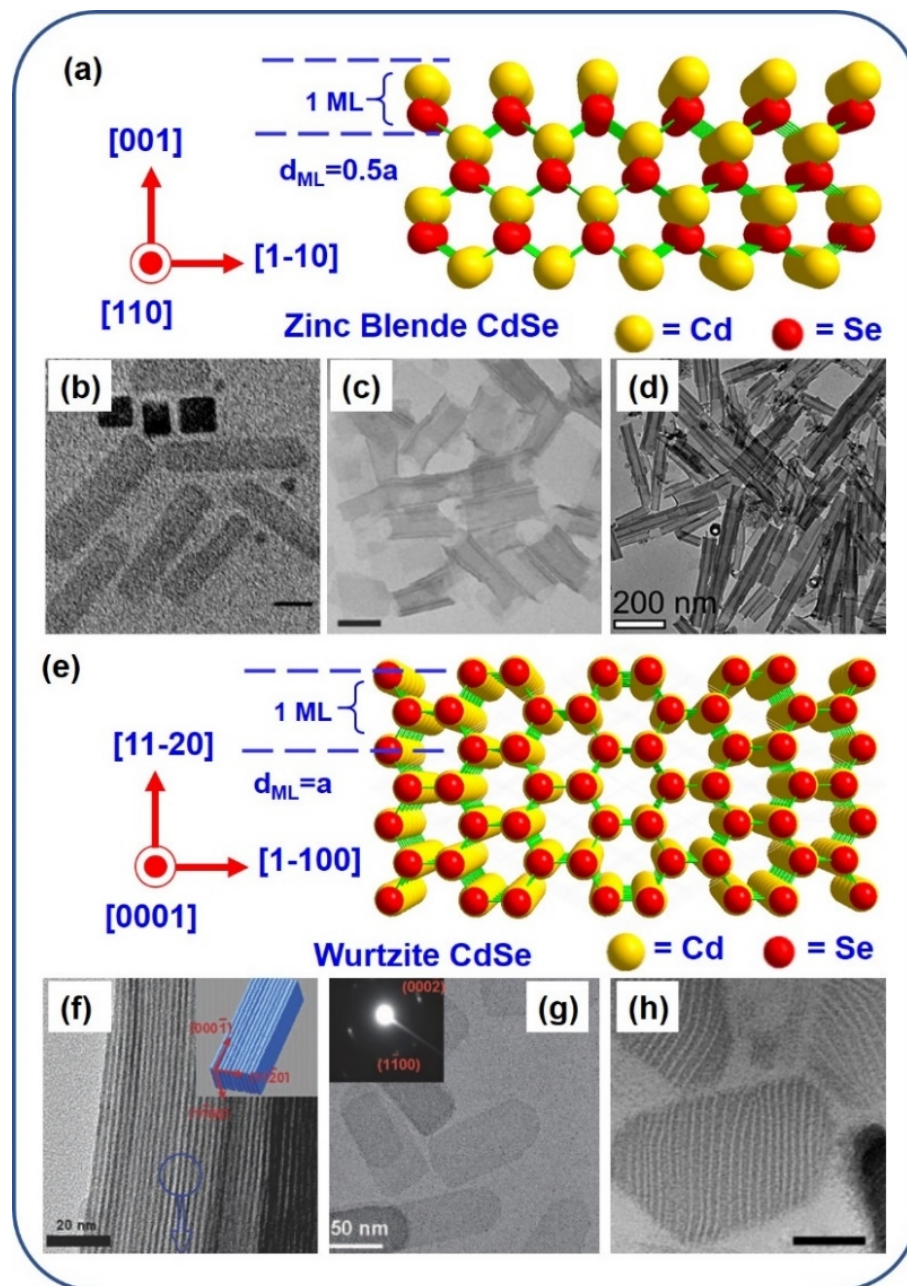


Figure 4.1 An overview of reported 2D colloidal CdSe NCs with atomically scale thickness. (a) Schematic of 2D zincblende CdSe NCs with a 3.5 MLs thickness. This type of nanostructure includes (b) nanoplates (reproduced from [23, 94] with permission), (c) nanodisks (reproduced from [95] with permission) and (d) nanoscrolls (reproduced from [98, 99] with permission). (e) Schematic of 2D wurtzite CdSe NCs with a 3 MLs thickness. This type of nanostructure includes (f) nanoribbons (reproduced from [22] with permission), (g) nanosheets (reproduced from [96] with permission) and (h) nanobelts (reproduced from [97] with permission).

In the past ten years, 2D CdSe NCs with atomically thin thickness have raised growth interests, as demonstrated by the reports including nanoribbons [22], nanoplatelets [23, 94], nanodisks [95], nanosheets [96], nanobelts [97] and nanoscrolls [98, 99] in Figure 4.1. In these nanostructures, only one dimension is smaller than the excitonic Bohr radius, leading to discrete absorption and emission spectra that can be well explained by a one-dimensional infinite potential quantum well model [5, 6, 23]. Despite

the successful synthesis of various 2D CdSe NCs, the underlying formation mechanism remains controversial. B. Dubertret et al. first synthesized zincblende CdSe nanoplatelets in 2008 and proposed a mechanism involving two steps: producing nanoseeds with fixed thickness and subsequent lateral extension via monomer feeding [100]. D. Norris et al further elucidated the anisotropic growth mechanism and showed that enhanced growth on narrow surface facets was energetically favored in island-nucleation-limited reactions [48]. In other work, X. Peng et al. suggested that the lateral extension is by oriented attachment rather than by monomer addition [101]. Unfortunately, although they observed the building blocks, named 2D embryos, evidence on the side-selective attachment of 2D embryos to form nanoplates seem deficient. It is obvious that a much more in-depth understanding of the formation of 2D zincblende CdSe NCs is needed.

A nanotube has been an appealing nanoscale object since the discovery of carbon nanotubes in 1991 and can be envisioned as a seamless roll-up of a 2D nanosheet [102, 103]. However, due to the hollow interior, most of CdSe nanotubes synthesis so far required the usage of sacrificial templates, like ZnO nanorods or Cd(OH)<sub>2</sub> nanowires [104, 105]. Uniform and ultrathin tube walls are difficult to achieve by these approaches. Considering the high symmetry of the zincblende structure, synthesis of CdSe nanotubes with atomically-flat walls is of great technical difficulty.

In this chapter, we disclose a template-free protocol to synthesize colloidal CdSe nanotubes evolved from 2D CdSe nanoplatelets and nanosheet by using acetate and dioctylamine ligands. An individual tube is identified to have 3 to 6 walls, each of which consists of 3.5 molecular monolayers (MLs) in thickness. The nanotubes have zincblende structure, with both top and bottom surfaces of each wall terminated by Cd {100} planes. We studied their properties and elucidated their formation mechanism by SEM, TEM, HRTEM, HAADF-STEM, SAED, XRD, UV-vis and PL spectroscopies.

## 4.2 Results and Discussion

### 4.2.1 Morphology and Crystal Structure of CdSe Nanotubes

A typical synthetic protocol of 2D CdSe nanotubes starts with preparing clear Cd precursor solutions by dissolving cadmium acetate dihydrate (Cd(Ac)<sub>2</sub>·2H<sub>2</sub>O) powder in DOAm at 200 °C, which we label as “Cd(Ac)<sub>2</sub>-DOAm Solution”. The latter was rapidly injected into a hot 1-octadecene (ODE) solution containing Se powder at 260 °C (Figure 4.2). White microparticles immediately precipitated and gradually turned into yellow and brown products during the reaction. A reaction time of 8 min gave well-defined bundles of CdSe nanotubes with hollow interior, as shown in the SEM graph of Figure 4.3a. Since no long-chain strong ligands, such as oleic acid or trioctyl phosphine oxide, were used in the process, which are known to result in stable individual QDs or nanoplatelets [106], nanotubes formed aggregates of several hundred of nanometers. Energy-dispersive X-ray spectra (EDX) mapping shows the presence of both Cd and Se elements over the whole nanostructure (Figure 4.3b,c). Our semi-quantitative analysis demonstrates the excess of Cd over Se with a ratio of 1.5:1 between Cd and Se atoms (Figure 4.4). The tubular architecture is also evident from (1) the sharp contrast between the

center and edge of the tube as visualized using STEM (Figure 4.2e), (2) an intact ring-shape opening of the tube visible in TEM (Figure 4.2f), and (3) an enlargement of the tube opening after tilting the TEM sample rod at an angle of 25 degrees (Figure 4.2g, h). Based on these microscopic observations, the diameter and length of a tube are estimated to be in the range of 25~50 nm and 60~200 nm, respectively.

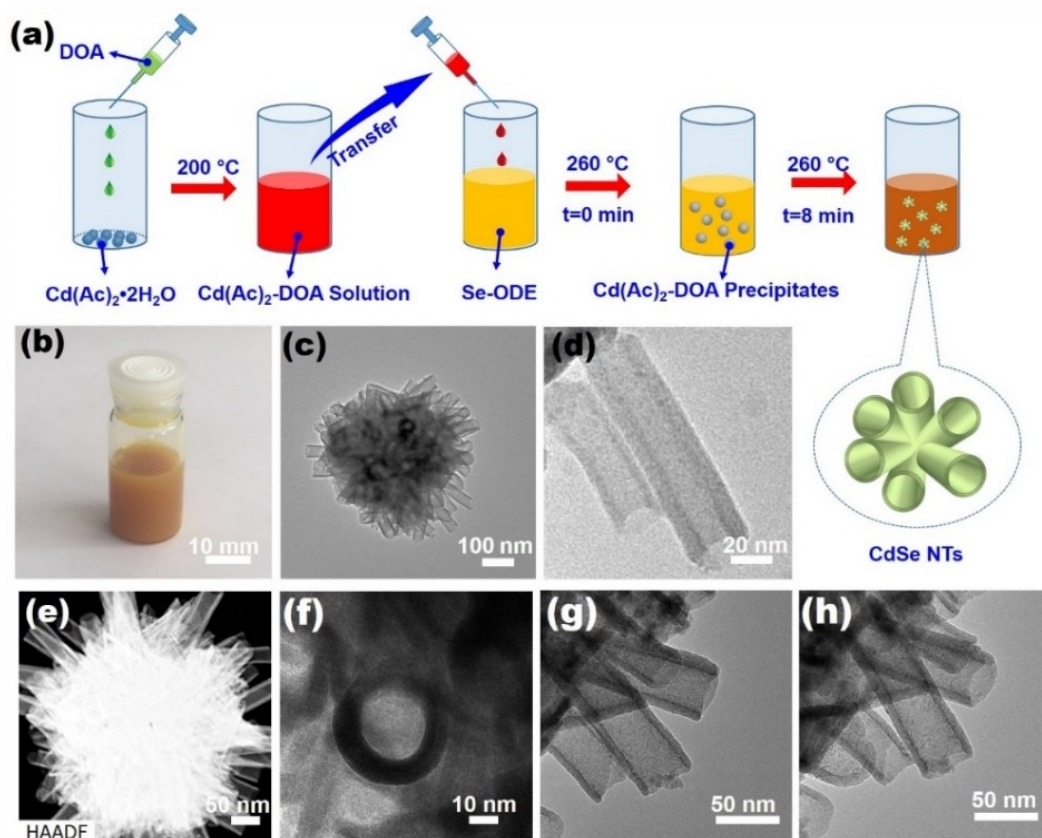


Figure 4.2 Synthesis and morphological characterization of the tubular CdSe structures. (a) Schematic drawing showing the procedures to synthesize the CdSe nanotubes. Optical image (b), TEM graphs (c, d), STEM graph (e) of CdSe nanotubes synthesized within 8 min at 260 °C. (f) TEM graphs of CdSe nanotubes showing an intact tube opening (f), as well as nanotubes viewed after tilting the TEM sample rod for 25 degrees (g, h).



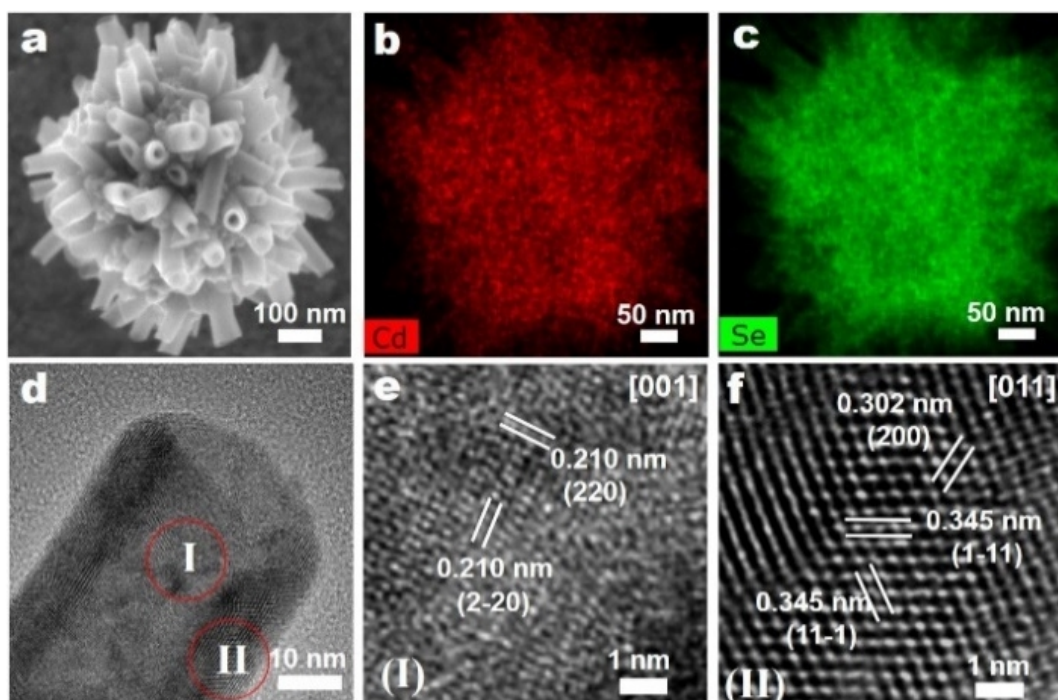


Figure 4.3 Structural and elemental characterization of CdSe nanotubes by SEM, EDX and HRTEM. (a) SEM graph of a bundle of CdSe nanotubes, with elemental mapping of (b) Cd and (c) Se. (d) HRTEM graph of a CdSe nanotube, with (e,f) close-ups of the center (e, part I in d), showing 0.210 nm lattice spacing corresponding to the {220} planes of the CdSe zincblende structure, and the edge (f, part II in d), showing 0.302 nm and 0.345 nm lattice spacings corresponding to the {200} and {111} planes, respectively, indicating that the growth direction along the thickness of the nanotube is  $\langle 100 \rangle$ .

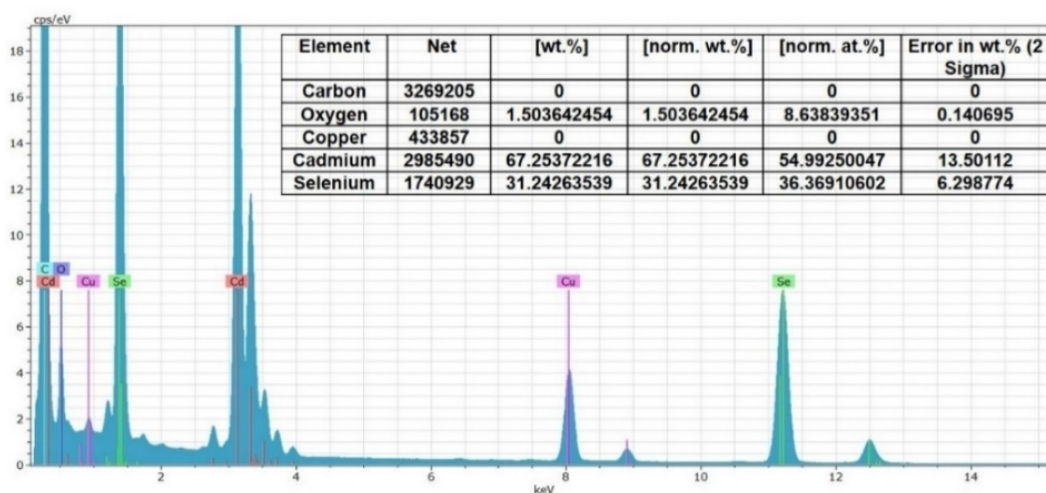


Figure 4.4 EDX spectra and semi-quantitative analysis of the elements in the CdSe nanotubes. EDX analysis of the CdSe nanotubes synthesized during 8 min, which shows the presence of Cd, Se, O, C and Cu. The table on the top right shows the semi-quantitative analysis among Cd, Se and O elements.

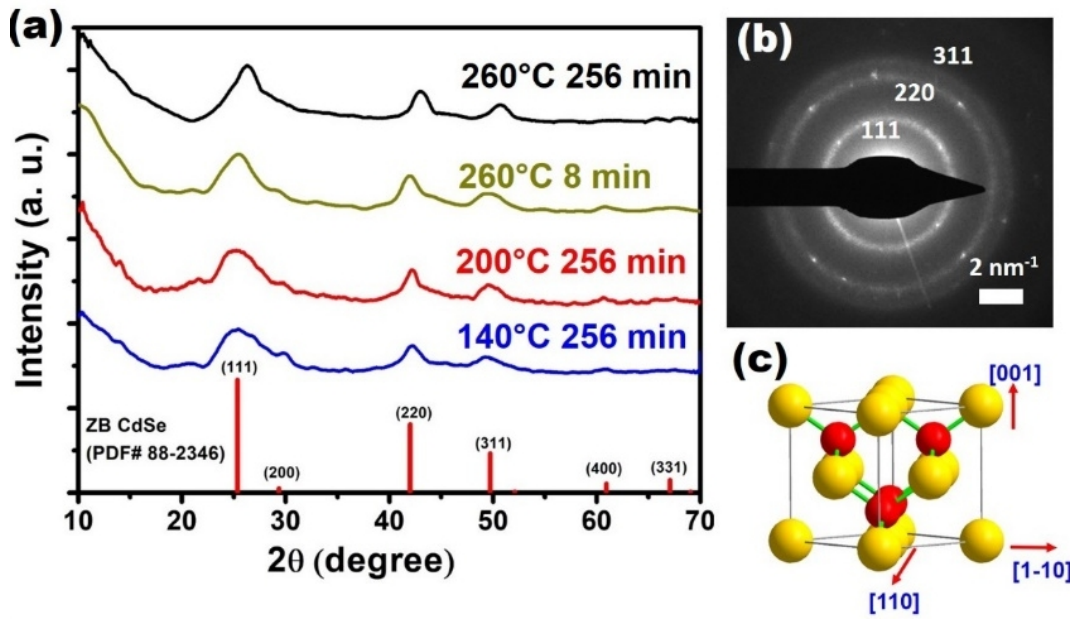


Figure 4.5 Crystallographic structure characterization of the 2D CdSe NCs. (a) XRD pattern of the 2D CdSe NCs synthesized at different conditions, including at 140 °C for 256 min (blue), at 200 °C for 256 min (red), at 260 °C for 8 min (yellow-green) and at 260 °C for 256 min (black), from the bottom to top. Vertical lines on the bottom represent the standard XRD pattern of bulk zincblende CdSe (PDF no. 88-2346). (b) SAED pattern of the 2D CdSe nanotubes synthesized within 8 min at 260 °C. (c) A schematic illustration of a unit cell of the zincblende CdSe crystal.

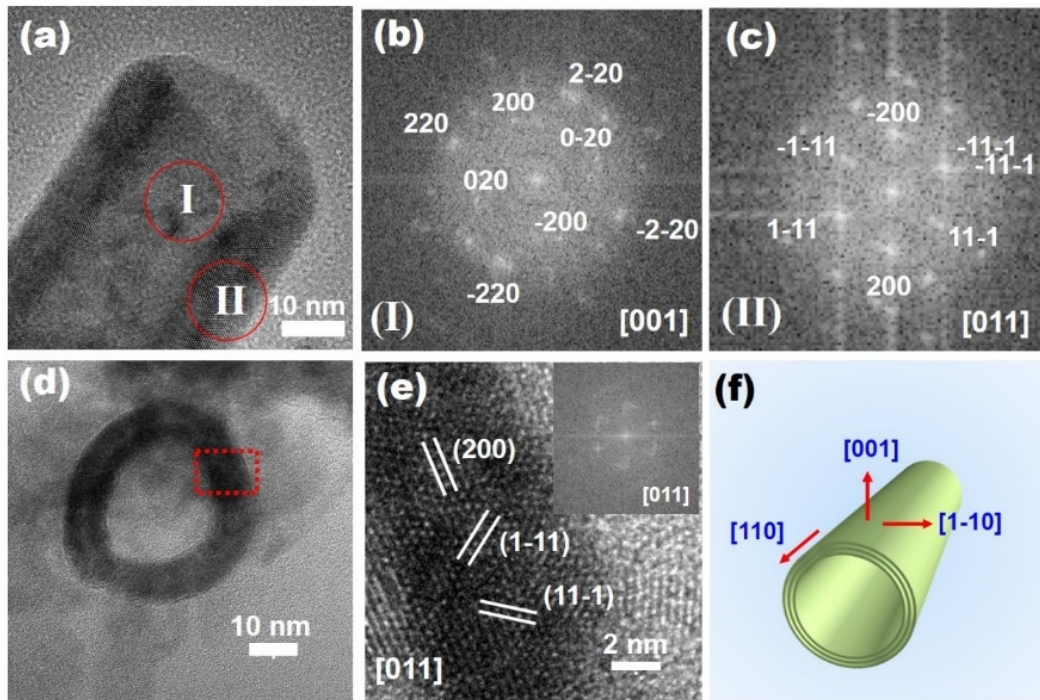


Figure 4.6 HRTEM characterization of the growth orientations in CdSe nanotubes. (a) HRTEM graph of a CdSe nanotube, with fast Fourier transform (FFT) pattern of (b) the center (location of area I in a), showing 4-fold rotational symmetry of a face-centered cubic (fcc) structure, as observed along the [001] zone axis, and of (c) the edge (location of area II in a), showing the characteristic pattern of a fcc structure, as observed along the [011] zone axis. (d) HRTEM graph of a CdSe nanotube, as observed normal to the tube opening, showing lattice spacings corresponding to the {200} and {111} planes of fcc CdSe. (e) Zoom on the rectangle in (d), the FFT pattern of the inset indicates that the observation zone axis is [011]. (f) Schematic illustration showing that the lateral, angular and thickness growth directions in the CdSe nanotube are [110], [1-10] and [001], respectively.

In classical synthetic protocols, 2D CdSe NCs with zincblende structure were obtained using both short- and long-chain Cd(carboxylate)<sub>2</sub> as precursors, while amine-containing solvent was mainly employed for those with wurtzite structure [5, 97]. Despite the addition of DOAm in our protocol, the crystal structure of our nanotubes was proven to be zincblende, as characterized by XRD and SAED (Figure 4.5). We then determined the crystallographic orientation on the tube using HRTEM. In the center of the nanotube (region I in Figure 1d), characteristic fringe spacings of 0.210 nm indicate the presence of two orthogonal {220} planes viewed along the <001> direction (Figure 4.3e), consistent with a fast Fourier transform (FFT) pattern presenting 4-fold rotational symmetry (Figure 4.6b). This suggests that both the lateral and angular growth directions on the surface of the nanotube are parallel to the <110> direction, while the thickness direction is parallel to the <001> direction. We further confirmed this by the observations on the edge of a nanotube (region II in Figure 4.3d), which presented characteristic fringe spacings of 0.345 nm, 0.345 nm and 0.302 nm, corresponding to two {111} planes and one {200} plane in zincblende CdSe, respectively (Figure 4.3f); the corresponding zone axis is in the <110> direction (Figure 4.6c). Similar results can be found when observing along the opening of a nanotube (Figure 4.6d,e).

#### 4.2.2 Multiwalled character of the CdSe nanotubes

For CdSe nanotubes synthesized within 8 min, the measured wall thickness is 6~12 nm. The nanotube of Figure 4.7a has a wall thickness of 10 nm, as determined by TEM, with some discernable stripes suggesting it might consist of sub-structures. The nanotubes optical spectra indicate an ensemble of 2D CdSe NCs with uniform thickness of 3.5 MLs [99] (Figure 4.7d). Two sharp peaks at 467 nm and 440 nm in the UV-vis absorption spectra are attributed to heavy-hole and light-hole transition in 2D CdSe NCs [5, 6, 23]. The sharp PL peak at 465 nm with a full width at half-maximum (FWHM) of 13 nm further validates the 1D quantum confinement of the nanotubes. The anti-stokes redshift of 2 nm in the absorption spectra could arise from strong inter-wall coupling inside the nanostructures [96] and scattering within the sample. The latter is deduced by comparison with the PL-excitation spectra, showing no scattering signal and no anti-stokes shift (Figure 4.8). We thus hypothesize that these nanotubes are comprised of 3 to 6 walls, each having a thickness of 3.5 MLs (Figure 4.7j). Moreover, both top and bottom surfaces of a wall are terminated with Cd atoms capped with acetate ligand along the <001> direction (Figure 4.7l), a configuration that results from the balance of van der Waals (VdW) attraction [107] and dipole-dipole repulsion [57] between adjacent walls.



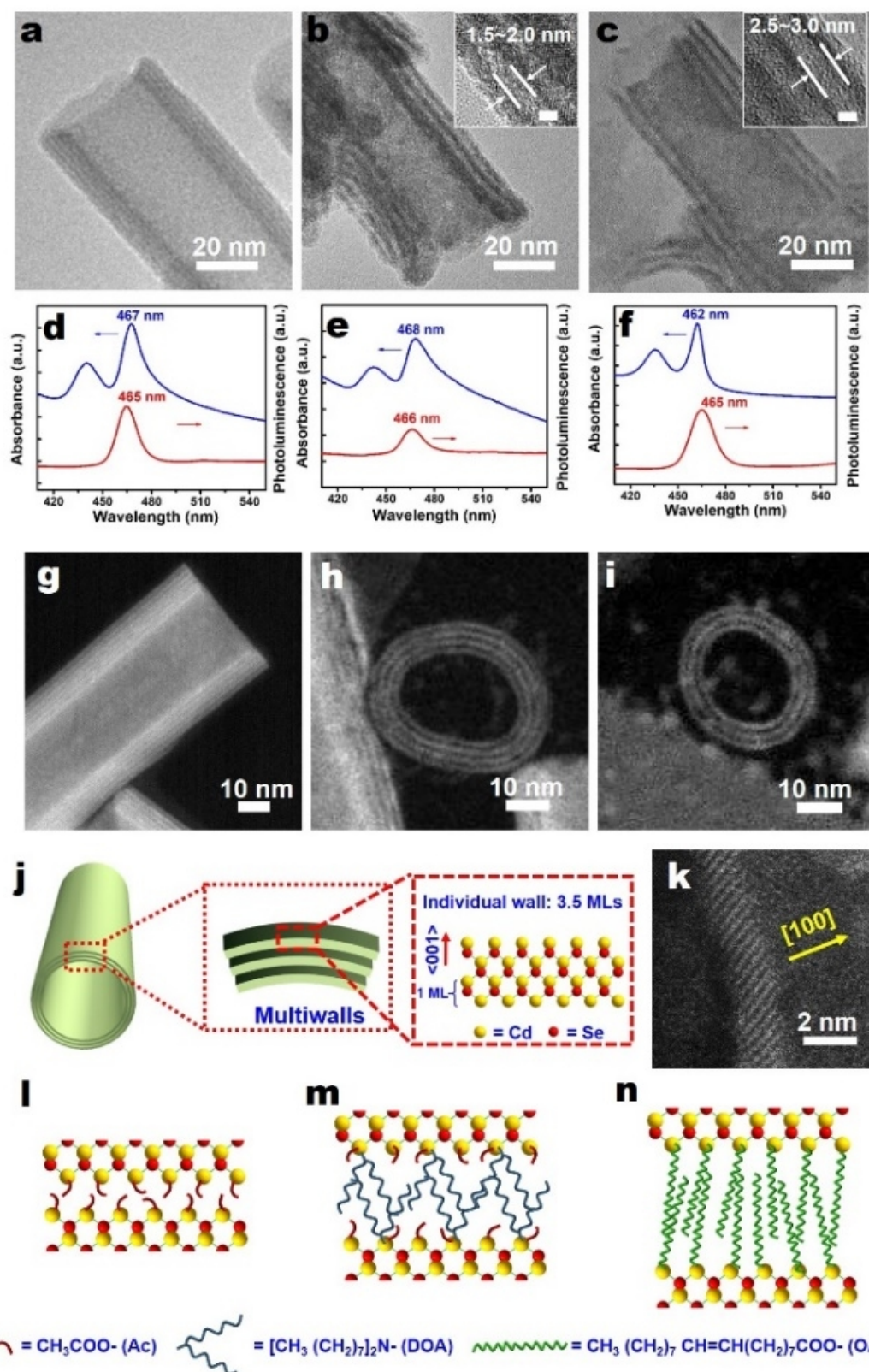


Figure 4.7 Multi-walled character of the CdSe nanotubes, as observed by TEM, STEM, PL, and UV-vis absorption spectroscopy. (a-c) TEM micrographs of CdSe nanotubes, synthesized from Cd acetate-dioctylamine (Cd(Ac)<sub>2</sub>-DOAm) and Se-octadecene (Se-ODE) precursor solutions at 260 °C during a reaction time of (a) 8 min, (b) 256 min, and (c) 8 min, with additional exchange of Ac ligands by oleic acid (OAc) at 200 °C in c. (d-f) UV-vis absorbance and PL spectra of a solution in hexane of CdSe nanotubes corresponding to the structures of a-c, respectively. The major absorbance and PL peaks are indicative for a quasi-2D CdSe nanostructure with an individual wall thickness of 3.5



MLs. (g-i) HAADF-STEM graphs of a CdSe nanotube synthesized within 8 min at 260 °C when observed along the tube-side direction (g) and tube-opening direction (h, i). (j) Schematic illustration of a multi-walled CdSe nanotube. (k) HAADF-STEM graph of an individual wall consisting of 3.5 MLs with  $\langle 100 \rangle$  normal direction. (l-n) Schematic illustrations of the CdSe nanotubes corresponding to the structures of a-c, showing how the use of different ligands leads to different spacings between individual walls.

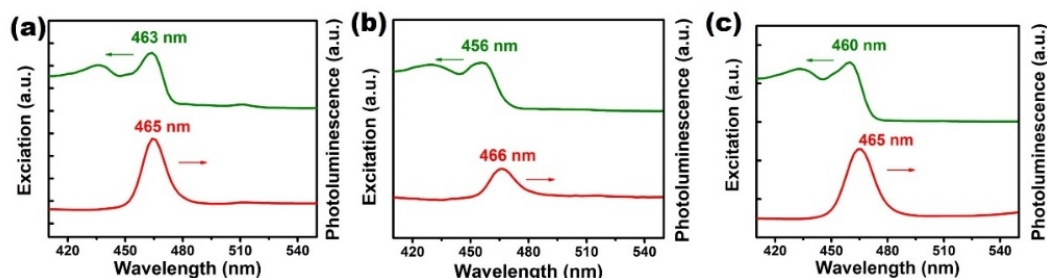


Figure 4.8 PLE and PL spectra of a CdSe nanotubes in hexane solution. The samples were synthesized from Cd acetate-dioctylamine ( $\text{Cd}(\text{Ac})_2$ -DOAm) and Se-octadecene (Se-ODE) precursor solutions at 260 °C during a reaction time of (a) 8 min, (b) 256 min, and (c) 8 min, with additional exchange of acetate ligands by oleic acid (OA) at 200 °C for 10 min.

We obtained evidence to support this hypothesis by directly observing the nanotubes with high-magnification STEM, which display multiple linear features with good contrast (Figure 4.7g). When observed along the opening of a nanotube, closure of nanotubes on an individual-wall scale can be observed, from which we deduce an inter-wall spacing of less than 1 nm (Figure 4.7h, i). By comparing the STEM and TEM graphs of the same nanotubes, we find the nanotubes synthesized within 8 min are highly sensitive to the electron beam used under high-magnification TEM (Figure 4.9), which eventually would lead to blurred images. We thus performed Fourier transform infrared spectroscopy (FTIR) to discern the capping ligand existing on the nanotubes. As shown in Figure 4.10, the peaks at  $1538\text{ cm}^{-1}$  and  $1408\text{ cm}^{-1}$ , corresponding to the asymmetric and symmetric stretching vibrations of  $\text{COO}^-$  on acetate, are much stronger than the peaks at  $2922\text{ cm}^{-1}$  and  $2852\text{ cm}^{-1}$  that represent the stretching vibrations of C-H on DOAm. This confirms that acetate rather than DOAm plays the leading role in capping the CdSe nanotubes synthesized within 8 min.

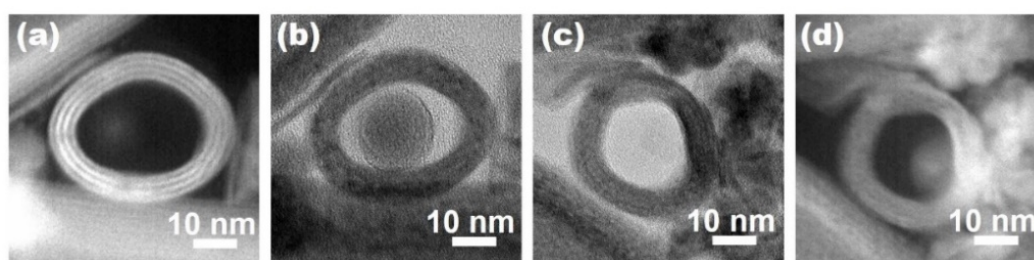


Figure 4.9 High-magnification (a, d) STEM and (b, c) TEM images of CdSe nanotubes observed along the tube-opening direction. (a, d) High-magnification STEM and (b, c) TEM images of nanotubes synthesized within 8 min observed along the tube opening direction. If we first imaged the nanotube under STEM mode, clear features on an individual-wall scale can be observed (a), which became blurred once we turned to TEM mode (b). Instead, if the TEM graphs were taken first (c), we found it was later more difficult to visualize clearly individual walls in the STEM mode too (d).

Assuming the walls are attracted to each other by VdW interaction, we envisaged that individual walls could be differentiated by substituting acetate with a longer-chain ligand. This idea was first verified by extending the synthesis time to 256 min. These samples, even though having quite similar absorption and emission spectra as those synthesized within 8 min (Figure 4.7e), present an obvious

multi-walled structure under TEM (Figure 4.7b). Apparently, even though DOAm is a weaker ligand compared to carboxylate [106], it is capable to intercalate the walls in presence of acetate ligand, when exposing over a long time in a non-polar environment. The FTIR spectrum confirms the dominant role of DOAm by a huge increase of the characteristic peaks of DOAm (Figure 4.10). According to the Tanford formula [108], the maximum extensional length of an 8-carbon chain is 1.17 nm. The measured spacing between walls is 1.5~2.0 nm, indicating a small interpenetration between two face-to-face alkylamines (Figure 4.7m). The XRD measurement of the sample prepared at 260 °C for 256 min (Figure 4.5) displays a high-angle shift of the whole pattern over about 1 degree, which can be due to surface-related effects that affect the overall sample structure and effective lattice constant [109].

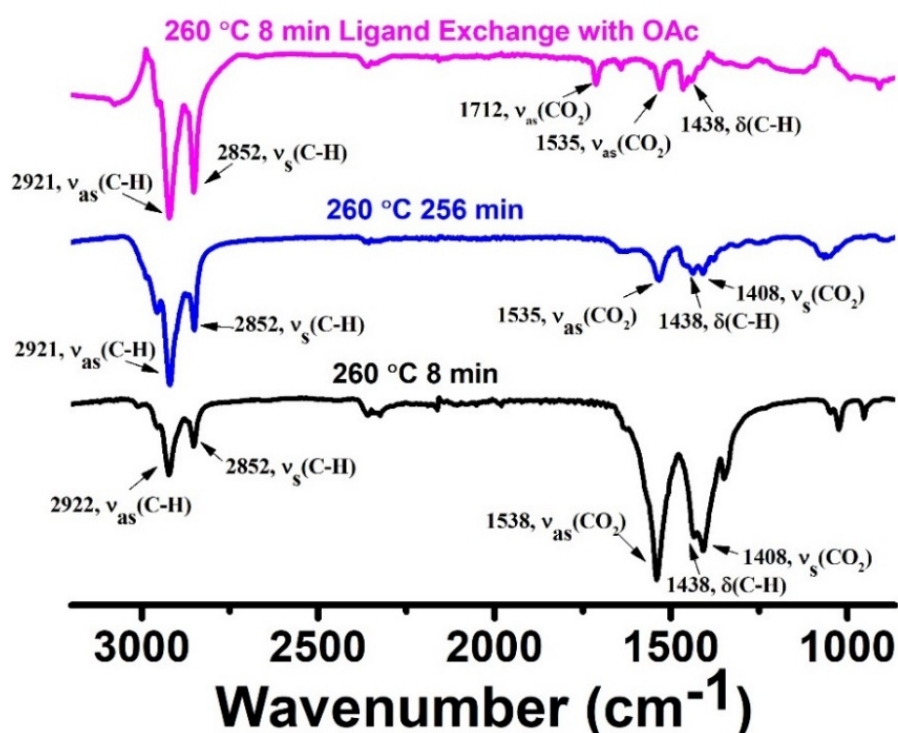


Figure 4.10 FTIR spectra of CdSe NCs synthesized at different conditions. FTIR spectra of CdSe NCs synthesized at 260 °C for 8 min (black), for 256 min (blue) and for 8 min followed by a further ligand exchange with OAc (pink). For samples synthesized at 260 °C for 8 min, the dominant peaks at 1538 and 1408  $\text{cm}^{-1}$  are assigned to the antisymmetric and symmetric stretching vibration mode of  $\text{COO}^-$  in the acetate group, respectively. For samples synthesized at 260 °C for 256 min, the major peaks are at 2921 and 2852  $\text{cm}^{-1}$ , corresponding to the antisymmetric and symmetric stretching vibration mode of C-H, indicative of presence of a large quantity of DOAm. For samples synthesized at 260 °C for 8 min with a further ligand exchange with OAc, a characteristic peak at 1712  $\text{cm}^{-1}$  related to the antisymmetric stretching vibration mode of  $\text{COO}^-$  in oleate is present.

Finally, we performed ligand exchange of the CdSe nanotubes synthesized within 8 min with oleic acid at 200 °C for 10 min (Figure 4.7c). Remarkably, most of nanotube aggregates are disintegrated and exfoliated into sheet-like nanostructures with more uniform and separate walls (Figure 4.11). The first excitonic peak shifts to 462 nm (Figure 4.7f), close to that of flat nanoplatelets. Some partly broken nanotubes of Figure 4.7c maintain the stacking arrangement of multiple walls, exhibiting a spacing of 2.5~3.0 nm between walls (Figure 4.7c,n), which is less than the maximum extensional length of 4.86 nm between two face-to-face oleic acids, as calculated according to Tan-ford formula. These two cases

convincingly demonstrate the multiwalled character of nanotubes. Based on the HAADF-STEM analysis (Figure 4.11c,d, Figure 4.7k), the thickness of the NCs was determined to be around 1.5 nm. In literature, an individual wall is considered to be composed of 3.5 MLs, i.e. 4 Cd layers and 3 Se layers alternating along the  $\langle 001 \rangle$  normal direction [99, 109].

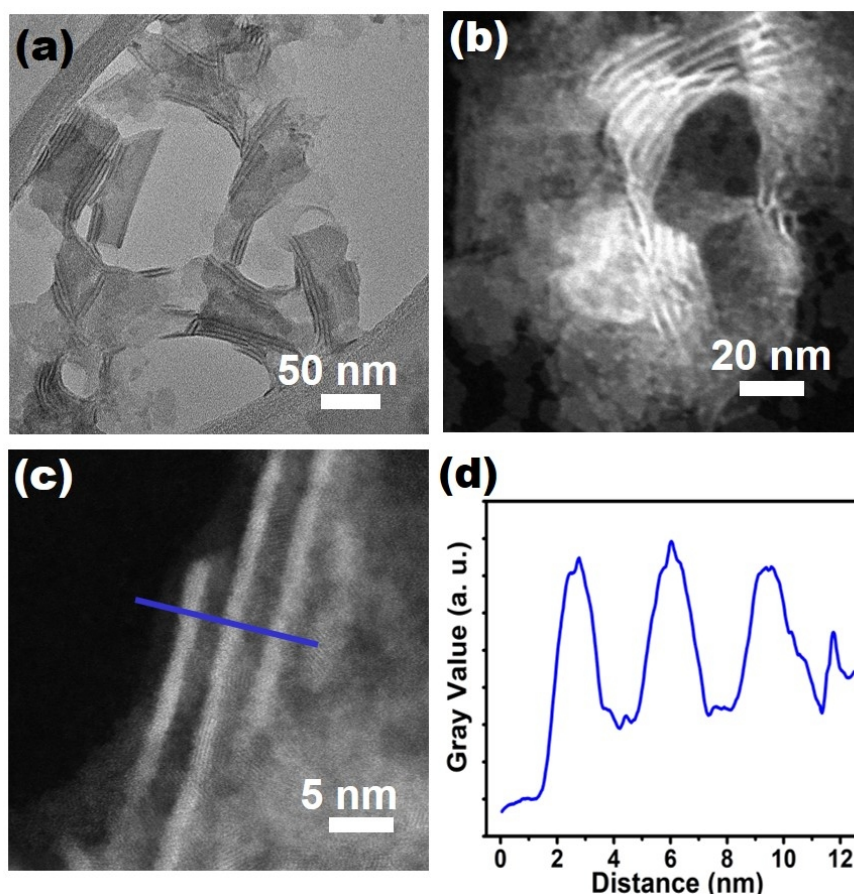


Figure 4.11 TEM and STEM graphs of the CdSe nanotubes after ligand exchange with oleic acid. (a, b) an overview and (c) a close-up of the CdSe nanotubes synthesized at 260 °C for 8 min followed by a further ligand exchange with OAc. (d) Profile analysis of the thickness based on the gray contrast in (c).

#### 4.2.3 Role of the amine and acetate ligands in CdSe nanotube synthesis

To understand the formation of the CdSe nanotubes, the role of DOAm was first investigated. We noticed the occurrence of white precipitates, once the clear  $\text{Cd}(\text{Ac})_2$ -DOAm solution was injected into the hot Se-ODE solution. In a control experiment, we replaced the Se-ODE solution with a Se-DOAm solution and, doing so, no precipitates appeared immediately after injecting Cd precursor, but a dark solution was obtained for a reaction time of 8 min. The TEM graph of Figure 4.12b shows the assembly of CdSe nanodots into mesocrystals [110] instead of CdSe nanotubes. Moreover, no peak is found in the UV-vis absorption spectra, suggesting no quantum-confinement behavior for these nanoscale assemblies (Figure 4.12g). Hence, ODE seems important and our experiments suggest that the precipitates play a role in formation of the nanotube. For further characterization, we therefore separated the precipitates in a pure hot ODE solution; which we label as  $\text{Cd}(\text{Ac})_2$ -DOAm precipitates.



Unexpectedly, FTIR spectra demonstrated that the latter had a strong signal originating from COO-bonds and a negligible signal due to C-H bonds, similar to the spectra of  $\text{Cd}(\text{Ac})_2 \cdot 2\text{H}_2\text{O}$  powder, but quite different from those of the precursor  $\text{Cd}(\text{Ac})_2$ -DOAm solution (Figure 4.13). Moreover, analysis based on TEM (Figure 4.14a,b), SAED (Figure 4.14c), HRTEM (Figure 4.14d-f) and XRD (Figure 4.15a) demonstrated their morphology is also essentially identical to  $\text{Cd}(\text{Ac})_2 \cdot 2\text{H}_2\text{O}$  powder, showing cadmium oxide (CdO) NCs less than 10 nm in diameter and uniformly dispersed in an amorphous matrix. The spectra therefore suggest that the  $\text{Cd}(\text{Ac})_2$ -DOAm precipitates are due to the precipitation of  $\text{Cd}(\text{Ac})_2$  in ODE solvent (hydrate water is removed because of the elevated temperature). This triggered the question if 2D CdSe NCs could be obtained solely from  $\text{Cd}(\text{Ac})_2 \cdot 2\text{H}_2\text{O}$  and Se powder precursors without use of DOAm.

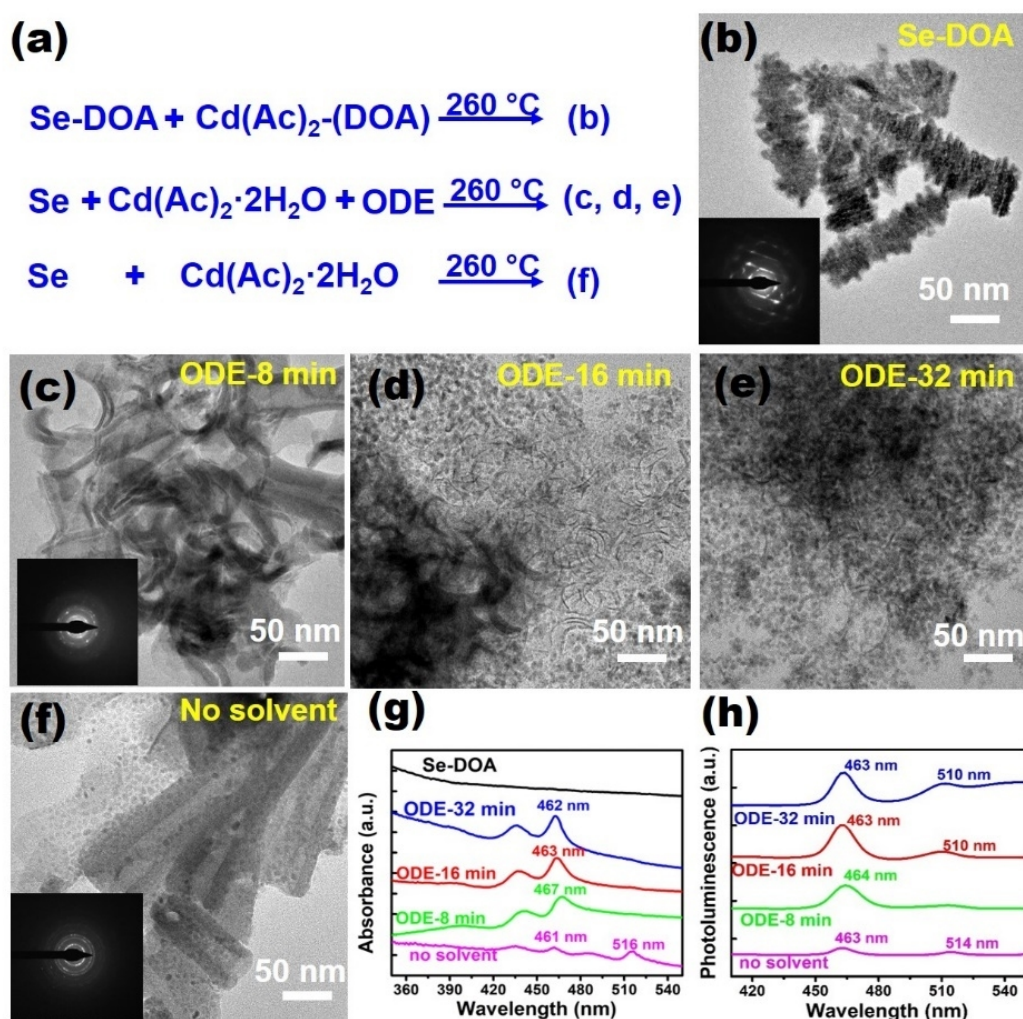


Figure 4.12 Control experiments to study the role of acetate and amine ligand in the synthesis of 2D CdSe NCs. (a) Formulas describing the design of control experiments to investigate the role of acetate and amine in the CdSe nanotube formation. (b) TEM graph of large-size CdSe mesocrystals assembled from QDs, which were synthesized by using  $\text{Cd}(\text{Ac})_2$ -DOAm and Se-DOAm as precursors at 260 °C for 256 min. The SAED pattern in the inset of (b) indicates the characteristic mesocrystal structure, as observed along [011] zone axis. (c-e) TEM graphs of CdSe NCs synthesized by reacting the mixture of Se and  $\text{Cd}(\text{Ac})_2 \cdot 2\text{H}_2\text{O}$  in ODE solvent at 260 °C for 8 min (c), 16 min (d) and 32 min (e). The SAED pattern in the inset of (c) indicates the characteristic CdSe NCs pattern of a tube-like structure. (f) TEM graph of CdSe NCs synthesized by reacting the mixture of Se and  $\text{Cd}(\text{Ac})_2 \cdot 2\text{H}_2\text{O}$  without solvent at 260 °C for 8 min. The SAED pattern in the inset shows the characteristic CdSe NCs pattern rather than the Cd precursor pattern. (g) UV-vis absorbance and (h) PL spectra of the samples as shown in (b-f), which were

labelled as Se-DOAm (black curve, sample in b), ODE-32 min (blue curve, sample in c), ODE-16 min (red curve, sample in d), ODE-8 min (green curve, sample in e) and no solvent (blue curve, sample in f), respectively.

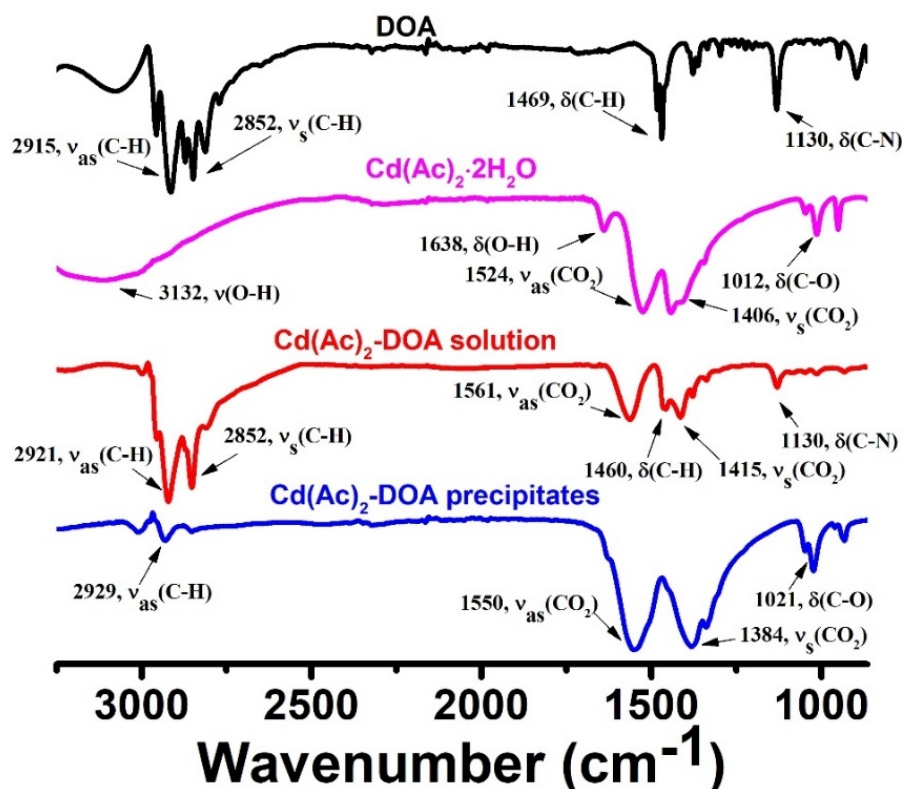


Figure 4.13 FTIR spectra of DOAm,  $\text{Cd}(\text{Ac})_2 \cdot 2\text{H}_2\text{O}$ ,  $\text{Cd}(\text{Ac})_2$ -DOAm solution and  $\text{Cd}(\text{Ac})_2$ -DOAm precipitates. FTIR spectra of DOAm with characteristic peaks at 2915, 2852, 1469, and 1130  $\text{cm}^{-1}$  (black), of  $\text{Cd}(\text{Ac})_2 \cdot 2\text{H}_2\text{O}$  (pink), of  $\text{Cd}(\text{Ac})_2$ -DOAm solution (red) and of  $\text{Cd}(\text{Ac})_2$ -DOAm precipitates (blue). For DOAm, characteristic peaks at 2915, 2852, 1469  $\text{cm}^{-1}$  are assigned to the vibration of C-H, and the peak at 1130  $\text{cm}^{-1}$  relate to the bending vibration of the C-N bond. For  $\text{Cd}(\text{Ac})_2 \cdot 2\text{H}_2\text{O}$ , the major peaks are at 1524 and 1406  $\text{cm}^{-1}$ , corresponding to the antisymmetric and symmetric stretching vibration mode of  $\text{COO}^-$  in the acetate group. The difference in wavenumber between the two peaks is 118  $\text{cm}^{-1}$ , indicating the role of acetate in coordinating to the Cd center is a chelating and bridging interaction<sup>23</sup>. For the  $\text{Cd}(\text{Ac})_2$ -DOAm solution, the spectra shows both features of the acetate group and DOAm, especially with the clear peak at 1130  $\text{cm}^{-1}$  corresponding to the bending vibration of C-N bond in DOAm. For  $\text{Cd}(\text{Ac})_2$ -DOAm precipitates, the spectra is almost similar to that of  $\text{Cd}(\text{Ac})_2 \cdot 2\text{H}_2\text{O}$ , with an increase of the difference in wavenumber between the antisymmetric and symmetric stretching vibration of  $\text{COO}^-$  in the acetate group (166  $\text{cm}^{-1}$ ) that can be explained by the loss of the hydrate water.

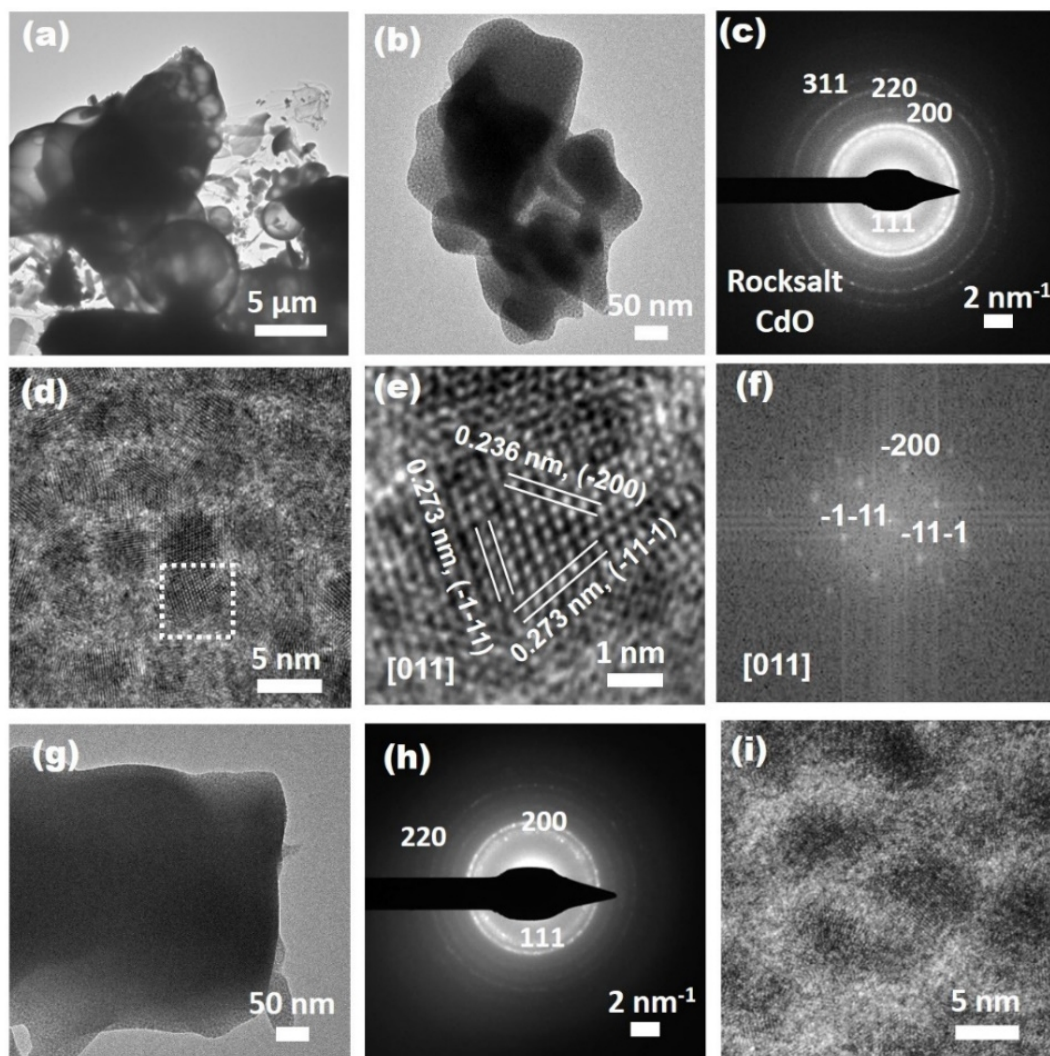


Figure 4.14 Morphological and structural characterization of  $\text{Cd}(\text{Ac})_2 \cdot 2\text{H}_2\text{O}$  powders and  $\text{Cd}(\text{Ac})_2$ -DOAm by TEM. (a,c) TEM graphs, (b) SAED pattern and (d,e) HRTEM graphs of the  $\text{Cd}(\text{Ac})_2 \cdot 2\text{H}_2\text{O}$  powder observed under an accelerating voltage of 200 kV. Rapid observation of the large-size crystals under low magnification shows the phase transition of the  $\text{Cd}(\text{Ac})_2 \cdot 2\text{H}_2\text{O}$  crystals under electron beam radiation (a). An amorphous matrix with distributed CdO NCs of 3–6 nm was found under high-magnification observation (b). The SAED pattern well matches with the low-index planes in rock-salt (fcc) structure (PDF no. 75-0593). The lattice fringes spacing of 0.273 nm and 0.236 nm in the NCs are corresponding to the {111} planes and {200} planes in bulk CdO NCs, which was verified by (f) the FFT analysis showing the characteristic pattern as observed along [011] zone axis. Formation of CdO NCs is attributed to the transformation of amorphous  $\text{Cd}(\text{Ac})_2 \cdot 2\text{H}_2\text{O}$  under electron beam radiation. (g) TEM graph, (h) SAED pattern and (i) HRTEM graph of the  $\text{Cd}(\text{Ac})_2$ -DOAm precipitate. Except the emergence of larger CdO NCs of 5–8 nm, the morphology and crystal structure of a  $\text{Cd}(\text{Ac})_2$ -DOAm precipitate are almost the same as that of  $\text{Cd}(\text{Ac})_2 \cdot 2\text{H}_2\text{O}$  powder.



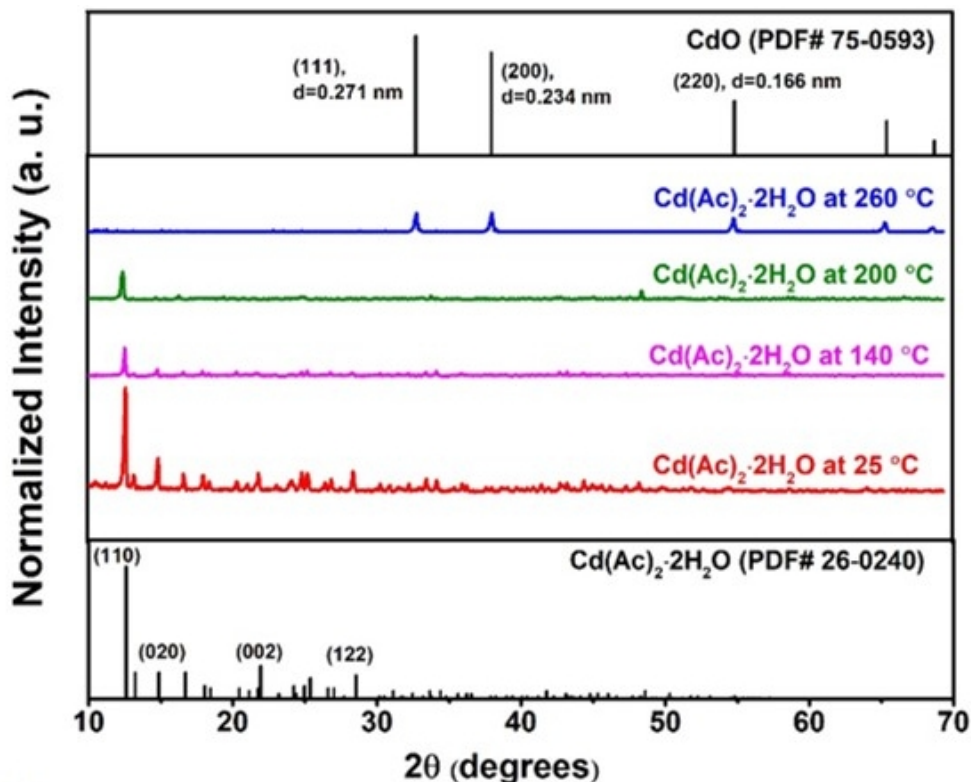


Figure 4.15 Structural characterization of Cd(Ac)<sub>2</sub>·2H<sub>2</sub>O powders treated at different temperatures. XRD pattern of Cd(Ac)<sub>2</sub>·2H<sub>2</sub>O powders treated at different temperatures, including 25 °C (red, no treatment), 140 °C (pink), 200 °C (green) and 260 °C (blue). The treatment was conducted by heating Cd(Ac)<sub>2</sub>·2H<sub>2</sub>O powders at the given temperature for 30 min, followed by cooling in air. A strong and clear signal of Cd(Ac)<sub>2</sub>·2H<sub>2</sub>O crystals was found without treatment (25 °C), while the intensity sharply decreased at 140 °C (pink) and 200 °C (green), indicating more and more crystals turned into an amorphous structure after heating. When the sample was treated at 260 °C, only the characteristic signal of CdO crystals was observed, demonstrating the transformation of Cd(Ac)<sub>2</sub>·2H<sub>2</sub>O into CdO crystals. Vertical lines on the top and bottom represent the standard XRD patterns of CdO crystal (PDF no. 75-0593) and Cd(Ac)<sub>2</sub>·2H<sub>2</sub>O (PDF no. 26-0240), respectively.

We therefore reacted the mixture of Cd(Ac)<sub>2</sub>·2H<sub>2</sub>O and Se powder in ODE at 260 °C. As shown in Figure 4.12c,g,h, a sample prepared within 8 min shows ill-defined multi-walled nanotubes with both lateral and angular extension, and their 2D electronic structure is verified by the sharp absorption at 467 nm and emission at 464 nm. Compared with the nanotubes prepared in the presence of DOAm, intact tubular architectures were difficult to find. We hypothesized this is because of the insufficient mass transfer between Cd(Ac)<sub>2</sub>·2H<sub>2</sub>O and Se powder, given that both solid ingredients have low solubility in ODE. Increasing the reaction time to 16 min, ultrathin and sheet-like nanostructures were observed in presence of numerous irregular nanodots (Figure 4.12d). For products synthesized within 32 min (Figure 4.12e), we see broken sheet-like nanostructures together with an increasing number of nanodots. Their absorption peak exhibits a blue shift to 462 nm, suggesting less inter-wall coupling. In brief, these experiments seem to indicate generation of the building blocks of 2D tube-like nanostructures, which gradually decompose into ultrathin sheet-like nanostructures and eventually into irregular nanodots, as the reaction time evolves. A possible explanation is that, because of the lack of DOAm medium-chain ligand, the reaction between Cd and Se precursors is extremely fast, leading to Ostwald ripening of the nanodots at the expense of 2D tube-like nanostructures.

To test the role of the ODE solvent, we simply heated the mixture of  $\text{Cd}(\text{Ac})_2 \cdot 2\text{H}_2\text{O}$  and Se powders at 260 °C in air without use of ODE. A previous report showed the formation of CdSe nanoplatelets by reacting  $\text{Cd}(\text{propionate})_2$  or  $\text{Cd}(\text{myristate})_2$  with Se powder at 200 °C [48]. Surprisingly, in our experiments, multi-walled CdSe nanotubes were also found, showing characteristic absorption and PL peaks of 2D CdSe NCs around 460 nm and 510 nm (Figure 4.12f-h), together with some unreacted Cd precursor. This could be ascribed to the high insolubility caused by the acetate ligand and high energy required for the assembly of the nanotubes. These investigations suggest that the anisotropic growth of the 2D CdSe NCs essentially originates from the acetate ligand that can passivate the growth of {100} planes of zincblende CdSe NCs in a solid (or partly melted) Cd precursor matrix, while the amine just plays an auxiliary role by regulating the reaction process and improving the mass transfer between Cd and Se precursors. We also investigated the influence of other alkylamines by replacing DOAm with primary amine like octylamine (OAm) and oleylamine (OLAm), and tertiary amine like tri-octylamine (TOAm). Due to the steric effect, the solubility of  $\text{Cd}(\text{Ac})_2$  in different alkylamines would follow: primary amine allows better solubility than secondary amine, and secondary amine allows better solubility than tertiary amine. As shown in Figure 4.16, if the solubility is good, we obtained CdSe nanobelts (Figure 4.16d) or irregular CdSe nanoparticle aggregates (Figure 4.16f) when using  $\text{Cd}(\text{Ac})_2$ -OAm and  $\text{Cd}(\text{Ac})_2$ -OLAm as the precursor, respectively. If the solubility is bad, less well defined tubular-like CdSe NCs were prepared, corresponding to the case of using  $\text{Cd}(\text{Ac})_2$ -TOAm as the precursor (Figure 4.16e). These results, together with the data of Figure 4.3, suggest that DOAm offers great advantages for producing better-defined tubular structures.



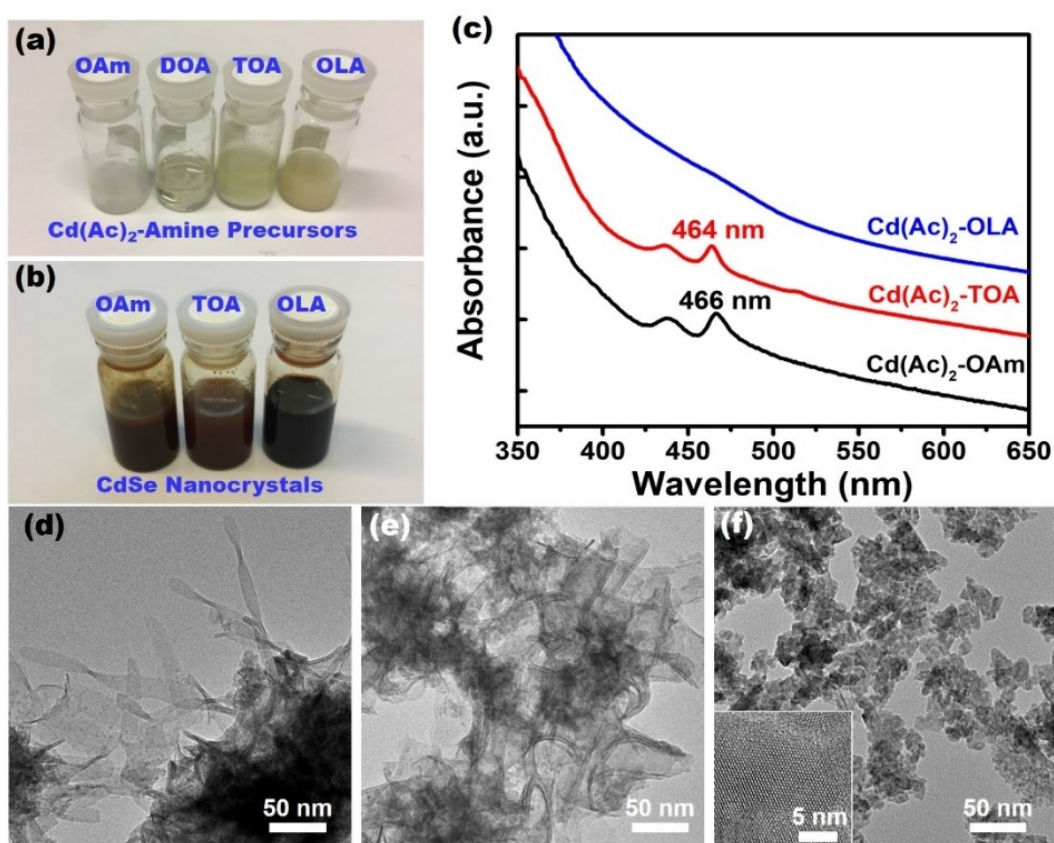


Figure 4.16 Influence of primary and tertiary alkylamines on the morphology of the CdSe NCs. (a) Photograph of the Cd(Ac)<sub>2</sub>-amine precursor solutions prepared by different alkylamines, including OAm, DOAm, TOAm and OLAm. Cd(Ac)<sub>2</sub> is well dissolved in OAm, DOA and OLAm, once heated, while it can only form a turbid suspension in TOAm due to the steric effect. In particular, clear Cd(Ac)<sub>2</sub>-OLAm and Cd(Ac)<sub>2</sub>-OLA solutions would be solids at room temperature. (b) Photograph, (c) UV-vis absorption and (d-f) TEM graphs of the CdSe NCs synthesized at 260 °C for 8 min using different Cd precursors, including (d) Cd(Ac)<sub>2</sub>-OAm, (e) Cd(Ac)<sub>2</sub>-TOAm and (f) Cd(Ac)<sub>2</sub>-OLAm. The inset in (f) indicates the high crystallinity of the CdSe nanoparticle aggregates.

#### 4.2.4 CdSe nanotubes growth mechanism.

To further elucidate the growth mechanism when using the Cd(Ac)<sub>2</sub>-DOAm solution as the Cd precursor, we performed a series of experiments to trace the evolution of the tubular structure by tailoring the reaction time at different temperatures, i.e. at 80, 140, 200 and 260 °C. All the samples exhibit characteristic absorption and emission spectra of 2D CdSe NCs with the first excitonic peak around 390 nm or 460 nm, depending on the synthetic temperature. The good continuity provided by the microscopic and spectroscopic results (Figure 4.17-4.20) clearly demonstrates the anisotropic growth of the 2D CdSe nanotubes by a non-planar 2D-oriented attachment approach, in which three critical stages are observable: formation of nanoplatelets, curved nanosheets and finally tubular NCs.

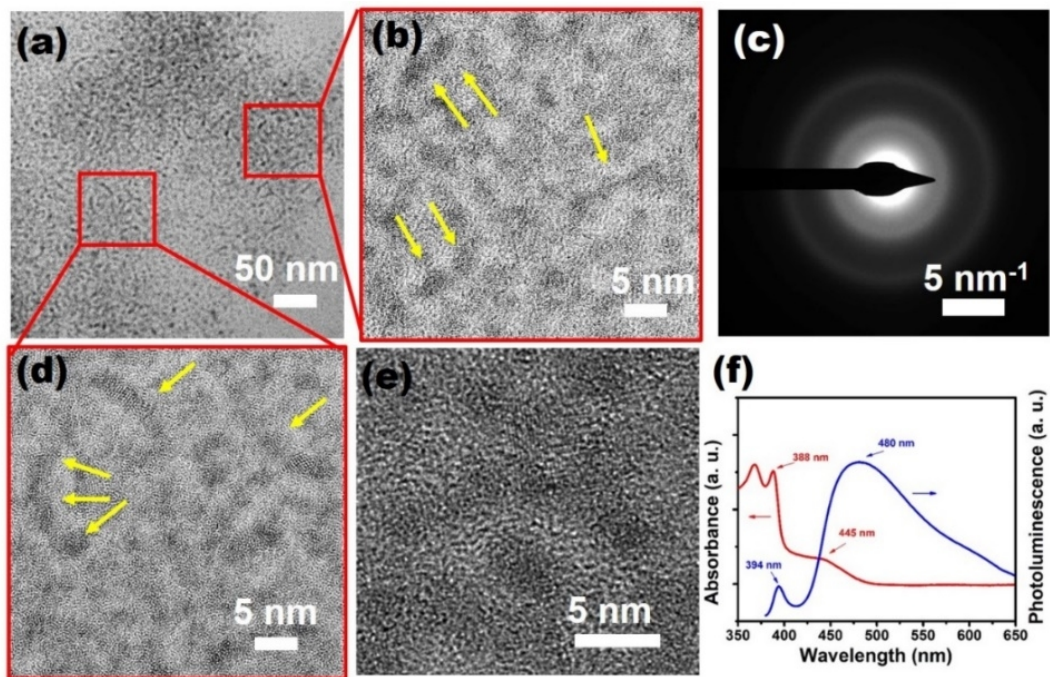


Figure 4.17 Characterization of 2D CdSe NCs synthesized at 80 °C for 17 hours. (a,b,d,e) TEM graphs, (c) SAED pattern, (f) UV-vis absorption and PL spectra of the 2D CdSe NCs synthesized at 80 °C for 17 hours. The graphs show the assembly of the nanoscale platelet-like structures of around 2 nm in thickness of (e) by a lateral (b) and angular (d) attachment mechanism. The SAED pattern of (c) indicates these NCs, synthesized at low temperature, have zincblende structure with relatively undeveloped crystallinity. The spectroscopic data of (f) exhibit the characteristic absorption and emission peak of 2D CdSe NCs at around 390 nm. The very broad PL peak at around 480 nm is ascribed to the deep trap emission in the 2D CdSe NCs. The absorption at 455 nm in the absorption spectra could be assigned to unpurified QDs of around 2 nm.

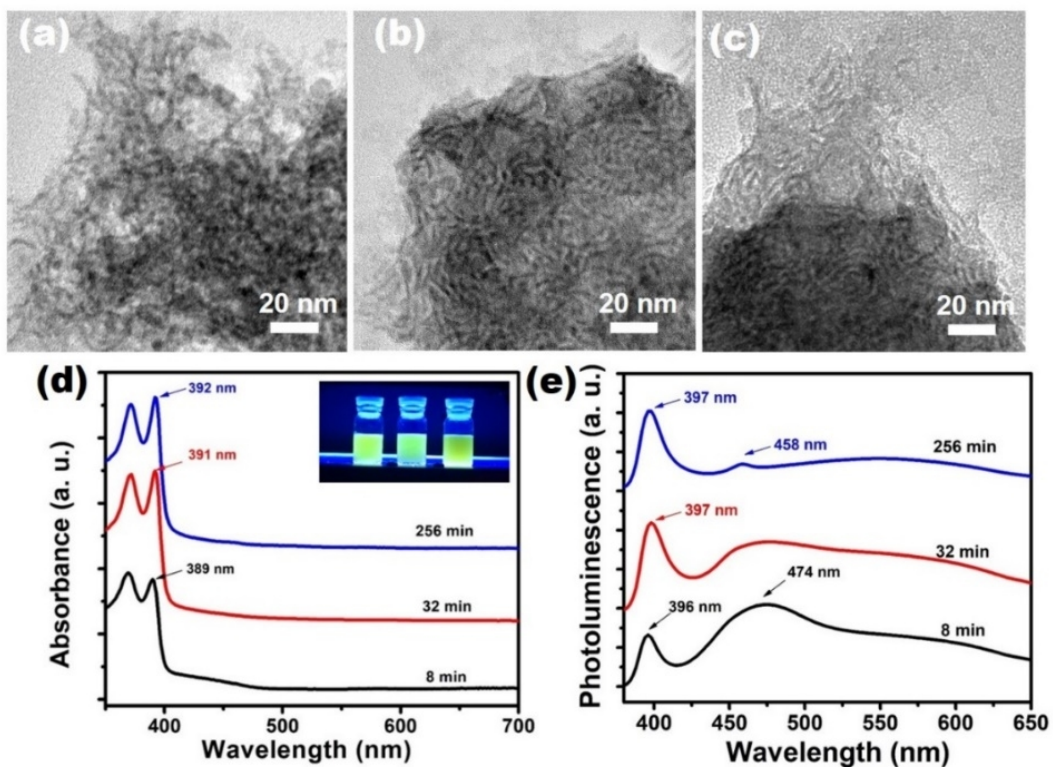


Figure 4.18 Characterization of 2D CdSe NCs synthesized at 140 °C for 8, 32 and 256 minutes. (a-c) TEM graphs, (d) UV-vis absorption, and (e) PL spectra of the 2D CdSe NCs synthesized at 140 °C for 8 (a), 32 (b) and 256 (c) min. The small redshift of the first excitonic peak

from 389 to 392 nm in (d) is ascribed to the growth of the 2D NCs in the lateral or angular direction. Consistently, the broad PL peak at around 474 nm in (e) gradually reduces with increasing reaction time because of crystal growth.

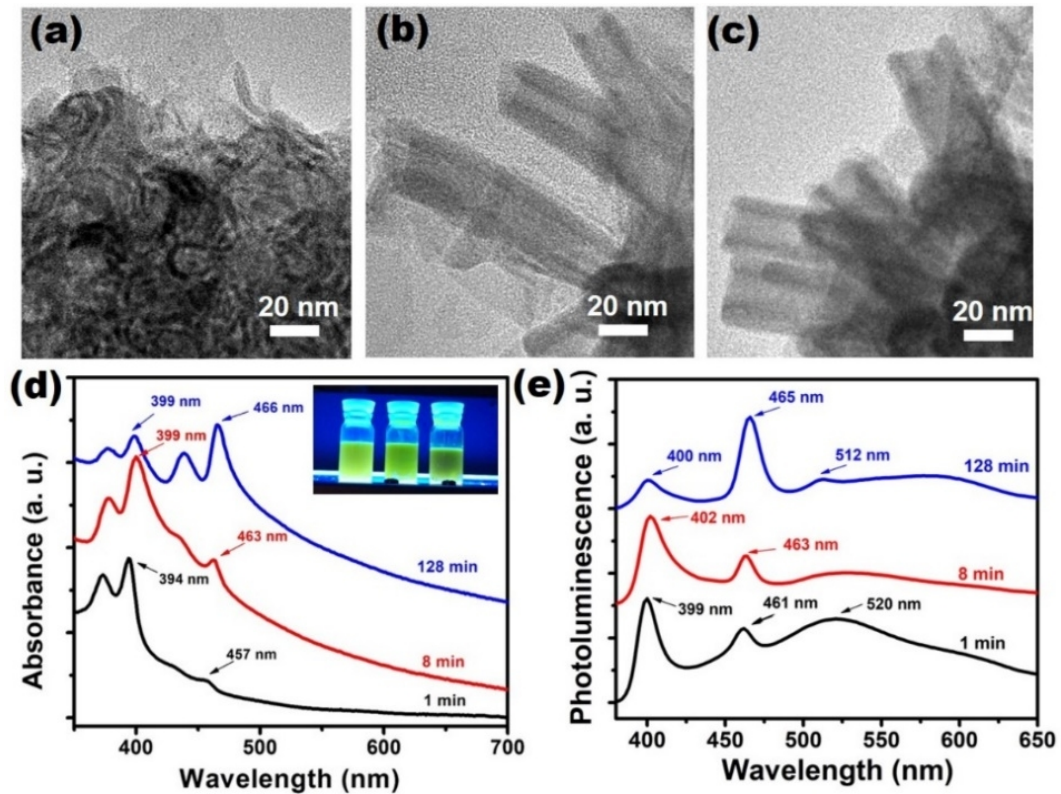


Figure 4.19 Characterization of 2D CdSe NCs synthesized at 200 °C for 1, 8 and 128 minutes. (a-c) TEM graphs, (d) UV-vis absorption and (e) PL spectra of the 2D CdSe NCs synthesized at 200 °C for 1 (a), 8 (b) and 128 (c) min. The redshift of the major excitonic peak from 394 to 399 nm as well as from 457 to 466 nm in (d) is ascribed to the growth of the 2D NCs. Consistently, growth of the 2D NCs results in the decrease of the broad PL peak at around 520 nm in (e) due to the deep trap emission, as well as the increase of the sharp PL peak at around 465 nm, as more 2D NCs with thickness of 6.5 MLs were formed.



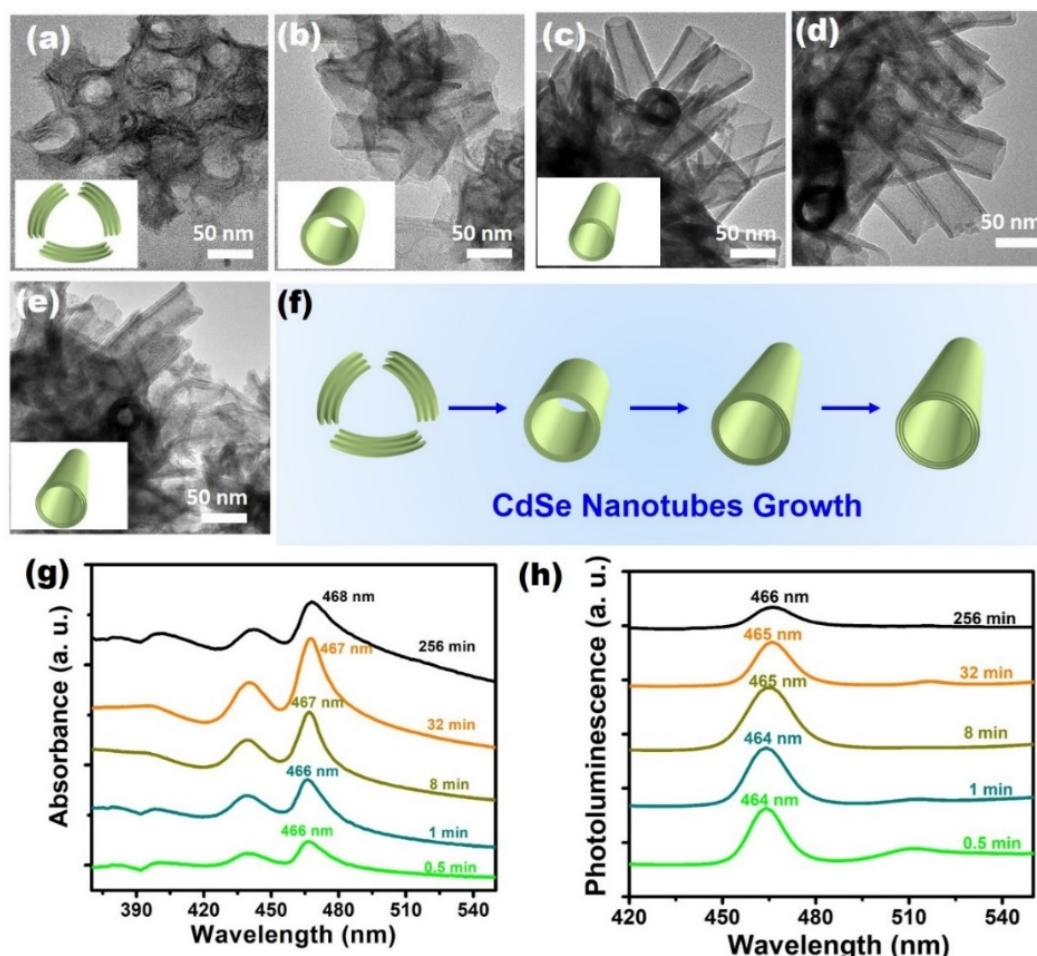


Figure 4.20 Characterization of 2D CdSe NCs synthesized at 260 °C for 0.5, 1, 8, 32 and 256 minutes. (a-e) TEM graphs, (g) UV-vis absorption, and (h) PL spectra of the 2D CdSe NCs synthesized at 260 °C for 0.5 (a), 1 (b), 8 (c), 32 (d) and 256 (e) and 128 (f) min. The small redshift of the first excitonic peak from 466 to 468 nm in (g) and of the PL peak from 464 to 466 nm in (h) are ascribed to the growth of the 2D NCs. (f) Schematic drawing of the assembly of the curved nanosheets into well-defined tubular structures that finally turn into nanotubes with visible multiple walls.

In the first stage, anisotropic nanoplates with thickness of 1~2 nm and length of 3~5 nm were found in samples prepared at 80 °C within 17 hours (Figure 4.17) and 140 °C within 8 minutes (Figure 4.21b,c, Figure 4.18a). Apart from the sharp peak at around 390 nm, their emission spectra also show a rather broad peak around 480 nm, which could be ascribed to deep trap-state emission [96]. Figure 4.22 reveals the formation of these anisotropic seeds by heterogenous nucleation from the amorphous Cd precursor matrix. This nucleation mode has a greatly reduced energy barrier, rapidly resulting in a large number of nuclei in a highly concentrated environment. The use of short-chain acetate plays an important role, since it provides a low solubility of ligand-capped monomers in the non-polar solvent. Also, owing to the low steric hindrance of the acetate ligand, the formed CdSe nuclei are highly reactive, ready for the further attachment with the adjacent ones. In terms of packing density and dangling bonds, the passivated surface energies of zincblende CdSe have following relation:  $\gamma_{\{100\}} < \gamma_{\{111\}} < \gamma_{\{110\}}$  [111]. Therefore, the growth is hindered along the polar  $\langle 100 \rangle$  direction while favored along the nonpolar  $\langle 110 \rangle$  direction, giving rise to nanoplatelets with two polar  $\{100\}$  planes at both top and bottom surface.

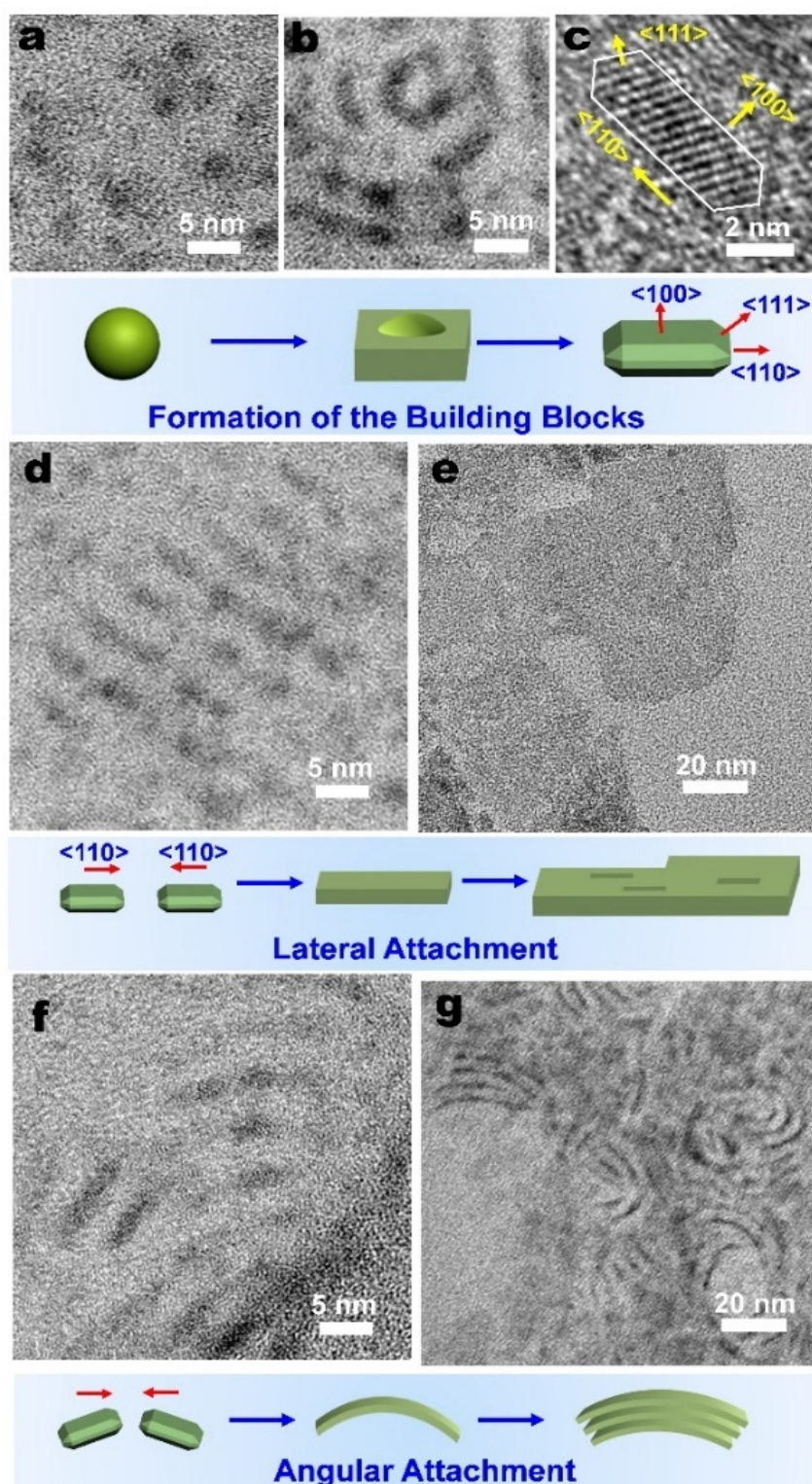


Figure 4.21 TEM and HRTEM study of early formation stages of CdSe nanotubes. Synthesis at a temperature of 140 °C (a-d,f) leads to (a) CdSe dots of around 2 nm, as well as (b) seeds that form nanotube building blocks in the form of elongated platelets. (c) HRTEM micrograph of a small assembly of building blocks showing {111} facets at the edge. The schematic shows the formation of building blocks from the CdSe dots to platelets with {100} terrace facets. (d) Lateral growth mechanism, as indicated by the attachment of the building blocks in the  $\langle 110 \rangle$  direction. Synthesis at a temperature of 200 °C (e,g) allows to observe (e) holes in the nanosheets, indicative of a growth mechanism by building block assembly. (f) Angular growth mechanism by the assembly of building blocks with a rotation with respect to the  $\langle 110 \rangle$  direction. (g) Formation of initial multi-walled structures as result of the angular growth mechanism and intermolecular forces between individual walls.

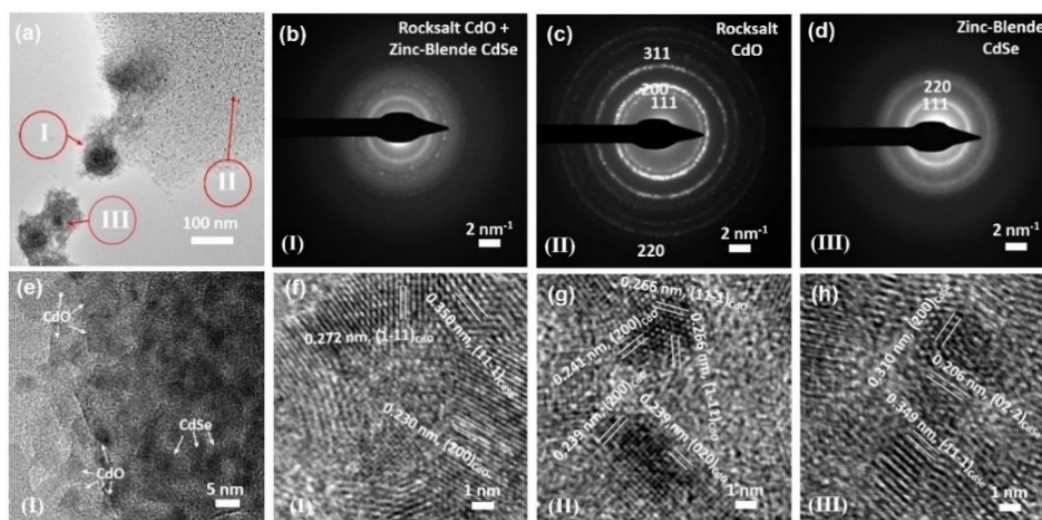


Figure 4.22 TEM characterization of early stage formation of the 2D CdSe NCs from Cd precursor matrix. (a) TEM graph, (b-d) SAED patterns, and (e-h) HRTEM graphs showing the early growth stage of the 2D CdSe NCs obtained from the samples prepared at 140 °C for 8 min. CdO NCs can be eventually generated from unreacted Cd precursor under electron beam radiation. Region I in (a) shows the coexistence of rocksalt CdO NCs and zincblende CdSe NCs (b,e,f), indicating the formation 2D CdSe NCs from solid Cd precursor matrix. Region II and III in (a) display the unreacted Cd precursor matrix filled with CdO NCs (c,g) and aggregates of 2D CdSe NCs (d, h).

In a second stage, the nanoplatelets are assembled into curved nanosheet by simultaneously lateral and angular attachment. Lateral attachment, such as that occurring for ultrathin PbS nanosheets [54], takes place on the most reactive {110} facets of two adjacent nanoplatelets (Figure 4.21d, 4.17b): the process involves alignment, contact, fusion and a post-recrystallization process to eliminate the crystal boundary [52]. The patch-like structure of Figure 4.21e provides evidence of growth by oriented attachment rather than by monomer addition. However, due to the low orientational degree of freedom inside the solid Cd pre-cursor matrix, the alignment and rotation of the building blocks is severely constrained. As a result, growth via angular attachment is more prevalent. Two main types of assembly contributing to the angular growth are observed: misoriented attachment and multiple oriented attachment. The former involves relatively small angular rotations ( $< 24^\circ$ ) between two neighboring {110} facets, resulting in crystal defects that include stacking faults (Figure 4a), lattice distortions (Figure 4.23b) and edge dislocations (Figure 4.23c,d). These defects are characteristic features of nanostructures formed via oriented attachment.<sup>28,31</sup> The latter can take place on a less reactive {111} facet through attachment with a {110} facet (Figure 4.23e) or via attachment of two {111} facets (Figure 4.23f), resulting in a large misoriented angle of  $35^\circ$  and  $70^\circ$ , respectively. The presence of a high number of crystal defects is expected, since otherwise there would be a large asymmetric strain on both sides of the tube wall.



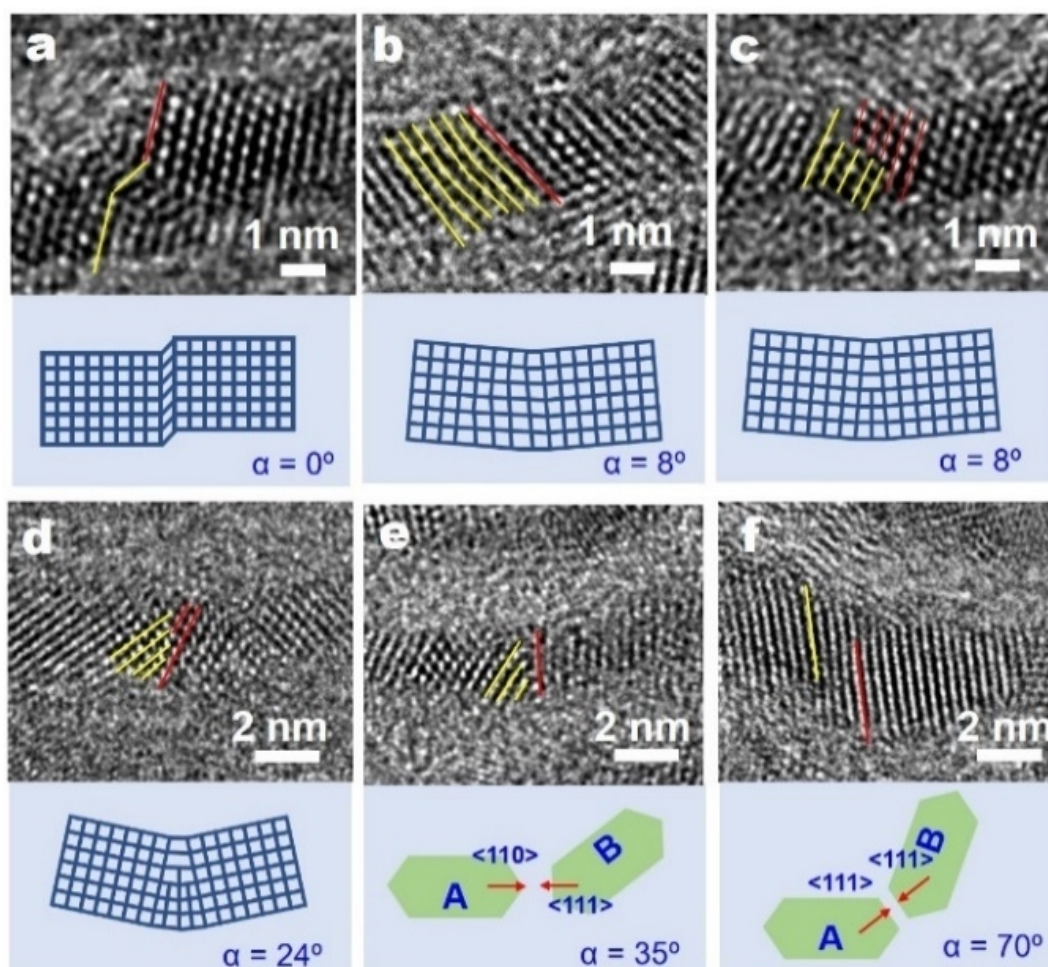


Figure 4.23 HRTEM study of the angular building block assembly mechanism. (a) HRTEM image of a distorted lattice plane due to a stacking fault along the  $\langle 111 \rangle$  direction, not resulting in a microscopic rotation of the crystallographic orientation ( $\alpha = 0^\circ$ ). (b) A small angular rotation ( $\alpha = 8^\circ$ ) is caused by a lattice distortion on the  $\{111\}$  facets. (c,d) Edge dislocations involving (c) one or (d) three half atomic planes into the  $\{111\}$  facets are also observed, contributing to an angular rotation of  $8^\circ$  and  $24^\circ$ , respectively. (e,f) Oriented attachment between (e)  $\{110\}$  and  $\{111\}$  planes, as well as (f) two adjacent  $\{111\}$  planes leads to a larger angular rotation of  $35^\circ$  and  $70^\circ$ , respectively. The red and yellow lines indicate the  $\{111\}$  facets in adjacent building blocks.

In the final stage, well-defined CdSe nanotubes are obtained via assembly of the curved nanosheets. This is clearly demonstrated by the arrangement of curved nanosheets into early-stage tube-like architectures within 0.5 min at  $260^\circ\text{C}$  (Figure 4.20a,b). Due to the high strain energy in a tubular nanostructure [112], both intact and incomplete assemblies are easily observed in the samples synthesized within 8 min (Figure 4.24). It is noticeable that nanotubes are only found when the reaction temperature is above  $200^\circ\text{C}$ , while samples prepared at  $80^\circ\text{C}$  and  $140^\circ\text{C}$  just show nanoplatelets (Figure 4.17) and curved nanosheets (Figure 4.18), respectively. This means the nucleation energy barrier is lower than the required energy for growth by attachment. We think that formation of well-defined tubular structures requires a balance between lateral and angular growth. Raising the temperature even higher would provide more energy to overcome the barrier of oriented attachment, and more importantly, facilitate the lateral attachment by enhancing the motion of building blocks in the precursor matrix.

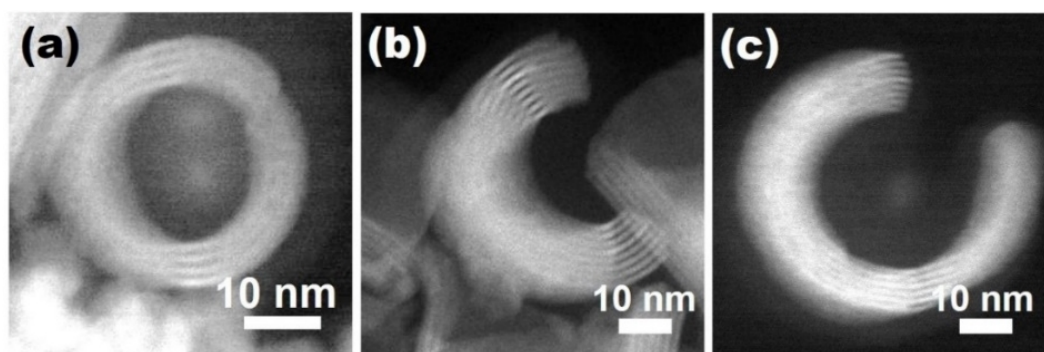


Figure 4.24 Final and incomplete formation of CdSe nanotubes observed along the tube opening direction. TEM graphs of CdSe nanotubes synthesized at 260 °C for a reaction time of 8 min, showing the (a) intact and (b,c) incomplete assembly of curved multi-layered nanosheets into nanotubes.

To check if these tubular nanostructures are similar to the nanoscrolls often found during growth of CdSe nanosheets with large lateral dimension [98, 99], an unfolding process by growing a CdS shell on the CdSe nanotube was performed. The CdSe nanotubes, synthesized at 260 °C within 8 min, were first reacted with a thiol ligand, thioacetamide (TTA), followed by the addition of a Cd(oleate)<sub>2</sub> precursor. As shown in Figure 4.25, we find fragmented nanosheets with lateral dimension less than 200 nm in our nanotubes after the treatment, which is different from the large-size rectangular nanosheets observed when unfolding nano-crolls [98, 99]. Further investigation allowed finding out that these sheet-like fragments already existed after reacting the nanotubes with TTA (Figure 4.26). This result is expected, as surface ligand exchange would diminish the inter-wall interaction formed by the acetate ligand, thus disintegrating tubular nanostructures into sheet-like fragments in the presence of crystal defects.

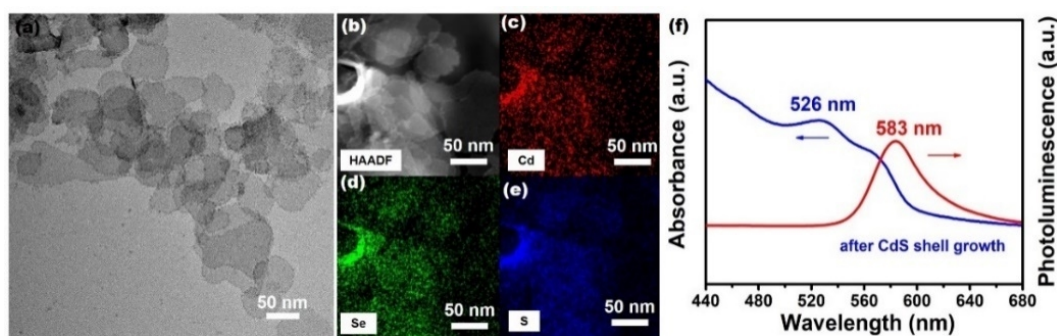


Figure 4.25 Characterization of nanostructures after growing a CdS shell on the CdSe nanotubes. (a) TEM, (b) HAADF-STEM, EDX mapping of (c) Cd, (d) Se and (e) S, (f) UV-vis and PL spectra of the nanostructures after growing a CdS shell on the CdSe nanotubes. The reaction was performed by reacting CdSe nanotubes with thioacetamide (TTA), followed by the addition of Cd(Ac)<sub>2</sub>.



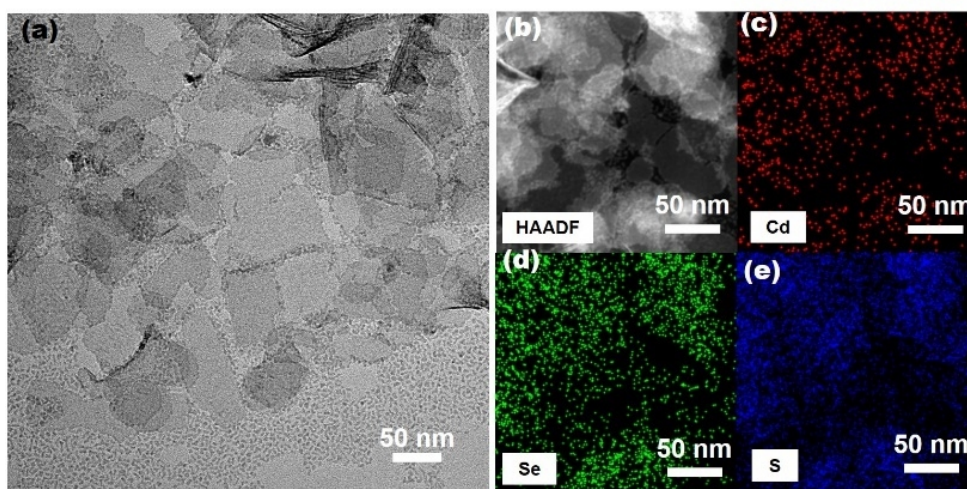


Figure 4.26 Characterization of nanostructures after reacting CdSe nanotubes with thioacetamide. (a) TEM, (b) HAADF-STEM, EDS mapping of (c) Cd, (d) Se and (e) S of the nanostructures after reacting CdSe nanotubes with thioacetamide (TTA), i.e. after ligand exchange rather than after growing a CdS shell.

## 4.3 Experimental Section

### 4.3.1 Synthetic Methods

**Materials.** Cadmium acetate hydrate ( $\text{Cd}(\text{Ac})_2 \cdot 2\text{H}_2\text{O}$ , 99.9% purity), cadmium oxide (CdO), 1-octadecene (ODE), oleic acid (OAc), dioctylamine (97% purity, DOAm), octylamine (99% purity, OLAm), trioctylamine (98% purity, TOAm), oleylamine (>98% purity, OLA), thioacetamide (TAA), trioctyl phosphine (TOP, 97% purity), selenium powder (Se), methanol, hexane, ethanol and dichloromethane were purchased from Sigma-Aldrich. All chemicals were used without further purification.

**Synthesis of CdSe nanotubes and 2D CdSe NCs.** A schematic drawing showing the synthesis procedures is shown in Figure 4.2. Before the synthesis of the CdSe nanotubes, the Cd precursor solutions were prepared in advance, as follows. 333 mg (1.25 mmol) of  $\text{Cd}(\text{Ac})_2 \cdot 2\text{H}_2\text{O}$  were sonicated in 1.5 mL (5 mmol) of DOAm (a molar ratio of 1:4 between Cd and DOAm was taken), followed by heating at 200 °C for 10 minutes to fully remove the water and get clear solution, which was labeled as “ $\text{Cd}(\text{Ac})_2$ -DOAm solution”. For a typical CdSe nanotubes synthesis, 7.9 mg of Se powder was first dissolved (partly dispersed) in 3.6 mL of ODE and stirred at 260 °C for 10 min, after which 0.3 mL of  $\text{Cd}(\text{Ac})_2$ -DOAm Solution (a molar ratio of 2.5:1 between Cd and Se) was quickly injected. The solution rapidly turned turbid, followed by a change in color from white into yellow, and finally into a brown solution. After a given time (e. g. 8 min), the reaction was stopped by removal of the heater and the mixture was cooled down in air. Tubular CdSe NCs were produced mainly in the form of aggregates, together with some QDs as byproducts. For the purification, the cooled solution was mixed with a solution containing hexane and TOP (3:1, v/v) and centrifuged at a speed of 3000 rpm for 3 min. TOP was used to remove the unreacted Se precursor. The resulting supernatant was discarded, while the precipitates, mainly containing CdSe nanotubes, were collected and washed in hexane-TOP solution for two more times for 5 min. Afterwards, the collected products were twice washed in methanol by a dispersion and

centrifugation process to remove the unreacted Cd precursor. Finally, the precipitates were dispersed in hexane for further characterization. Other 2D CdSe NCs such as nanoplatelets and curved nanosheets were prepared through similar procedures by changing the reaction temperature and time. It is worth mentioning that, different from the classical hot injection method used for CdSe QDs preparation,<sup>1</sup> neither degassing the reactant before the reaction nor creating an inert atmosphere for the reaction is needed.

**Surface ligand exchange with oleic acid on 2D CdSe NCs.** First, the purified 2D CdSe NCs in hexane were centrifuged. After discarding the supernatant, the precipitate containing the 2D NCs was dispersed in 2 mL of a solution containing ODE and oleic acid (8:2, v/v). Then the solution was stirred at 200 °C for 10 min with a speed of 800 rpm. After cooling to room temperature, the resulting solution was purified in hexane for further characterization by centrifugation and redispersion.

**Control experiments to investigate the role of acetate and amine in CdSe nanotubes synthesis.** Control experiments were designed and performed in the absence of DOAm or/and ODE; obtained reaction products are shown in Figure 4.12. In case of synthesis using DOAm in the absence of ODE (Figure 4.12b), 7.9 mg of Se powder was stirred in 3.6 mL of DOAm at 260 °C to get the Se-DOAm solution. Afterwards, 0.3 mL of Cd(Ac)<sub>2</sub>-DOAm (a molar ratio of 2.5:1 between Cd and Se) was quickly injected into the Se precursor solution and the reaction was kept going for 8 min. In case of synthesis using ODE in the absence of DOAm (Figure 4.12c-e), 15.8 mg of Se were mixed with 266 mg of Cd(Ac)<sub>2</sub>·2H<sub>2</sub>O, and then ground into powder of homogenous color with a mortar and pestle. Then, 140.9 mg of the mixture were rapidly injected into a 3.6 mL ODE solution which was already heated to 260 °C. The reaction was kept for a variable time, like 8 min (Figure 4.12c), 16 min (Figure 4.12d) and 32 min (Figure 4.12e). For all control experiments, a further purification by repeating the centrifugation and redispersion of the precipitates in hexane three times was required. In case of synthesis without using DOAm and ODE, 140.9 mg of the Cd(Ac)<sub>2</sub>·2H<sub>2</sub>O-Se mixture, as prepared in the last step were heated for 8 min at 260 °C on a glass substrate. After that, the product was collected in a vial and dispersed in hexane for further characterization. In addition, to obtain the Cd(Ac)<sub>2</sub>-DOAm precipitates for further characterization, 0.3 mL of Cd(Ac)<sub>2</sub>-DOAm solution was quickly injected into 3.2 mL of ODE solvent at 200 °C at a stirring speed of 800 rpm. After 5 min, the white precipitate was collected by centrifugation and washed twice in hexane by repeating the dispersion and centrifugation process. To investigate the influence of other alkylamines, Cd(Ac)<sub>2</sub>-OLAm, Cd(Ac)<sub>2</sub>-TOAm and Cd(Ac)<sub>2</sub>-DLAm precursors were first prepared by adding 333 mg (1.25 mmol) of Cd(Ac)<sub>2</sub>·2H<sub>2</sub>O into the corresponding amines at a molar ratio of 1:4 between Cd and amines, followed by heating at 200 °C for 10 minutes to fully remove the water. The synthesis of CdSe NCs using these Cd(Ac)<sub>2</sub>-amine precursors was performed, in which the protocol was similar to that for CdSe nanotubes synthesis using Cd(Ac)<sub>2</sub>-DOAm at 260 °C for a reaction time of 8 min.

**Growth of a CdS shell to unfold the CdSe nanotubes.** The growth of a CdS shell using thioacetamide (TAA) and Cd(OAc)<sub>2</sub> was performed using the method reported by B, Dubertret et al. Typically, 20 mg of TAA dissolved in 200 µL of OLAm were added into 10 mg of purified CdSe nanotubes

dissolved in 2 mL of dichloromethane. After a stirring mixing at 800 rpm for 10 min, 200  $\mu\text{L}$  of the solution was fetched for further characterization (as shown in Figure 4.26). 200  $\mu\text{L}$  of  $\text{Cd}(\text{OAc})_2$  dissolved in the OLAm (0.1 M) was then added to the remaining solution and the stirring was stopped after a reaction time of 3 h (corresponding to the sample as shown in Figure 4.25). The purification of these samples was performed by repeating the dispersion and centrifugation process in the solution containing dichloromethane and ethanol (5:1, v/v).

#### 4.3.2 Characterization

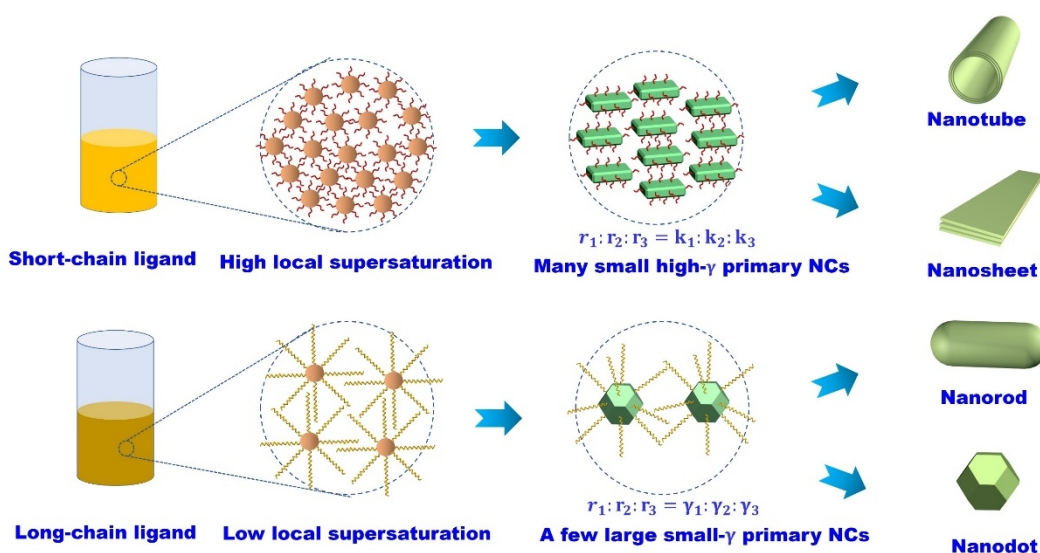
UV-vis absorption spectroscopy was performed on a Varian Cary 50 Scan UV-vis spectrophotometer. PL and PLE spectra were measured by a Horiba fluorescence spectrometer, in which an excitation wavelength was set as 350 nm for the PL spectra and an emission wavelength was set as 600 nm for the PLE spectra. TEM, HRTEM, STEM, EDX, SAED images were captured by a Talos transmission electron microscope (FEI Co.) and a Titan Themis (FEI Co.); prior to that, the CdSe NCs dissolved in hexane were dropped and dried on ultrathin carbon-supported copper grids. SEM images were taken on Zeiss Gemini 300 field emission scanning electron microscopes under the in-lens mode operating at an accelerating voltage of 3 kV. Powder XRD measurement was performed on a Bruker D8 discover X-ray powder diffractometer. Fourier-transform infrared spectroscopy (FTIR) spectra were recorded by a Nicolet iS10 FT-IR Spectrometer (Thermo Scientific) equipped with a smart diamond attenuated total reflectance (ATR) accessory. Thermal gravimetric analysis (TGA) curve was measured by a TGA 4000 from Perkin Elmer.

#### 4.4 Conclusions

In this chapter, we demonstrated by carefully selecting the surface ligands, zincblende CdSe nanotubes with atomically flat walls can be fabricated. They are featuring a multi-walled structure, sharp absorption and emission at around 460 nm, and Cd-terminated {100} planes as top and bottom surface in the wall thickness direction. Anisotropic growth is found to result from the utilization of acetate ligand; meanwhile, the addition of DOAm assists in formation of more regular tubular structures. We further elucidated the growth mechanism through a non-planar 2D oriented attachment approach; that is, simultaneous lateral and angular attachment of early-stage nanoplatelets into curved nanosheets and finally a tubular architecture.



# Chapter 5 Anisotropic Growth of CdSe Nanocrystals via Particle Attachment of Intrinsically Different Building Blocks



In this chapter, we further elucidate the formation mechanism of anisotropic CdSe NCs in the presence of a dioctylamine and other carboxylate ligands with different chain length. A morphological transition from nanotubes and nanosheets to irregular nanorods and finally to QDs was observed when the carbon number of the carboxylate ligands increased from 2 to 18. We proposed that both short- and long-chain carboxylate ligands can lead to the growth of CdSe NCs by attachment of early-formed NC building blocks, a non-classical particle-mediated growth approach through the reactive facets of the latter. Different carboxylate ligands produce NC building blocks with different reactive facets as a result of different local monomer supersaturation effect. We provided experimental observations and first-principle simulations to support this hypothesis.

The work in this chapter is summarized and in submission:

X. Huang, V. K. Parashar, Z. Ao, M. A.M. Gijs, "Anisotropic Growth of CdSe Nanocrystals via Particle Attachment of Intrinsically Different Building Blocks", 2019, in submission.

## 5.1 Introduction

Over the past two decades, colloidal semiconductor NCs with anisotropic morphologies have attracted considerable attention due to their shape-related properties [24, 38, 113]. Compared with the beautiful morphologies acquired by experiments, the understanding of the underlying mechanisms behind the anisotropic growth always fell behind. A recent topic intriguing extensive discussion is the formation mechanism of 2D ultrathin platelet-like or sheet-like CdSe NCs with atomically scale thickness. Buhro et al proposed the anisotropic growth was due to the assembly of nanoclusters in a soft template created by long-chain carboxylate ligands [97], while recent reports suggest that 2D zincblende CdSe nanoplatelets can be obtained without the use of long-chain carboxylate ligand [114]. Based on observation of insoluble precursors, D. Norris et al provided an improved 2D nucleation and growth model, showing that 2D planar growth is intrinsically favorable because of the reduced nucleation barrier compared with 3D isotropic growth [48]. Unfortunately, the issue why the thickness plane is consisting of the {100} facets rather than other facets, like the closest packing {111} facets, was not clearly elucidated. Recently, Dubertret et al directly synthesized 2D nanoplatelets by using medium-chain carboxylate ligands in solution, suggesting the addition of insoluble precursor is not necessary [115]. In the last chapter, we also found the CdSe nanoplatelets and nanosheets could be evolved into CdSe NTs with multiple atomically-flat walls in the presence of short-chain acetate ligand, which is difficult to be explained by a classical monomer-mediated growth model. Instead, a nonclassical particle-mediated mechanism, in which the early-formed nanoplatelets having reactive {110} facets were assembled into curved nanosheets and finally into tubular nanoarchitectures via lateral and angular attachment was established [116]. We noticed a similar growth behavior is also proposed by Weller and coworkers. They reported the 2D oriented attachment of NC building blocks with reactive {110} facets into ultrathin PbS nanosheets when short-chain chlorine-containing reagents were used [58]. However, it remains unsettled why such energetically unstable nanoscale building blocks can be formed in the presence of short-chain carboxylate ligand, and what happens if we use long-chain carboxylate ligands to stabilize the NCs.

The role of surface ligands has proven to be of great importance in controlling the anisotropic growth of NCs via the classical monomer-mediated approach. In the synthesis of 1D CdSe NCs with a wurtzite (hexagonal) structure, diverse morphologies including tetrapod-, rod-, rice- and dot-like shapes appear in sequence by decreasing the monomer concentration [18, 42, 45]. To obtain non-spherical anisotropic nanostructures, the addition of alkylphosphoric acid was critical; moreover, shorter-chain ligands resulted in more elongated and branched rod-like nanostructure. In this regard, the phosphoric ligand had two roles, including 1) a surface energy adjuster, which selectively passivates the side surface of the rod-like nanostructure [43], and 2) a growth kinetic modulator, which promotes the anisotropic growth in a way similar to the increase of monomer supersaturation. This inspired us to consider if ligands would play similar roles in the synthesis of anisotropic NCs formed via non-classical particle attachment, where initially-formed nanoscale building blocks are assembled and fused to larger objects[49-51]. A work reported by Murray et al has clearly demonstrated their role as surface energy

adjuster: by using different long-chain ligands, the shape of building blocks can be tuned, which leads to a diversity of 1D PbSe NCs, such as zigzag, straight and star-shape branched nanowires after oriented attachment [57]. However, as far as we know, their role as growth kinetic modulator is still not clearly elucidated in particle-mediated growth, despite of numerous evidences revealing that anisotropic growth is favorable in the presence of shorter-chain carboxylate ligands in colloidal NCs [42, 79, 80, 117-119].

In this study, we investigated the influence of carboxylate ligands having different chain length on the anisotropic growth of CdSe NCs via a particle attachment approach. We propose that carboxylate ligands can play the role of growth kinetic controller, which leads to intrinsically different building blocks: kinetically-controlled and thermodynamically-controlled NCs. The formation of 2D CdSe NCs is due to the oriented attachment of kinetically-controlled building blocks in the presence of short-chain carboxylate ligand, which controls the reaction by inducing a high local monomer supersaturation. By increasing the chain length of carboxylate ligand, the building blocks would become thermodynamically stable, leading to 1D CdSe NCs after attachment. Experimental characterization including transmission electron microscopy (TEM), high-resolution TEM (HRTEM), high-angle annular dark-field scanning transmission electron microscopy (HAADF-STEM), selected-area electron diffraction (SAED), X-Ray diffraction (XRD), and ultraviolet-visible (UV-Vis) absorption spectroscopy were used to investigate the structure, morphology and surface chemistry. Density Functional Theory (DFT) simulation was performed to understand the surface energy and adsorption state by the ligands.

## 5.2 Results and Discussion

### 5.2.1 Particle-mediated Anisotropic growth of CdSe NCs in the Presence of Different Carboxylate Ligands

In the last chapter, we have shown that well-defined multiwalled CdSe NTs can be obtained by reacting cadmium acetate dissolved in dioctylamine ( $\text{Cd}(\text{Ac})_2\text{-DOAm}$ ) and Se powder in a hot 1-octadecene (ODE) solution. Based on this recipe, in this study, we used  $\text{Cd}(\text{carboxylate})_2\text{-DOAm}$  solutions as the cadmium source, which were prepared by reacting CdO with various carboxylic acids having a carbon number of 2, 4, 6, 8, 12 and 18 respectively, namely, acetic acid, butyric acid, hexanoic acid, octanoic acid, lauric acid and oleic acid respectively, followed by the addition of the secondary alkylamine, DOAm. The reaction between CdO and carboxylic acids results in cadmium carboxylates in the bidentate chelating and bridging coordination form, which are easily dissolved in DOAm. The synthesis of the CdSe NCs was performed at 260 °C by injecting the  $\text{Cd}(\text{carboxylate})_2\text{-DOAm}$  into an ODE solution containing TOP-Se as the selenium precursor. Figure 5.1 shows the microscopic, spectroscopic and structural characterization of the CdSe NCs synthesized in the presence of different carboxylate ligands. Obviously, within a reaction time of 8 min, we obtained CdSe nanotubes, nanosheets (Figure 5.1g,h), nanorods (Figure 5.1k,l) and nanodots (Figure 5.1o,p) when acetate, butyrate, laurate and oleate ligand was used, respectively. The tubular nanostructures, similar to those obtained

by using Se powder as the anionic source in chapter 4, are easily aggregated and are proposed to consist of 3 to 6 walls attracted by the van der Waals interaction (Figure 5.1c,d) [116]. An individual wall is 3.5 MLs in thickness, or 4 cadmium layers and 3 selenium, which is deduced from the sharp first excitonic peak at around 460 nm (Figure 1q) in the UV-vis absorption spectra. It has been widely acknowledged that typical 2D zincblende CdSe NCs have discrete first absorption peaks at around 390, 462, 512 and 564 nm, corresponding to a thickness of 2.5, 3.5, 4.5 and 5.5 molecular monolayers (MLs), respectively [5, 94]. The redshift of the absorption spectra was likely ascribed to strong inter-wall coupling and scattering within the sample [96]. Samples prepared within 1 min show early-formed nanoplatelets and curved nanosheets arranged in the shape of tube opening, an indication of forming the CdSe nanotubes via a particle attachment approach (Figure 5.1a,b). When butyrate ligand was employed, multilayered sheet-like nanostructures were obtained within a reaction time of 8 min, showing a characteristic first absorption peak at 463 nm (Figure 5.1g,h,q). Samples synthesized within 1 min, as shown in Figure 5.1f, clearly demonstrate the anisotropic growth is via lateral assembly of the nanoplatelets of 2~4 nm in size.

Further increasing the carbon number of the carboxylate ligands to 6 and 8, the characteristic absorption peak of 2D CdSe NCs at around 460 nm fades away, accompanied with the emergence of the absorption peak after 500 nm, which is indicative of either 0D or 1D CdSe NCs (Figure 5.1q, 5.2c,d). The absorption peak at 460 nm completely disappeared in the case of laurate ligand, in which an absorption peak increasingly evolving from 505 to 578 nm was observed during a reaction time from 30 s to 8 min (Figure 5.2e). Interestingly, TEM and STEM graphs shows the samples hold the shape of elongated and branched CdSe nanorods for a reaction time of 8 min (Figure 5.1 k,l), which were even chain-like 1D nanostructure when reacted for 1 min (Figure 5.1 i,j). Similarly, the chain-like morphology was also found in the CdSe NCs synthesized within 1 min when oleate ligand was used (Figure 5.1 i,j), which turned into more isotropic, dot-like nanostructure, although some elongated rod-like nanostructure can still be seen (Figure 5.1 o,p). We notice these elongated and branched CdSe NCs were ever reported by using long-chain carboxylate ligands [27, 117, 118], yet the chain-like morphology occurring at the early reaction stage was seldom observed. Considering the good continuity of the morphological change when the chain length of the ligand was increased, we proposed the chain-like nanostructures were formed by the assembly of the early-formed nanodot building blocks. As reaction evolved, they would undergo intraparticle ripening and become less anisotropic rod-like or dot-like NCs as a result of diffusion-controlled growth in the presence of long-chain ligands, which will be discussed in more detail below. These results demonstrate that the anisotropic growth of CdSe NCs is due to the particle attachment that occurs in specific directions. By using carboxylate ligand with a longer carbon chain, the growth of CdSe NCs gradually becomes isotropic, converting from nanotubes and nanosheets to nanorods and nanodots.



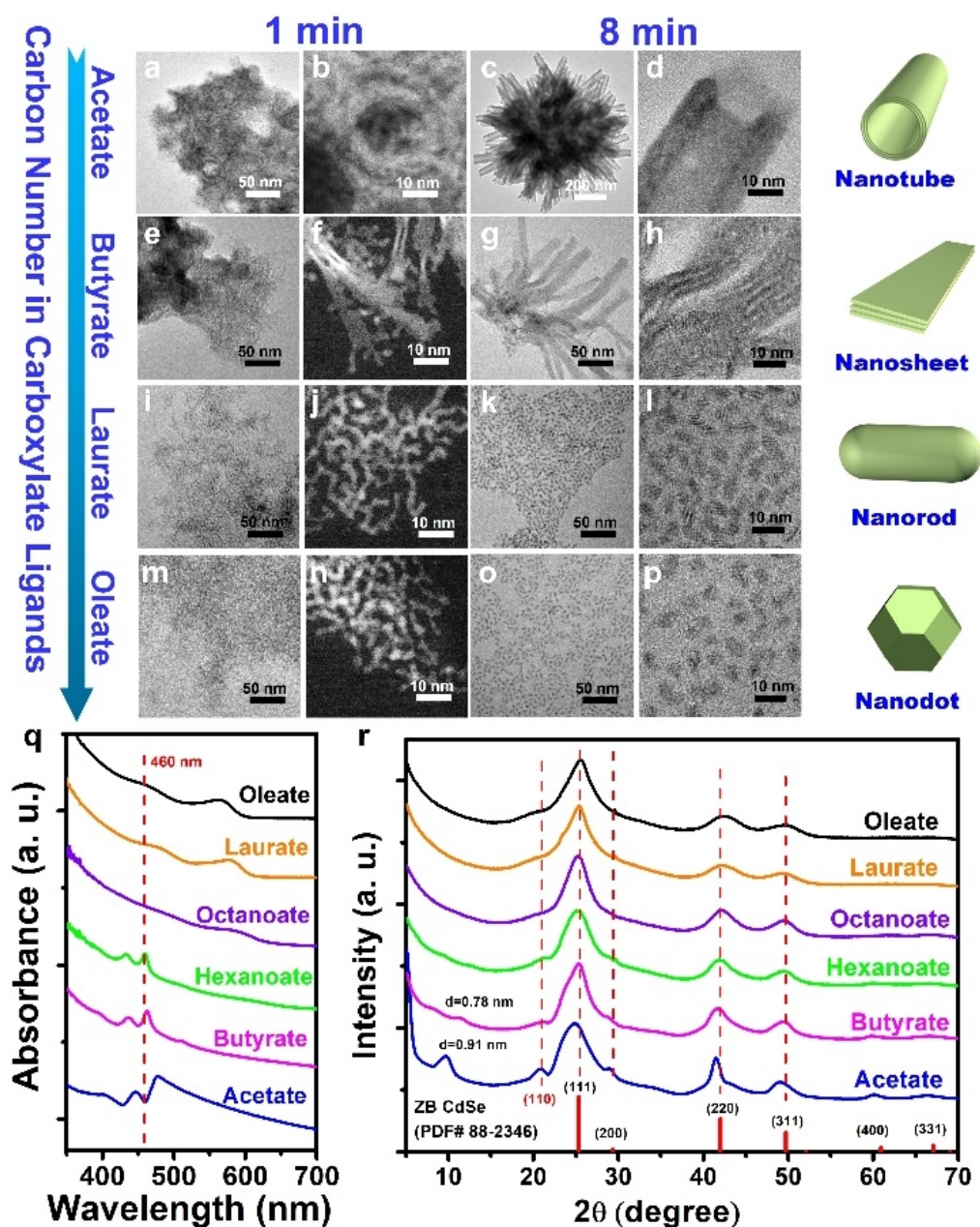


Figure 5.1 Optical, structural and morphological characterization of CdSe NCs synthesized in the presence of carboxylate ligands having different chain length. (a-p) TEM and STEM images of the CdSe NCs synthesized within (a, b, e, f, i, j, m, n) 1 min and (c, d, g, h, k, l, o, p) 8 min using various carboxylate ligands, including (a-d) acetate, (e-h) butyrate, (i-l) laurate, and (m-p) oleate. The schematic drawings on the right corresponds to the main nanostructures synthesized within 8 min. All the reactions were performed by reacting Cd(carboxylate)<sub>2</sub>-DOAm with TOP-Se in ODE at 260 °C. (q) UV-vis absorption spectra and (r) XRD powder diffraction pattern of the CdSe NCs synthesized within 8 min using various carboxylate ligands, including acetate (blue curve), butyrate (pink curve), hexanoate (green curve), octanoate (violate curve), laurate (orange curve), oleate (black curve) as the capping ligands.

All the CdSe NCs synthesized within 8 min had the zincblende crystal structure, as determined from XRD patterns in Figure 5.1r. In case of 0D and 1D CdSe NCs prepared by carboxylate ligands having a chain length longer than octanoate, the peak intensity and position agree well with the standard bulk structure. In contrast, the diffraction pattern of the NCs with atomically-flat thickness, including the nanotubes and nanosheets, has some distinguishable differences. Firstly, a (110) peak appears, which is forbidden in the zincblende structure because of systematic extinction. Secondly, the

(200), (220) and (400) peaks are much more pronounced. Thirdly, the main peaks, including (111), (220) and (311) peaks, shift to the low-angle direction. All these characteristics can be explained by the ultrathin thickness of NCs along  $\langle 100 \rangle$  direction which limits the periodicity in the thickness direction [109]. Moreover, clear peaks at around  $10^\circ$ , corresponding to layer spacings of 0.96 and 0.78 nm, were seen for the nanotubes and nanosheets respectively. This is consistent with the observed multiwalled structure in nanotubes and multilayered features in the nanosheets (Figure 5.1d,h).

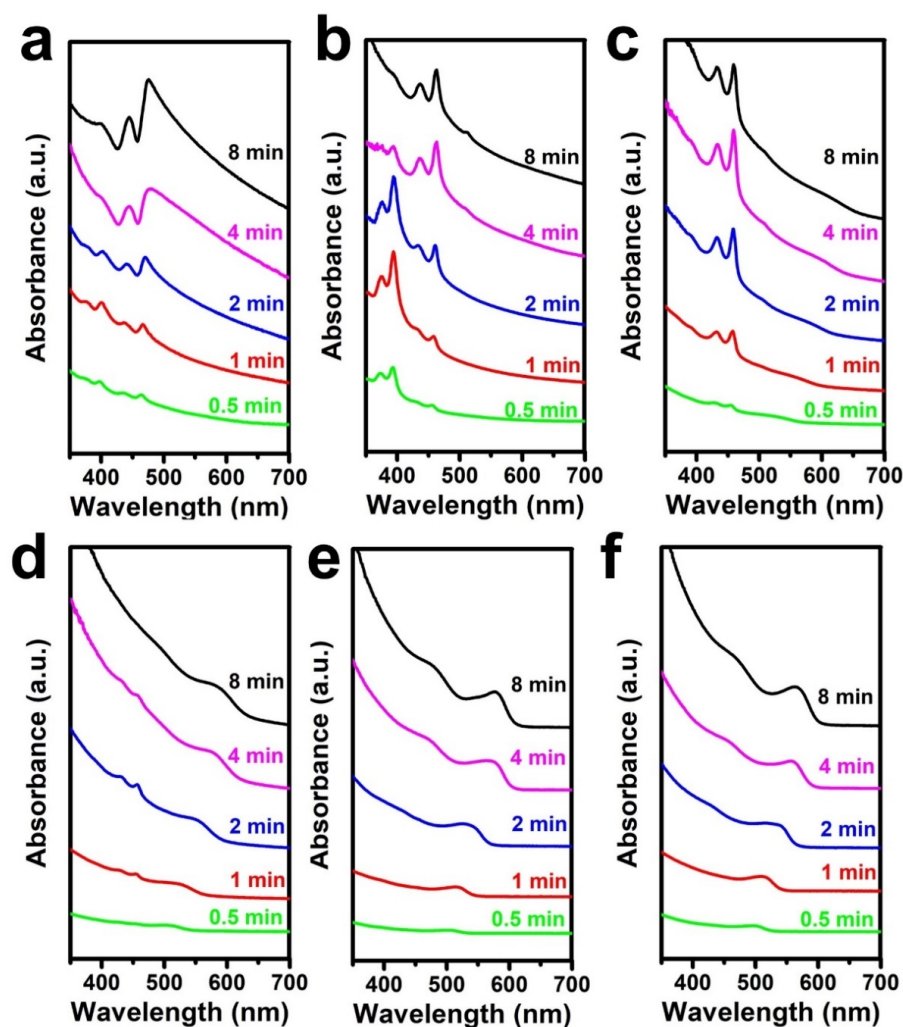


Figure 5.2 Temporal evolution of the absorption spectra of CdSe NCs synthesized in the presence of carboxylate ligands having different chain length, including (a) acetate, (b) butyrate, (c) hexanoate, (d) octanoate, (e) laurate and (f) oleate. All the reactions were performed by reacting  $\text{Cd}(\text{carboxylate})_2\text{-DOAm}$  with TOP-Se in ODE at  $260^\circ\text{C}$ .

To identify the crystallographic orientation of the CdSe NCs, HRTEM characterization was performed, as displayed in Figure 5.3. As expected, the lateral and angular extension directions of CdSe nanotubes prepared using acetate ligand are determined to be parallel to the  $\langle 011 \rangle$  direction, while the thickness direction is parallel to the  $\langle 001 \rangle$  direction (Figure 5.3c,d). In last chapter, we have demonstrated the existence of various crystal imperfections in this configuration. In CdSe nanosheets prepared using butyrate ligand, the thickness direction is also determined as the  $\langle 001 \rangle$  direction

(Figure 5.3g,h), similar to most of the reported 2D zincblende CdSe NCs. In this regard, considering a growth mechanism through particle attachment, the crystalline building blocks for these two anisotropic structures are proposed to be the same, mainly enclosed by passivated {100} facets and reactive {110} facets [116] [101]. In case of using acetate ligand where the solubility of cadmium precursor is very poor, the motion and rotation of the building blocks is highly constrained, thus resulting in tube-like nanostructure via lateral and angular attachment (Figure 5.3a). In case of using butyrate ligand where the solubility of cadmium precursor is relatively good, assembling the building blocks along the reactive {110} facets in lateral in-plane directions is favorable, eventually forming sheet-like nanoarchitecture after fusion and post-crystallization (Figure 5.3e). The situation of using laurate ligand is much more complicated, as both the chain-like nanostructures and branched nanorods were present in multiple forms. We mainly focused on analyzing the lattice fringe of the branched nanorods, which were more crystalized and suitable for HRTEM imaging. Although the assembly of building blocks were supposed to take place earlier than the formation of chain-like morphology, useful information of the building blocks would still be kept in the branched rod-like nanostructures. Figure 5.3 j-n demonstrate HRTEM images of several branched NCs, most of which can be viewed as the attachment of two or three building blocks along the {111} facets, even though a small chance of attachment along the {100} facets exists (bottom left corner of Figure 5.3n). In this regard, the crystallite building blocks should be enclosed with {111} and {100} facets, instead of the {110} and {100} facets as suggested in the case of nanotubes and nanosheets. In other words, two distinguishable crystalline building blocks exist when carboxylate ligands with different carbon chain were employed, resulting in two intrinsically different assembled NCs with either 1D or 2D anisotropic shapes. According to the short-axis direction of the nanorods, the building blocks were classified into two types: one is terminated with {100} facets and the other is terminated with {111} facets, as marked as the gold and green color in Figure 5.3i, respectively. Dot-like CdSe NCs prepared by using oleate ligands, as shown in Figure 5.3o, can be regarded as a polyhedron terminated with {111} and {100} facets.



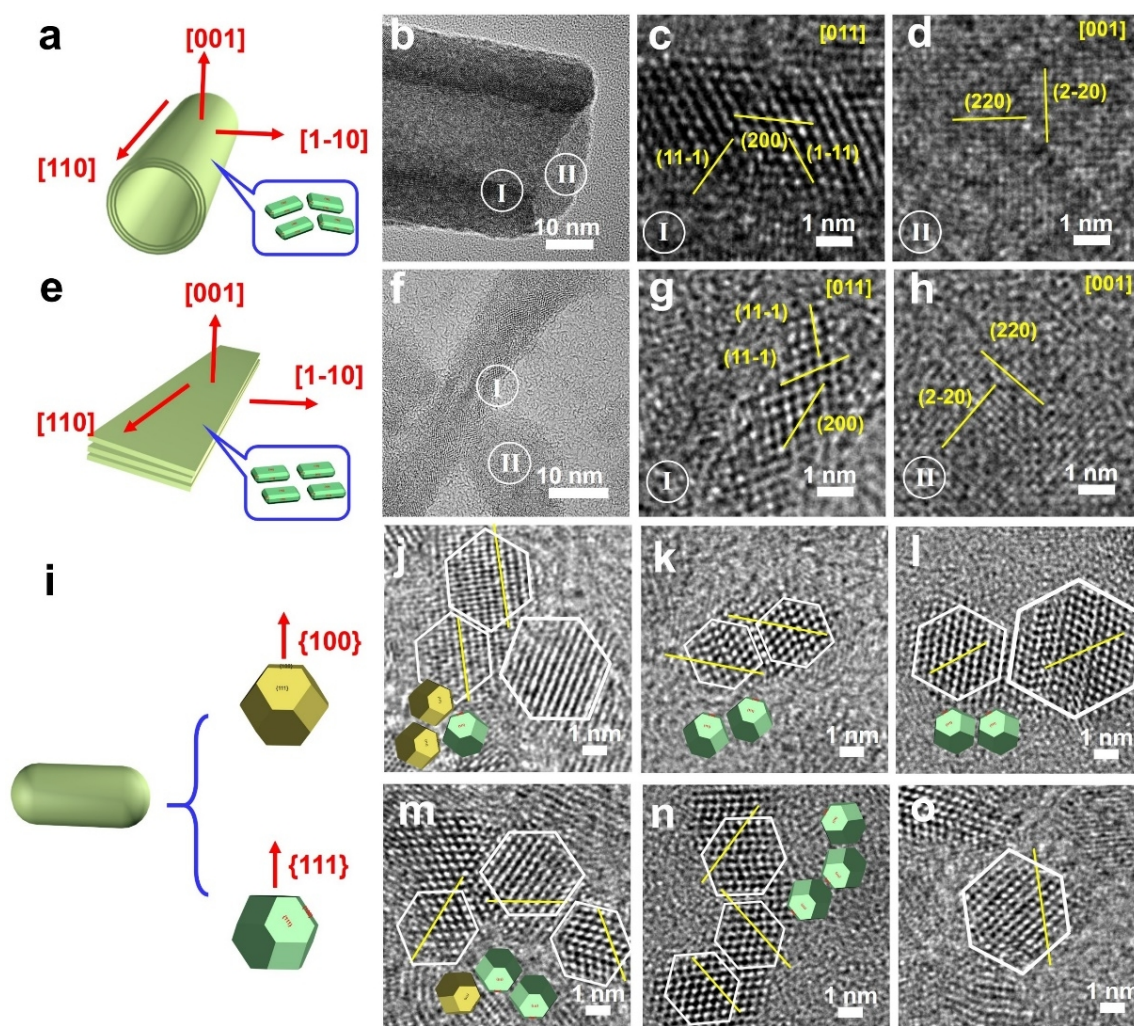


Figure 5.3 HRTEM characterization of crystallographic orientation in the as-synthesized CdSe nanotubes, nanosheets, nanorods and nanodots. (a-d) In a CdSe nanotube synthesized in presence of acetate ligand, its lateral and angular extension directions are in the  $\langle 110 \rangle$  direction, and the thickness direction is  $\langle 001 \rangle$  direction. (e-h) In a CdSe nanosheet synthesized in presence of butyrate ligand, its lateral extension directions are in the  $\langle 110 \rangle$  direction, and the thickness direction is in the  $\langle 001 \rangle$  direction. (i) Schematic illustration of the nanodot building blocks for branched CdSe nanorods, which is enclosed by  $\{100\}$  facets (gold) or  $\{111\}$  facets (green) in thickness direction. (j-n) Branched CdSe nanorods synthesized in presence of laurate ligand can be viewed as assemblies of nanodot building blocks along the  $\langle 111 \rangle$  direction (j-n) or  $\langle 100 \rangle$  direction (n, bottom left). (o) Zincblende CdSe nanodots synthesized in presence of oleate ligand. The yellow lines in (j-o) indicate the  $\{200\}$  facets of the nanodot building blocks.

## 5.2.2 Factors Triggering the Shape Conversion between 2D and 1D CdSe NCs

The above results clearly suggest that the shape of CdSe NCs can be varied between 2D and 1D anisotropic nanostructures using carboxylate ligands with different chain length. This phenomenon reminds us of the classical synthesis of branched CdSe nanorods, where the conversion between the spherical nanodots and branched nanorods can be implemented using alkyl phosphoric acid with different chain length [42, 79]. In that case, besides tuning the chain length of the alkyl ligand, changing the monomer concentration can also result in such a shape conversion behavior. In other words, a shape conversion between 2D and 1D NCs might also be achieved by varying the monomer concentration in our case, if that can be achieved by changing ligands. This hypothesis is supported by adjusting the concentration of both Cd(hexanoate)<sub>2</sub>-DOAm and TOP-Se precursors, as shown in Figure

5.4. At a low precursor concentration, branched and elongated nanorods were observed from the TEM imaging, together with the tunable absorption peaks after 550 nm indicating the quantum confinement effect (Figure 5.4a,e). No signal of 2D CdSe NCs was detected. As the precursor concentration was increased by a factor of 2, 4 and 16, we started to find some platelet-like nanostructures, which were developed into multilayered sheet-like nanostructures (Figure 5.4b-d). The characteristic absorption peak of 3.5-ML nanoplatelets at around 460 nm was detected by spectroscopy, and became more notable with the increase of the precursor concentration (Figure 5.4f-h). Since the monomer concentration is positively related with the precursor concentration, this data powerfully demonstrates that a high monomer concentration, or high chemical potential, is responsible for driving the 2D anisotropic growth of NCs, while 1D anisotropic growth is beneficial at a low monomer concentration. Considering the growth of NCs via a particle attachment approach, this implies the 2D and 1D crystalline building blocks are favorable at high and low monomer concentration, respectively (Figure 5.4 h).

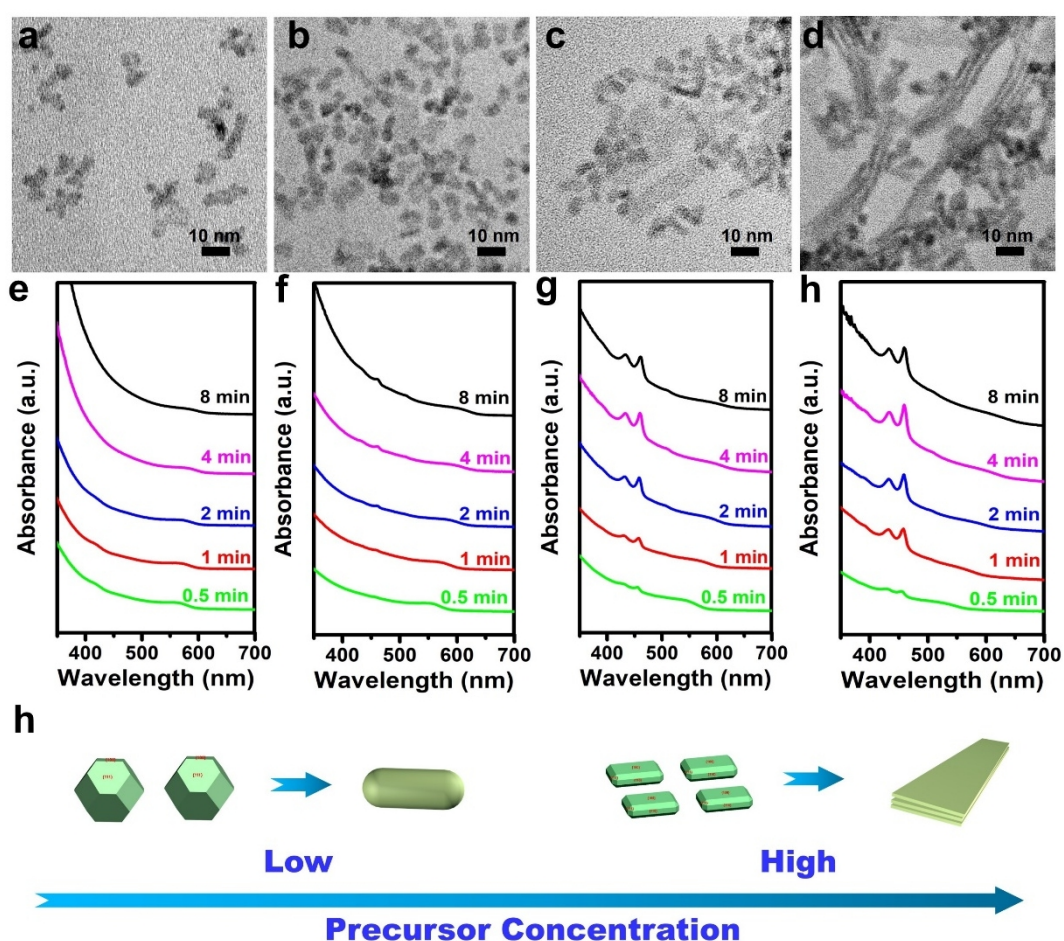


Figure 5.4 Morphological and spectroscopic characterization of CdSe NCs synthesized in the presence of hexanoate ligand at different precursor concentration. (a-d) TEM images and (e-h) UV-vis absorption spectra of CdSe NCs synthesized by reacting Cd(hexanoate)<sub>2</sub>-DOAm and TOP-Se in ODE at 260 °C. The samples used for TEM characterization were synthesized within 8 min. The added amount of Cd(hexanoate)<sub>2</sub>-DOAm is (a, e) 15.6, (b, f) 62.5, (c, g) 125, (d, h) 250 μmol, respectively. The molar ratio between Cd and Se precursor is fixed at 2.5:1.



Another factor influencing the shape conversion is the reaction temperature. Figure 5.5 shows the TEM images and UV-vis absorption spectra of CdSe NCs synthesized by reacting Cd(hexanoate)<sub>2</sub>-DOAm and TOP-Se in ODE at 140 °C, 200 °C and 260 °C. We can find the formation of multilayered platelet-like 2D CdSe NCs in all the three cases (Figure 5.5a-c). A characteristic absorption peak at around 390 nm corresponding to 2.5-ML nanoplatelets appeared at the temperature of 140 °C and 200 °C, and shifted to long-wavelength position at around 460 nm corresponding to 3.5-ML nanoplatelets at the temperature of 260 °C, suggesting the formation of thicker 2D CdSe NCs with the increase of reaction temperature. More importantly, tunable absorption peaks after 550 nm were observed in the sample synthesized 260 °C, together with some branched rod-like morphology, suggesting that high temperature facilitates the 1D anisotropic growth (Figure 5.5c,f). It is worth mentioning that hexanoate ligands provide an effective control between the 2D and 1D NCs because of its medium carbon chain, neither too short to induce purely 2D anisotropic growth like acetate nor too long to induce purely 1D anisotropic growth like oleate.

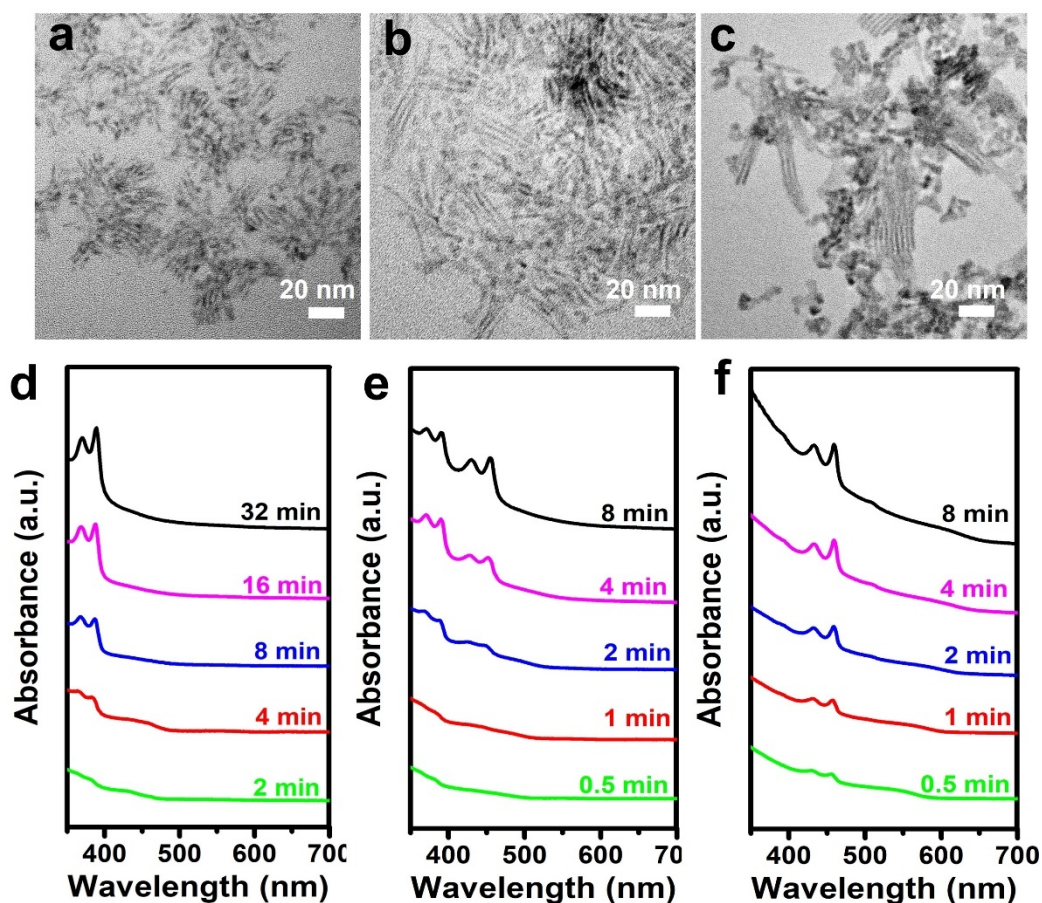


Figure 5.5 Morphological and spectroscopic characterization of CdSe NCs synthesized in the presence of hexanoate ligand at different reaction temperature. (a-c) TEM images and (d-f) UV-vis absorption spectra of CdSe NCs synthesized by reacting Cd(hexanoate)<sub>2</sub>-DOAm and TOP-Se in ODE at (a) 140 °C, (b) 200 °C and (c) 260 °C. The samples used for TEM characterization were synthesized within 8 min. The added amount of Cd(hexanoate)<sub>2</sub>-DOAm is 250 μmol, respectively. The molar ratio between Cd and Se precursor is fixed at 2.5:1.

### 5.2.3 DFT simulation of CdSe surface structure with and without carboxylate passivation

To understand the surface structure of zincblende CdSe NCs before and after passivated with the carboxylate ligands, density function (DFT) simulation was performed. A slab model in a vacuum box was employed to evaluate the surface energy of three low-index facets, namely the {100}, {111} and {110} facets. Using a generalized gradient approximation (GGA) functional, the slab geometry was optimized to a relaxed configuration, as shown in the top and side view of the of {100}, {111} and {110} surfaces in Figure 5.6a-f [120]. The top two layers of non-polar {110} surface shows an obvious rearrangement due to the ionicity of Cd-Se bonds, similar to previous reports [121, 122]. The surface energy was calculated based on the comparison of the relaxed slab geometry and bulk structure. As displayed in Figure 5.1k and Table 5.1, the calculated surface energy of the bare slab surface follows  $\gamma_{\{110\}} < \gamma_{\{111\}} < \gamma_{\{100\}}$ , suggesting {100} surface is most reactive while {110} surface is most inert. As surface energy intrinsically originates from the unsaturated surface dangling bonds, this trend is reasonable when comparing the dangling bond density on each surface, which shows a similar trend, that is, a large, medium and small density on {100}, {111} and {110} surfaces, respectively (Table 5.1).

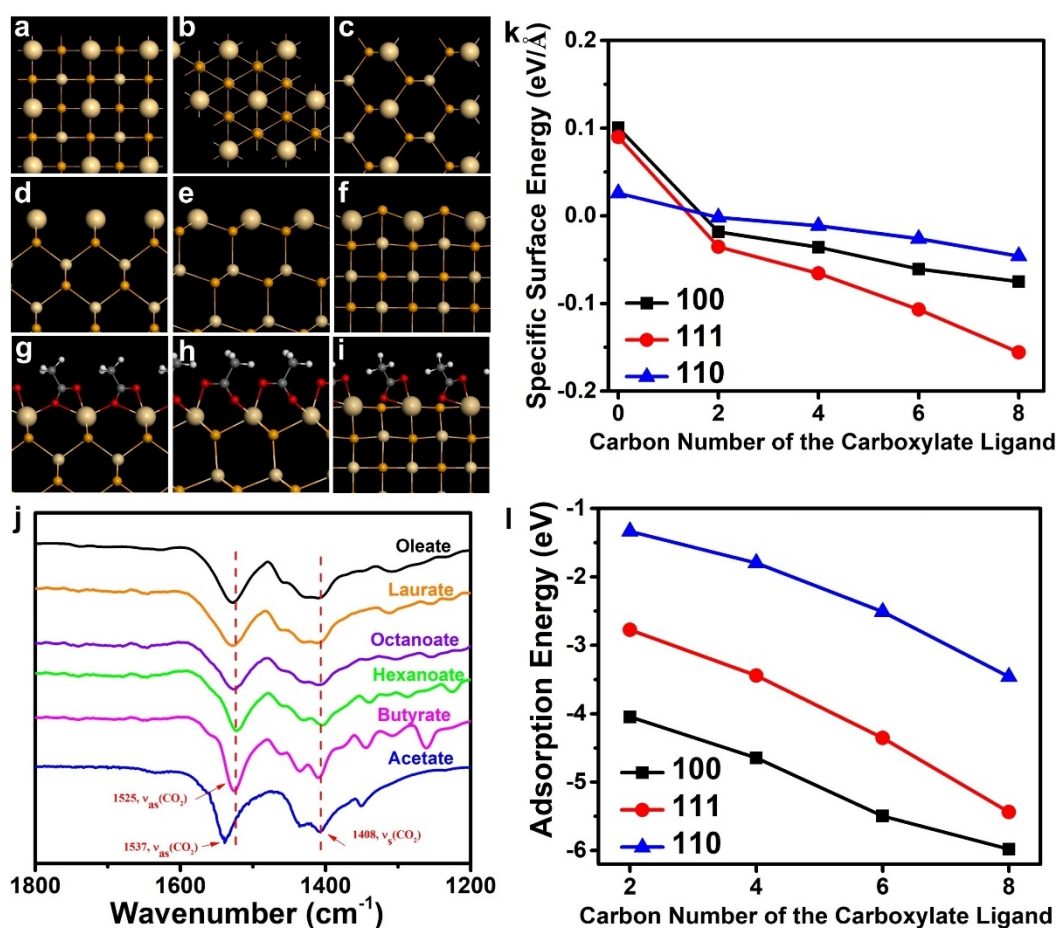


Figure 5.6 DFT simulation of surface structure of the zincblende CdSe slabs before and after passivated with different chain-length carboxylate ligands. (a-c) Top view and (d-f) side view of the relaxed (a, d) {100}, (b, e) {111} and (c, f) {110} slab surface of unpassivated CdSe NCs. (g-i) Side view of the relaxed surface structure of (g) {100}, (h) {111} and (i) {110} slabs after passivated with acetate ligand. The surface cadmium atoms are shown in larger size for easy recognition. (j) FTIR spectra of the CdSe NCs synthesized in the presence of different carboxylate ligands, including acetate, butyrate, hexanoate, octanoate, laurate and oleate. (k) The calculated surface energy and (l) adsorption

energy of {100} (square), {111} (circle), {110} (triangle) slab surface before passivation (carbon number of 0) and after passivated with carboxylate ligands having a carbon number of 2 (acetate), 4 (butyrate), 6 (hexanoate) and 8 (octanoate).

Slab	Surface area per CdSe unit ( $\text{\AA}^2$ )	Dangling bond density ( $/\text{\AA}^2$ )	Specific surface energy (unpassivated, $\text{eV}/\text{\AA}^2$ )	Specific surface energy (acetate passivating, $\text{eV}/\text{\AA}^2$ )
100	17.04	0.23	0.100	-0.018
111	11.07	0.18	0.090	-0.035
110	24.10	0.17	0.026	-0.002

Table 5.1 The surface area per CdSe unit, dangling bond density, surface energy of unpassivated and acetate-passivated surface of {100}, {111} and {110} slabs.

We then passivated the dangling bonds on the slab surface with the carboxylate ligand like acetate (Figure 5.6 g-i). Considering a case of full passivation for every surface cadmium atom, a distinct result of the surface energy was obtained, showing that  $\gamma_{\{111\}} < \gamma_{\{100\}} < \gamma_{\{110\}}$ . In other words, after capped with the acetate, the originally inert {110} surface became the most reactive one, while the originally reactive {100} and {111} surfaces turned to be more stable. This change is attributed to the different adsorption energy on each surface. As shown in Figure 5.6l, the adsorption energy of acetate is largest on the {100} surface, medium on the {111} surface and smallest on the {110} surface. This reveals that the originally reactive surface attracts the ligands more strongly, resulting in a drastic decline of surface energy. The optimized binding state of the carboxylate group on each surface is also different, showing a bridging and chelating mode for the {100} surface, a bridging mode for the {111} surface and a chelating mode for the {110} surface, respectively. This is in accord with FTIR characterization, which demonstrates the acetate coordinating to the surface of CdSe nanotubes in a bridging and chelating mode, as deduced from a difference of  $129\text{ cm}^{-1}$  between antisymmetric and symmetric stretching vibration (Figure 5.6 j) [123].

Furthermore, the slab surface was passivated with longer-chain carboxylate ligands including butyrate, hexanoate and octanoate for comparison (Figure 5.7). As shown in Figure 5.8, the calculated adsorption energies present a rising trend with the increase of ligand chain. We speculated this was a result of enhanced steric stabilization effect coming from the alkyl chain that made the passivated surface more stable, thus resulting in higher adsorption energy. Through calculating the energy of the relaxed carboxylates in a vacuum box, we were able to separate the adsorption energy into two contributing parts: the binding energy and the inter-ligand interaction (see experimental section). The former originates from the coordination bonding between a carboxylate group and a surface cadmium atom, and the latter mainly results from steric interaction between the alkyl chains of the ligand. As shown in Figure 5.8, we can find that with increasing chain length the binding energy shows little change, while the inter-ligand interaction exhibits an evident rise, especially for {111} facets which have the smallest surface area per molecule unit (Table 5.1). As a result of the increasing adsorption energies, the surface energies of the passivated slab surfaces showed a continuous decrease when longer-chain carboxylate was used (Figure 5.1j). Even so, they all exhibit the same relationship among the {100}, {111} and {110} slab surfaces, that is,  $\gamma_{\{111\}} < \gamma_{\{100\}} < \gamma_{\{110\}}$ . The optimized configurations of carboxylate groups binding to cadmium are also quite similar to the case of acetate passivation, showing a bidentate bridging and/or chelating mode. FTIR spectra present a difference of  $117\text{ cm}^{-1}$  between the



antisymmetric and symmetric stretching vibration, smaller than the  $129\text{ cm}^{-1}$  formed in the case of acetate ligand, indicating that the portion of binding in the bridging mode is reduced, which is presumably due to the enhanced steric effect (Figure 5.6k). It should be noted that in view of an assumption of full passivation, namely, passivating each surface cadmium atom with one carboxylate, the obtained surface energies of passivated surfaces are all negative. This situation might be difficult to be achieved in practical conditions, especially for long-chain ligands having great steric hindrance effect. However, we believe the simulation results under this ideal situation can still well reflect the trend of surface energy change in the presence of different carboxylate ligands.

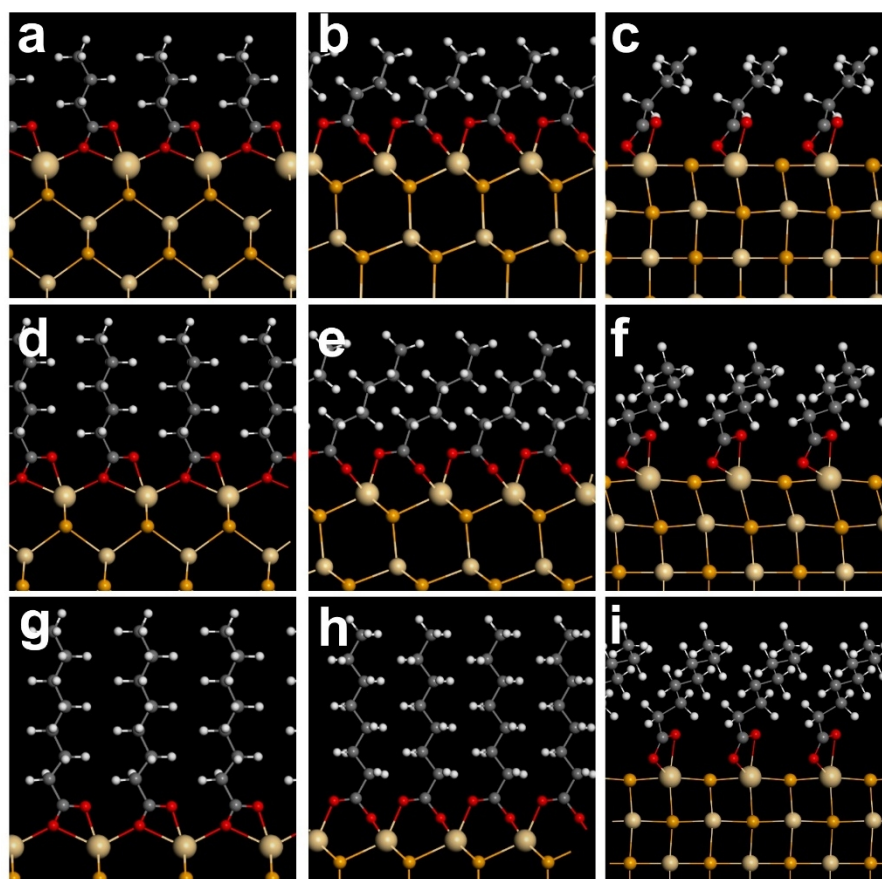


Figure 5.7 Side view of the relaxed surface structure of (a,d,g) {100}, (b,e,h) {111} and (c,f,i) {110} slabs after passivated with (a-c) butyrate, (d-f) hexanoate and (g-i) octanoate, obtained by DFT simulation.

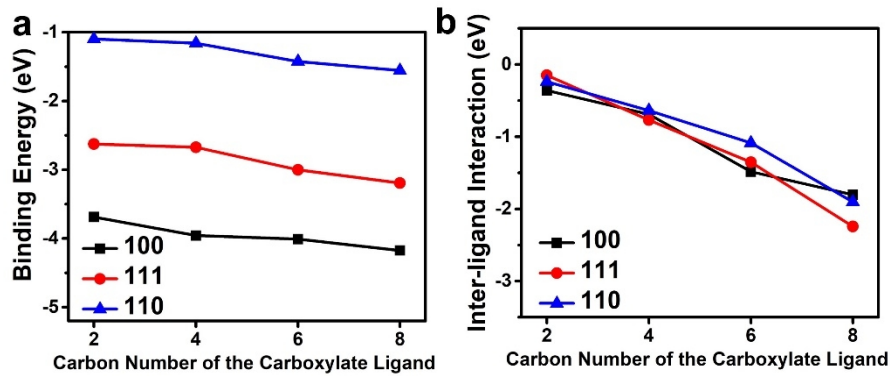


Figure 5.8 (a) The calculated binding energy and (b) inter-ligand interaction of {100} (triangle), {111} (circle), {110} (square) slabs surface after passivated with carboxylate ligands having a carbon number of 2 (acetate), 4 (butyrate), 6 (hexanoate) and 8 (octanoate).

## 5.2.4 Formation Mechanism of Intrinsically Different Building Blocks

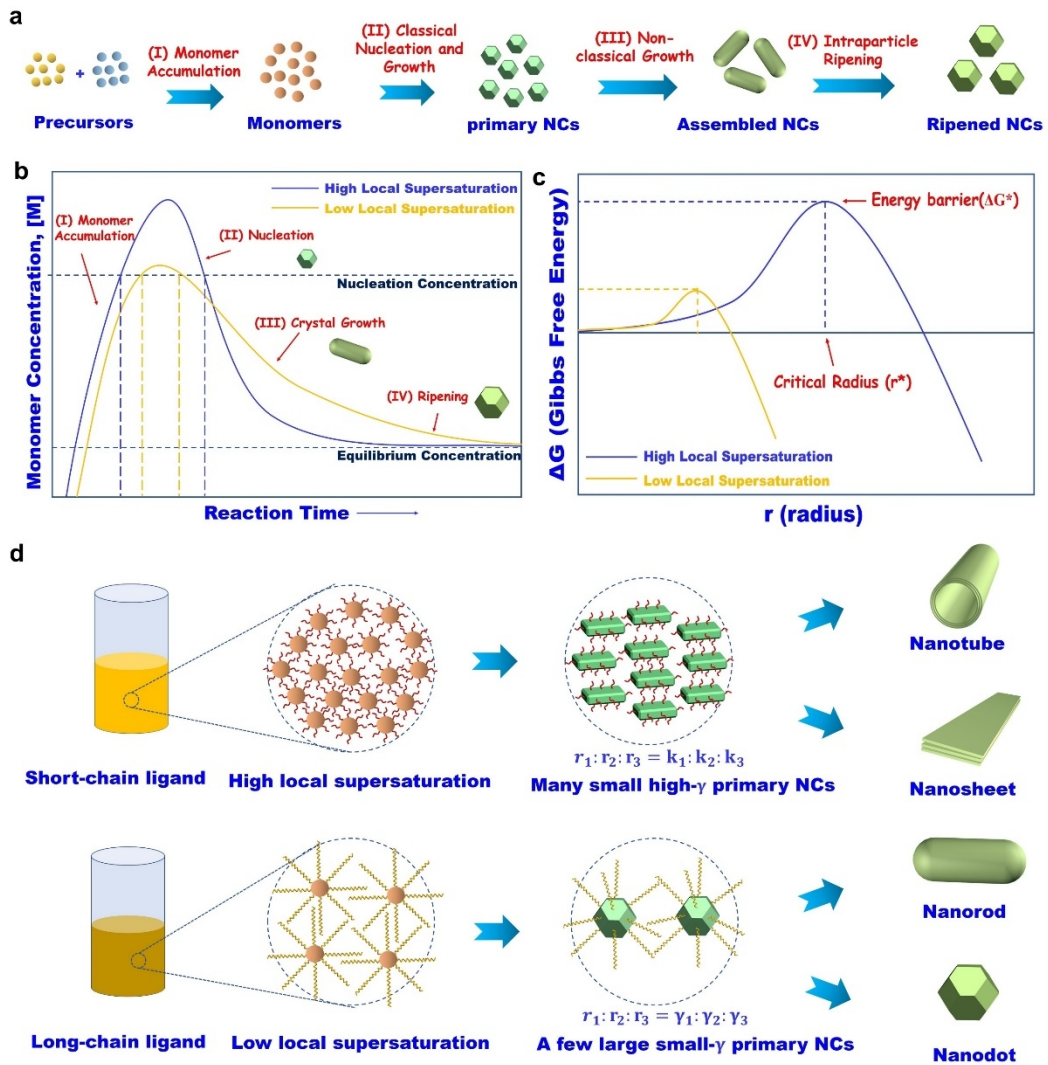


Figure 5.9 Schematic illustration showing the formation mechanism of the anisotropic CdSe NCs. (a) The proposed formation process for the anisotropic growth of NCs via a non-classical particle-mediated growth. (b) Formation process the anisotropic growth of NCs based on the La Mer model, in which the blue and yellow curves correspond to a high and low local monomer supersaturation, respectively. (c) The

change of Gibbs free energy with the increase of NC size, in which the blue and yellow curves correspond to a high and low local monomer supersaturation, respectively. (d) Short-chain ligands cause high local monomer supersaturation, promoting the formation of a large number of kinetically stable primary NCs with reactive facets. On the other hand, long-chain ligands induce low local supersaturation, favoring the formation of a few number of thermodynamically stable primary NCs with small surface energy ( $\gamma$ ).

To explain the shape evolution of CdSe NCs observed in this study, especially the data in Figure 5.1, a proposed formation process showing the critical stages during the anisotropic growth of NCs involving a non-classical particle-mediate growth is schematically illustrated in Figure 5.9a. In which the growth of nanodots in the presence of oleate ligand is used as an example. The process starts from the conversion of the precursors to monomers (stage I), followed by the nucleation and growth into early-stage NCs after reaching the nucleation limit (stage II). These NCs, named as primary NCs, act as the role of building blocks which could evolve into assembled NCs via an attachment, rearrangement and post-crystallization process once the thermodynamically and kinetically condition allow (stage III) [54, 55]. Once the monomer concentration is lowered, the assembled NCs become less stable and gradually turn into more thermodynamically ripened NCs via intraparticle ripening (stage IV). Basically, this process can also be described by the classical LaMer model, as shown in Figure 5.9b. Noted that in the nucleation stage the growth of NCs is not fully excluded, as observed by the coexistence of the nucleation and growth stage in many examples of the CdSe NCs synthesis [91, 124]. In this way, the chain-like nanostructures in Figure 5.1m,n and dot-like nanostructures in Figure 5.1o,p, both synthesized in the presence of oleate, can be ascribed as assembled NCs and ripened NCs, respectively. In comparison, the platelet-like aggregates in Figure 5.1a,b and the nanotubes in Figure 5.1o,p, both synthesized in the presence of acetate, are attributed as primary NCs and assembled NCs, respectively. This suggests the use of acetate leads to a longer period of non-classical growth, which points to the possibility of higher monomer concentration when short-chain ligand was used.

The growth of NCs via particle-mediated approach does not exclude the concurrence of the classical monomer-mediated growth, which is supported by the evolution of CdSe nanosheets from a thickness of 2.5 MLs to 3.5 MLs in Figure 5.2b and the continuous redshift of the first adsorption peak in CdSe NCs synthesized using octanoate (Figure 5.2d), laurate (Figure 5.2e) and oleate (Figure 5.2f) ligand. In fact, the classical growth approach plays an important role in determining the shape of primary NCs. According to the classical diffusion-reaction growth model, a NC growing in the diffusion-controlled regime would adopt a thermodynamically stable Wulff shape, as shown in Equation 1.29, that is

$$r_1:r_2:r_3 = \gamma_1:\gamma_2:\gamma_3$$

where  $\gamma_i$  and  $r_i$  are the surface energy of  $i$ th facet and its growth distance, respectively. In this case, NCs formed in this condition are inclined to expose the facets with low surface energy to minimize the total surface energy. On the other hand, the shape of a NC growing in the reaction-controlled regime would be kinetically stable, relying on the growth rate of each facet, as shown in Equation 1.28, such as

$$r_1:r_2:r_3 = k_1:k_2:k_3$$

where  $k_i$  is the growth rate constant of the  $i$ th facet. Generally,  $k_i$  is inversely proportional to the adsorption of the surface ligand. Accordingly, the growth of a facet with strong ligand adsorption would be extremely inhibited while a facet weakly passivated with ligand would grow in a preferential way.

The DFT simulation results above suggest that the primary NCs that are mainly enclosed by {100} and {110} facets, obtained by using short-chain ligands, are kinetically stable and energetically unfavorable, while those enclosed by {100} and {111} facets, acquired by using long-chain ligands, are more thermodynamically stable. Based on the experimental result and the theoretical simulation, we propose that carboxylate ligands are able to control the growth kinetics of building blocks during the growth of CdSe NCs involving a particle attachment approach: short-chain ligands facilitate the crystal growth in a reaction-limited mode, thus forming kinetically stable primary NCs, whereas long-chain ligands benefit to the crystal growth in a diffusion-limited mode, eventually resulting in kinetically stable primary NCs.

Acids	Partition coefficient (logP <sub>oct/wat</sub> )
Acetic acid	0.09
Butyric acid	0.87
Hexanoic acid	1.65
Octanoic acid	2.43
Lauric acid	3.99
Oleic acid	6.11
1-octadecene	7.04

Table 5.2 Partition coefficient (logP<sub>oct/wat</sub>) of carboxylic acids with different chain length and the solvent, ODE.

The key point of producing different growth models for the BB NCs is that the addition of short-chain ligand, even with the same precursor and ligand concentration to the case of long-chain ligand, would lead to a high local monomer concentration, or monomer supersaturation due to 1) low compatibility with the solvent and 2) a low steric hinderance effect (Figure 5.9d). The first reason is that short-chain carboxylic acids is more polar and less lipophilic, therefore difficult to be mixed with the non-polar ODE solvent, as supported by the partition coefficient listed in Table 2. This leads to very poor dispersion of CdSe NCs in solvent once passivated with short-chain ligands, as known from the easy aggregation of CdSe nanotubes (Figure 5.1g, h) and nanosheets (Figure 5.1g, h). Consequently, in the place where monomers exist, the local concentration would be very high. The second reason is involved with chain length of the ligand. According to the Tanford formula, the full extensional length of an acetate and an oleate is 0.4 and 2.4 nm, respectively [108]. Apparently, in a given volume, the allowed monomer concentration in the presence of short-chain ligand would be much higher than that in the presence of long-chain ligand. This is also the reason why we cannot obtain 2D CdSe just based on oleate ligand, even if no solvent is used. The steric effect could also inhibit the contact between monomers, making the diffusion process more a rate-limiting step. In contrary, the high monomer concentration induced by short-chain ligand favors the rapid mass exchange between monomers in a confined space, causing the surface reaction more a key factor for further growth. Besides, according to the classic nucleation and growth theory, a higher monomer supersaturation helps in producing more smaller nuclei as a result of reduced nucleation barrier higher and increased nucleation period, as

illustrated in Figure 5.9c,d, which would in turn suppress the growth via monomer addition. On the other hand, particle-mediated growth would be greatly promoted as its rate constant is second order of the concentration of primary NCs [125]. This further explains the observation of nanotubes and nanodots within a reaction time of 8 min by using acetate and oleate, respectively.

## 5.3 Experimental Section

### 5.3.1 Synthetic Methods

**Materials.** Cadmium oxide (CdO), 1-octadecene (ODE), acetic acid (99% purity), hexanoic acid (98% purity), octanoic acid (98% purity), lauric acid, oleic acid (98% purity), dioctylamine (97% purity, DOAm), trioctyl phosphine (TOP, 97% purity), selenium powder (Se), methanol, hexane, ethanol and dichloromethane were purchased from Sigma-Aldrich. Butyric acid was provided from Fluka (98% purity). All chemicals were used without further purification.

**Preparation of precursors.** Before the synthesis of the CdSe NTs, the Cd precursor solutions with different carboxylate ligands were prepared in advance. Typically, 128 mg (1.00 mmol) of CdO powders were mixed with 2.5 mmol of carboxylic acids including acetic acid, butyric acid, hexanoic acid, octanoic acid, lauric acid and oleic acid in a 5 mL vial, vigorously vibrated for 5 min and then heated at 200 °C until clear solution formed. Cadmium acetate would obtain in the form of white powder. Afterwards, 1.2 mL (4 mmol) of DOAm solution was added and the mixture was heated for 5 min to get clear solution, which was labeled as "Cd(carboxylate)<sub>2</sub>-DOAm solution". A stock TOP-Se solution was prepared by injecting the trioctylphosphine (TOP) with (a ratio of 1:1 between Se and TOP) into the selenium powder under the protection of argon atmosphere, followed by dilution using ODE to a concentration of 0.5 M. It was kept stirring for more than 12 hours to ensure complete dissolution and finally stored in refrigerator.

**Synthesis of CdSe NCs in the presence different carboxylate ligands.** For a typical CdSe NC synthesis, 200 μL of TOP-Se powder was mixed with in 3.6 mL of ODE and stirred at 260 °C for 5 min, after which 0.3 mL of Cd(carboxylate)<sub>2</sub>-DOAm Solution (a molar ratio of 2.5:1 between Cd and Se) was quickly injected. The reaction was kept at 260 °C for a given time. Aliquot volumes of the solution were fetched at different time interval for further analysis. For the purification, NCs prepared by Cd(acetate)<sub>2</sub>-DOAm and Cd(butyrate)<sub>2</sub>-DOAm were mixed with hexane, and centrifuged at a speed of 3000 rpm for 3 min. NCs prepared by other cadmium precursors, in which OD/1D NCs were included, were mixed with a solution containing dichloromethane and methane (1:1, v/v) and centrifuged at a speed of 4000 rpm for 5 min. After the purification, the precipitates were dispersed in hexane for further characterization.

### 5.3.2 Characterization

UV-vis absorption spectroscopy was performed on a Varian Cary 50 Scan UV-vis spectrophotometer. Transmission electron microscopy (TEM) graphs, high-resolution TEM (HRTEM)

graphs, selected area electron diffraction (SAED) patterns, scanning transmission electron microscopy (STEM) images and energy-dispersive x-ray spectroscopy (EDX) images were captured by a Talos transmission electron microscope (FEI Co.) and a Titan Themis (FEI Co.); prior to that, the CdSe NCs dissolved in hexane were dropped and dried on ultrathin carbon-supported copper grids. Powder X-ray diffraction (XRD) measurement was performed on Empyrean with Cu LEF sealed tube and Pixcel1D detector from PANalytical. Fourier-transform infrared (FTIR) spectra were recorded by a Nicolet iS10 FT-IR Spectrometer (Thermo Scientific) equipped with a smart diamond attenuated total reflectance (ATR) accessory.

### 5.3.3 DFT simulation

The DFT simulation was performed using a DMol 3 program embedded in Materials Studio (Accelrys Co.). A generalized-gradient approximation (GGA) with the PW91 functional, together with using a double numerical plus polarization (DNP) basis set and an effective core potentials (ECP) treatment, was used for the calculation. A dispersion correction was employed using PW91-OBS modules in view of the presence of non-covalent interaction between carboxylate molecules. Regarding to the geometry optimization, the convergence tolerance of energy is 0.00027 eV per atom, and the maximum allowed displacement and force are 0.005 Å and 0.054 eV/Å, respectively. For the bulk zincblende CdSe structure, we obtained a calculated lattice constant of 6.17 Å, which is close to the experiment constant of 6.05 Å. We built slab of {100}, {110} and {111} surfaces in a vacuum box, where a spacing of 30 Å between the slabs was applied to avoid the interaction of slab in the thickness direction. Each of the slab was consisted of 6 Cd and 6 Se atoms. A k-point mesh of 6 × 6 × 1 and 6 × 6 × 6 was used for the calculation of the bulk crystal and slab structure, respectively. The surface energies were calculated by comparing the difference between the optimized energy of the bulk and slab structure with same cadmium and selenide atoms, that is,

$$E_{\text{surface}} = \frac{(E_{\text{slab}} - nE_{\text{b}})}{2A}$$

Equation 5.1 Formula used for the surface energy calculation of bare surface.

where A is the surface area of the slab structure, n is number of the CdSe unit in the slab, E<sub>b</sub> is the bulk energy per unit cell, E<sub>slab</sub> is the total energy of the slab. The factor of 1/2 is used in consideration of the top and bottom surface of the slab. After passivating the slab surface with carboxylate ligands, the surface energy calculation was modified as

$$E_{\text{surface}} = \frac{(E_{\text{passivated}} - nE_{\text{b}} - E_{\text{carboxylate}})}{2A}$$

Equation 5.2 Formula used for the surface energy calculation of carboxylate-passivated surface.

where E<sub>passivated</sub> is the total energy of the passivated slab with different carboxylates. E<sub>carboxylate</sub> is the total energy of the carboxylate molecule. The calculation of adsorption energy (E<sub>adsorption</sub>) was based on the following formula,

$$E_{\text{adsorption}} = (E_{\text{passivated}} - E_{\text{slab}} - E_{\text{carboxylate}})$$

Equation 5.3 Formula used for adsorption energy calculation.

Noted that this adsorption energy includes the contribution of the VdW interaction between neighboring carboxylate ligands. To offset the inter-ligand interaction,  $E_{\text{carboxylate}}$  was replaced by  $E'_{\text{carboxylate}}$ , which is the total energy of the carboxylate molecule in the vacuum box after removing the slab structure. In this case, only the coordination interaction between the carboxylate group and surface Cd is considered, which leads to the expression of binding energy ( $E_{\text{binding}}$ ), that is,

$$E_{\text{binding}} = (E_{\text{passivated}} - E_{\text{slab}} - E'_{\text{carboxylate}})$$

Equation 5.4 Formula used for binding energy calculation.

The contribution of VdW interaction between neighboring carboxylate ligands ( $E_{\text{inter-ligand}}$ ) can be thus calculated based on the comparison between adsorption energy and binding energy, that is,

$$E_{\text{inter-ligand}} = E_{\text{adsorption}} - E_{\text{binding}}$$

Equation 5.5 Formula used for inter-ligand interaction calculation.

## 5.4 Conclusions

In this part, we mainly studied the shape evolution using a  $\text{Cd}(\text{carboxylate})_2$  and a TOP-Se precursor, where carboxylate ligands with different chain length were used. A morphological transition from nanotubes and nanosheets to irregular nanorods and finally to QDs were observed for samples synthesized within a reaction time of 8 min when the carbon number of carboxylate ligands increased from 2 to 18. The further characterization of sample synthesized within a reaction time of 1 min suggests the all the CdSe NCs are formed via a non-classical particle-mediate growth approach, where two kinds of crystalline building blocks exposed by different facets are found. A conversion from 2D to 1D/0D CdSe NCs can be achieved by using a medium-chain carboxylate ligand at different concentration and temperature. DFT simulation results reveal one of the building blocks is kinetically stable, while the other is thermodynamically stable. Combining the experimental results and the theoretical models, we proposed short-chain ligands can induce a high local monomer supersaturation, facilitate the crystal growth in a reaction-limited mode, thus forming kinetically stable building blocks; whereas long-chain ligands benefit the crystal growth in a diffusion-limited mode, eventually resulting in kinetically stable building blocks.





# Chapter 6 Conclusion

## 6.1 Main results achieved in this thesis

In this thesis, we tried to explore a mysterious and amazing world on the scale of a nanometer, where extremely tiny CdSe NCs could engender and grow into various shapes resulting from homogenous solution. We investigated the shape and size evolution of NCs in the presence of two important organic capping ligands, carboxylates and amines, addressing questions such as how many of them appeared in an environment with limited sources, how they competed with each other to grow, what shapes they would grow into, what the underlying mechanism was that determined their growth and so on. As a result, NCs with a diversity of shapes have been obtained, such as nanodots, nanorods, nanotetrapods, nanotubes, nanosheets, nanoplatelets and chain-like nanostructures. Based on the experimental observations and theoretical models discussed from chapter 2 to 5, some major achievements that might contribute to the field of colloidal nanochemistry can be summarized as follows.

First of all, carboxylate ligands play a crucial role in controlling the shape of NCs, which can be manipulated by varying the chain length of the ligands. As demonstrated in chapter 2, 4 and 5, the use of short-chain carboxylate ligands would result in nanorods, nanotetrapods, nanosheets, nanotubes and other non-spherical morphologies. Single use of long-chain carboxylate ligands, or together with long-chain primary amines can produce high-quality CdSe QDs (chapter 2 and 3). The underlying mechanism, as shown in chapter 5, is mainly due to the variation of local monomer supersaturation, which cause the growth of NCs in a reaction-limited mode or diffusion-limited mode. The former allows the formation of more kinetically stable anisotropic nanostructures, while the latter leads to more thermodynamically stable isotropic morphologies.

Second, alkylamines play an important auxiliary role in determining the shape of NCs. As shown in chapter 4, in the case of cadmium acetate precursor, the addition of medium-chain amines with different branched chains, including primary amine, secondary amine, and tertiary amines, results in nanobelts and well-defined and ill-defined nanotubes, respectively. Moreover, the chain length of amine also matters. Using long-chain primary amine results in large-size nanoparticle aggregates, which is quite distinct from the nanobelts obtained by using medium-chain primary amine. These phenomena can be ascribed to the different coordination ability of the amines to the cadmium center, thus influencing the solubility of the precursor at different degrees. A good solubility of the precursor helps in the isotropic growth of the NCs, while a bad solubility of the precursor normally produces unwanted inhomogeneous NCs due to the poor mass transfer between precursors.

Third, the combined use of long-chain carboxylate ligands and long-chain amine ligands plays a synergistic effect in producing high-quality spherical NCs. As seen from chapter 2, single use of long-chain carboxylic acids or long-chain primary amines typically leads to anisotropic NCs with poor optical quality. With the aim of synthesizing high-quality spherical QDs, an optimum choice is to simultaneously use both long-chain carboxylate ligands and long-chain primary amines, which is also shown in chapter 3.

Fourth, primary amine ligands play a dual role in determining the nucleation and growth of QDs, which is based on the amount they are added. As indicated in chapter 3, at high amine concentration, the precursor reaction would be inhibited to some degree, resulting in less NC concentration and relatively faster growth rate, which is known as passivation effect. In contrast, at low amine concentration, the precursor reaction is weakly affected, while the nucleation is highly improved, eventually leading to NCs with smaller size, which is named as nucleation promoting effect. These results also imply we cannot judge the precursor reactivity just based on the growth rate of QDs, as the growth rate might also be severely influenced by the nucleation rate.

Fifth, combined use of long-chain and short-chain carboxylate ligands provides an interesting strategy to control the shape of NCs. Their synergistic effect has been widely recognized in the classical approach of synthesizing zincblende 2D CdSe NCs. In a sense, their combined role can be regarded as a medium-chain carboxylate ligand, as we also obtained 2D CdSe NCs by using medium-chain carboxylate in chapter 5. However, this strategy is more controllable and flexible due to the capacity of varying the ratio between long-chain and short-chain carboxylate ligands. In chapter 2, we observed the formation of branched nanorods including nanotetrapods by this mean, which suggests there is plenty of room for obtaining more complicated anisotropic NCs through this approach.

Last but not least, non-classical particle attachment approach provides an important approach towards more complex anisotropic NCs. Chapter 5 clearly displays various anisotropic NCs grown by this approach. In particular, we have demonstrated the possibility to produce CdSe nanotubes with atomically uniform walls via 2D non-planar attachment of early-formed nanoplatelets, which is a template-free route and inaccessible by other techniques to date.

## 6.2 Future development

The important findings in this thesis on the shape and size control of CdSe NCs by carboxylate and amine ligands might future trigger interests in nanochemistry field to explore more anisotropic shapes, seek more size control strategies, investigate more roles of surface ligands and develop deeper understanding of crystal growth. Some outlooks and promising directions worthy to be studied are shown below.

First, the proposed mechanism in chapter 5 that short-chain carboxylate ligand is favorable for the formation of kinetically stable anisotropic NCs and building blocks for more complicated

morphologies can be tested in other ligand systems like phosphoric acid, thiol and chloride as well as and other colloidal NCs like metal and metal oxide NCs. The further understanding of the applicability of this mechanism would extremely boost the development of synthesizing anisotropic NCs.

Second, as demonstrated in chapter 4, multiwalled CdSe nanotubes were obtained in a template-free way by a 2D non-planar oriented attachment approach. It remains to be demonstrated that if this method can be applied to NCs made of other materials. Moreover, studies on preparing monodisperse CdSe nanotubes with atomically uniform multiple walls and single wall are of great importance to expand the application of these novel nanostructures.

Third, in chapter 3, we demonstrated the size-focusing effect when additional reagents were injected after the nucleation, which was suggested due to the supersaturation quenching that separates the nucleation and growth stages. Taking advantage of the concept of superstation quenching, a promising outlook is investigating that if more size-focusing strategies aiming at monodisperse high-quality spherical NCs can be found.

Fourth, the synergistic effect on synthesizing QDs with better optical quality has been observed by the combined use of a long-chain carboxylate ligand and a long-chain primary amine ligand in chapter 2. Considering carboxylates and alkylamines are categorized to X-type and L-type ligands respectively, the test of the generality of such a concept by other ligand combination systems is of great practical significance for industrial production of QDs or other spherical NCs.

Lastly, as mentioned in section 6.1, both 1D branched nanorods and 2D nanoplates are reported to be obtainable by simultaneously using short-chain and long-chain carboxylates ligands. The high turnability and flexibility of strategy can be exploited to find more fascinating anisotropic nanostructures.



# References

1. Bera, D., et al., *Quantum dots and their multimodal applications: a review*. *Materials*, 2010. 3(4): p. 2260-2345.
2. Peng, X., J. Wickham, and A. Alivisatos, *Kinetics of II-VI and III-V colloidal semiconductor nanocrystal growth: "focusing" of size distributions*. *Journal of the American Chemical Society*, 1998. 120(21): p. 5343-5344.
3. Rogach, A.L., *Semiconductor nanocrystal quantum dots*. Synthesis, Assembly, 2008.
4. Alivisatos, A.P., *Perspectives on the physical chemistry of semiconductor nanocrystals*. *Journal of Physical Chemistry*, 1996. 100(31): p. 13226-13239.
5. Wang, F., et al., *Two-dimensional semiconductor nanocrystals: properties, templated formation, and magic-size nanocluster intermediates*. *Accounts of Chemical Research*, 2014. 48(1): p. 13-21.
6. Son, J.S., et al., *Colloidal Synthesis of Ultrathin Two - Dimensional Semiconductor Nanocrystals*. *Advanced Materials*, 2011. 23(28): p. 3214-3219.
7. Nasilowski, M., et al., *Two-dimensional colloidal nanocrystals*. *Chemical Reviews*, 2016. 116(18): p. 10934-10982.
8. Bouet, C., et al., *Flat colloidal semiconductor nanoplatelets*. *Chemistry of Materials*, 2013. 25(8): p. 1262-1271.
9. Hu, J., et al., *Linearly polarized emission from colloidal semiconductor quantum rods*. *Science*, 2001. 292(5524): p. 2060-2063.
10. Brus, L., *A simple model for the ionization potential, electron affinity, and aqueous redox potentials of small semiconductor crystallites*. *Journal of Chemical Physics*, 1983. 79(11): p. 5566-5571.
11. Murray, C., D.J. Norris, and M.G. Bawendi, *Synthesis and characterization of nearly monodisperse CdE (E= sulfur, selenium, tellurium) semiconductor nanocrystallites*. *Journal of the American Chemical Society*, 1993. 115(19): p. 8706-8715.
12. Peng, Z.A. and X. Peng, *Formation of high-quality CdTe, CdSe, and CdS nanocrystals using CdO as precursor*. *Journal of the American Chemical Society*, 2001. 123(1): p. 183-184.
13. Qu, L., Z.A. Peng, and X. Peng, *Alternative routes toward high quality CdSe nanocrystals*. *Nano Letters*, 2001. 1(6): p. 333-337.
14. Yu, W.W. and X. Peng, *Formation of high-quality CdS and other II-VI semiconductor nanocrystals in noncoordinating solvents: tunable reactivity of monomers*. *Angewandte Chemie International Edition*, 2002. 41(13): p. 2368-2371.
15. Hines, M.A. and P. Guyot-Sionnest, *Synthesis and characterization of strongly luminescing ZnS-capped CdSe nanocrystals*. *The Journal of Physical Chemistry*, 1996. 100(2): p. 468-471.
16. Li, J.J., et al., *Large-scale synthesis of nearly monodisperse CdSe/CdS core/shell nanocrystals using air-stable reagents via successive ion layer adsorption and reaction*. *Journal of the American Chemical Society*, 2003. 125(41): p. 12567-12575.
17. Talapin, D.V., et al., *Highly luminescent monodisperse CdSe and CdSe/ZnS nanocrystals synthesized in a hexadecylamine- trioctylphosphine oxide- trioctylphosphine mixture*. *Nano letters*, 2001. 1(4): p. 207-211.
18. Peng, X., et al., *Shape control of CdSe nanocrystals*. *Nature*, 2000. 404(6773): p. 59.
19. Yu, H., et al., *Cadmium selenide quantum wires and the transition from 3D to 2D confinement*. *Journal of the American Chemical Society*, 2003. 125(52): p. 16168-16169.
20. Manna, L., E.C. Scher, and A.P. Alivisatos, *Synthesis of soluble and processable rod-, arrow-, teardrop-, and tetrapod-shaped CdSe nanocrystals*. *Journal of the American Chemical Society*, 2000. 122(51): p. 12700-12706.
21. Manna, L., et al., *Controlled growth of tetrapod-branched inorganic nanocrystals*. *Nature materials*, 2003. 2(6): p. 382.

22. Joo, J., et al., *Low-temperature solution-phase synthesis of quantum well structured CdSe nanoribbons*. Journal of the American Chemical Society, 2006. 128(17): p. 5632-5633.
23. Ithurria, S. and B. Dubertret, *Quasi 2D colloidal CdSe platelets with thicknesses controlled at the atomic level*. Journal of the American Chemical Society, 2008. 130(49): p. 16504-16505.
24. Ithurria, S., et al., *Colloidal nanoplatelets with two-dimensional electronic structure*. Nature Materials, 2011. 10(12): p. 936.
25. Yang, Y.A., et al., *Synthesis of CdSe and CdTe nanocrystals without precursor injection*. Angewandte Chemie International Edition, 2005. 44(41): p. 6712-6715.
26. Chan, E.M., A.P. Alivisatos, and R.A. Mathies, *High-temperature microfluidic synthesis of CdSe nanocrystals in nanoliter droplets*. Journal of the American Chemical Society, 2005. 127(40): p. 13854-13861.
27. Nightingale, A.M., et al., *Large-scale synthesis of nanocrystals in a multichannel droplet reactor*. Journal of Materials Chemistry A, 2013. 1(12): p. 4067-4076.
28. Wang, F., et al., *Kinetics and mechanisms of aggregative nanocrystal growth*. Chemistry of Materials, 2013. 26(1): p. 5-21.
29. Reiss, H., *The growth of uniform colloidal dispersions*. Journal of Chemical Physics, 1951. 19(4): p. 482-487.
30. Thanh, N.T., N. Maclean, and S. Mahiddine, *Mechanisms of nucleation and growth of nanoparticles in solution*. Chemical Reviews, 2014. 114(15): p. 7610-7630.
31. Kwon, S.G. and T. Hyeon, *Formation mechanisms of uniform nanocrystals via hot-injection and heat-up methods*. Small, 2011. 7(19): p. 2685-2702.
32. Mullin, J.W., *Crystallization*. 2001: Elsevier.
33. Sugimoto, T., *Monodispersed particles*. 2001: Elsevier.
34. Voorhees, P.W., *The theory of Ostwald ripening*. Journal of Statistical Physics, 1985. 38(1-2): p. 231-252.
35. Park, J., et al., *Synthesis of monodisperse spherical nanocrystals*. Angewandte Chemie International Edition, 2007. 46(25): p. 4630-4660.
36. Sugimoto, T., *Formation of monodispersed nano- and micro-particles controlled in size, shape, and internal structure*. Chemical Engineering & Technology: Industrial Chemistry - Plant Equipment - Process Engineering - Biotechnology, 2003. 26(3): p. 313-321.
37. Wulff, G., *Xxv. zur frage der geschwindigkeit des wachstums und der auflösung der krystallflächen*. Zeitschrift für Kristallographie-Crystalline Materials, 1901. 34(1-6): p. 449-530.
38. Xia, Y., et al., *Shape-controlled synthesis of metal nanocrystals: simple chemistry meets complex physics?* Angewandte Chemie International Edition, 2009. 48(1): p. 60-103.
39. Bealing, C.R., et al., *Predicting nanocrystal shape through consideration of surface-ligand interactions*. ACS Nano, 2012. 6(3): p. 2118-2127.
40. Sugimoto, T., *Stable crystal habits of general tetradecahedral microcrystals and monodisperse agbr particles: I. Equilibrium forms and steady forms*. Journal of Colloid and Interface Science, 1983. 91(1): p. 51-68.
41. Sugimoto, T., *Stable crystal habits of general tetradecahedral microcrystals and monodisperse agbr particles. II. Steady forms in open systems*. Journal of Colloid and Interface Science, 1983. 93(2): p. 461-473.
42. Wang, W., et al., *Ligand control of growth, morphology, and capping structure of colloidal CdSe nanorods*. Chemistry of Materials, 2007. 19(10): p. 2573-2580.
43. Puzder, A., et al., *The effect of organic ligand binding on the growth of CdSe nanoparticles probed by ab initio calculations*. Nano Letters, 2004. 4(12): p. 2361-2365.
44. Peng, Z.A. and X. Peng, *Mechanisms of the shape evolution of CdSe nanocrystals*. Journal of the American Chemical Society, 2001. 123(7): p. 1389-1395.
45. Peng, X., *Mechanisms for the shape - control and shape - evolution of colloidal semiconductor nanocrystals*. Advanced Materials, 2003. 15(5): p. 459-463.



46. Lofton, C. and W. Sigmund, *Mechanisms controlling crystal habits of gold and silver colloids*. *Advanced Functional Materials*, 2005. 15(7): p. 1197-1208.
47. Viswanath, B., et al., *Mechanistic aspects of shape selection and symmetry breaking during nanostructure growth by wet chemical methods*. *Journal of Physical Chemistry C*, 2009. 113(39): p. 16866-16883.
48. Riedinger, A., et al., *An intrinsic growth instability in isotropic materials leads to quasi-two-dimensional nanoplatelets*. *Nature Materials*, 2017. 16(7): p. 743.
49. Niederberger, M. and H. Cölfen, *Oriented attachment and mesocrystals: non-classical crystallization mechanisms based on nanoparticle assembly*. *Physical Chemistry Chemical Physics*, 2006. 8(28): p. 3271-3287.
50. De Yoreo, J.J., et al., *Crystallization by particle attachment in synthetic, biogenic, and geologic environments*. *Science*, 2015. 349(6247): p. aaa6760.
51. You, H. and J. Fang, *Particle-mediated nucleation and growth of solution-synthesized metal nanocrystals: a new story beyond the LaMer curve*. *Nano Today*, 2016. 11(2): p. 145-167.
52. Penn, R.L. and J.F. Banfield, *Imperfect oriented attachment: dislocation generation in defect-free nanocrystals*. *Science*, 1998. 281(5379): p. 969-971.
53. Yuk, J.M., et al., *High-resolution EM of colloidal nanocrystal growth using graphene liquid cells*. *Science*, 2012. 336(6077): p. 61-64.
54. Li, D., et al., *Direction-specific interactions control crystal growth by oriented attachment*. *Science*, 2012. 336(6084): p. 1014-1018.
55. Liao, H.-G., et al., *Real-time imaging of Pt3Fe nanorod growth in solution*. *Science*, 2012. 336(6084): p. 1011-1014.
56. Tang, Z., N.A. Kotov, and M. Giersig, *Spontaneous organization of single CdTe nanoparticles into luminescent nanowires*. *Science*, 2002. 297(5579): p. 237-240.
57. Cho, K.-S., et al., *Designing PbSe nanowires and nanorings through oriented attachment of nanoparticles*. *Journal of the American Chemical Society*, 2005. 127(19): p. 7140-7147.
58. Schliehe, C., et al., *Ultrathin PbS sheets by two-dimensional oriented attachment*. *Science*, 2010. 329(5991): p. 550-553.
59. Liu, Y.-H., et al., *Lamellar assembly of cadmium selenide nanoclusters into quantum belts*. *Journal of the American Chemical Society*, 2011. 133(42): p. 17005-17013.
60. Meng, F. and S. Jin, *The solution growth of copper nanowires and nanotubes is driven by screw dislocations*. *Nano Letters*, 2011. 12(1): p. 234-239.
61. Morin, S.A., et al., *Screw dislocation-driven growth of two-dimensional nanoplates*. *Nano Letters*, 2011. 11(10): p. 4449-4455.
62. Boles, M.A., et al., *The surface science of nanocrystals*. *Nature Materials*, 2016. 15(2): p. 141.
63. Anderson, N.C., et al., *Ligand exchange and the stoichiometry of metal chalcogenide nanocrystals: spectroscopic observation of facile metal-carboxylate displacement and binding*. *Journal of the American Chemical Society*, 2013. 135(49): p. 18536-18548.
64. Owen, J., *The coordination chemistry of nanocrystal surfaces*. *Science*, 2015. 347(6222): p. 615-616.
65. Garcia-Rodriguez, R., et al., *Conversion reactions of cadmium chalcogenide nanocrystal precursors*. *Chemistry of Materials*, 2013. 25(8): p. 1233-1249.
66. Owen, J.S., et al., *Reaction chemistry and ligand exchange at cadmium– selenide nanocrystal surfaces*. *Journal of the American Chemical Society*, 2008. 130(37): p. 12279-12281.
67. Sowers, K.L., B. Swartz, and T.D. Krauss, *Chemical mechanisms of semiconductor nanocrystal synthesis*. *Chemistry of Materials*, 2013. 25(8): p. 1351-1362.
68. García-Rodríguez, R.I. and H. Liu, *Mechanistic insights into the role of alkylamine in the synthesis of CdSe nanocrystals*. *Journal of the American Chemical Society*, 2014. 136(5): p. 1968-1975.
69. Klimov, V.I., et al., *Single-exciton optical gain in semiconductor nanocrystals*. *Nature*, 2007. 447(7143): p. 441.
70. Yin, Y. and A.P. Alivisatos, *Colloidal nanocrystal synthesis and the organic–inorganic interface*. *Nature*, 2004. 437(7059): p. 664.

71. Gur, I., et al., *Air-stable all-inorganic nanocrystal solar cells processed from solution*. *Science*, 2005. 310(5747): p. 462-465.
72. Michalet, X., et al., *Quantum dots for live cells, in vivo imaging, and diagnostics*. *Science*, 2005. 307(5709): p. 538-544.
73. Tessler, N., et al., *Efficient near-infrared polymer nanocrystal light-emitting diodes*. *Science*, 2002. 295(5559): p. 1506-1508.
74. Saxena, P. and N. Thirupathi, *Reactions of Cd (OAc) 2· 2H<sub>2</sub>O with variously substituted pyridines. Efforts to unravel the factors that determine structure/nuclearity of the products*. *Polyhedron*, 2015. 98: p. 238-250.
75. Harrison, W. and J. Trotter, *Crystal and molecular structure of cadmium diacetate dihydrate*. *Journal of the Chemical Society, Dalton Transactions*, 1972(8-9): p. 956-960.
76. Yener, D.O., et al., *Synthesis of nanosized silver platelets in octylamine-water bilayer systems*. *Langmuir*, 2002. 18(22): p. 8692-8699.
77. García-Rodríguez, R. and H. Liu, *Solution structure of cadmium carboxylate and its implications for the synthesis of cadmium chalcogenide nanocrystals*. *Chemical Communications*, 2013. 49(71): p. 7857-7859.
78. García-Rodríguez, R.I. and H. Liu, *Mechanistic study of the synthesis of CdSe nanocrystals: release of selenium*. *Journal of the American Chemical Society*, 2012. 134(3): p. 1400-1403.
79. Morris, T. and T. Zubkov, *Steric effects of carboxylic capping ligands on the growth of the CdSe quantum dots*. *Colloids and Surfaces A: Physicochemical and Engineering Aspects*, 2014. 443: p. 439-449.
80. Pang, Q., et al., *CdSe nano-tetrapods: controllable synthesis, structure analysis, and electronic and optical properties*. *Chemistry of Materials*, 2005. 17(21): p. 5263-5267.
81. Hassinen, A., et al., *Nuclear magnetic resonance spectroscopy demonstrating dynamic stabilization of CdSe quantum dots by alkylamines*. *Journal of Physical Chemistry Letters*, 2010. 1(17): p. 2577-2581.
82. Yu, W.W., et al., *Experimental determination of the extinction coefficient of CdTe, CdSe, and CdS nanocrystals*. *Chemistry of Materials*, 2003. 15(14): p. 2854-2860.
83. Drijvers, E., et al., *Ligand displacement exposes binding site heterogeneity on CdSe nanocrystal surfaces*. *Chemistry of Materials*, 2018. 30(3): p. 1178-1186.
84. Talapin, D.V., et al., *Synthesis and surface modification of amino-stabilized CdSe, CdTe and InP nanocrystals*. *Colloids and Surfaces A: Physicochemical and Engineering Aspects*, 2002. 202(2-3): p. 145-154.
85. Huang, X., V. Parashar, and M. Gijs, *Synergistic effect of carboxylic and amine ligands on the synthesis of CdSe nanocrystals*. *RSC Advances*, 2016. 6(91): p. 88911-88915.
86. Li, L.S., et al., *High quality ZnSe and ZnS nanocrystals formed by activating zinc carboxylate precursors*. *Nano letters*, 2004. 4(11): p. 2261-2264.
87. Pradhan, N., et al., *Surface ligand dynamics in growth of nanocrystals*. *Journal of the American Chemical Society*, 2007. 129(30): p. 9500-9509.
88. Foos, E.E., et al., *Synthesis and surface composition study of CdSe nanoclusters prepared using solvent systems containing primary, secondary, and tertiary amines*. *Chemistry of Materials*, 2006. 18(12): p. 2886-2894.
89. Jose, R., et al., *Structure– property correlation of CdSe clusters using experimental results and first-principles DFT calculations*. *Journal of the American Chemical Society*, 2006. 128(2): p. 629-636.
90. Sun, Z., et al., *Ligand effects of amine on the initial nucleation and growth processes of CdSe nanocrystals*. *The Journal of Physical Chemistry C*, 2010. 114(22): p. 10126-10131.
91. van Embden, J. and P. Mulvaney, *Nucleation and growth of CdSe nanocrystals in a binary ligand system*. *Langmuir*, 2005. 21(22): p. 10226-10233.
92. Liu, H., J.S. Owen, and A.P. Alivisatos, *Mechanistic study of precursor evolution in colloidal group II–VI semiconductor nanocrystal synthesis*. *Journal of the American Chemical Society*, 2007. 129(2): p. 305-312.

93. Leatherdale, C.A., et al., *On the absorption cross section of CdSe nanocrystal quantum dots*. The Journal of Physical Chemistry B, 2002. 106(31): p. 7619-7622.
94. Ithurria, S., et al., *Colloidal nanoplatelets with two-dimensional electronic structure*. Nat Mater, 2011. 10(12): p. 936-41.
95. Li, Z. and X. Peng, *Size/shape-controlled synthesis of colloidal CdSe quantum disks: ligand and temperature effects*. Journal of the American Chemical Society, 2011. 133(17): p. 6578-86.
96. Son, J.S., et al., *Large-scale soft colloidal template synthesis of 1.4 nm thick CdSe nanosheets*. Angew Chem Int Ed, 2009. 48(37): p. 6861-4.
97. Liu, Y.H., et al., *Lamellar assembly of cadmium selenide nanoclusters into quantum belts*. Journal of the American Chemical Society, 2011. 133(42): p. 17005-13.
98. Bouet, C., et al., *Two-Dimensional Growth of CdSe Nanocrystals, from Nanoplatelets to Nanosheets*. Chemistry of Materials, 2013. 25(4): p. 639-645.
99. Mahler, B., et al., *Core/shell colloidal semiconductor nanoplatelets*. Journal of the American Chemical Society, 2012. 134(45): p. 18591-18598.
100. Ithurria, S., G. Bousquet, and B. Dubertret, *Continuous transition from 3D to 1D confinement observed during the formation of CdSe nanoplatelets*. Journal of the American Chemical Society, 2011. 133(9): p. 3070-7.
101. Chen, Y., et al., *Symmetry-Breaking for Formation of Rectangular CdSe Two-Dimensional Nanocrystals in Zinc-Blende Structure*. Journal of the American Chemical Society, 2017. 139(29): p. 10009-10019.
102. Yu, D. and F. Liu, *Synthesis of carbon nanotubes by rolling up patterned graphene nanoribbons using selective atomic adsorption*. Nano Letters, 2007. 7(10): p. 3046-3050.
103. Iijima, S., *Helical microtubules of graphitic carbon*. Nature, 1991. 354(6348): p. 56.
104. Zhou, M., et al., *CdSe Nanotube Arrays on ITO via Aligned ZnO Nanorods Templating*. Chemistry of Materials, 2010. 22(1): p. 64-69.
105. Kim, J.W., et al., *Thorny CdSe nanotubes via an aqueous anion exchange reaction process and their photoelectrochemical applications*. Journal of Materials Chemistry, 2012. 22(39): p. 20889.
106. Chen, P.E., et al., *Tight Binding of Carboxylate, Phosphonate, and Carbamate Anions to Stoichiometric CdSe Nanocrystals*. Journal of the American Chemical Society, 2017. 139(8): p. 3227-3236.
107. Wu, Z., et al., *Self-assembly of nanoclusters into mono-, few-, and multilayered sheets via dipole-induced asymmetric van der waals attraction*. ACS Nano, 2015. 9(6): p. 6315-6323.
108. Tanford, C., *Micelle shape and size*. The Journal of Physical Chemistry, 1972. 76(21): p. 3020-3024.
109. Chen, D., et al., *Structure identification of two-dimensional colloidal semiconductor nanocrystals with atomic flat basal planes*. Nano Letters, 2015. 15(7): p. 4477-4482.
110. Colfen, H. and M. Antonietti, *Mesocrystals: inorganic superstructures made by highly parallel crystallization and controlled alignment*. Angew Chem Int Ed, 2005. 44(35): p. 5576-91.
111. Debnath, S., R. Cherian, and P. Mahadevan, *The role of passivants on the stoichiometry of CdSe and GaAs nanocrystals*. Journal of Physical Chemistry C, 2013. 117(42): p. 21981-21987.
112. Remškar, M., *Inorganic nanotubes*. Encyclopedia of Inorganic and Bioinorganic Chemistry, 2011.
113. Jun, Y.w., J.s. Choi, and J. Cheon, *Shape control of semiconductor and metal oxide nanocrystals through nonhydrolytic colloidal routes*. Angewandte Chemie International Edition, 2006. 45(21): p. 3414-3439.
114. Lyashchova, A., et al., *Optical absorption, induced bleaching, and photoluminescence of CdSe nanoplatelets grown in cadmium octanoate matrix*. Nanoscale Research Letters, 2014. 9(1): p. 88.
115. Jiang, Y., et al., *Synthesis of CdSe Nanoplatelets without Short-Chain Ligands: Implication for Their Growth Mechanisms*. ACS Omega, 2018. 3(6): p. 6199-6205.
116. Huang, X., V.K. Parashar, and M.A. Gijs, *Spontaneous Formation of CdSe Photoluminescent Nanotubes with Visible-Light Photocatalytic Performance*. ACS Central Science, 2019.
117. Cozzoli, P.D., et al., *Shape and phase control of colloidal ZnSe nanocrystals*. Chemistry of Materials, 2005. 17(6): p. 1296-1306.

118. Yong, K.-T., et al., *Shape control of CdS nanocrystals in one-pot synthesis*. Journal of Physical Chemistry C, 2007. 111(6): p. 2447-2458.
119. Christodoulou, S., et al., *Chloride-Induced thickness control in CdSe nanoplatelets*. Nano Letters, 2018. 18(10): p. 6248-6254.
120. Zherebetsky, D., et al., *Hydroxylation of the surface of PbS nanocrystals passivated with oleic acid*. Science, 2014. 344(6190): p. 1380-1384.
121. Alves, J., K. Watari, and A. Ferraz, *Calculated atomic structures of ZnS, ZnSe and ZnTe (110) surfaces*. Solid State Communications, 1993. 87(11): p. 1001-1004.
122. Watari, K., J. Alves, and A. Ferraz, *Atomic Structures of CdTe and CdSe (110) Surfaces*. Brazilian Journal of Physics, 1996. 26: p. 271-273.
123. Deacon, G. and R. Phillips, *Relationships between the carbon-oxygen stretching frequencies of carboxylato complexes and the type of carboxylate coordination*. Coordination Chemistry Reviews, 1980. 33(3): p. 227-250.
124. Huang, X., V. Parashar, and M.A. Gijs, *Nucleation and Growth Behavior of CdSe Nanocrystals Synthesized in the Presence of Oleylamine Coordinating Ligand*. Langmuir, 2018. 34(21): p. 6070-6076.
125. Penn, R.L., *Kinetics of oriented aggregation*. Journal of Physical Chemistry B, 2004. 108(34): p. 12707-12712.

# Curriculum Vitae

---

## PERSONAL INFORMATION

**Name:** Xiaopeng Huang **Date of Birth:** 09/1989  
**Gender:** Male **Citizenship:** People's Republic of China  
**Email:** [xiaopeng.huang@epfl.ch](mailto:xiaopeng.huang@epfl.ch)  
**Address:** BM 3132 (Bâtiment BM), Station 17, CH-1015 Lausanne  
ResearchGate: [https://www.researchgate.net/profile/Xiaopeng\\_Huang9](https://www.researchgate.net/profile/Xiaopeng_Huang9)

---

## EDUCATIONAL BACKGROUND

**2007—2011:** Acquiring **bachelor's degree** in School of Materials Science and Engineering, Shandong University (SDU), Jinan, 250061, Shandong Province, P.R. China

**Major:** Materials science and engineering

**2009—2010:** Visiting Study as an **Exchange Student** in Collage of Materials Science and Engineering, Huazhong University of Science and Technology (HUST), Wuhan, 430074, Hubei Province, P.R. China,

**Major:** Materials science and engineering

**2011—2014:** Studying for a **master's degree** in Department of Chemistry, Renmin University of China (RUC), No. 59 Zhongguancun Street, Haidian District, Beijing, 100872, P.R. China

**Major:** Applied chemistry, supervised by **Prof. Yapei Wang**

**2014—2015:** **Research assistant** in the Morbidelli Group at ETHZ in Switzerland, supervised by **Prof. Hua Wu**

**2015-present:** **PhD student** in Lab of Microsystem at EPFL in Switzerland, supervised by **Prof. Martin Gijs**

---

## RESEARCH EXPERIENCES

- i. "Controllable synthesis of 2D CdSe colloidal nanocrystals", supervised by **Prof. Martin Gijs**, Swiss Federal Institute of Technology in Lausanne (EPFL), Switzerland, 2015-present
  - ii. "High-loading cathode materials for Li-S battery", supervised by **Prof. Hua Wu**, Swiss Federal Institute of Technology in Zurich (ETHZ), Switzerland, 2014-2015.
  - iii. "Anisotropic multifunctional polymer particles preparation and application", supervised by **Prof. Yapei Wang**, Renmin University of China (RUC), 2012-2014.
  - iv. "The growth mechanism research of the artificial diamonds under high temperature and high pressure (HTHP) based on acoustic emission technique", supervised by **Prof. Musen Li**, Shandong University (SDU), 2011
  - v. "TiB<sub>3</sub> particles enhanced composites for the optimization in automobile piston", supervised by **Prof. Xiangfa Liu**, Shandong University (SDU), 2009
- 

## PUBLICATIONS

- 1) X. Huang, Q. Qian, X. Zhang, W. Du, H. Xu, Y. Wang, "Assembly of Carbon Nanotubes on Polymer articles: Towards Rapid Shape Change by Near-Infrared Light", *Part. Part. Syst. Charact.* **2013**, *30*, 235–240  
<http://onlinelibrary.wiley.com/doi/10.1002/ppsc.201200130/full>

- 2) X. Huang, Q. Qian, Y. Wang, “Anisotropic Particles from a One-Pot Double Emulsion Induced by Partial Wetting and Their Triggered Release”, *Small* **2014**, *10*, 1412-1420. (highlighted by Materials Views China)  
<http://onlinelibrary.wiley.com/doi/10.1002/sml.201302743/epdf>
- 3) X. Huang, R. Fang, D. Wang, J. Wang, H. Xu, Y. Wang, “Tuning the Polymer Amphiphilicity Towards One-step Multiple Emulsion”, *Small* **2014**, DOI: 10.1002/sml.201402271. (highlighted by Materials Views China)  
<http://onlinelibrary.wiley.com/doi/10.1002/sml.201402271/full>
- 4) X. Huang, D. Wang, Y. Wang, “Managing the Phase Separation in Double Emulsion by Tuning Amphiphilicity via a Supramolecular Route”, *Langmuir* **2014**, *30*, 14460–14468. (Co-first author)  
<http://onlinelibrary.wiley.com/doi/10.1002/sml.201400087/full>
- 5) X. Huang, Y. Yang, J. Shi, H. T. Ngo, C. Shen, W. Du, Y. Wang, “High Internal Phase Emulsion via Tailoring Polymer Amphiphilicity Towards Efficient NIR-sensitive Bacterial Filter”, *Small* **2015**, *11*, 4876-4883. (Co-first author, **frontispiece cover, highlighted by Materials Views China**)  
<https://onlinelibrary.wiley.com/doi/abs/10.1002/sml.201501396>
- 6) X. Huang, V. K. Parashar, M. A.M. Gijs, “Synergistic Effect of Carboxylic and Amine ligands on the Synthesis of CdSe Nanocrystals”, *RSC Adv.* **2016**, *6*, 88911-88915.  
<https://pubs.rsc.org/en/content/articlelanding/2016/ra/c6ra20812f/unauth#1divAbstract>
- 7) X. Huang, V. K. Parashar, M. A.M. Gijs, “Nucleation and Growth Behavior of CdSe Nanocrystals Synthesized in Presence of Oleylamine Coordinating Ligand”, *Langmuir* **2018**, *34*, 6070-6076.  
<https://pubs.acs.org/doi/abs/10.1021/acs.langmuir.7b01337>
- 8) X. Huang, V. K. Parashar, M. A.M. Gijs, “Spontaneous Formation of CdSe Photoluminescent Nanotubes with Visible-light Photocatalytic Performance”, *ACS Cent. Sci.* **2019**, *accepted* (**supplementary cover**).
- 9) Q. Qian, X. Huang, X. Zhang, Z. Xie, Y. Wang, “One-step Preparation of Macroporous Polymer Microspheres with Multichamber Interconnected Structure: A Candidate for Trapping Biomacromolecules”, *Angew. Chem. Int. Ed.* **2013**, *52*, 10625-10629  
<http://onlinelibrary.wiley.com/doi/10.1002/anie.201305003/full>
- 10) J. Wang, X. Zhang, X. Huang, S. Wang, Q. Qian, W. Du and Y. Wang, “Forcing water-dispersible carbon nanotubes continuously trapped in paper for cheap gas sensors”, *Small* **2013**, *9*, 3759-3764.  
<http://onlinelibrary.wiley.com/doi/10.1002/sml.201300655/full>
- 11) X. Zhang, J. Zhu, X. Huang, Q. Qian, Y. Wang, “Controllable and Facile Fabrication of Gold Nanostructures for Selective Metal-assisted Etching of Silicon”, *Small* **2014**, *10*, 2451-2458.  
<http://onlinelibrary.wiley.com/doi/10.1002/sml.201400087/full>
- 12) Y. Yang, X. Huang, X. Zhang, F. Jiang, X. Zhang, Y. Wang, “Supercritical Fluid Driven Polymer Phase Separation for Microlens with Tunable Dimension and Curvature”, *ACS Appl. Mater. Interfaces*, **2016**, *8*, 8849–8858  
<https://pubs.acs.org/doi/abs/10.1021/acsami.6b01951>
- 13) L. Jin, X. Huang, G. Zeng, H. Wu, M. Morbidelli, “Conductive Framework of Inverse Opal Structure for Sulfur Cathode in Lithium-Sulfur Batteries.” *Sci. Rep.* **2016**, DOI: 10.1038/srep32800  
<https://www.nature.com/articles/srep32800/figures/>

---

## **AWARDS**

- i. Third prize for excellent student of Shandong University (2010)
  - ii. Individual award for the excellent performance in the “second-campus experience” of Shandong University (2010)
  - iii. First prize for excellent student of Renmin University of China (2012-2013)
  - iv. China Scholarship Council (CSC) Scholarship for Doctoral Study (2014-2018)
- 

## **EXPERIMENT SKILLS**

Emulsion preparation, colloidal nanocrystal preparation, cleanroom process, SEM, AFM, XRD, TEM, STEM, FTIR, NMR, florescent microscope, UV-vis, fluorescence, DLS, DSC-TGA, GC characterization, interfacial intension and contact angle measures and so forth





